Charles University in Prague
Faculty of Science

Developmental and Cell Biology

Anastasiya Klebanovych, M.Sc.

REGULATORY MECHANISMS OF CENTROSOMAL MICROTUBULE NUCLEATION

Ph.D. Thesis

Supervisor: doc. RNDr. Pavel Dráber, DSc.

Laboratory of Biology of Cytoskeleton
Institute of Molecular Genetics of the Czech Academy of Sciences

Prague, 2021

Prohlášení:

Prohlašuji, že jsem závěrečnou práci zpracovala samostatně a že jsem uvedla všechny použité informační zdroje a literaturu. Tato práce ani její podstatná část nebyla předložena k získání jiného nebo stejného akademického titulu.

V Praze dne 15. 3. 2021   Anastasiya Klebanovych, M.Sc.

Prohlášení:

Jménem ostatních spoluautorů publikací, které tvoří základ disertační práce Anastasiya Klebanovych, potvrzuji, že podíl autorky na jejich přípravě je popsaný v komentářích k jednotlivým publikacím pravdivě.

V Praze dne 15. 3. 2021   doc. RNDr. Pavel Dráber, DSc.

Acknowledgment:

ABBREVIATIONS

Ag	Antigen
AFM	Atomic force microscopy
BMMC(s)	Bone marrow-derived mast cell(s)
DAG	Diacylglycerol
DDRGK1	DDRGK domain-containing protein 1
EB(s)	End-binding protein(s)
ER	Endoplasmic reticulum
FcεRI	High-affinity IgE receptor
GAP	GTPase-activating protein
GRIP1	N-terminal γ-tubulin ring protein 1 domain
CDK5RAP2	Cyclin-dependent kinase 5 regulatory subunit associated protein 2
CDK5RAP3	CDK5 regulatory subunit-associated protein 3
GCP	γ-Tubulin complex protein
GEF	Guanine nucleotide exchange factor
GIT1	G-protein-coupled receptor (GCPR)-kinase-interacting protein 1
IgE	Immunoglobulin E
ITAM	Immunoreceptor tyrosine-based activation motif
IPA-3	Selective non-ATP competitive group I PAKs inhibitor
IP_3	Inositol trisphosphate
KD	Knockdown (reduction of protein level by RNAi technique)
KO	Knockout (deletion of protein by gene-editing technique)
LAT	Linker for activation of T cells
MAP(s)	Microtubule associated protein(s)
MOZART1	Mitotic-spindle organizing protein associated with a ring of γ-tubulin 1, MZT1
MOZART2	Mitotic-spindle organizing protein associated with a ring of γ-tubulin 2, MZT2
MTOC(s)	Microtubule-organizing center(s)
MTBP(s)	Microtubule-binding protein(s)
NA	Numerical aperture of the microscopy objective
NEDD1	Neural precursor cell expressed developmentally downregulated 1, GCP-WD
NTAL	Non-T-cell activation linker
PAK1	p21 protein Cdc42/Rac-activated kinase 1
PCM	Pericentriolar material
PIP_2	Phosphatidylinositol (4,5)-bisphosphate
PIP_3	Phosphatidylinositol (3,4,5)-trisphosphate
PI3K	Phosphatidylinositol-3-kinase
PKCβ	Conventional protein kinase C isoforms βI and βII
PTM(s)	Post-translational modification(s)
PTP(s)	Protein tyrosine phosphatase(s)
P-Tyr	Protein, phosphorylated on tyrosine
ROI	Region of interest
SH2	Src Homology 2 domain
SHP-1	Src homology region 2 domain-containing phosphatase-1

SPB	Spindle pole body
SOCE	Store-operated Ca^{2+} entry
TBA(s)	Tubulin-binding agent(s)
TEM	Transmission electron microscopy
UFL1	E3 UFM1-protein ligase 1
UFM1	Ubiquitin-fold modifier 1
XMAP215	Xenopus microtubule assembly protein 215 kDa
βPIX	p21-activated kinase interacting exchange factor β
γTuSC	γ-Tubulin small complex
γTuRC	γ-Tubulin ring complex
+TIP(s)	Microtubule plus (+)-end tracking protein(s)
−TIP(s)	Microtubule minus (−)-end tracking protein(s)

ABSTRACT

The spatio-temporal organization and dynamic behavior of microtubules accurately react to cellular needs during intracellular transport, signal transduction, growth, division, and differentiation. The cell generates centrosomal microtubules *de novo* with the help of γ-tubulin complexes (γTuRCs). The post-translational modifications fine-tune microtubule nucleation by targeting the proteins, interacting with γTuRCs. However, the exact signaling pathways, regulating centrosomal microtubule nucleation, remain mostly unknown.

In the presented thesis, we functionally characterized protein tyrosine phosphatase SHP-1 and E3 UFM-protein ligase 1 (UFL1) with its interacting protein CDK5RAP3 (C53) in the regulation of centrosomal microtubule nucleation. We also elucidated the role of actin regulatory protein profilin 1 in this process. We found that SHP-1 formed complexes with γTuRC proteins and negatively regulated microtubule nucleation by modulating the amount of γ-tubulin/γTuRC at the centrosomes in bone marrow-derived mast cells (BMMCs). We suggested a novel mechanism with centrosomal tyrosine-phosphorylated Syk kinase, targeted by SHP-1 during Ag-induced BMMCs activation, regulating microtubules.

We showed for the first time that UFL1/C53 protein complex is involved in the regulation of microtubule nucleation. The C53, which protein level is regulated by UFL1, could associate with centrosomes. Upon induced ER stress, C53 detached from centrosomes, which resulted in the increased microtubule nucleation and ER expansion. Our findings point to a new mechanism for ER stress relief by stimulation of microtubule nucleation.

We reported that profilin 1 extends its regulation functions not only to actin filament polymerization but also to microtubule nucleation. We suggest that profilin 1 plays a dual role as a coordinator of actin and microtubule organization in mammalian cells. Finally, we found that both plant and animal highly purified γ-tubulins lacking associated proteins have the intrinsic property of self-polymerization into filaments.

SOUHRN

Organizace a dynamika mikrotubulů se mění s ohledem na potřeby buňky při jejím růstu, dělení a diferenciaci, a také při vnitrobuněčném transportu i přenosu signálů. Centrozomální mikrotubuly se tvoří pomocí γ-tubulinových komplexů (γTuRC). Ačkoliv signální dráhy regulující mikrotubulární nukleaci zůstávají do značné míry neznámé, posttranslační modifikace stavebních proteinů γTuRC a jejich interakčních partnerů hrají důležitou úlohu při modulaci nukleace. V předkládané disertační práci jsme funkčně charakterizovali úlohu protein tyrosin fosfatázy SHP-1 a E3 UFM-protein ligázy 1 (UFL1) interagující s proteinem CDK5RAP3 (C53) při regulaci centrozomální mikrotubulární nukleace. Rovněž jsme v tomto procesu objasnili roli profilinu 1, regulačního proteinu aktinových filament.

Zjistili jsme, že SHP-1 v žírných buňkách kostní dřeně (BMMC) tvoří komplexy s γTuRC proteiny a inhibuje nukleaci mikrotubulů snížením množství γ-tubulinu/γTuRC v centrozómech. Navrhli jsme nový mechanismus, při kterém aktivní centrozomální Syk kináza, fosforylovaná na tyrosinu a regulovaná SHP-1, moduluje nukleaci mikrotubulů během aktivace BMMC pomocí antigenu.

Poprvé jsme ukázali, že proteinový komplex UFL1/C53 se může podílet na regulaci nukleace mikrotubulů. Protein C53, jehož množství je regulováno UFL1, se váže na centrozómy. Při generování ER stresu se C53 uvolňuje z centrozómů, což vede ke zvýšení nukleace mikrotubulů a dochází také k expanzi ER. Tyto nálezy ukazují na nový mechanismus k uvolnění ER stresu stimulací nukleace mikrotubulů.

Popsali jsme doposud neznámou funkci profilinu 1, který se vedle regulace polymerace aktinu účastní i centrozomální nukleace mikrotubulů. Profilin 1 tak u savčích buněk koordinuje organizaci mikrotubulů a aktinových filament. Zjistili jsme také, že jak rostlinné, tak živočišné vysoce purifikované γ-tubuliny mají schopnost polymerovat i v nepřítomnosti asociovaných proteinů.

TABLE OF CONTENTS

I   INTRODUCTION

Proper spatial and mechanical properties of the eukaryotic cell are governed by the cytoskeleton, the system of three major protein filaments – actin filaments, microtubules, and intermediate filaments. While actin filaments and microtubules are present in all eukaryotes, intermediate filaments are found only in some metazoans. Cytoskeleton spatially organizes the cytoplasm of eukaryotic cells. All cytoskeletal filaments are composed of subunits that form end-to-end and side-to-side protein contacts. Differences in the mechanical properties of cytoskeletal filaments are mainly driven by differences in their subunit structure and assembly manner.

Unlike intermediate filaments, both actin and tubulin can bind and hydrolyze ATP and GTP, respectively, and assemble in a head-to-tail fashion to generate polarized filaments with two distinct ends, a slower-growing minus (–) end and a faster-growing plus (+) end.

As my Ph.D. thesis focuses primarily on regulatory mechanisms of centrosomal microtubule nucleation, the structure and regulation of microtubules are discussed in greater detail in the following chapters.

I.1   Microtubules

The flexible, dynamic structure of microtubules determines essential biological functions in eukaryotic cells. Microtubules play a crucial role in the directed intracellular transport, cellular organelle positioning, cellular signaling, cell motility, ciliogenesis, and segregation of chromosomes during cell division. The spatio-temporal organization and dynamic behavior of microtubules accurately react to cellular needs during growth, differentiation, and division. Various microtubule arrangements are coordinated by tubulin isotypes, tubulin Post-Translational Modifications (PTMs), and Microtubule-Binding Proteins (MTBPs).

I.1.1. Microtubule structure and dynamics

Microtubules are composed of tubulin heterodimers formed by α- and β-tubulin monomers, bound by non-covalent forces in a GTP-dependent manner (Fig. 1A). Soluble tubulin heterodimers form longitudinal contacts and assemble in a head-to-tail fashion into a protofilament. In contrast, "α-α" and "β-β" tubulin lateral contacts are perpendicular to longitudinal and run between the adjacent protofilaments. *In vivo*, the microtubule contains preferably 13 protofilaments polymerized into a hollow tube of about 25 nm in outer diameter. Protofilaments can be arranged into two formations: "A-lattice" or "B-lattice" (Fig. 1B) [1].
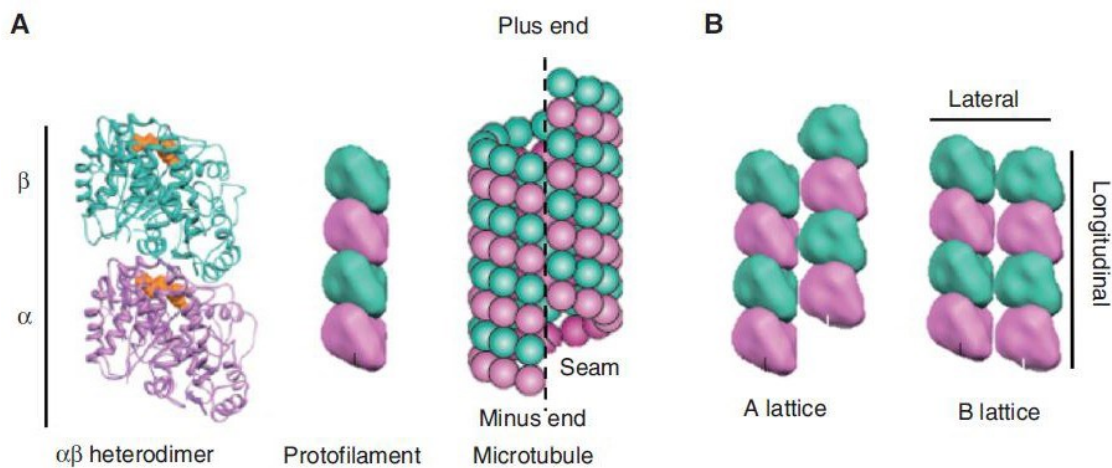
Figure 1 Microtubule assembly. (**A**) Each microtubule heterodimer comprises α- (magenta) and β-tubulin (cyan) subunits, which bind GTP (orange) and assemble in a head-to-tail fashion. Tubulin subunits polymerize into a polarized protofilament with two distinct ends, called "plus (+) end" with exposed β-tubulin, and "minus (-) end" with α-tubulin. (**B**) Predominantly, microtubules consist of 13 protofilaments with lateral bonds formed between two α-tubulins and two β-tubulins of adjacent protofilaments. Because of microtubule helical symmetry, α- and β-tubulin of adjacent protofilaments interact laterally, creating a "seam." Adapted from [2].

In "B-lattice," α-tubulins of neighboring protofilaments lie next to each other, so the lateral interactions connect the same types of tubulin. In "A-lattice," α-tubulins of one protofilament form bonds with β-tubulins of adjacent protofilament. Such thirteen-fold B-lattice geometry results in the formation of a "seam," a disconnection in the microtubule lattice, where lateral interactions occur between α- and β-tubulins of the neighboring 1st and 13th protofilaments.

Microtubules are intrinsically polar filaments as their tubulin subunits always polymerize in a head-to-tail orientation, and protofilaments arrange in the same parallel direction (Fig. 1A). Consequently, the microtubule has two distinct ends: "plus (+) end" with exposed β-

tubulins and "minus (–) end" with α-tubulins. In cells, the microtubule (+)-end grows toward the cell periphery, whereas the (–)-end is anchored in Microtubule-Organizing Center (MTOC).

Microtubules undergo phases of polymerization and depolymerization, a process known as "dynamic instability." GTP hydrolysis and conformational changes in tubulin subunits drive the switching between the growth and shrinkage phases (Fig. 2) [3-5].
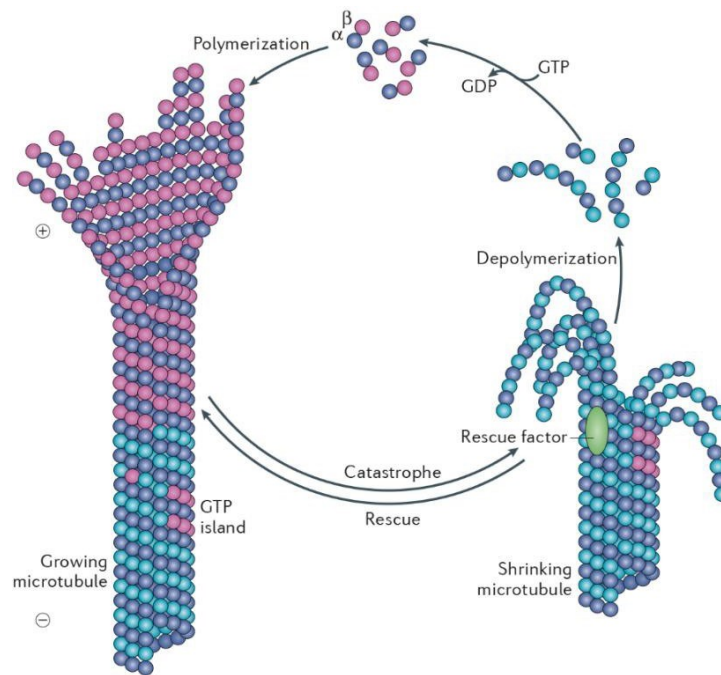
Figure 2 Dynamic instability of microtubules. Binding, hydrolysis, and exchange of GTP in β-tubulin monomer drive the assembly (polymerization) and disassembly (depolymerization) of microtubules. Hydrolysis of GTP molecule is necessary for switching between catastrophe (shrinking microtubule) and rescue phases (growing microtubule). Adapted from [6].

The hydrolysis of GTP, bound to β-tubulin on exchangeable E-site, enables microtubules to switch between polymerization and depolymerization cycles. "Microtubule catastrophe" is defined as the sudden switch from polymerization to depolymerization. The switch from depolymerization to polymerization is called "microtubule rescue" [7]. As GTP hydrolysis is somewhat delayed, growing microtubule ends harbor a stabilizing "GTP cap." The microtubule shaft, on the other hand, consists mostly of GDP-tubulin. Loss of such GTP cap promotes catastrophe and rapid microtubule depolymerization. *In vitro*, "aging" microtubules have a higher chance of switching to catastrophe. In cells, microtubules undergo catastrophe when they meet an obstacle (e.g., the cell cortex), applying pushing forces on growing microtubule ends [8]. Microtubule rescue is induced in the presence of rescue factors and "GTP islands"

found in the microtubule lattice (Fig. 2) [9, 10]. In cells, GTP islands are generated during self-repair by incorporating GTP-bound tubulin into the damaged microtubule wall [11].

I.1.2. Tubulin code

The tubulin code greatly determines the intrinsic properties of microtubules and their subsequent functions. The "tubulin code" stands for a combination of molecular patterns created by α/β-tubulin isotypes and Post-Translational Modifications (PTMs) of these isotypes (Fig. 3). The human tubulin gene superfamily comprises multiple genes encoding the following
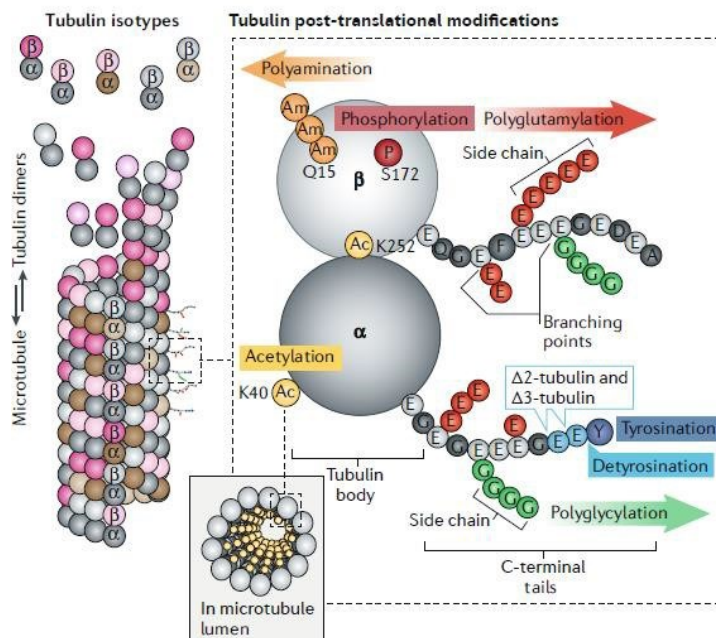
Figure 3 The tubulin code. α-Tubulins are colored in brown and dark grey; β-tubulins are colored in pink and light grey. The differential expression of multiple tubulin genes leads to a combination of mosaic incorporation of tubulin isotypes and PTMs. PTMs decorate either N-terminal globular domains (acetylation (**Ac**), phosphorylation (**P**) and polyamination (**Am**)) or C-terminal tails of tubulins (tyrosination, detyrosination, glycylation, glutamylation, removal of glutamate residues resulting in Δ2-tubulin and Δ3-tubulin) within the microtubule lattice [12, 13].

tubulins: α-, β-, γ-, δ-, and ε-tubulins [14]. However, only α- and β-tubulins can assemble microtubules. On the other hand, γ-tubulin (described in *Chapter I.2.1*) is essential for *de novo* microtubule nucleation. In the human genome, ten protein-coding genes were described for α-tubulin, and ten genes for β-tubulin [15, 16].

Both α-tubulins and β-tubulins have conserved N-terminal globular domains and unstructured C-terminal tails, showing sequence diversity among all tubulin isotypes. The C-terminal tails protrude from the microtubule wall, allowing multiple MTBPs to dock on the C-terminal tail flexible surface. The tubulin genes differential expression and the mosaic incorporation of tubulin isotypes affect microtubule's assembly, dynamics, and interactions with MTBPs [17]. Interestingly, mostly β-tubulin isotypes contribute to the "specialization" of microtubule functions. On the contrary, we know less about the impact of α-tubulin isotypes [12]. Generally, tubulin isotypes incorporate freely into the microtubule lattice, creating a heterogeneous wall. However, a few exceptions show specific tubulin isotypes enrichment. For example, platelets express β1-tubulin, enriched in a specialized microtubule array called "marginal band" [18]. In *D. melanogaster,* β3-tubulin is essential for axoneme (microtubule-based core components of cilia) assembly and spindle formation in the testes [19].

Tubulins carry a wide range of PTMs (Fig. 3). Modifications such as acetylation, methylation, phosphorylation, palmitoylation, ubiquitylation, polyamination, and sumoylation can be found on other proteins. However, some modifications were first discovered for tubulins: enzymatic ribosome-independent tyrosination, glutamylation, polyglutamylation, glycylation, and polyglycylation. The modifications typical for tubulins comprise detyrosination (enzymatic removal of tyrosin on C-terminal tail of α-tubulin), irreversible generation of Δ2-tubulin and Δ3-tubulin (removal of glutamate residues from detyrosinated α-tubulin C-terminal tails) [12]. PTMs create a code pattern, the "tubulin code," resulting in specialized microtubule subpopulations with presumably specific functions. Thus, the tubulin code creates complex yet locally restricted coding language read by multiple MTBPs, which help regulate microtubules' assembly and organization.

I.1.3.   Microtubule-binding proteins

Microtubule intrinsic physical properties and MTBPs spatially and temporally regulate microtubule dynamics. The MTBPs are classified based on (i) binding sites: microtubule (+)-end-tracking proteins (+TIPs), microtubule (–)-end-tracking proteins (–TIPs), lattice-binding proteins, tubulin dimer-binding proteins; or based on (ii) their functions in the regulation of microtubule organization: stabilizing, destabilizing, capping, and cross-linking proteins (Fig. 4). Generally, MTBPs combine multiple activities and, therefore, can be found in different
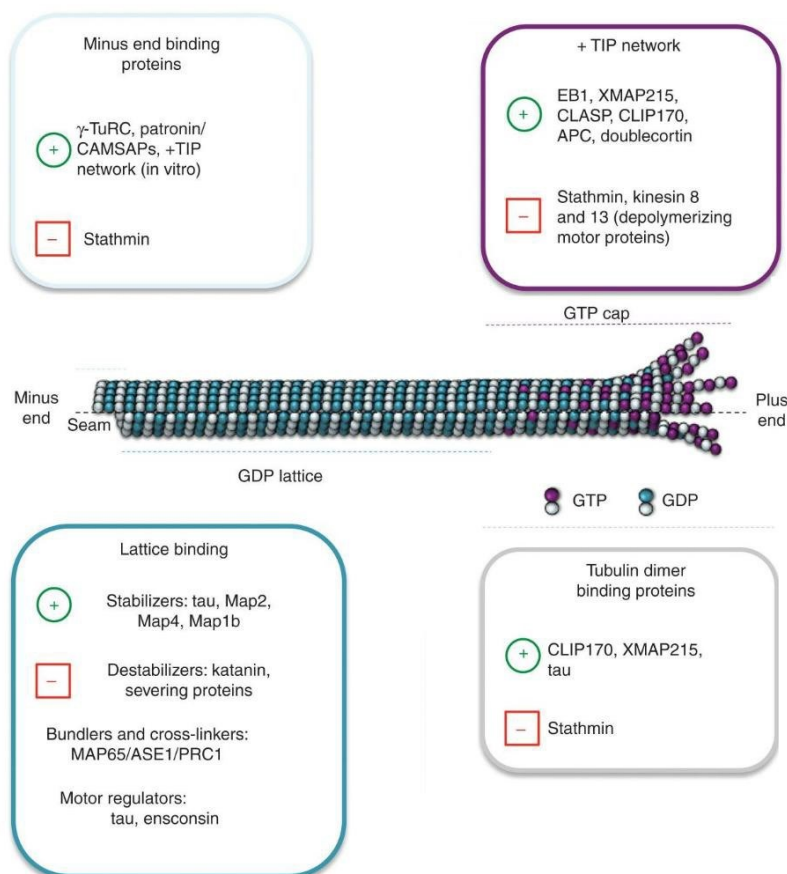
Figure 4 Microtubule-binding proteins (MTBPs). The scheme shows major MTBPs grouped into categories based on their binding sites and functions. The (+) symbol represents positive regulation (stabilization, growth), and the (–) symbol represents negative regulation (destabilization, depolymerization). The figure is modified from [2].

functional groups at the same time. Microtubule motor proteins – mechanochemical ATPases, kinesins, and dyneins – represent a specific class of MTBPs that uses microtubules as railways for the directed intracellular transport. They also affect the microtubule organization and

dynamics during interphase and mitosis, take part in the cell signaling [20]. Motor proteins are not discussed in this chapter in detail.

+TIP proteins such as EB (end-binding) family, CLASP family, CAP-Gly family (CLIP170, CLIP115), and some motor proteins (kinesin 13, kinesin 14, and dynein family) can localize to the microtubule (+)-ends. EB proteins bind to the stabilizing cap of microtubule (+)-ends by sensing the tubulin nucleotide state [21]. *In vitro,* EB proteins are also found at the sites of microtubule repair [22]. Typically in mammals, three members of the EB family are expressed, the EB1, EB2, and EB3. EB proteins, wearing the fluorescent tag and expressed in cells, represent a great tool to study microtubule dynamics in cell cultures. The regulation of +TIPs loading onto microtubule ends is a complex and multilayered process. It is achieved by intermolecular interactions, locally controlled PTMs, and motor-specific transportation, resulting in very specialized microtubule subpopulations [6].

Recently, it was shown that microtubule (–)-end dynamics also exist and play a crucial physiological role in the cells, especially in neurons. These proteins autonomously bound to the microtubule (–)-ends are KANSL1/KANSL3 and CAMSAP/Patronin protein families [23-25]. Microtubule-Associated Proteins (MAPs) represent a subset of MTBPs that co-sediment with microtubules during multiple cycles of polymerization-depolymerization. Structural MAPs comprise the tau/MAP2/MAP4 family and MAP1A/1B family [26]. Tau/MAP2/MAP4 family bind to microtubule lattice along the microtubules and stabilize them. Moreover, they contribute to the regulation of microtubule-mediated transport, bind to F actin [27], and recruit signaling proteins.

Destabilizing MTBPs include the following protein groups: (i) sequestering proteins (e.g., stathmin) that destabilize microtubules by binding free tubulin dimers and preventing them from assembly into microtubule lattice; (ii) severing proteins (e.g., katanin, spastin, fidgetin) that cut microtubules in ATP-dependent manner; (iii) some +TIPs, such as depolymerizing kinesin-13 family. Interestingly, microtubule-severing enzymes, such as ATPases spastin and katanin using ATP hydrolysis's energy, exhibit a dual role in regulating microtubule dynamics. Enhanced activity of these severing proteins causes microtubule fragmentation and depolymerization, as enzymes can extract tubulins from the microtubule lattice and cut off stabilizing GTP caps. As severing enzymes "bite off" tubulins from the microtubule wall, the

microtubule lattice is repaired by incorporating the GTP-tubulins. Thus, the transient presence of GTP-islands, generated by severing enzymes, promotes microtubule rescue [28].

The functional group of cross-linking proteins makes lateral contacts to connect microtubules into networks and bundles. MAP65/Ase1/PRC1 proteins are working on antiparallel spindle microtubules. Cytoskeletal integrators make bonds between microtubules and other cytoskeletal components or cell cortex (e.g., APC, spectraplakins, formins, myosin 10, tau) [29].

In addition to MTBPs, microtubules target small molecules called Tubulin-Binding Agents (TBAs), affecting microtubule dynamics and altering microtubule-dependent cellular processes. Therefore, several TBAs are applied in cancer therapeutics, in treatments of fungal and bacterial infections, and some are under investigation to treat neurological disorders [30]. Aside from the medical application, TBAs are used as photoswitchable tools, optically operated to control changes in microtubule dynamics [31]. The TBAs either destabilize microtubules (vinca alkaloids: vincristine, vinblastine, vinorelbine; colchicine, nocodazole) or stabilize them (taxanes, laulimalide, and epothilones) when applied at micromolar concentrations. Even though some TBAs share similar functions, they do not have the same mode of action in the stabilization/destabilization of microtubules [32].

I.2   Microtubule nucleation

The organization of the microtubule network greatly contributes to the organization of cellular morphology. Microtubules can assemble into polymers at high tubulin concentrations *in vitro*. However, *in vivo,* free soluble tubulin concentration is lower, and, therefore, microtubule polymerization is kinetically unfavorable. The cell generates new microtubules from MTOCs – *de novo* microtubule nucleation – to facilitate microtubule formation *in vivo*. MTOCs represent defined sites that capture the (−)-ends and help nucleate, anchor, and stabilize microtubules. Despite the universal functions of MTOCs, they greatly vary in the size, shape, and structure among biological species and even within different cell types. In animal cells, the major MTOC is the centrosome. In *S. cerevisiae*, the organelle homologous to the centrosome is Spindle Pole Body (SPB), embedded in the nuclear envelope. Interestingly, not all organisms or cell types necessarily nucleate their microtubules from centrosomes. For

example, plants and oocytes are deprived of centrosomes, exhibiting non-centrosomal MTOCs. Moreover, animal dividing cells possess non-centrosomal MTOCs: the Golgi apparatus, existing microtubules, nuclear envelope, meiotic spindle, and chromatin. The nucleation of new microtubules is a complex process, governed by multiple proteins present in MTOCs. One of the best-studied microtubule nucleators is γ-tubulin, another tubulin superfamily member [33-35].

I.2.1   γ-Tubulin

γ-Tubulin is a highly conserved member of the tubulin protein superfamily and is ubiquitous across all eukaryotes. Many species contain only one γ-tubulin gene. Nonetheless, in some species, γ-tubulin is encoded by multiple genes similarly to α- and β-tubulins (in flowering plants, mammals, some fungi) [36]. Compared to the other vertebrates, all mammals have two tandemly arrayed γ-tubulin genes located in a cluster, suggesting the γ-tubulin duplication might have occurred in their last common ancestor. Humans contain two genes, *TUBG1* and *TUBG2*, located on chromosome 17 [37]. In mammals, the absence of γ-tubulin 1 isotype (encoded by *TUBG1*) is lethal, while the γ-tubulin 2 isotype (encoded by *TUBG2*) is not [38]. The other difference between these two isotypes comes from their tissue-specific expression. γ-Tubulin 1 is present in all tissues, whereas the γ-tubulin 2 expression is generally very low, but it is enriched in the brain [38]. We know little about the functional differences between γ-tubulin 1 and γ-tubulin 2, as both isotypes can nucleate microtubules [39]. Despite the predominant expression of γ-tubulin 1, the accumulation of γ-tubulin 2 during oxidative stress suggests a γ-tubulin 2 prosurvival role in mature neurons and neuroblastoma cells [40].

Given the high sequence conservation in the tubulin superfamily, the tertiary structure of γ-tubulin is similar to that of α- and β-tubulin with the protruding "tail" helix H11-H12 [41]. The crystal structure of human γ-tubulin revealed the γ-tubulin:γ-tubulin interactions that replicate the lateral contacts between α- or β-tubulins in the microtubule, implying possible γ-tubulin oligomerization. In cells, γ-tubulin exists in several macromolecular assemblies, ranging from low-molecular-weight forms to several MDa [41]. γ-Tubulin shows multiple charge variants in 2D-electrophoresis experiments, indicating the presence of several PTMs, such as phosphorylation and ubiquitination [42-44]. γ-Tubulin accumulates at both

centrosomal and non-centrosomal MTOCs, but the main pool (80% of total γ-tubulin) stays in a soluble form in the cytoplasm [45].

I.2.2   γ-Tubulin complexes

γ-Tubulin interacts with γ-tubulin complex proteins (called GCPs in *H. sapiens*, Spc in *S. cerevisiae*, Dgrip in *D. melanogaster*, Xgrip in *X. laevis*). γ-Tubulin and GCPs assemble into macromolecular complexes essential for microtubule nucleation, γ-Tubulin Small Complex (γTuSC) [46] and large γ-Tubulin Ring Complex (γTuRC) [47, 48].
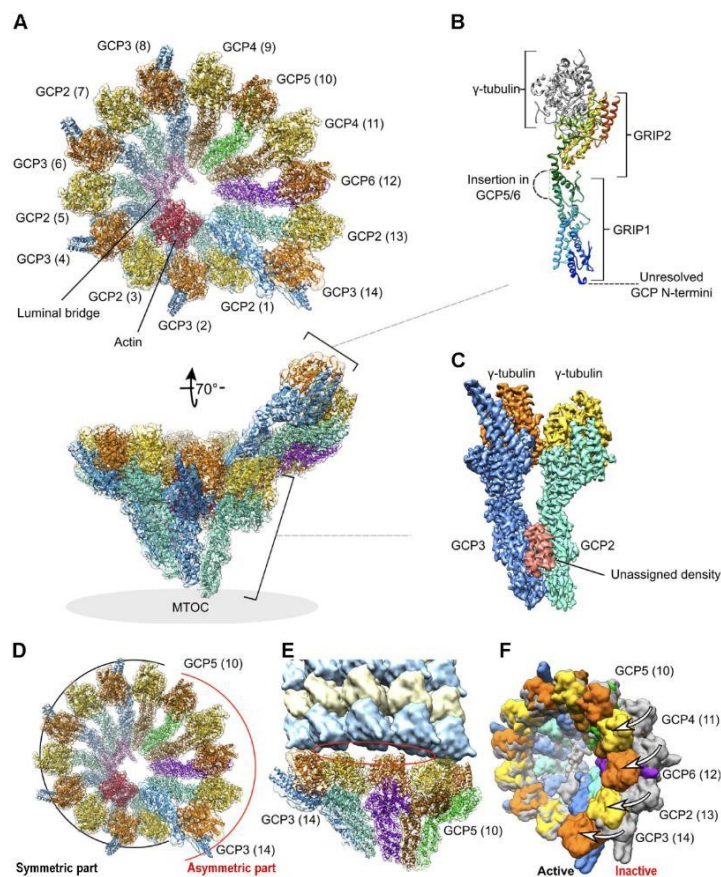
Figure 5 Reconstruction of human γTuRC. (**A**) Structure of γTuRC defined by the cryo-EM structure (top and tilted side view). γ-Tubulins are colored in yellow and orange. CGP/γ-tubulin subunit positions are indicated in brackets. (**B**) The structure of GCP/γ-tubulin stalk. The GCPs domains, GRIP1 and GRIP2, are shown. GCP structure is encoded in rainbow colors, where N-terminus is blue, and C-terminus is red. (**C**) The unassigned density segment's location (light red) is present on the GCP(2-3) subcomplex. (D) Structural asymmetry of γTuRC (top view). (**E**) The variable helical pitch is not compatible with microtubule symmetry and generates a gap (red ellipse). (**F**) Superposition of experimentally observed inactive conformation (grey) and extrapolated activated conformation (colored). Modified from [49].

Two molecules of γ-tubulin and one molecule each of GCP2 (Spc97p in *S. cerevisiae*) and GCP3 (Spc98p in *S. cerevisiae*) assemble into the Y-shaped heterotetramer, the 300-kDa γTuSC (Fig 5C) [50-52]. Budding yeast *S. cerevisiae* has only γTuSC components. Multiple γTuSCs, with additional GCPs and accessory proteins, form the 2.3-MDa γTuRC, resembling a cone or spiral ring. After a ring closure, γTuRC adopts a 13-fold symmetry to nucleate microtubules [53-55]. In metazoans, γTuRCs are stable complexes, and their assembly is independent of the recruitment to centrosomes. All eukaryotes have GCP2 and GCP3. While most eukaryotes except budding yeasts additionally have GCP4 and GCP5, only animals and filamentous fungi have GCP6 [56, 57]. Human GCP2, GCP3, GCP4, GCP5, GCP6 are members of the conserved protein family [58]. The GCP proteins contain a conserved N-terminal γ-tubulin Ring Protein 1 (GRIP1) domain and a conserved C-terminal GRIP2 domain, binding to γ-tubulin (Fig 5B). Using cryo-electron microscopy (cryo-EM) and mass spectroscopy, research groups made a tremendous leap towards our understanding of native human γTuRC architecture [56, 57, 59-63]. In addition to the core subunits (γ-tubulin and GCP2-6), they identified MOZART1/MZT1, MOZART2/MZT2 [64], and surprisingly actin [59], [61] as building components of γTuRCs.

The γTuRC arranges into "stalks," the GCP protomers, forming an open left-handed spiral of 30-nm width and 20-nm height (Fig. 5). GCP stalks support 14 γ-tubulins on the top, similar to the general γ-TuSC architecture. At the top of the spiral, subunit No. 14 (GCP stalk with γ-tubulin) aligns with the lowermost subunit No. 1 (Fig. 5A) [63]. Subunits No. 1-8 arrange tightly, forming a compact interface, while subunits No. 9-14 make flexible interactions, introducing strong asymmetry at the cone's tip (Fig. 5D, F). The arrangement of GCP proteins in the γTuRC complex appears as GCP(2-3)$_4$-GCP(4-5)-GCP(4-6)-GCP(2-3), resulting in a 5:5:2:1:1 stoichiometry for the different GCP variants (Fig 5A). The cryo-EM studies confirmed that γTuRCs are not initially in a microtubule nucleation-competent conformation. γTuRCs have to be activated by a conformation change of the ring diameter and height (Fig 5D-F) [59, 61, 63].

The γTuRC contains at least four distinct subcomplexes, the MZT/GCP modules, composed of MZT proteins and N-terminal α-helical domains of GCPs [62]. Two modules are located within the γTuRC lumen, so-called "luminal bridge," and two additional MZT/GCP modules are located at the γTuRC outer surface (Fig 5A). Actin has contacts with the GCP6 N-terminus in the luminal bridge and binds to GCP3 and the associated γ-tubulin at position No. 2. While the

role of γTuRC-associated actin in microtubule nucleation was confirmed, its role in the nucleation of F-actin filaments was excluded experimentally [61].

Contrary to previous models, the native human γTuRC has an asymmetric conformation. Only one side of the γTuRC complex, the γTuSC core, has a ''compact'' conformation, matching the microtubule geometry. The opposite side has a ''loose'' nucleation-incompetent conformation (Fig 5D-F) [59]. Such conformation results in structural asymmetry, explaining the low experimental nucleation efficiency of purified human γTuRCs. The location of the interaction partners – actin in the luminal bridge of γTuSC core and MTZ1, MZT2 at the outer perimeter – appears to stabilize the closed conformation. It suggests possible regulatory mechanisms for microtubule nucleation by γTuRC closure [59, 61, 62].

I.2.3   Other functions of γ-tubulin

New studies indicate that γ-tubulin has other functions beyond microtubule nucleation. It stabilizes the (–)-ends of free microtubules [65], affects +TIPs loading on microtubules [66], and regulates cell cycle progression [67]. Moreover, γ-tubulin resides in different cellular locations, presumably executing specific tasks. γ-Tubulin accumulates in the nuclei and nucleoli of the interphase cells [68]. The nuclear γ-tubulin mediates the activity of E2F transcription factors in mammalian cells [69]. Human Ser/Thr kinase SadB phosphorylates γ-tubulin on Ser385, causing chromatin-bound γ-tubulin to interact with E2Fs [70]. Thus, SadB kinase regulates the γ-tubulin cellular localization, and thereby nuclear γ-tubulin indirectly controls S-phase progression. γ-Tubulin binds to tumor suppressor protein CDK5RAP3 and modulates CDK5RAP3 activity during the G2/M DNA damage checkpoint [68]. γ-Tubulin also interacts with Rad51 during recombination repair of DNA double-strand breaks [71]. Association of γ-tubulin with nuclear proteins was shown for LINCs (Linker of Nucleo- and Cytoskeleton complexes), specifically for SUN and KASH protein families. Thus, γ-tubulin establishes a molecular bridge, connecting the cytoskeleton with lamins (nucleoskeletal intermediate filaments) [72, 73]. Additionally, γ-tubulins form a meshwork around the chromatin, connecting the cytoplasm and the nuclear compartment and aiding in nuclear formation [74].

Interestingly, γ-tubulin has an intrinsic ability to form oligomers and filaments organized into a meshwork in plant and animal cells [75-77]. The type II chaperonin CCT binds to γ-tubulin monomers and promotes γ-tubulin aggregation into so-called γ-strings, the fibrillar γ-tubulin assemblies 4–6 nm in diameter, found both *in vitro* and *in vivo* [78]. However, neither the formation mechanisms of the γ-tubulin assemblies nor their role in the cell architecture is known.

I.2.4   Centrosomal and non-centrosomal nucleation

The centrosome is a non-membrane barrel-shaped organelle. It assembles from two conserved, microtubule-derived templates – the mother and daughter centrioles – surrounded by a PeriCentriolar Material (PCM). The PCM architecture is long thought to be an amorphous protein "cloud." However, recent super-resolution microscopy techniques revealed the PCM to be a complex multi-component protein platform that brings together γTuRCs and multiple signaling proteins, adjusting its content and mass during the cell cycle [79, 80]. PCM components are divided into categories, based on their γTuRC interactions and microtubule-related functions at the centrosome: (i) targeting/anchoring γTuRC, (ii) activating γTuRC, and (iii) modulating PCM protein factors. Apart from being a coordination center governing the spindle assembly, the chromosome separation, cellular polarity and motility, intracellular signaling, and trafficking [81], the centrosome can organize both microtubules [82] and actin filaments [83-85].

The microtubule network organization varies wildly, depending on the cell type, differentiation stage, cell cycle, and non-centrosomal MTOCs. Even in cells with a radial microtubule network, the microtubule (–)-ends can be attached to the membranous organelles (mitochondria, the Golgi apparatus, nuclear envelope, plasma membrane-associated sites) or other locations (existing microtubules, chromatin, mitotic spindles). In differentiated cells, MTOC function is reassigned to non-centrosomal sites, such as the nuclear envelope in skeletal muscle, the apical membrane in epithelial cells, and along the existing microtubules in axons and dendrites [86].

The centrosome activity is upregulated during mitosis, whereas the microtubule nucleation activity of the Golgi apparatus is downregulated [87]. In mammalian retinal pigment epithelial

cells (RPE1), nearly half of all cellular microtubules emanate from the Golgi apparatus [88]. In migrating cells, the Golgi-attached microtubules help position the centrosome in the direction of migration [89]. During the interphase, centrosomes mature in Plk1-independent manner and promote cytokine production in innate immune cells, responding to inflammation [90]. Conversely, the differentiation of specific cell types (e.g., epithelial cells and neurons) induces the centrosome attenuation [91], the relocation of γTuRCs, and subsequent downregulation of individual PCM components, followed by reassigned non-centrosomal microtubule nucleation [86, 92, 93].

I.3. Regulation of centrosomal microtubule nucleation

I.3.1 γTuRC-targeting and activating proteins

In mammalian cells, one of the critical components in the PCM organization is pericentrin [94]. Pericentrin contains the C-terminal PACT (pericentrin-AKAP450 centrosomal targeting) domain, responsible for targeting the centriole wall. Pericentrin also recruits other PCM components essential for microtubule nucleation, such as γTuRC, CDK5RAP2 (CDK5 Regulatory subunit–Associated Protein 2), NEDD1 (Neural precursor cell Expressed Developmentally Downregulated 1, GCP-WD), and CEP192 [95].

γTuRC integrity is a prerequisite for interaction with the targeting factor NEDD1 essential in humans [96]. MZT2 A/B (GCP7/8) interacts with (i) γTuRC to enable its NEDD-mediated targeting, and with (ii) CDK5RAP2, stimulating the γTuRC nucleation activity [97]. Hence, MZT2 is a two-level γTuRC targeting factor, allowing the spatial regulation of microtubule nucleation during interphase. MZT1 (GCP9) performs a similar function only during mitosis [98].

CDK5RAP2 can target γ-tubulin to the pericentrin. Through its N-terminal CM1 (Centrosomin Motif 1) domain, CDK5RAP2 binds to γTuRC [99], and via its C-terminal CM2 domain, it binds to pericentrin and/or AKAP450 (CG-NAP) [100]. AKAP450 interacts with γTuRCs via GCP2 or GCP3 and secures sites for microtubule nucleation at the mammalian centrosome [101]. The γTuRC-binding site of CDK5RAP2, called "γ-TuNA", can activate γ-tubulin-mediated microtubule nucleation, even when expressed ectopically (e.g., at the cellular cortex) [92, 99]. Conversely, the γTuRC-binding region of NEDD1 recruits γTuRC to the ectopic sites but cannot activate microtubule nucleation. In humans, even though the

14

accessory γTuRC proteins (MZT1, MZT2, NEDD1, and CDK5RAP2) can recruit γ-tubulins to the centrosome, their effects may vary among species or can be the cell type-dependent [92].

In mammalian cells, a centrosomal protein CEP192 contributes to the balance of centrosomal and con-centrosomal microtubules during interphase and mitotic spindle formation. CEP192 activities are mediated by the recruitment to numerous proteins, such as γ-tubulin and pericentrin [102]. Ninein is a centrosomal protein bound to the mother centriole [103]. Via its N-terminus, ninein interacts with γTuRC and indirectly promotes microtubule nucleation by docking γTuRCs at the centrosome. Thus, ninein is a molecular link between the microtubule nucleation and microtubule anchoring at the centrosome [104]. Another activation protein that co-purifies with γTuRC is NME7 (nucleoside-diphosphate kinase 7), facilitating the microtubule nucleation in a kinase-dependent manner [105]. Some centrosomal factors can be reused by other nucleation sites [95]. Overall, γ-tubulin-dependent microtubule nucleation relies on a set of redundant components that can be utilized in multiple combinations by different species.

I.3.2   γTuRC-modulating proteins

Many (+)-end proteins bind to PCM components and modulate microtubule formation and stability. For instance, XMAP215 (Xenopus microtubule assembly protein 215 kDa), the microtubule polymerase from the TOG/XMAP215 family, interacts with γ-tubulin complexes [106-108]. The XMAP215 N-terminal TOG domains bind to αβ-tubulin dimers and promote microtubule polymerization, whereas the C-terminus directly binds to γ-tubulin and assists in efficient microtubule nucleation. Human polymerase chTOG (XMAP215 homolog) acts synergistically with TPX2, which directly stabilizes growing microtubule ends and early microtubule nucleation intermediates [109].

TACC3, centrobin, myomegalin, and GIT/PIX signaling proteins belong to the modulating proteins involved in regulating of microtubule nucleation at the centrosomes. TACC3, a member of the human transforming acidic coiled-coil (TACC) protein family, promotes the regulation of microtubule nucleation and γTuRC assembly at the centrosome during mitosis. [110]. Centrobin, the daughter centriole marker, is engaged in duplication and elongation of the centriole [111]. Centrobin also regulates microtubule nucleation and organization by

controlling the amount of PCM [112]. Myomegalin, CDK5RAP2 paralog in vertebrates, is required for centrosomal microtubule growth[113].

Initially, GIT1 and βPIX were implicated in the modulation of actin-related structures in migrating cells [114]. These proteins are participate in the modulation of centrosomal microtubule nucleation. GIT1 (G-protein-coupled receptor (GCPR)-kinase-interacting protein 1) forms complexes with βPIX (p21-activated kinase (PAK) interacting exchange factor β). PAK1 kinase (p21 protein-activated kinase 1) targets both GIT1 and βPIX. GIT1 has multiple domains, serving as a scaffold for interacting partners, including ADP ribosylation factor ARF, Rac1 and Cdc42 GTPases, mitogen-activated protein kinase kinase 1 (MEK1), PAK kinases, βPIX, phospholipase C γ (PLCγ), and an adaptor protein paxillin [115]. βPIX acts as a guanine nucleotide exchange factor (GEF) for Rac2, Cdc42, and Rho, involved in cytoskeleton regulation [115]. βPIX makes a molecular link that connects GIT1 with PAK kinases; Rac1 with Cdc42 GTPases [116]. Since both GIT1 and βPIX proteins can make homodimers, they are often found in the form of 1–2-MDa oligomers named a "GIT/PIX signaling cassette" [117]. We have shown that GIT1 and βPIX represent positive and negative regulators of microtubule nucleation, respectively, in different cell lines [118, 119].

I.3.2.1 Role of protein kinases and phosphatases

Fine-tuning of centrosome MTOC-related activity often depends on a set of protein kinases and phosphatases, targeting specific γTuRC-associated proteins during different cell cycle stages. At the G2/M transition, the centrosome undergoes maturation, expands the PCM, and increases microtubule-organizing activity. Mitotic kinases Plk1 and Aurora A are essential for centrosome maturation [120]. Plk1 phosphorylates pericentrin and initiates spindle pole-specific PCM lattice [121]. Moreover, Plk1 enhances centrobin microtubule-stabilizing activity for proper spindle formation during mitosis [122]. Additionally, sequential phosphorylation of NEDD1 by Cdk1 and Plk1 regulates γTuRC targeting to the centrosome [123]. NEDD1 is phosphorylated on multiple sites, modulated by its association with the CEP192 protein [124]. CEP192, in turn, activates centrosomal Aurora A [125]. Cytoplasmic tyrosine kinase JAK2 localizes around the mother centriole and phosphorylates ninein involved in microtubule nucleation and anchoring [126].

The GIT/PIX/PAK complex is present at the centrosomes, providing a molecular platform for signaling pathways during interphase and mitosis [119, 127]. PAK1 appears to be a dynamic partner of the GIT/PIX cassette, reaching its highest level at the centrosomes during mitosis [127]. Interestingly, PAK1 becomes activated by centrosome targeting via Rho GTPase-independent mechanism, requiring centrosome integrity. Active PAK1 phosphorylates the centrosomal GIT1. Once activated, PAK1 dissociates from the GIT/PIX cassette and interacts with centrosomal kinase Aurora A instead, resulting in Aurora A kinase activation in mitosis [127]. The Src family protein tyrosine kinases regulate GIT1 and βPIX activities [128, 129].

Protein tyrosine phosphatases also play an important role in the regulation of microtubule nucleation. βPIX carries a phosphorylation site on proline-rich-motif (PXXP), which allows the interaction with serine/threonine phosphatases of the PP2C family (POPX1 and POPX2), leading to the inactivation of PAK1 kinase activity [130]. We recently reported that the cytoplasmic protein tyrosine phosphatase SHP-1 (Src homology region 2 domain-containing phosphatase-1) modulates the centrosomal microtubule nucleation in mast cells [131]. SHP-1 (encoded by the *PTPN6* gene) is expressed primarily in cells of hematopoietic origin, where it plays a vital role in the regulation of immune cell functions [132]. SHP-1 consists of two Src Homology 2 (SH2) domains, Tyr-phosphatase domain (PTPase domain), and C-terminal tail with important phosphorylation sites for its activation/inhibition. Additionally, SHP-1 can make intramolecular interactions between its own N-terminal SH2 domain and PTPase domain, thereby inhibiting its basal phosphatase activity [133]. Another possible regulation level is available upon ligand binding to the SH2 domains, resulting in a stabilization of its open/active conformation [134]. SHP-1 functions are also affected by its cellular localization [132]. SHP-1 switches off activating signals, triggered by ITAM-containing proteins (Immunoreceptor Tyrosine-based Activation Motifs), such as FcRs (receptors for immunoglobulin Fc regions), to balance the signaling. Interestingly, SHP-1 regulates different signaling pathways, depending on a subset of myeloid cells where it is expressed [132, 135].

Protein tyrosine kinases and protein tyrosine phosphatases control the cellular equilibrium of tyrosine phosphorylation level essential for signal transduction during cytoskeleton remodeling events.

I.3.2.2   Role of UFL1/C53 protein complex

It was shown that tumor suppressor BRCA1 (breast cancer type 1 susceptibility protein) was associated with centrosomes and interacted with γ-tubulin. The BRCA1/BARD1-dependent (BRCA1-associated RING domain protein 1) ubiquitination of γ-tubulin and associated proteins inhibited microtubule nucleation [42, 136]. Our recent data showed that tumor suppressor CDK5RAP3 (CDK5 regulatory subunit-associated protein 3), interacting with γ-tubulin, also inhibited microtubule nucleation [137]. CDK5RAP3 is associated with protein ligase UFL1 (E3 UFM-protein ligase 1), responsible for the ligation of the ubiquitin-fold modifier (UFM1) to proteins. This novel ubiquitin-like PTM is called ufmylation [138]. Although the ufmylation process is analogous to ubiquitination, it differs functionally and serves as a non-proteolytic signal.

The ufmylation regulates multiple cellular processes, including ER stress, cell differentiation, ribosome functions, gene expression, and DNA damage response [139]. The UFM1 and its conjugating machinery are conserved in metazoans and plants [138]. The 9.1-kDa UFM1 modifiers are covalently linked to the target proteins during an enzymatic cascade analogous to ubiquitination, involving UFM1-specific proteases (UFSP1, UFSP2), E1 activating (UBA5), E2 conjugating (UFC1), and E3 ligating enzymes (UFL1) [138]. UFL1 and most of the UFM1 pathway components are mainly distributed at the cytosolic side of the ER membrane [138]. UFL1 is expressed ubiquitously with an exceptionally high level in the liver [138].

UFL1 can stabilize two adaptor proteins, CDK5RAP3 and UFBP1, involved in ER homeostasis [140]. The UFM1-binding protein 1 (UFBP1, DDRGK1) was first described as an ufmylation substrate [141]. Later on, UFBP1/DDRGK1 was identified as the UFM1 pathway component, enabling docking of the UFM1 enzyme complex at the ER. Also, UFBP1/DDRGK1 acts as a UFL1 adaptor [142]. UFBP1/DDRGK1 has many described functions, including the maintenance of ER homeostasis and membrane expansion regulation [143, 144].

CDK5RAP3 (C53, LZAP) interacts with UFL1 and serves as a UFL1 substrate adaptor [145]. CDK5RAP3 contributes to the maintenance of ER homeostasis, vesicle trafficking, cell cycle regulation, DNA damage response, cell adherence, invasion, and metastasis [146-150]. We showed that CDK5RAP3 formed complexes with nuclear γ-tubulin, antagonizing the inhibitory effect of CDK5RAP3 on G2/M checkpoint activation by DNA damage [68].

I.3.2.3 Role of actin filament regulators

The centrosome's proteomic analysis revealed the presence of actin-binding proteins sustaining actin dynamics [151]. Purified centrosomes also contained profilin, cofilin, myosin, L-plastin, and β-filamin [151]. Additionally, the presence of actin was confirmed using immunofluorescence microscopy and the specific antibody, recognizing actin dimers [152]. Moreover, the centrosome can directly promote actin assembly. During interphase, protein PCM-1 (Pericentriolar Material-1), transiently regulating Actin-Related Protein 2/3 complex (Arp2/3) and recruitment of WASH to the centrosome, modulates the centrosomal actin network. Both Arp2/3 complex and WASH are involved in actin filament formation.

Centrosomal actin nucleation is required for proper mitotic spindle formation [153]. Enhanced formation of cytoplasmic actin filament network, relying on WASH and the Arp2/3 complex, accompanies the mitotic exit. As cells enter the anaphase, actin accumulates around the centrosomes, leading to a reduced density of centrosomal microtubules [84]. Thus, the centrosomal actin nucleation adjusts the levels of centrosomal microtubules during mitotic exit.

In lymphocytes, the increased actin filaments density correlates with a reduced level of microtubules at the centrosome. Eventually, the lymphocyte activation ends in the disassembly of centrosomal actin and an increased number of microtubules. *In vitro* assays showed that actin filaments blocked the elongation of nascent microtubules. It suggests a novel mechanism, regulating the number of centrosomal microtubules by cell adhesion and actin network [85].

The GIT/PIX/PAK signaling cassette, found at the centrosome, is involved in the actin remodeling [114] and microtubule nucleation. The GIT/PIX/PAK cassette likely plays a role in the centrosome-proximal actin organization. Hence, the centrosome acts as an actin filament-organizing center, indicating a crosstalk between two cytoskeletal systems [83].

Profilin coordinates actin and the microtubule (+)-end dynamics [154-156]. Recently, we demonstrated that profilin was localized at the centrosomes, acting as a negative regulator of microtubule nucleation [157].

I.4. Model systems used in the study

I.4.1 Mast cells

Mast cells act as effector cells during innate and adaptive immune responses. They also affect the biology of immune cells, such as T cells, B cells, natural killer cells, granulocytes, monocytes/macrophages, and dendritic cells [158]. Mast cells originate from hematopoietic stem cells in bone marrow or other hematopoietic tissues. Hematopoietic stem cells give rise to mast-cell progenitors, circulating in the blood until they reside in vascularized peripheral tissues. The mast-cell progenitors then undergo differentiation, becoming mature mast cells [158-160]. Mature mast cells adjust their phenotype, depending on the local cellular environment – presence or absence of growth factors, cytokines, and chemokines; specific tissue location [161, 162]. In vertebrates, mast cells stay beneath the tissues exposed to environmental agents (in the skin, airways, and gastrointestinal tract), such as invading pathogens, allergens, and toxins. In the brain, mast cells accumulate on the brain side of the blood-brain barrier and interact with blood vessels, other hematopoietic cells, neurons, and glia [160].

Various stimuli (allergens, pathogen products, physical agents, products of complement activation, chemokines, and cytokines) can activate mast cells to release biologically active products. These products are stored inside the secretion granules, mediating pro-inflammatory, anti-inflammatory or immunosuppressive functions [163]. During the regulated exocytosis (the degranulation), mast cells release pre-formed mediators (e.g., histamine, heparin, proteases, serotonin). Activation also leads to *de novo* synthesis and secretion of bioactive components, including lipid-derived products, cytokines, and growth factors [164]. Mast cells express a large variety of receptors, activating or inhibiting their functions [165]. High-affinity receptor for immunoglobulin E IgE (known as FcεRI) and c-Kit (the receptor of the stem cell factor SCF) are characteristic receptors for mast cells [165]. One of the best-studied mast cell activation mechanisms is an antigen (Ag)/IgE-mediated aggregation of FcεRI receptors (Fig. 6). Ag/IgE-mediated activation of mast cells is a multistep process, involving the tyrosine phosphorylation of Immunoreceptor Tyrosine-based Activation Motifs (ITAMs), located at the cytoplasmic tails of FcεRIs β and γ subunits [167, 168].
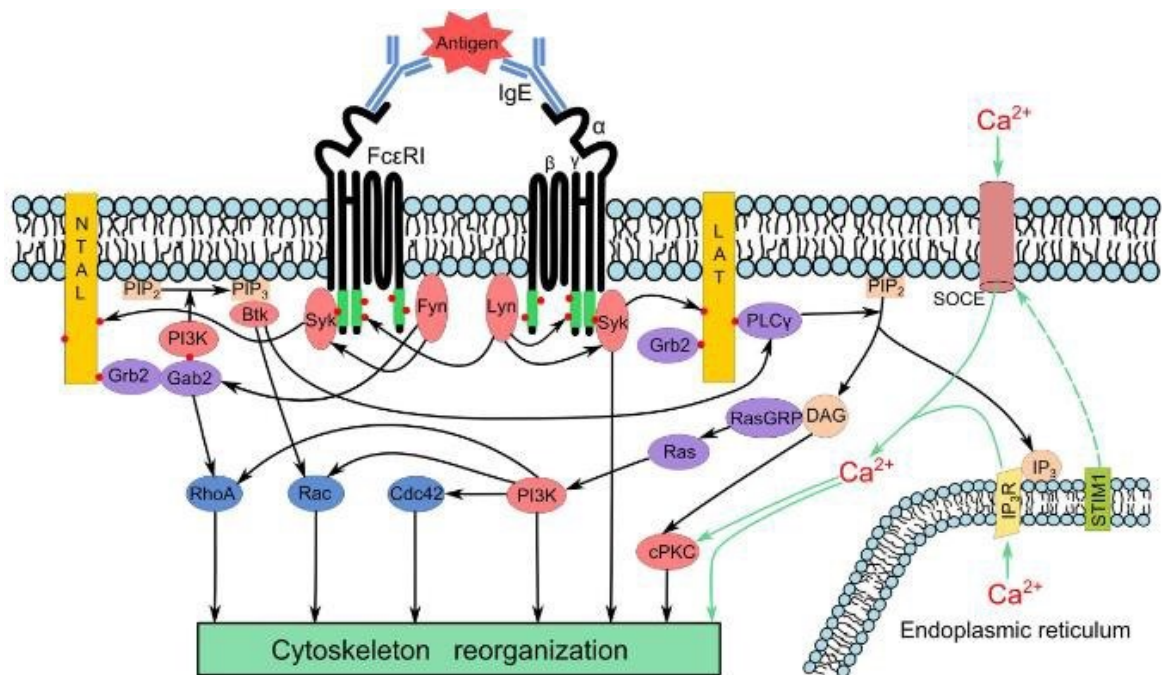
Figure 6 Simplified model of FcεRI-mediated signaling. Multivalent antigen (Ag) cross-links the high-affinity receptor for IgE (**FcεRI**), thereby triggering mast cells. This activates protein tyrosine kinase Lyn or Fyn, which phosphorylate (red dots) ITAMs on FcεRIs. It is followed by attachment of protein tyrosine kinase Syk to FcεRI. Kinases phosphorylate downstream targets to activate multiple signaling pathways. PLCγ generates the second messengers, diacylglycerol (**DAG**) and inositol trisphosphate (**IP₃**). IP₃ binds to its receptor on the ER (**IP₃R**) and triggers the release of Ca^{2+} from the ER. Ca^{2+} depletion in the ER leads to the opening of the plasma membrane-bound Ca^{2+} channels and influx of extracellular Ca^{2+} into the cytoplasm. Ultimately, the signaling cascades converge, resulting in the enhanced cytoskeleton remodeling and mast cell degranulation, chemotaxis, and migration. Regulatory proteins are colored according to their function: kinases are pink, transmembrane linkers are yellow, adaptors and other signaling proteins are violet, lipids and their products are flesh, Rho GTPases are blue. Illustration source [166].

Protein tyrosine kinases, balanced by protein tyrosine phosphatases mediate the signal transduction downstream of FcεRI. Specifically, Lyn, from the Src protein tyrosine kinases family [169], phosphorylates multiple ITAMs [170], followed by the recruitment of protein tyrosine kinase Syk from the Syk/Zap protein family [171]. This results in the autophosphorylation and activation of Syk. Lyn and Syk kinases then phosphorylate transmembrane adapter proteins Non-T-cell Activation Linker (NTAL, LAT2) [172] and Linker for Activation of T cells (LAT) [173]. NTAL/LAT2 and LAT then acquire docking sites for various downstream SH2 domain-containing proteins, e.g., cytosolic adaptor molecule Grb2, phospholipase Cγ1 (PLCγ1), phosphoinositide 3-kinase (PI3K). The adaptor proteins

interactions with LAT and NTAL allow the diversification of downstream signaling, ultimately leading to calcium mobilization, cytoskeleton remodeling, enhanced chemotaxis, and degranulation.

Subsequently, PLCγ1 hydrolyses phosphatidylinositol (4,5)-bisphosphate (PIP$_2$) and generates the second messengers, diacylglycerol (DAG) and inositol trisphosphate (IP$_3$). IP$_3$ binds to the ER-bound IP$_3$ receptor (IP$_3$R) and triggers the release of Ca^{2+} from the ER. Ca^{2+} depletion from the ER leads to the interaction of STIM1 (sensor of Ca^{2+} level in the ER) with Orai1 (calcium release-activated calcium channel protein 1), resulting in the opening of the plasma membrane-bound Ca^{2+} channels and influx of extracellular Ca^{2+} by the Store-Operated Ca^{2+} Entry (SOCE). DAG and enhanced Ca^{2+} cytosolic concentration activate conventional protein kinase C family (cPKC). DAG also recruits Ras guanyl nucleotide-releasing proteins (RasGRPs) for subsequent activation of the Ras family proteins, stimulating PI3K involved in further signal propagation. PI3K also phosphorylates PIP$_2$ and generates phosphatidylinositol (3,4,5)-trisphosphate (PIP$_3$), which recruits nucleotide exchange factors GEFs. It, in turn, results in the activation of the Rho family of GTPases (RhoA, Rac, and Cdc42), modulating the cytoskeleton [174]

A complementary FcεRI-mediated signaling pathway, the Fyn–Gab2–PI3K, exists to amplify the signal, leading to mast cell activation, degranulation, and cytokine production [175]. This pathway requires the Src family kinase Fyn but does not require the interaction of LAT with PLCγ1. Instead, it results in the activation of PI3K downstream of the cytosolic adaptor molecule Gab2.

The FcεRI-mediated signaling cascade results in degranulation. The degranulation can also be non-specifically triggered by thapsigargin, inhibiting the Ca(2+)-ATPase pumps in the ER membrane [176]. Pervanadate, which robustly inhibits protein tyrosine phosphatases and mimics the FcεRI aggregation effect, can also trigger the degranulation [177]. The degranulation process is accompanied by cytoskeleton remodeling and increased spreading on the substrate [178]. Particularly, during the Ag-induced degranulation, the cortical actin barrier disassembles, followed by the F actin polymerization at the plasma membrane. This step allows vesicles to fuse with the plasma membrane and release their mediators [178, 179]. Additionally, mast cells activation leads to a rapid reorganization of microtubules [180]. Microtubules are important for the granules movement from the interior to the cell periphery

[181-183], driven by molecular motors [184]. Granules can travel along the intact microtubule network as well as actin [185, 186].

We showed that activation of bone marrow-derived mast cells (BMMCs) led to the rapid, transient formation of plasma membrane protrusions, containing microtubules. This event depended on STIM1 and the influx of extracellular Ca^{2+} [180]. We found that tyrosine kinases Lyn, Fyn, and Syk associated with γ-tubulin-containing complexes and tyrosine-phosphorylated proteins [183, 187]. These complexes contained the GIT1/βPIX signaling proteins, modulating microtubule nucleation [119]. Finally, we showed that Ca^{2+}-dependent PKCs were essential for microtubule remodeling during BMMCs activation events [188].

BMMCs represent the excellent model system for studying signaling pathways that leads to the rapid changes in microtubule organization.

I.4.2   Other cell types

Along with BMMCs, we used other cell lines to perform our experiments. Adherent human osteosarcoma cell line U2OS is very useful for microscopic observation owing to its epithelial morphology and high transfection efficiency [189]. We verified obtained results using the following human cell lines: non-transformed retinal pigmented epithelium (hTERT-RPE1), embryonic kidney (HEK-293T), cervix adenocarcinoma (HeLa S3), breast adenocarcinoma (MCF7), colorectal epithelial adenocarcinoma (Caco-2). Additionally, rat basophilic leukemia (RBL-2H3), mouse embryonal carcinoma (P19), mouse melanoma (B16-F1) cell lines were used in some experiments.

II   AIMS OF THE STUDY

The Laboratory of biology of cytoskeleton is focused on studying the molecular pathways implicated in the regulation of microtubule organization under normal and pathological conditions. Particularly, we have been studying the regulatory mechanisms of microtubule nucleation, depending on γ-tubulin and its complexes. As protein kinases and phosphatases play an important role in this process, in the presented study, we aimed to functionally characterize newly describes proteins, interacting with γ-tubulin complexes, and analyze γ-tubulin oligomers. We also intended to improve live-cell imaging and data processing obtained from microtubule nucleation assays.

Objectives of the Ph.D. thesis

1) Development of new tools for quantification of microtubule nucleation

2) Functional analysis of new regulatory proteins SHP-1 and CDK5RAP3/C53 complex involved in the microtubule nucleation

3) Functional characterization of centrosomal profilin 1

4) Characterization of large γ-tubulin assemblies

III   COMMENTS ON PRESENTED PUBLICATIONS

III.1   Regulation of microtubule nucleation mediated by γ-tubulin complexes (Review)

Sulimenko, V., Hájková, Z., **Klebanovych, A.,** Dráber, P. (2017). Regulation of microtubule nucleation mediated by γ-tubulin complexes. Protoplasma *254 (3)*, 1187-1199.

The nucleation of microtubules depends on γ-tubulin complexes that are present in all eukaryotes. Current mechanistic understanding of the microtubule nucleation strongly relies on cryo-EM approaches [59, 60, 63]. Despite the progress in the characterization of γ-tubulin complexes, the regulatory mechanisms implicated in the fine-tuning of the microtubule nucleation remains unclear.

In this requested review, we summarized recent findings about the regulatory mechanisms, affecting centrosomal and non-centrosomal microtubule nucleation in different model systems. We described the structure of γ-tubulin complexes, stressing the organism-specific differences in building components, and listed known factors, regulating microtubule nucleation at the centrosomal and non-centrosomal sites in animal cells. We discussed in detail three microtubule nucleation locations: yeast spindle pole bodies (SPBs), centrosomes, and non-centrosomal sites. Non-centrosomal nucleation occurs at the Golgi apparatus, nuclear envelope, chromatin and kinetochores, the surface of pre-preformed microtubules, and plasma membrane-associated sites. We categorized the regulating proteins according to their microtubule nucleation role as γTuRC-targeting, activating, anchoring, and modulating. Finally, we proposed future directions to understand better, how microtubule nucleation is initiated, how cells adjust their nucleation capacity during the cell cycle, and what signaling pathways regulate the cytoskeleton remodeling. A thorough understanding of microtubule nucleation will clarify the relevance of γTuRC proteins dysregulation in cancer cells.

I summarized all recent data about building components of γ-tubulin complexes and proteins, regulating microtubule nucleation from centrosomes. I prepared corresponding tables and participated in writing the manuscript and in responding to the reviewer's comments.

III.2 γ-Tubulin has a conserved intrinsic property of self-polymerization into double stranded filaments and fibrillar networks

Chumová, J., Trögelová, L., Kourová, H., Volc, J., Sulimenko, V., Halada, P., Kučera, O., Benada, O., Kuchařová, A., **Klebanovych, A.,** Dráber, P., Daniel, G., Binarová, P. (2018) γ-Tubulin has a conserved intrinsic property of self-polymerization into double stranded filaments and fibrillar networks. Biochim Biophys Acta Mol Cell Res *1865(5)*:734-748.

γ-Tubulin is essential for microtubule nucleation in acentrosomal plant cells, whereas other homologs of γ-tubulin complex components, characteristic for animal cells, are often absent in plants. A higher amount of γ-tubulin is present in acentrosomal plant cells compared to animal cells [190]. Additionally, plant γ-tubulin can form heterogeneous high-molecular-weight protein complexes [191]. The sequence and structural features of human γ-tubulin, important for longitudinal and lateral interaction interfaces within γ-tubulins, predicted that γ-tubulin might form dimers and oligomers [192]. Surprisingly, fibrillar structures of γ-tubulin, called γ-tubules, were found in mammalian cells [76].

In this work, we characterized large γ-tubulin assemblies, isolated from *Arabidopsis thaliana* cell suspension culture or cells, expressing GFP-tagged γ-tubulin. We also analyzed γ-tubulin assemblies isolated from human U2OS cells, expressing TagRFP-tagged human γ-tubulin (γ-tubulin-TagRFP); and endogenous γ-tubulin isolated from porcine brain. *Arabidopsis* γ-tubulin, immunoprecipitated with anti-γ-tubulin peptide antibody from pellets after high-speed centrifugation (P100 pellets), was eluted with immunizing peptide and then was analyzed by transmission electron microscopy (TEM). Purified γ-tubulin formed (i) amorphous aggregates, (ii) short filaments, (iii) double-strand filaments, tending to bundle *in vitro*. Similarly, fluorescence microscopy of isolated γ-tubulin lacking GCPs, revealed dimers and filaments. The average double-stranded filament width measured by TEM and atomic force microscopy (AFM) was approximately 8.5 nm.

Additionally, we used purified human γ-tubulin-TagRFP to test if γ-tubulin oligomerization was not limited to plants. γ-Tubulin-TagRFP immunopurified from P100 extracts was able to form fibrillar structures. In contrast, a negative control, PAK1-TagRFP, did not form any organized structures, suggesting that TagRFP alone did not mediate γ-tubulin oligomerization. Examined by TEM and fluorescence microscope, γ-tubulin-TagRFP samples immunopurified

either in the absence of SDS or in the presence of SDS (stripping off GCPs), formed (i) fibrillary structures or (ii) short γ-tubulin double-filament structures, respectively. The next step was to examine whether γ-tubulin purified from the porcine brain could form oligomers as well. For that, γ-tubulin was precipitated from microtubule proteins, using an anti-γ-tubulin peptide antibody eluted with specific peptide, and then subjected to native electrophoresis. Although we did not detect αβ-tubulin heterodimers in the eluted fractions, containing γ-tubulin, multiple γ-tubulin oligomers were present. These data indicated that γ-tubulin alone could form oligomers under conditions of native electrophoresis. Both human γ-tubulin-TagRFP and porcine brain γ-tubulin showed the intrinsic ability to polymerize, as it was observed in plant cells. While purified plant γ-tubulin filaments assembled into long, tightly bound bundles *in vitro*, the filaments of human γ-tubulin formed loose bundles. The stronger lateral interaction of plant γ-tubulin filaments might reflect specific characteristics of *Arabidopsis* γ-tubulin or might be explained by a generally higher amount of γ-tubulin present in acentrosomal plant cells than in animal cells. We studied the localization of γ-tubulin with stimulated emission depletion (STED) microscopy to determine if γ-tubulin filament bundles and clusters were present in *Arabidopsis* cells. In cells, the γ-tubulin organization reflected the *in vitro* polymerization ability of the protein. The basic γ-tubulin form was fine short fibril-like structures localized at the microtubules, mitotic microtubular arrays, membranes, nuclear envelope, and the interior of nuclei in a cell-cycle-dependent manner.

Given the TEM and AFM data obtained with *Arabidopsis* γ-tubulins, we suggest that γ-tubulin formed filaments with the tendency to cluster, lengthen and align by lateral contacts. Similar results were obtained with the human and porcine γ-tubulins. Previously, larger molecular assemblies of γ-tubulin with microtubules were found in the brain [43, 193]. γ-Tubulin is present in aggresomes and inclusion bodies detected in neurodegenerative diseases [194]. Interestingly, the γ-tubulin filaments resembled protofilaments formed by bacterial tubulins BTubA and BTubB [195]. The plant and mammalian γ-tubulin filaments were structurally different from those (i) with 13-fold symmetry assembled from the *S. cerevisiae in vitro* reconstituted γTuSCs, (ii) γ-tubules composed of γTuRC and pericentrin in mammalian cells [54, 76]. Evidently, the GCPs were not required for γ-tubulin oligomerization in plant and mammalian samples *in vitro*. Yet how γ-tubulin fibrillar structures (with or without GCPs) interplay in the cell requires further investigation.

The ability to form fibrillar assemblies *in vitro* is the γ-tubulin intrinsic feature. While fine γ-tubulin filaments were visualized by super-resolution microscopy at all dispersed localization sites of γ-tubulin, the robust γ-tubulin rod-like fibrils were observed only sporadically in nuclei and in the cytoplasm of non-dividing *Arabidopsis* cells. Some rods-like fibrils appeared to be microtubular bundles decorated with γ-tubulin in the form of the clustered filament. Supposedly, γ-tubulin assemblies participate in scaffolding or provide structural support for interacting proteins. γ-Tubulin ability to form oligomers/polymers greatly contributes to the heterogeneity of γ-tubulin forms. We suggest that γ-tubulin ability to form oligomers/polymers might have a dual role. It nucleates microtubules and has scaffolding or sequestration functions, analogous to the prokaryotic bundling tubulin filaments.

I participated in preparing immunopurified human γ-tubulin-TagRFP and control (human PAK1-TagRFP) for further analysis and performed fluorescence microscopy of mammalian γ-tubulin assemblies. I prepared photo documentation and participated in writing the manuscript and responding to the reviewer's comments.

III.3   Regulation of microtubule nucleation in mouse bone marrow-derived mast cells by protein tyrosine phosphatase SHP-1

Different agents can initiate signaling cascades in mast cells, which ultimately must converge to allow the downstream pathways propagation required for the degranulation, cytokines and chemokines synthesis. The manifestation of mast cell activation is driven by multiple receptors expressed on the mast cell's surface. Among those are the high-affinity receptors for IgE (FcεRIs), which, after the Ag-driven aggregation, initiate a "principal" signaling cascade [196]. Other receptors, however, can potentiate FcεRI-mediated activation and/or stimulate mast cell responses themselves. The signal transduction downstream of FcεRIs is mediated by multiple kinases and phosphatases [167, 175, 197]. Specifically, those implicated in the early signaling events are transient "activators" from the Src tyrosine kinases protein family (Lyn, Fyn), tyrosine kinase from the Syk Syk/Zap protein family; and "inhibitors" such as non-receptor protein tyrosine phosphatases (SHP-1, SHP-2) [166, 169]. The Ag-induced activation of mast cells results in increased formation of microtubules and transient generation of protrusion-containing microtubules (microtubule protrusions) [183, 198]. While the importance of microtubule network for mast cell degranulation is well established, the molecular mechanisms responsible for microtubule reorganization in activated mast cells are mostly unknown.

In this study, we examined the hypothesis that phosphor-tyrosine proteins (P-Tyr) associated with γ-tubulin could modulate microtubule nucleation in activated mast cells. After Ag-induced BMMCs activation, we observed a time correlation between transient changes in the P-Tyr level and the generation of microtubule protrusions. Thus, our data on BMMCs support the previous findings on mast cells, isolated from other sources, that active tyrosine phosphatases are involved in the later stages of an Ag-induced activation [199]. Potentially, protein tyrosine phosphatases (PTPs) might also be necessary for the regulation of microtubule nucleation in BMMCs. We identified that both protein tyrosine phosphatase SHP-

1 and SHP-2 were expressed in BMMCs, but only SHP-1 could form complexes with γ-tubulin, GCP2, and GCP4.

Additionally, we independently confirmed the SHP-1 interaction with γ-tubulin by immunoprecipitation using HEK cells, expressing EGFP-SHP-1. Gel filtration chromatography on Superose 6B showed that SHP-1 co-distributed with high molecular-weight fractions, corresponding to large γ-tubulin ring complexes (γTuRCs). The formation of complexes, containing γ-tubulin and SHP-1, was not limited to BMMCs only, as we obtained similar results in the human breast adenocarcinoma MCF7 cell line. We suggest that the direct or indirect interactions between SHP-1 and γ-tubulin complex proteins occur in various cell types.

We prepared BMMC lines lacking SHP-1, using CRISP/Cas9 editing system for deletion of 5'-region, containing the canonical and alternative start codons. We established three independent cell lines (SHP-1_KO1, SHP-1_KO2, and SHP-1_KO3) with the deletions in the targeted region and undetectable SHP-1 in immunoblotting. Upon Ag-induced activation, the absence of SHP-1 resulted in the increased total P-Tyr protein level. SHP-1-deficient cells had a hampered proliferation, an increased production of cytokines and prostaglandins. After Ag-induced activation, SHP-1_KO cells showed an enhanced Ca^{2+} influx, increased degranulation, and a significantly higher number of cells with microtubule protrusions.

We investigated whether SHP-1 could affect microtubule nucleation using a microtubule regrowth assay. The microtubule regrowth assay requires nocodazole-treatment to depolymerize microtubules in living cells. Followed by a nocodazole washout, fixation at defined time intervals stops the formation of new centrosomal microtubules. Newly generated microtubules are stained with an anti-α-tubulin antibody. The extent of nucleation is accessed as a fluorescence signal emanating from centrosomes (marked by anti-γ-tubulin antibody). We designed a Fiji-based semi-automated macro to quantify α- and γ-tubulin signals. Microtubule regrowth analysis showed an enhanced α-tubulin and γ-tubulin accumulation at the centrosomes in cells lacking SHP-1. Conversely, the pericentrin level at the centrosome was not affected. We performed rescue experiments, expressing SHP-1 in SHP-1_KO cells to verify the specificity of observed changes in microtubule nucleation. The SHP-1 expression in SHP-1-deficient cells decreased the microtubule regrowth level to that in control cells. Moreover, the inhibition of SHP-1 activity with SHP-1 phosphatase inhibitors TPI-1 or NSC87877 augmented the microtubule nucleation. Thus, SHP-1 represents a negative

regulator of microtubule nucleation and might directly or indirectly modulate γ-tubulin accumulation at the centrosome.

Although SHP-1 affected centrosomal microtubule nucleation, we could not detect SHP-1 at the centrosome using a limited set of commercial antibodies. Syk kinase was reported to localize at the centrosomes in different cell types [200, 201], and we showed that SHP-1 formed complexes with Syk, regulating its activity in BMMC. We could speculate that SHP-1 transiently interacted with the centrosome components and regulated microtubule nucleation indirectly by Syk activity modulation. In BMMCs, SHP-1 might balance the stimulating effect of the Src and Syk/ZAP protein kinases, affecting microtubule nucleation. Alternatively, SHP-1 might affect microtubule nucleation by modulating a P-Tyr level of proteins essential for γTuRC activation or centrosomal anchoring. For instance, the proteomic studies described the tyrosine phosphorylation of CDK5RAP2, NEDD1, ninein, pericentrin, and γ-tubulin [202].

Our data suggest that SHP-1 might be involved in the spatio-temporal regulation of degranulation by modulation of microtubule nucleation.

I modified the microtubule regrowth assay for suspension cells and participated in designing a semi-automated Fiji-based macro for regrowth assay data analysis. I performed microtubule regrowth assays with subsequent data analysis, carried out all fluorescence microscopy experiments, and prepared photo documentation. I participated in conceiving and designing experiments, suggesting the hypothesis. I participated in the writing the manuscript and responding to the reviewer's comments.

III.4 The actin regulator profilin 1 is functionally associated with the mammalian centrosome

The centrosome acts as a major microtubule-organizing organelle in almost all eukaryotic cells. It plays a crucial role in intracellular architecture, cell polarity, migration, and division [120]. The centrosome is also closely connected to the actin filaments, reflecting the tight crosstalk between microtubule and actin organization [83, 85, 152, 203, 204]. Several actin regulators, such as WASH, Arp2/3, cofilin, and members of the formin family [83, 152, 205], associate with the centrosome and potentially drive centrosome-linked actin organization [84].

Recent cryo-EM data revealed that the lumen of γTuRC accommodated an actin-like molecule associated with both γ-tubulins and GCPs [59, 61-63]. Further reports emphasized the connection between actin and γ-tubulin, as the latter was localized at the actin-rich cell periphery, influencing stress fiber formation [206].

Profilin 1 is ubiquitous and, with a few exceptions, the most abundant profilin variant present in vertebrate cells [207]. Profilin 1 is a principal control component of actin polymerization together with actin nucleation and elongation factors, such as members of the Ena/Vasp, formins, WASP, and WAVE families [156]. Profilin brings ATP-bound actin monomers to polymerization-competent sites [208, 209]. It was recently discovered that profilin 1 also acted as a control component of microtubule elongation at the cell periphery [155, 210].

In this study, we report that 1 (in the following text referred to as "profilin") extends its regulatory functions to microtubules and the centrosome. In agreement with previous mass spectroscopy data, identifying profilin as a component of isolated centrosomes [83], we observed profilin distribution at sites, corresponding to the centrosomes. Using confocal fluorescence microscopy and anti-profilin antibody, we observed profilin at the interphase centrosomes and noticed 1.6x higher profilin signal in mitotic mouse melanoma B16 cells. For localization studies, we also used a fluorescent variant of profilin with citrine fused intra-

molecularly, which did not affect profilin functions [211]. Chimeric profilin-citrine was expressed in B16 cells, and after gentle digitonin extraction and fixation, we observed citrine-profilin at the centrosomes of interphase and mitotic cells. Reciprocal immunoprecipitation with antibodies to γ-tubulin, GCP2, or profilin demonstrated that profilin was in complexes containing γTuRC components (γ-tubulin, GCP2, GCP4).

Moreover, the association of profilin with γTuRC was not limited to mouse B16 cells, as we obtained similar results in human colorectal adenocarcinoma Caco-2 cells. GST-fused truncated versions of γ-tubulin were used in pull-down experiments to test whether profilin interacted with γ-tubulin directly. We did not confirm such interaction, indicating that the profilin association with γTuRC was indirect and required additional components.

We used microtubule regrowth assay to follow *de novo* microtubule formation from interphase centrosomes in profilin 1-deficient B16 cells (hereafter denoted as "KO27"). Quantification of the α-tubulin immunofluorescence (corresponding to microtubules) revealed approximately three times higher signal in KO27 cells than in control B16 cells. Interestingly, quantification of γ-tubulin immunofluorescence showed γ-tubulin accumulation above wild-type level at the centrosomes in KO27 cells. We observed no difference in the amount of nocodazole-resistant microtubules between control B16 and KO27 cells, excluding a possibly higher number of nocodazole-resistant microtubules in KO27 cells. Moreover, untreated KO27 cells had higher microtubule content than in control cells. We compared the nucleation rate of centrosomal microtubules in control and KO27 cells to verify obtained results independently. Taking advantage of spinning disc confocal microscopy, we imaged 3D time-lapse series of cells, expressing mNeonGreen-tagged microtubule end-binding protein 3 (EB3), decorating the growing microtubule (+)-ends [212]. We followed the nucleation rate, calculated as the quantity of EB3 comets leaving the centrosome per unit of time. The nucleation rate was 2.2 times higher in KO27 cells than that in control. The phenotypic rescue experiments showed that the citrine-profilin introduction into KO27 cells restored the nucleation rate to the control level. These data demonstrated that centrosomal microtubule nucleation was increased in the absence of profilin. As profilin-actin moiety provides nucleation-competent actin for microfilament polymerization, we suggest that the centrosomal functions of profilin are related to centrosomal functions of actin [83]. The loss of profilin might result in two possible outcomes. Analogous to those events at the cell edge,

profilin might affect actin polymerization at the centrosome and eliminate the steric hindrance, preventing *de novo* microtubule formation. Alternatively, centrosomal profilin might fine-tune the actin availability for γ-TuRC. If it was a case, the deletion of profilin could increase the actin accessibility, potentiating the γ-TuRC activity and *de novo* microtubule nucleation.

Collectively, profilin plays a dual role in the organization of actin filaments and microtubules in mammalian cells. Several proteins have already been characterized as coordinators of actin and microtubule cytoskeleton [156, 213]. Our study points to a unique position of profilin among these proteins, as it can regulate both actin turnover and microtubule nucleation.

I performed microtubule regrowth assays with subsequent image visualization and data analysis. I performed live-cell imaging to quantify the microtubule nucleation rate and to localize chimeric profilin-citrine. I participated in conceiving and designing experiments, suggesting the hypothesis. I also participated in the writing the manuscript and responding to the reviewer's comments.

III.5 C53 interacting with UFM1-protein ligase 1 regulates microtubule nucleation in response to ER stress

Klebanovych, A., Vinopal, S., Dráberová, E., Sládková, V., Sulimenko, T., Sulimenko, V., Vosecká, V., Macůrek, L., Legido, A., Dráber, P. (2021) C53 interacting with UFM1-protein ligase 1 regulates microtubule nucleation in response to ER stress (bioRxiv 10.1101/2020.12.23.424116)

The organization of the endoplasmic reticulum (ER) relies on microtubules and microtubule motor proteins, generating pulling forces to position membranous ER parts [214]. Growing microtubules can generate pulling forces even in a motor-independent way [215]. For example, the microtubule (+)-ends recruit EB proteins to create a molecular platform for EB-binding partners such as ER-associated Ca^{2+} sensor STIM1 [216]. STIM1/EB/microtubule "tip attachment complex" (TAC) represents an alternative mechanism of ER distribution [217].

It is well established that ER stress is ameliorated by signaling pathways, triggering the unfolded protein response, which restores ER homeostasis [218]. Upon stress, ER undergoes rapid luminal expansion and an increase in tubule number to alleviate imbalanced ER homeostasis [219]. Interestingly, newly discovered PTM, the ufmylation, – the attachment of ubiquitin-fold modifier 1 (UFM1) to targeted proteins – also regulates ER stress response [138]. Furthermore, ER stress affects the expression of ufmylation pathway components [139]. In the present study, we provide evidence that C53 associates with UFL1 (E3 UMF1-protein ligase) and γTuRC components and participate in the modulation of centrosomal microtubule nucleation under ER stress. We identified UFL1 as an interacting partner for membrane-bound γ-tubulin. For this, we performed immunoprecipitation with an anti-peptide antibody to γ-tubulin and microsomal fraction extracts. The bound proteins, eluted with immunization peptide, were subjected to MALDI/MS fingerprinting analysis. Reciprocal immunoprecipitations confirmed the association of UFL1 and C53 with complexes containing γ-tubulin and GCPs. Furthermore, the separation of extracts by gel filtration revealed the co-distribution of UFL1, C53, γ-tubulin, and GCP2 in high-molecular-weight fractions, corresponding to large γTuRCs complexes. In addition, we showed that exogenous UFL1 and C53 could bind to γ-tubulin and GCPs. Finally, pull-down assays with GST-tagged C53, UFL1, or γ-tubulin confirmed that γ-tubulin and GCP2 bound to GST-UFL1 or GST-C53. The formation of complexes was not restricted to membranous fractions, as we got the same results, using whole-cell extracts.

We checked whether UFL1 and C53 could be found at the centrosomes. Using a limited number of commercial antibodies, we failed to localize these proteins at the centrosomes. C53-TagRFP, nevertheless, was localized at the interphase centrosomes, cytosol, and nuclei. Whereas UFL1-TagRFP was distributed in the cytosol, similar to control cells, expressing SHP-1-TagRFP. Although UFL1 and C53 interacted with each other and with γTuRC components, only C53 was detected at the centrosome of interphase cells.

Using CRISPR/Cas 9 gene editing, we prepared several cell lines, lacking either UFL1 (UFL1_KO) or C53 (C53_KO). The absence of UFL1 resulted in a substantial C53 and DDRGK1 decrease. Conversely, C53-deficient cells showed only a moderate decrease in the amount of UFL1 and DDRGK1. Our results, thus, confirmed other studies [140], suggesting that UFL1 plays a vital role in the regulation of the C53 protein level.

We demonstrated that UFL1 and C53 represent negative regulators of microtubule nucleation from interphase centrosomes. The deletion of either UFL1 or C53 resulted in increased centrosomal microtubule nucleation and γ-tubulin accumulation at the centrosomes. Increased nucleation was confirmed by quantification of nucleation rate during live-cell imaging. To verify the specificity of observed changes in microtubule nucleation, we performed rescue experiments by expressing either (i) UFL1-TagRFP or TagRFP alone in UFL1_KO cells; or (ii) C53-TagRFP or TagRFP alone in C53_KO cells. In both cases, microtubule nucleation returned to the wild-type level. Additionally, we introduced C53-TagRFP into UFL1_KO. As a result, C53 alone rescued the increased microtubule nucleation phenotype in UFL1_KO cells. Interestingly, both UFL1 and C53 affected the centrosomal γ-tubulin/γTuRCs levels. The reduced amount of centrosomal C53 likely explains the UFL1-mediated modulation of microtubule nucleation. Thus, the UFL1 regulatory role in microtubule nucleation could be indirect (i) through modulation of the C53 amount or (ii) through C53 relocation.

In UFL1_KO and C53_KO cells, live-cell imaging of ER indicated the generation of ER stress. As expected, we observed an increased expression of calnexin and PDI, markers of unfolded protein response occurring upon ER stress. During ER stress, one of the relief mechanisms involves ER expansion [218]. Microtubules regulate ER homeostasis, as the dynamics of ER and microtubules are tightly connected [220]. Therefore, we wanted to evaluate whether *de novo* microtubule nucleation could promote ER expansion in stressed cells. For that, we pre-treated U2OS cells with tunicamycin, an inhibitor of protein glycosylation and ER stress activator [221]. We detected the elevated expression of calnexin and PDI, both in transcript and protein levels. We also detected the increased ER expansion, accompanied by increased microtubule nucleation. These results suggest that centrosomal microtubule nucleation is enhanced during pharmacologically induced ER stress. Potentially, newly formed interactions between ER and microtubules could promote ER enlargement to restore ER homeostasis.

After tunicamycin-induced ER stress in cells expressing C53-TagRFP, we observed a decrease of overall C53-TagRFP signal and suppressed C53 association with the centrosomes. Immunoblotting indicated that the C53-TagRFP amount diminished in tunicamycin-treated cells. Whereas UFL1, endogenous C53, or γ-tubulin levels were similar in control and drug-treated cells, we did not observe such changes in tunicamycin-treated cells, expressing only TagRFP. In tunicamycin-treated cells, the lower amount of C53 was associated with P1

fraction, comprising centrosomes and nuclei with connected membranes. On the other hand, in control and tunicamycin-treated cells, the pericentrin amount in P1 fractions was comparable. Therefore, our data indicate that tunicamycin induced C53 relocation away from the centrosome. Such C53 relocation could unblock microtubule nucleation at the centrosomes in cells upon ER stress.

We suggest that the ER stress, induced either by tunicamycin treatment or by UFL1 or C53 deletion, stimulates centrosomal microtubule nucleation. The ER interaction with newly formed microtubules could promote ER expansion and restoration of ER homeostasis.

I performed microtubule regrowth assays with subsequent image visualization and data analysis. I conducted live-cell imaging to quantify the microtubule nucleation rate. I carried the majority of the fluorescence microscopy experiments and prepared photo documentation. I participated in conceiving and designing experiments, suggesting the hypothesis, writing the manuscript, and responding to the reviewer's comments.

IV   UNPUBLISHED RESULTS

IV.1   Microtubule nucleation during mast cell activation

Our previous data showed increased tubulin polymerization during pervanadate-induced activation of BMMC [183]. We made a similar observation in the case of Ag-induced activation (unpublished data). We have started experiments evaluating the nucleation rate of centrosomal microtubules upon activation to verify if it could reflect the increased microtubule nucleation. In order to obtain BMMCs, transiently expressing mNeon-Green-tagged EB3 (mNeonGreen-EB3-7 plasmid; Allele Biotechnology), we used Amaxa^{TM} nucleofector kit. The nucleofection was performed 24 h before activation and live-cell imaging. The next day, cells were cultured in an 8-well µSlide with fibronectin-coated Ibidi polymer coverslip bottom (Ibidi GmbH); 1 hour before imaging, the medium was replaced with RPMI for live-cell imaging. Cells were activated with a pervanadate solution for various time intervals, followed by 1-min time-lapse imaging.

Time-lapse sequences were collected in 6 optical slices with 0.1-µm steps at the 1-s interval for 1 min total. Images were acquired with the Andor Dragonfly 503 spinning disc confocal system (Oxford Instruments) equipped with a stage top microscopy incubator (Okolab), 488 nm solid-state 150 mW laser, HC PL APO 63x water objective, NA 1.20, and a 16-bit Ixon EMCCD scientific camera. At least five cells were imaged for each experiment with the following acquisition parameters: 40-µm pinhole size, 15% laser power, 50-ms exposure time, 525/50 nm emission filter. The time-lapse sequences were deconvoluted with Huygens Professional software v. 19.04 (Scientific Volume Imaging). A maximum intensity projection of a z stack was made for each time point in Fiji [222].

Newly nucleated microtubules were detected by manual counting of EB3 "comets," emanating from the centrosomes.
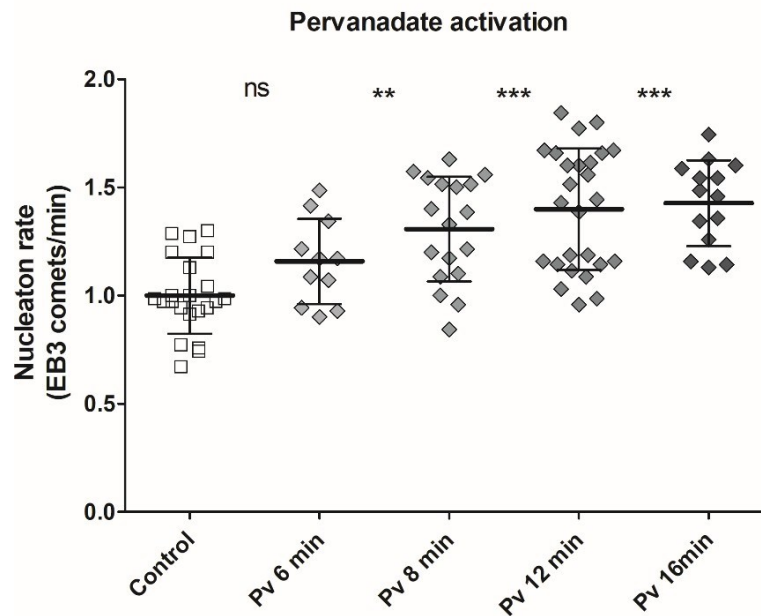
Figure S1 Nucleation rate in activated BMMCs. Microtubule nucleation rate in pervanadate-activated cells relative to control non-activated cells. Cells were treated with a pervanadate solution for 5-, 7-, 11-, and 15-min time intervals, followed by 1-min time-lapse imaging. Three independent experiments (at least 5 cells counted in each experiment). Bold and thin lines represent mean ± SD, *, $p < 0.05$; **, $p < 0.01$; ***, $p < 0.0001$, ns, $p \geq 0.05$. One-way ANOVA followed by a Sidak's post hoc test were performed to determine statistical significance.

The pervanadate activation resulted in a significantly higher number of nucleated microtubules, reaching its highest level around the 12th-min of activation (Fig. S1). These data demonstrate that inhibition of protein tyrosine phosphatases stimulates microtubule nucleation. Therefore, tyrosine phosphorylation kinases play an important role in the regulation of *de novo* microtubule nucleation in BMMCs.

IV.2   Role of PAK1 kinase in regulation of microtubule nucleation in mast cells

We reported that PAK1 represents a positive regulator of microtubule nucleation in human osteosarcoma cell line U2OS [118]. We started the experiments on BMMCs to corroborate this finding in other cell types of different species. For PAK1 depletion, we used the RNAi approach. shRNAs, targeting all transcript variants of mouse PAK1 (Open Biosystems), were cloned into lentiviral pLKO.1 vectors. Cells, transduced with pLKO.1 vector with non-target shRNA (Sigma), were used as negative controls. Lentiviral transductions were done as described previously, using HEK 293FT packaging cells for virus preparation [180]. Based on immunoblotting and

quantitative RT-PCR results, we selected the cells with the highest reduction of PAK1, denoted as PAK1-KD1 and PAK1-KD2 (Fig. S2A). Microtubule regrowth experiments were performed as described [180].
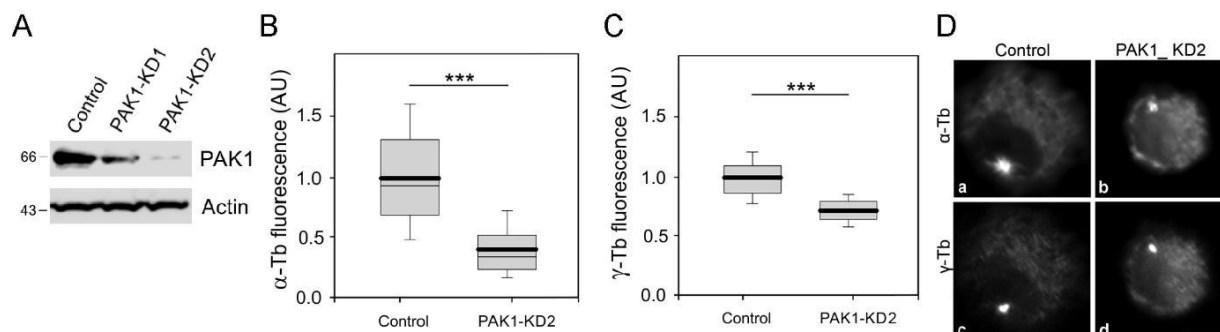

Figure S2 Effect of PAK1 depletion on microtubule nucleation. (A) The PAK1 protein level in control and PAK1-deficient cell lines (PAK1_KD1, PAK1_KD2), analyzed by immunoblotting of whole-cell lysates. Actin served as the loading control. (B-C) The distribution of α-tubulin or γ-tubulin fluorescence intensities (arbitrary units, AU) in 1.5-μm ROI at 1 min of microtubule regrowth is shown as box plots. Three independent experiments, >70 cells counted for each experimental condition. (B) The box plot of α-tubulin fluorescence in PAK1-KD2 cells (N=262) relative to the control cells (Control, N=215). (C) The box plot of γ-tubulin fluorescence PAK1-KD2 cells (N=248) relative to the control cells (Control, N=239). Bold and thin lines within the box represent mean and median (the 50th percentile), respectively. The bottom and top of the box represent the 25th and 75th percentiles. Whiskers below and above the box indicate the 10th and 90th percentiles. ***, p <0.0001. Two-tailed unpaired Student's *t*-test was performed to determine statistical significance in B-C. (D) Staining of α-tubulin or γ-tubulin in microtubule regrowth experiments in control cells (Control; a, c) and PAK1-deficient cells (PAK1-KD2; b, d). The pairs of images a, b and c, d were collected and processed in the same manner. Scale bar, 5 μm.

Briefly, cells were treated with 10 μM nocodazole to depolymerize microtubules completely. Cells were then washed with PBS buffer at 4°C to remove the drug and then transferred to a complete RPMI medium. Microtubule regrowth was allowed for 1 min at 28°C and stopped by fixation in formaldehyde. Cells were double-labeled with a rabbit anti-α-tubulin antibody GTX15246 (GeneTex) and a mouse anti-γ-tubulin antibody TU 30 [223] to visualize microtubules and centrosomes, respectively. Images for analysis were acquired as consecutive z-stacks with 0.2-μm step, using the inverted fluorescence microscope Olympus IX-71 with Delta Vision Core, 60x oil objective, NA 1.42. Using Fiji software, we accessed fluorescence intensity of α-tubulin and γ-tubulin signals in a 1.5-μm region of interest (ROI), centered at the centrosome.

Quantification of immunofluorescence intensity of α-tubulin (Fig S2B) and γ-tubulin (Fig S2C) revealed a significant decrease in microtubule regrowth and the amount of centrosomal

40

γ-tubulin in PAK1-KD2 cells. Similar results were obtained for PAK1-KD1. Conversely, the amount of pericentrin, PCM marker, was not affected (data not shown). Typical staining of α-tubulin and γ-tubulin in control and PAK1-KD2 cells is shown in Fig S2D. These results suggest that the regulatory role of PAK1 kinase is most likely conveyed by the number of γTuRCs at the centrosomes.

To evaluate whether the enzymatic activity of PAK1 is essential for this regulation, we performed microtubule regrowth assay in cells pre-treated with IPA-3 inhibitor, selectively inhibiting group I PAKs, comprising PAK1-3 [224]. BMMCs were pre-treated with 10 µM IPA-3 (Merck) or DMCO carrier (Control) for 1 h before the assay. As shown in Fig. S3A-C, we obtained similar results as in cells with depleted PAK1.
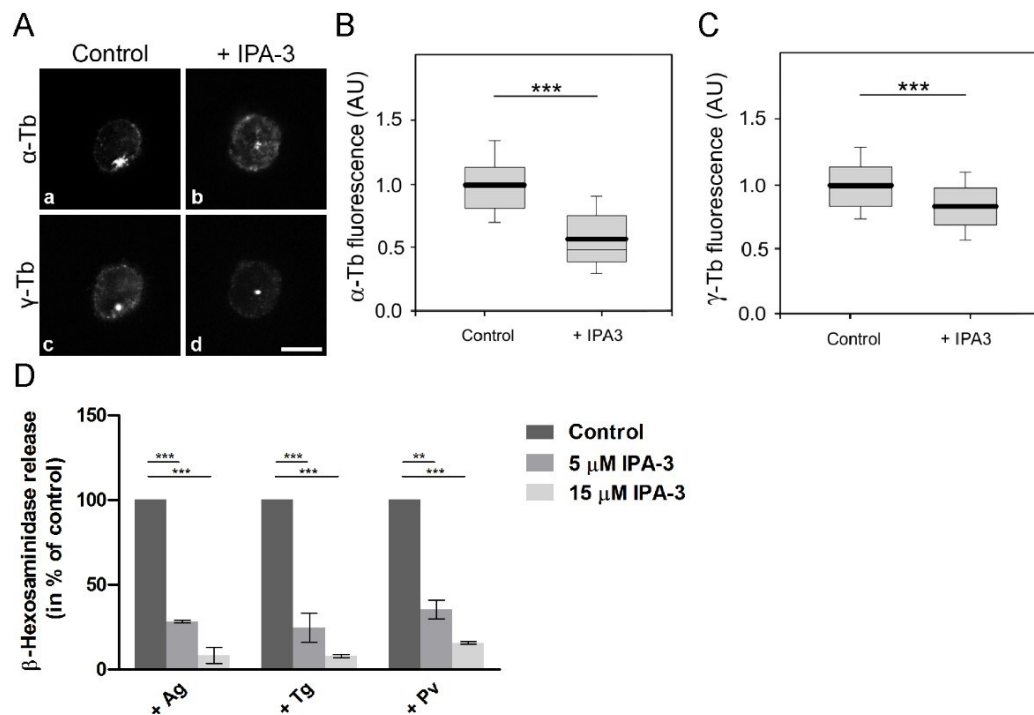
Figure S3 Effect of PAK1 kinase inhibition on microtubule nucleation and degranulation.

(**A**) Staining of α-tubulin or γ-tubulin in microtubule regrowth experiments in control cells (**a, c**) and after inhibition of PAK1 with IPA-3 (**+IPA-3**, 10 µM for 1 h, **b, d**). The pairs of images in a, b and c, d were collected and processed in the same manner. Scale bar, 10 µm. (**B-C**) The distribution of α-tubulin or γ-tubulin fluorescence intensities (arbitrary units, AU) in 1.5-µm ROI at 1 min of microtubule regrowth in Control and IPA-3-treated cells (10 µM for 1 h) is shown as box plots. Three independent experiments, >70 cells counted for each experimental condition. (**B**) The box plot of α-tubulin fluorescence in IPA-3-treated cells (N=221) relative to control cells (N=266). (**C**) The box plot of γ-tubulin fluorescence intensity in IPA-3-treated cells (N=334) relative to control cells (N=461). Bold and thin lines within the box represent mean and median (the 50th percentile), respectively. The bottom and top of the box represent the 25th and 75th percentiles. Whiskers below and above the box indicate the 10th and 90th percentiles. ***, p <0.0001. (**D**) The degranulation was measured as a β-hexosaminidase release in the control

BMMCs and IPA-3-treated cells. BMMCs were activated with antigen (**+Ag**, 0.1 µg/mL), thapsigargin (**+Tg**, 2 µM), and pervanadate solution (**+Pv**, 1:100). The data represent the mean±SD. ***p<0.0001. Two-tailed unpaired Student's *t*-test was performed to determine statistical significance in B-C.

To study the effect of PAK1 inhibition on degranulation in BMMCs, we quantified the release of β-hexosaminidase in Ag-, thapsigargin-, or pervanadate-activated cells, using 4-NAG as a substrate [181]. The total content of the enzyme was evaluated in supernatants from cells lysed with 0.1% Triton X-100. The extent of degranulation was calculated as absorbance of culture supernatant×100/absorbance of total cell lysate and normalized to control cells. After IPA-3 treatment, the degranulation level was impaired, suggesting that active PAK1 kinase is required for degranulation (Fig. S3D).

Our data document that active PAK1 represents a positive regulator of microtubule nucleation from interphase centrosomes in BMMCs. Moreover, the regulatory role of PAK1 in microtubule nucleation correlates with degranulation in activated BMMCs.

IV.3   Role of PKCβ in regulation of microtubule organization in activated mast cells

We showed that the inhibition of diacylglycerol- and Ca^{2+}-dependent conventional protein kinase C (cPKC), critical in signal transduction pathways in activated BMMCs, suppresses the microtubule reorganization, degranulation, and Ag-induced chemotaxis [188]. Conventional PKCs comprise α, $β_I$, $β_{II}$, and γ isoforms. In BMMCs, we detected both PKCα and PKCβ isoforms, but PKCβ isoforms were abundant. To evaluate if PKCβ could regulate microtubule nucleation, we performed a microtubule regrowth assay in PKCβ-depleted cells. For depletion of PKCβ, we used the RNAi approach. Specific shRNAs (targeting all transcript variants of mouse PKCβ1 and PKCβ2) were cloned into the lentiviral pLKO.1. The PKCβ_KD cell line, with the highest

reduction of PKCβ, was selected for further investigation (Fig. S4A). Microtubule regrowth experiments were performed as described in Chapter IV.2.
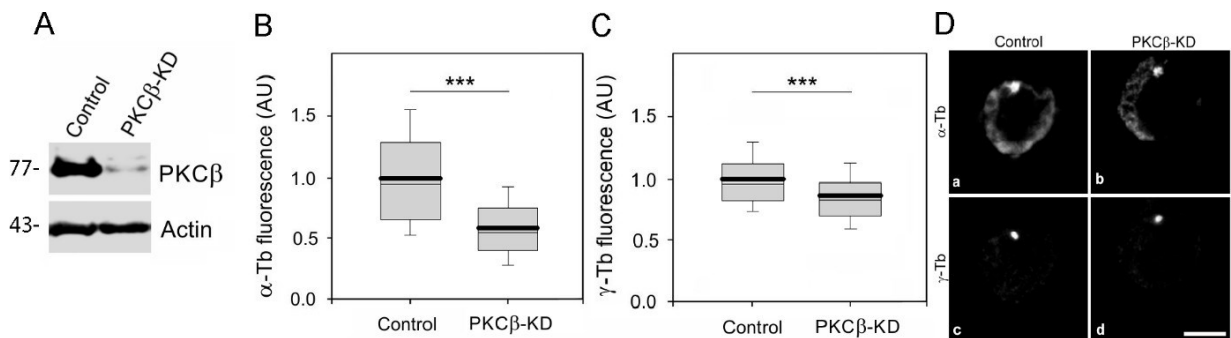

Figure S4 Effect of PKCβ1 depletion on microtubule regrowth in BMMCs. (A) The PKCβ protein level in control and PKCβ-deficient cell lines were analyzed by immunoblotting of whole-cell lysates. Actin served as the loading control. (B-C) The distribution of α-tubulin or γ-tubulin fluorescence intensities (arbitrary units, AU) in 1.5-μm ROI at 1 min of microtubule regrowth in BMMCs (Control) and PKCβ-deficient BMMCs (PKCβ-KD) are shown as box plots. Three independent experiments, >70 cells counted for each experimental condition. (B) The box plot of α-tubulin fluorescence in PKCβ-KD (N=254) relative to control (N=208). (C) The box plot of γ-tubulin fluorescence in PKCβ-KD (N=347) relative to control (N=337). Bold and thin lines within the box represent mean and median (the 50th percentile), respectively. The bottom and top of the box represent the 25th and 75th percentiles. Whiskers below and above the box indicate the 10th and 90th percentiles. ***, p <0.0001. Two-tailed unpaired Student's t-test was performed to determine statistical significance. (D) Staining of α-tubulin or γ-tubulin in microtubule regrowth experiments in control cells (a, c) and PKCβ-KD (b, d). The pairs of images in a, b and c, d were collected and processed in the same manner. Scale bar, 5 μm.

Quantification of immunofluorescence intensity for α-tubulin (Fig S4B) and γ-tubulin (Fig S4C) showed a significant decrease in microtubule regrowth and the amount of centrosomal γ-tubulin in PKCβ-depleted cells. Conversely, the amount of pericentrin, PCM marker, was not affected by (data not shown). Typical staining of α-tubulin and γ-tubulin in control and PKCβ1-depleted cells is shown in Fig. S4D. The PKCβ1 kinase could represent a positive regulator of microtubule nucleation. This modulatory role is most likely conveyed by the number of γTuRCs at the centrosomes.

PKCβ kinase, similarly to PAK1, represents a positive regulator of microtubule nucleation. We have previously shown that PAK1 phosphorylates GIT1, the adaptor protein associating with the centrosome, and positively regulating the microtubule nucleation. We suggested that activated PAK1 phosphorylates GIT1, which resulted in a release of autoinhibitory conformation of GIT1. Activated GIT1 enables the accumulation of γ-tubulin/γ-TuRCs, leading

to increased microtubule nucleation. Alternatively, activated GIT1 stimulates so far uncharacterized protein(s) to bind more γ-tubulin/γTuRCs [118]. Recently, we found that PKCβ also phosphorylates GIT1 (V. Sulimenko, unpublished data). In activated BMMCs, microtubule nucleation might be regulated by the concerted action of PAK1 and PKCβ.

V CONCLUSIONS

1) We modified the microtubule regrowth assay for non-adherent BMMCs and developed Fiji-based semi-automated macro to quantify α- and γ-tubulin signals. We modified live-cell imaging for the quantification of microtubule nucleation. Described methods have been used in subsequent projects and during testing of nanosecond pulsed electric field lab-on-chip integrated with super-resolution microscope described in [225]. This work, included in Supplements VIII, was not commented in the frame of this thesis.

2) Transient increase of polymerized microtubules is a characteristic feature of activated BMMCs. We found that protein tyrosine phosphatase SHP-1 forms complexes with γ-tubulin and GCPs in BMMCs. Analysis of SHP-1-deficient cell lines prepared by CRISPR/Cas9 editing revealed that SHP-1 represents a negative regulator of microtubule nucleation. We suggest that non-receptor tyrosine kinase Syk, activated by phosphorylation on tyrosine during early stages of Ag-induced activation and located at the centrosome, might be a potential target for SHP-1. We proposed a novel regulatory mechanism of microtubule formation that is linked with degranulation in activated BMMCs.

ER distribution depends on microtubules, and ER stress results in ER remodeling. We found that UFL1 and C53 were associated with γ-TuRC proteins. Knockout of UFL1 or C53 induced ER stress, increased centrosomal microtubule nucleation, and ER expansion. Unlike UFL1, C53 could associate with the centrosomes of human U2OS cells. Considering that C53 rescued microtubule nucleation in UFL1-deficient cells, the regulatory role of UFL1 in microtubule nucleation could be indirect. Such an indirect role might be conveyed by modulating the C53 amount or by C53 detachment from centrosomes. Pharmacologically induced ER stress also resulted in the increased microtubule nucleation and ER expansion. Our findings suggest that newly formed microtubules could promote the expansion and restoration of ER homeostasis under ER stress.

3) We showed that profilin 1, a principal component of actin polymerization, localizes to the interphase and mitotic centrosomes, forming complexes with γTuRCs. We demonstrated for the first time that profilin is a regulator of centrosomal microtubule

nucleation. This finding opens new directions in the microfilament-microtubule cross-talk studies.

4) We found that both plant and animal highly purified γ-tubulins without GCPs had the intrinsic property of self-polymerization into filaments *in vitro*. γ-Tubulin fibrillary structures were imaged with super-resolution microscopy in *Arabidopsis* cells. We suggest that γ-tubulin in the form of oligomers/polymers also perform scaffolding or sequestration functions.

VI REFERENCES

1.   McIntosh, J.R., Morphew, M.K., Grissom, P.M., Gilbert, S.P., and Hoenger, A. (2009). Lattice structure of cytoplasmic microtubules in a cultured mammalian cell. J Mol Biol *394*, 177-182.
2.   Goodson, H.V., and Jonasson, E.M. (2018). Microtubules and microtubule-associated proteins. Cold Spring Harb Perspect Biol *10*, a022608.
3.   Mitchison, T., and Kirschner, M. (1984). Dynamic instability of microtubule growth. Nature *312*, 237-242.
4.   Hyman, A.A., Chretien, D., Arnal, I., and Wade, R.H. (1995). Structural changes accompanying GTP hydrolysis in microtubules: information from a slowly hydrolyzable analogue guanylyl-(α,β)-methylene-diphosphonate. J Cell Biol *128*, 117-125.
5.   Alushin, G.M., Lander, G.C., Kellogg, E.H., Zhang, R., Baker, D., and Nogales, E. (2014). High-resolution microtubule structures reveal the structural transitions in αβ-tubulin upon GTP hydrolysis. Cell *157*, 1117-1129.
6.   Akhmanova, A., and Steinmetz, M.O. (2015). Control of microtubule organization and dynamics: two ends in the limelight. Nat Rev Mol Cell Biol *16*, 711-726.
7.   Gardner, M.K., Zanic, M., and Howard, J. (2013). Microtubule catastrophe and rescue. Curr Opin Cell Biol *25*, 14-22.
8.   Janson, M.E., de Dood, M.E., and Dogterom, M. (2003). Dynamic instability of microtubules is regulated by force. J Cell Biol *161*, 1029-1034.
9.   Dimitrov, A., Quesnoit, M., Moutel, S., Cantaloube, I., Pous, C., and Perez, F. (2008). Detection of GTP-tubulin conformation in vivo reveals a role for GTP remnants in microtubule rescues. Science *322*, 1353-1356.
10.   Aumeier, C., Schaedel, L., Gaillard, J., John, K., Blanchoin, L., and Thery, M. (2016). Self-repair promotes microtubule rescue. Nat Cell Biol *18*, 1054-1064.
11.   Gardner, M.K. (2016). Cell Biology: Microtubule Collisions to the Rescue. Curr Biol *26*, R1287-R1289.
12.   Janke, C., and Magiera, M.M. (2020). The tubulin code and its role in controlling microtubule properties and functions. Nat Rev Mol Cell Biol *21*, 307-326.
13.   Magiera, M.M., and Janke, C. (2014). Post-translational modifications of tubulin. Curr Biol *24*, R351-354.
14.   Luduena, R.F. (2013). A hypothesis on the origin and evolution of tubulin. Int Rev Cell Mol Biol *302*, 41-185.
15.   Amargant, F., Barragan, M., Vassena, R., and Vernos, I. (2019). Insights of the tubulin code in gametes and embryos: from basic research to potential clinical applications in humansdagger. Biol Reprod *100*, 575-589.
16.   Fagerberg, L., Hallstrom, B.M., Oksvold, P., Kampf, C., Djureinovic, D., Odeberg, J., Habuka, M., Tahmasebpoor, S., Danielsson, A., Edlund, K., et al. (2014). Analysis of the human tissue-specific expression by genome-wide integration of transcriptomics and antibody-based proteomics. Mol Cell Proteomics *13*, 397-406.
17.   Gadadhar, S., Bodakuntla, S., Natarajan, K., and Janke, C. (2017). The tubulin code at a glance. J Cell Sci *130*, 1347-1353.
18.   Schwer, H.D., Lecine, P., Tiwari, S., Italiano, J.E., Jr., Hartwig, J.H., and Shivdasani, R.A. (2001). A lineage-restricted and divergent β-tubulin isoform is essential for the biogenesis, structure and function of blood platelets. Curr Biol *11*, 579-586.
19.   Hoyle, H.D., and Raff, E.C. (1990). Two Drosophila β-tubulin isoforms are not functionally equivalent. J Cell Biol *111*, 1009-1026.
20.   Sweeney, H.L., and Holzbaur, E.L.F. (2018). Motor Proteins. Cold Spring Harb Perspect Biol *10*.
21.   Maurer, S.P., Fourniol, F.J., Bohner, G., Moores, C.A., and Surrey, T. (2012). EBs recognize a nucleotide-dependent structural cap at growing microtubule ends. Cell *149*, 371-382.

22. Vemu, A., Szczesna, E., Zehr, E.A., Spector, J.O., Grigorieff, N., Deaconescu, A.M., and Roll-Mecak, A. (2018). Severing enzymes amplify microtubule arrays through lattice GTP-tubulin incorporation. Science *361,* eaau1504.

23. Akhmanova, A., and Hoogenraad, C.C. (2015). Microtubule minus-end-targeting proteins. Curr Biol *25*, R162-171.

24. Hendershott, M.C., and Vale, R.D. (2014). Regulation of microtubule minus-end dynamics by CAMSAPs and Patronin. Proc Natl Acad Sci U S A *111*, 5860-5865.

25. Meunier, S., Shvedunova, M., Van Nguyen, N., Avila, L., Vernos, I., and Akhtar, A. (2015). An epigenetic regulator emerges as microtubule minus-end binding and stabilizing factor in mitosis. Nat Commun *6*, 7889.

26. Dehmelt, L., and Halpain, S. (2005). The MAP2/Tau family of microtubule-associated proteins. Genome Biol *6*, 204.

27. Roger, B., Al-Bassam, J., Dehmelt, L., Milligan, R.A., and Halpain, S. (2004). MAP2c, but not tau, binds and bundles F-actin via its microtubule binding domain. Curr Biol *14*, 363-371.

28. Roll-Mecak, A., and McNally, F.J. (2010). Microtubule-severing enzymes. Curr Opin Cell Biol *22*, 96-103.

29. Amos, L.A., and Schlieper, D. (2005). Microtubules and MAPs. Adv Protein Chem *71*, 257-298.

30. Coulup, S.K., and Georg, G.I. (2019). Revisiting microtubule targeting agents: α-Tubulin and the pironetin binding site as unexplored targets for cancer therapeutics. Bioorg Med Chem Lett *29*, 1865-1873.

31. Borowiak, M., Nahaboo, W., Reynders, M., Nekolla, K., Jalinot, P., Hasserodt, J., Rehberg, M., Delattre, M., Zahler, S., Vollmar, A., et al. (2015). Photoswitchable inhibitors of microtubule dynamics optically control mitosis and cell death. Cell *162*, 403-411.

32. Katsetos, C.D., and Dráber, P. (2012). Tubulins as therapeutic targets in cancer: from bench to bedside. Curr Pharm Des *18*, 2778-2792.

33. Joshi, H.C., Palacios, M.J., McNamara, L., and Cleveland, D.W. (1992). γ-Tubulin is a centrosomal protein required for cell cycle-dependent microtubule nucleation. Nature *356*, 80-83.

34. Oakley, B.R., Oakley, C.E., Yoon, Y., and Jung, M.K. (1990). γ-Tubulin is a component of the spindle pole body that is essential for microtubule function in *Aspergillus nidulans*. Cell *61*, 1289-1301.

35. Stearns, T., Evans, L., and Kirschner, M. (1991). γ-Tubulin is a highly conserved component of the centrosome. Cell *65*, 825-836.

36. Oakley, B.R. (2000). An abundance of tubulins. Trends Cell Biol *10*, 537-542.

37. Findeisen, P., Muhlhausen, S., Dempewolf, S., Hertzog, J., Zietlow, A., Carlomagno, T., and Kollmar, M. (2014). Six subgroups and extensive recent duplications characterize the evolution of the eukaryotic tubulin protein family. Genome Biol Evol *6*, 2274-2288.

38. Yuba-Kubo, A., Kubo, A., Hata, M., and Tsukita, S. (2005). Gene knockout analysis of two γ-tubulin isoforms in mice. Dev Biol *282*, 361-373.

39. Vinopal, S., Černohorská, M., Sulimenko, V., Sulimenko, T., Vosecká, V., Flemr, M., Dráberova, E., and Dráber, P. (2012). γ-Tubulin 2 nucleates microtubules and is downregulated in mouse early embryogenesis. PLoS One *7*, e29919.

40. Dráberova, E., Sulimenko, V., Vinopal, S., Sulimenko, T., Sládková, V., D'Agostino, L., Sobol, M., Hozák, P., Kren, L., Katsetos, C.D., et al. (2017). Differential expression of human γ-tubulin isotypes during neuronal development and oxidative stress points to a γ-tubulin-2 prosurvival function. FASEB J *31*, 1828-1846.

41. Aldaz, H., Rice, L.M., Stearns, T., and Agard, D.A. (2005). Insights into microtubule nucleation from the crystal structure of human γ-tubulin. Nature *435*, 523-527.

42. Starita, L.M., Machida, Y., Sankaran, S., Elias, J.E., Griffin, K., Schlegel, B.P., Gygi, S.P., and Parvin, J.D. (2004). BRCA1-dependent ubiquitination of γ-tubulin regulates centrosome number. Mol Cell Biol *24*, 8457-8466.

43. Sulimenko, V., Sulimenko, T., Poznanovic, S., Nechiporuk-Zloy, V., Bohm, K.J., Macůrek, L., Unger, E., and Dráber, P. (2002). Association of brain γ-tubulins with αβ-tubulin dimers. Biochem J *365*, 889-895.

44. Vogel, J., Drapkin, B., Oomen, J., Beach, D., Bloom, K., and Snyder, M. (2001). Phosphorylation of γ-tubulin regulates microtubule organization in budding yeast. Dev Cell *1*, 621-631.

45. Moudjou, M., Bordes, N., Paintrand, M., and Bornens, M. (1996). γ-Tubulin in mammalian cells: the centrosomal and the cytosolic forms. J Cell Sci *109 (Pt 4)*, 875-887.

46. Oegema, K., Wiese, C., Martin, O.C., Milligan, R.A., Iwamatsu, A., Mitchison, T.J., and Zheng, Y. (1999). Characterization of two related *Drosophila* γ-tubulin complexes that differ in their ability to nucleate microtubules. J Cell Biol *144*, 721-733.

47. Stearns, T., and Kirschner, M. (1994). *In vitro* reconstitution of centrosome assembly and function: the central role of γ-tubulin. Cell *76*, 623-637.

48. Zheng, Y., Wong, M.L., Alberts, B., and Mitchison, T. (1995). Nucleation of microtubule assembly by a γ-tubulin-containing ring complex. Nature *378*, 578-583.

49. Zupa, E., Liu, P., Wurtz, M., Schiebel, E., and Pfeffer, S. (2020). The structure of the γ-TuRC: a 25-years-old molecular puzzle. Curr Opin Struct Biol *66*, 15-21.

50. Geissler, S., Pereira, G., Spang, A., Knop, M., Soues, S., Kilmartin, J., and Schiebel, E. (1996). The spindle pole body component Spc98p interacts with the γ-tubulin-like Tub4p of *Saccharomyces cerevisiae* at the sites of microtubule attachment. EMBO J *15*, 3899-3911.

51. Knop, M., Pereira, G., Geissler, S., Grein, K., and Schiebel, E. (1997). The spindle pole body component Spc97p interacts with the γ-tubulin of *Saccharomyces cerevisiae* and functions in microtubule organization and spindle pole body duplication. EMBO J *16*, 1550-1564.

52. Vinh, D.B., Kern, J.W., Hancock, W.O., Howard, J., and Davis, T.N. (2002). Reconstitution and characterization of budding yeast γ-tubulin complex. Mol Biol Cell *13*, 1144-1157.

53. Kollman, J.M., Greenberg, C.H., Li, S., Moritz, M., Zelter, A., Fong, K.K., Fernandez, J.J., Sali, A., Kilmartin, J., Davis, T.N., et al. (2015). Ring closure activates yeast γTuRC for species-specific microtubule nucleation. Nat Struct Mol Biol *22*, 132-137.

54. Kollman, J.M., Polka, J.K., Zelter, A., Davis, T.N., and Agard, D.A. (2010). Microtubule nucleating γ-TuSC assembles structures with 13-fold microtubule-like symmetry. Nature *466*, 879-882.

55. Kollman, J.M., Zelter, A., Muller, E.G., Fox, B., Rice, L.M., Davis, T.N., and Agard, D.A. (2008). The structure of the γ-tubulin small complex: implications of its architecture and flexibility for microtubule nucleation. Mol Biol Cell *19*, 207-215.

56. Kollman, J.M., Merdes, A., Mourey, L., and Agard, D.A. (2011). Microtubule nucleation by γ-tubulin complexes. Nat Rev Mol Cell Biol *12*, 709-721.

57. Teixidó-Travesa, N., Roig, J., and Lüders, J. (2012). The where, when and how of microtubule nucleation - one ring to rule them all. J Cell Sci *125*, 4445-4456.

58. Murphy, S.M., Urbani, L., and Stearns, T. (1998). The mammalian γ-tubulin complex contains homologues of the yeast spindle pole body components spc97p and spc98p. J Cell Biol *141*, 663-674.

59. Consolati, T., Locke, J., Roostalu, J., Chen, Z.A., Gannon, J., Asthana, J., Lim, W.M., Martino, F., Cvetkovic, M.A., Rappsilber, J., et al. (2020). Microtubule nucleation properties of single human γTuRCs explained by their cryo-EM structure. Dev Cell *53*, 603-617.

60. Liu, P., Wurtz, M., Zupa, E., Pfeffer, S., and Schiebel, E. (2020). Microtubule nucleation: the waltz between γ-tubulin ring complex and associated proteins. Curr Opin Cell Biol *68*, 124-131.

61. Liu, P., Zupa, E., Neuner, A., Bohler, A., Loerke, J., Flemming, D., Ruppert, T., Rudack, T., Peter, C., Spahn, C., et al. (2020). Insights into the assembly and activation of the microtubule nucleator γ-TuRC. Nature *578*, 467-471.

62. Wieczorek, M., Huang, T.L., Urnavicius, L., Hsia, K.C., and Kapoor, T.M. (2020). MZT proteins form multi-faceted structural modules in the γ-tubulin ring complex. Cell Rep *31*, 107791.

63. Wieczorek, M., Urnavicius, L., Ti, S.C., Molloy, K.R., Chait, B.T., and Kapoor, T.M. (2020). Asymmetric molecular architecture of the human γ-tubulin ring complex. Cell *180*, 165-175.

64. Hutchins, J.R., Toyoda, Y., Hegemann, B., Poser, I., Heriche, J.K., Sykora, M.M., Augsburg, M., Hudecz, O., Buschhorn, B.A., Bulkescher, J., et al. (2010). Systematic analysis of human protein complexes identifies chromosome segregation proteins. Science *328*, 593-599.

65. Wiese, C., and Zheng, Y. (2000). A new function for the γ-tubulin ring complex as a microtubule minus-end cap. Nat Cell Biol *2*, 358-364.

66. Cuschieri, L., Miller, R., and Vogel, J. (2006). γ-Tubulin is required for proper recruitment and assembly of Kar9-Bim1 complexes in budding yeast. Mol Biol Cell *17*, 4420-4434.

67. Prigozhina, N.L., Oakley, C.E., Lewis, A.M., Nayak, T., Osmani, S.A., and Oakley, B.R. (2004). γ-Tubulin plays an essential role in the coordination of mitotic events. Mol Biol Cell *15*, 1374-1386.

68. Hořejší, B., Vinopal, S., Sládková, V., Dráberova, E., Sulimenko, V., Sulimenko, T., Vosecká, V., Philimonenko, A., Hozák, P., Katsetos, C.D., et al. (2012). Nuclear γ-tubulin associates with nucleoli and interacts with tumor suppressor protein C53. J Cell Physiol *227*, 367-382.

69. Hoog, G., Zarrizi, R., von Stedingk, K., Jonsson, K., and Alvarado-Kristensson, M. (2011). Nuclear localization of γ-tubulin affects E2F transcriptional activity and S-phase progression. FASEB J *25*, 3815-3827.

70. Eklund, G., Lang, S., Glindre, J., Ehlen, A., and Alvarado-Kristensson, M. (2014). The nuclear localization of γ-tubulin is regulated by SadB-mediated phosphorylation. J Biol Chem *289*, 21360-21373.

71. Lesca, C., Germanier, M., Raynaud-Messina, B., Pichereaux, C., Etievant, C., Emond, S., Burlet-Schiltz, O., Monsarrat, B., Wright, M., and Defais, M. (2005). DNA damage induce γ-tubulin-RAD51 nuclear complexes in mammalian cells. Oncogene *24*, 5165-5172.

72. Chumová, J., Kourová, H., Trögelová, L., Halada, P., and Binarová, P. (2019). Microtubular and nuclear functions of γ-tubulin: are they LINCed? Cells *8,* 259.

73. Corvaisier, M., and Alvarado-Kristensson, M. (2020). Non-canonical functions of the γ-tubulin meshwork in the regulation of the nuclear architecture. Cancers (Basel) *12*, 3102.

74. Rossello, C.A., Lindström, L., Glindre, J., Eklund, G., and Alvarado-Kristensson, M. (2016). γ-Tubulin coordinates nuclear envelope assembly around chromatin. Heliyon *2*, e00166.

75. Chumová, J., Trögelová, L., Kourová, H., Volc, J., Sulimenko, V., Halada, P., Kučera, O., Benada, O., Kuchařová, A., Klebanovych, A., et al. (2018). γ-Tubulin has a conserved intrinsic property of self-polymerization into double stranded filaments and fibrillar networks. Biochim Biophys Acta Mol Cell Res *1865*, 734-748.

76. Lindström, L., and Alvarado-Kristensson, M. (2018). Characterization of γ-tubulin filaments in mammalian cells. Biochim Biophys Acta Mol Cell Res *1865*, 158-171.

77. Rossello, C.A., Lindström, L., Eklund, G., Corvaisier, M., and Kristensson, M.A. (2018). γ-Tubulin-γ-tubulin interactions as the basis for the formation of a meshwork. Int J Mol Sci *19, 3245*.

78. Pouchucq, L., Lobos-Ruiz, P., Araya, G., Valpuesta, J.M., and Monasterio, O. (2018). The chaperonin CCT promotes the formation of fibrillar aggregates of γ-tubulin. Biochim Biophys Acta Proteins Proteom *1866*, 519-526.

79. Fu, J., and Glover, D.M. (2012). Structured illumination of the interface between centriole and peri-centriolar material. Open Biol *2*, 120104.

80. Sonnen, K.F., Schermelleh, L., Leonhardt, H., and Nigg, E.A. (2012). 3D-structured illumination microscopy provides novel insight into architecture of human centrosomes. Biol Open *1*, 965-976.

81. Joukov, V., and De Nicolo, A. (2019). The Centrosome and the primary cilium: the yin and yang of a hybrid organelle. Cells *8,* 701.

82. Bornens, M. (2012). The centrosome in cells and organisms. Science *335*, 422-426.

83. Farina, F., Gaillard, J., Guerin, C., Coute, Y., Sillibourne, J., Blanchoin, L., and Thery, M. (2016). The centrosome is an actin-organizing centre. Nat Cell Biol *18*, 65-75.

84. Farina, F., Ramkumar, N., Brown, L., Samandar Eweis, D., Anstatt, J., Waring, T., Bithell, J., Scita, G., Thery, M., Blanchoin, L., et al. (2019). Local actin nucleation tunes centrosomal microtubule nucleation during passage through mitosis. EMBO J *38, e99843*.

85. Inoue, D., Obino, D., Pineau, J., Farina, F., Gaillard, J., Guerin, C., Blanchoin, L., Lennon-Dumenil, A.M., and Thery, M. (2019). Actin filaments regulate microtubule growth at the centrosome. EMBO J *38*, e99630.

86. Yang, R., and Feldman, J.L. (2015). SPD-2/CEP192 and CDK are limiting for microtubule-organizing center function at the centrosome. Curr Biol *25*, 1924-1931.

87. Maia, A.R., Zhu, X., Miller, P., Gu, G., Maiato, H., and Kaverina, I. (2013). Modulation of Golgi-associated microtubule nucleation throughout the cell cycle. Cytoskeleton (Hoboken) *70*, 32-43.

88. Efimov, A., Kharitonov, A., Efimova, N., Loncarek, J., Miller, P.M., Andreyeva, N., Gleeson, P., Galjart, N., Maia, A.R., McLeod, I.X., et al. (2007). Asymmetric CLASP-dependent nucleation of noncentrosomal microtubules at the trans-Golgi network. Dev Cell *12*, 917-930.

89. Wu, J., de Heus, C., Liu, Q., Bouchet, B.P., Noordstra, I., Jiang, K., Hua, S., Martin, M., Yang, C., Grigoriev, I., et al. (2016). Molecular pathway of microtubule organization at the Golgi apparatus. Dev Cell *39*, 44-60.

90. Vertii, A., Ivshina, M., Zimmerman, W., Hehnly, H., Kant, S., and Doxsey, S. (2016). The Centrosome undergoes Plk1-independent interphase maturation during Inflammation and mediates cytokine release. Dev Cell *37*, 377-386.

91. Magescas, J., Zonka, J.C., and Feldman, J.L. (2019). A two-step mechanism for the inactivation of microtubule organizing center function at the centrosome. Elife *8*, e47867.

92. Muroyama, A., Seldin, L., and Lechler, T. (2016). Divergent regulation of functionally distinct γ-tubulin complexes during differentiation. J Cell Biol *213*, 679-692.

93. Yau, K.W., van Beuningen, S.F., Cunha-Ferreira, I., Cloin, B.M., van Battum, E.Y., Will, L., Schatzle, P., Tas, R.P., van Krugten, J., Katrukha, E.A., et al. (2014). Microtubule minus-end binding protein CAMSAP2 controls axon specification and dendrite development. Neuron *82*, 1058-1073.

94. Delaval, B., and Doxsey, S.J. (2010). Pericentrin in cellular function and disease. J Cell Biol *188*, 181-190.

95. Meiring, J.C.M., Shneyer, B.I., and Akhmanova, A. (2020). Generation and regulation of microtubule network asymmetry to drive cell polarity. Curr Opin Cell Biol *62*, 86-95.

96. Lüders, J., Patel, U.K., and Stearns, T. (2006). GCP-WD is a γ-tubulin targeting factor required for centrosomal and chromatin-mediated microtubule nucleation. Nat Cell Biol *8*, 137-147.

97. Cota, R.R., Teixidó-Travesa, N., Ezquerra, A., Eibes, S., Lacasa, C., Roig, J., and Lüders, J. (2017). MZT1 regulates microtubule nucleation by linking γTuRC assembly to adapter-mediated targeting and activation. J Cell Sci *130*, 406-419.

98. Teixidó-Travesa, N., Villen, J., Lacasa, C., Bertran, M.T., Archinti, M., Gygi, S.P., Caelles, C., Roig, J., and Lüders, J. (2010). The γTuRC revisited: a comparative analysis of interphase and mitotic human γTuRC redefines the set of core components and identifies the novel subunit GCP8. Mol Biol Cell *21*, 3963-3972.

99. Choi, Y.K., Liu, P., Sze, S.K., Dai, C., and Qi, R.Z. (2010). CDK5RAP2 stimulates microtubule nucleation by the γ-tubulin ring complex. J Cell Biol *191*, 1089-1095.

100. Wang, Z., Wu, T., Shi, L., Zhang, L., Zheng, W., Qu, J.Y., Niu, R., and Qi, R.Z. (2010). Conserved motif of CDK5RAP2 mediates its localization to centrosomes and the Golgi complex. J Biol Chem *285*, 22658-22665.

101. Takahashi, M., Yamagiwa, A., Nishimura, T., Mukai, H., and Ono, Y. (2002). Centrosomal proteins CG-NAP and kendrin provide microtubule nucleation sites by anchoring γ-tubulin ring complex. Mol Biol Cell *13*, 3235-3245.

102. O'Rourke, B.P., Gomez-Ferreria, M.A., Berk, R.H., Hackl, A.M., Nicholas, M.P., O'Rourke, S.C., Pelletier, L., and Sharp, D.J. (2014). Cep192 controls the balance of centrosome and non-centrosomal microtubules during interphase. PLoS One *9*, e101001.

103. Bouckson-Castaing, V., Moudjou, M., Ferguson, D.J., Mucklow, S., Belkaid, Y., Milon, G., and Crocker, P.R. (1996). Molecular characterisation of ninein, a new coiled-coil protein of the centrosome. J Cell Sci *109 (Pt 1)*, 179-190.

104. Delgehyr, N., Sillibourne, J., and Bornens, M. (2005). Microtubule nucleation and anchoring at the centrosome are independent processes linked by ninein function. J Cell Sci *118*, 1565-1575.

105. Liu, P., Choi, Y.K., and Qi, R.Z. (2014). NME7 is a functional component of the γ-tubulin ring complex. Mol Biol Cell *25*, 2017-2025.

106. Flor-Parra, I., Iglesias-Romero, A.B., and Chang, F. (2018). The XMAP215 ortholog Alp14 promotes microtubule nucleation in fission yeast. Curr Biol *28*, 1681-1691.

107. Gunzelmann, J., Ruthnick, D., Lin, T.C., Zhang, W., Neuner, A., Jakle, U., and Schiebel, E. (2018). The microtubule polymerase Stu2 promotes oligomerization of the γ-TuSC for cytoplasmic microtubule nucleation. Elife *7,* e39932.

108. Thawani, A., Kadzik, R.S., and Petry, S. (2018). XMAP215 is a microtubule nucleation factor that functions synergistically with the γ-tubulin ring complex. Nat Cell Biol *20*, 575-585.

109. Roostalu, J., Cade, N.I., and Surrey, T. (2015). Complementary activities of TPX2 and chTOG constitute an efficient importin-regulated microtubule nucleation module. Nat Cell Biol *17*, 1422-1434.

110. Singh, P., Thomas, G.E., Gireesh, K.K., and Manna, T.K. (2014). TACC3 protein regulates microtubule nucleation by affecting γ-tubulin ring complexes. J Biol Chem *289*, 31719-31735.

111. Gudi, R., Zou, C., Li, J., and Gao, Q. (2011). Centrobin-tubulin interaction is required for centriole elongation and stability. J Cell Biol *193*, 711-725.

112. Jeffery, J.M., Grigoriev, I., Poser, I., van der Horst, A., Hamilton, N., Waterhouse, N., Bleier, J., Subramaniam, V.N., Maly, I.V., Akhmanova, A., et al. (2013). Centrobin regulates centrosome function in interphase cells by limiting pericentriolar matrix recruitment. Cell Cycle *12*, 899-906.

113. Roubin, R., Acquaviva, C., Chevrier, V., Sedjai, F., Zyss, D., Birnbaum, D., and Rosnet, O. (2013). Myomegalin is necessary for the formation of centrosomal and Golgi-derived microtubules. Biol Open *2*, 238-250.

114. Frank, S.R., and Hansen, S.H. (2008). The PIX-GIT complex: a G protein signaling cassette in control of cell shape. Semin Cell Dev Biol *19*, 234-244.

115. Hoefen, R.J., and Berk, B.C. (2006). The multifunctional GIT family of proteins. J Cell Sci *119*, 1469-1475.

116. Zhao, Z.S., Manser, E., Loo, T.H., and Lim, L. (2000). Coupling of PAK-interacting exchange factor PIX to GIT1 promotes focal complex disassembly. Mol Cell Biol *20*, 6354-6363.

117. Premont, R.T., Perry, S.J., Schmalzigaug, R., Roseman, J.T., Xing, Y., and Claing, A. (2004). The GIT/PIX complex: an oligomeric assembly of GIT family ARF GTPase-activating proteins and PIX family Rac1/Cdc42 guanine nucleotide exchange factors. Cell Signal *16*, 1001-1011.

118. Černohorská, M., Sulimenko, V., Hájková, Z., Sulimenko, T., Sládková, V., Vinopal, S., Dráberová, E., and Dráber, P. (2016). GIT1/βPIX signaling proteins and PAK1 kinase regulate microtubule nucleation. Biochim Biophys Acta *1863*, 1282-1297.

119. Sulimenko, V., Hájková, Z., Černohorská, M., Sulimenko, T., Sládková, V., Dráberová, L., Vinopal, S., Dráberová, E., and Dráber, P. (2015). Microtubule nucleation in mouse bone marrow-derived mast cells is regulated by the concerted action of GIT1/βPIX proteins and calcium. J Immunol *194*, 4099-4111.

120. Conduit, P.T., Wainman, A., and Raff, J.W. (2015). Centrosome function and assembly in animal cells. Nat Rev Mol Cell Biol *16*, 611-624.

121. Lee, K., and Rhee, K. (2011). PLK1 phosphorylation of pericentrin initiates centrosome maturation at the onset of mitosis. J Cell Biol *195*, 1093-1101.

122. Lee, J., Jeong, Y., Jeong, S., and Rhee, K. (2010). Centrobin/NIP2 is a microtubule stabilizer whose activity is enhanced by PLK1 phosphorylation during mitosis. J Biol Chem *285*, 25476-25484.

123. Zhang, X., Chen, Q., Feng, J., Hou, J., Yang, F., Liu, J., Jiang, Q., and Zhang, C. (2009). Sequential phosphorylation of Nedd1 by Cdk1 and Plk1 is required for targeting of the γTuRC to the centrosome. J Cell Sci *122*, 2240-2251.

124. Gomez-Ferreria, M.A., Bashkurov, M., Helbig, A.O., Larsen, B., Pawson, T., Gingras, A.C., and Pelletier, L. (2012). Novel NEDD1 phosphorylation sites regulate γ-tubulin binding and mitotic spindle assembly. J Cell Sci *125*, 3745-3751.

125. Meng, L., Park, J.E., Kim, T.S., Lee, E.H., Park, S.Y., Zhou, M., Bang, J.K., and Lee, K.S. (2015). Bimodal interaction of mammalian polo-like kinase 1 and a centrosomal scaffold, Cep192, in the regulation of bipolar spindle formation. Mol Cell Biol *35*, 2626-2640.

126. Jay, J., Hammer, A., Nestor-Kalinoski, A., and Diakonova, M. (2015). JAK2 tyrosine kinase phosphorylates and is negatively regulated by centrosomal protein Ninein. Mol Cell Biol *35*, 111-131.

127. Zhao, Z.S., Lim, J.P., Ng, Y.W., Lim, L., and Manser, E. (2005). The GIT-associated kinase PAK targets to the centrosome and regulates Aurora A. Mol Cell *20*, 237-249.

128. Feng, Q., Baird, D., Peng, X., Wang, J., Ly, T., Guan, J.L., and Cerione, R.A. (2006). Cool-1 functions as an essential regulatory node for EGF receptor- and Src-mediated cell growth. Nat Cell Biol *8*, 945-956.

129. Feng, Q., Baird, D., Yoo, S., Antonyak, M., and Cerione, R.A. (2010). Phosphorylation of the cool-1/β-Pix protein serves as a regulatory signal for the migration and invasive activity of Src-transformed cells. J Biol Chem *285*, 18806-18816.

130. Koh, C.G., Tan, E.J., Manser, E., and Lim, L. (2002). The p21-activated kinase PAK is negatively regulated by POPX1 and POPX2, a pair of serine/threonine phosphatases of the PP2C family. Curr Biol *12*, 317-321.

131. Klebanovych, A., Sládková, V., Sulimenko, T., Vosecká, V., Čapek, M., Dráberova, E., Dráber, P., and Sulimenko, V. (2019). Regulation of microtubule nucleation in mouse bone marrow-derived mast cells by protein pyrosine Phosphatase SHP-1. Cells *8*, e345.

132. Abram, C.L., and Lowell, C.A. (2017). SHP-1 function in myeloid cells. J Leukoc Biol *102*, 657-675.

133. Yang, J., Liu, L., He, D., Song, X., Liang, X., Zhao, Z.J., and Zhou, G.W. (2003). Crystal structure of human protein-tyrosine phosphatase SHP-1. J Biol Chem *278*, 6516-6520.

134. Wang, W., Liu, L., Song, X., Mo, Y., Komma, C., Bellamy, H.D., Zhao, Z.J., and Zhou, G.W. (2011). Crystal structure of human protein tyrosine phosphatase SHP-1 in the open conformation. J Cell Biochem *112*, 2062-2071.

135. Abram, C.L., Roberge, G.L., Pao, L.I., Neel, B.G., and Lowell, C.A. (2013). Distinct roles for neutrophils and dendritic cells in inflammation and autoimmunity in motheaten mice. Immunity *38*, 489-501.

136. Sankaran, S., Starita, L.M., Groen, A.C., Ko, M.J., and Parvin, J.D. (2005). Centrosomal microtubule nucleation activity is inhibited by BRCA1-dependent ubiquitination. Mol Cell Biol *25*, 8656-8668.

137. Klebanovych, A., Vinopal, S., Dráberová, E., Sládková, V., Sulimenko, T., Sulimenko, V., Vosecká, V., Macůrek, V., Legido, A., and Dráber, P. (2020). C53 interacting with UFM1-protein ligase 1 regulates microtubule nucleation in response to ER stress. In bioRxiv 10.1101/2020.12.23.424116.

138. Komatsu, M., Chiba, T., Tatsumi, K., Iemura, S., Tanida, I., Okazaki, N., Ueno, T., Kominami, E., Natsume, T., and Tanaka, K. (2004). A novel protein-conjugating system for UFM1, a ubiquitin-fold modifier. EMBO J *23*, 1977-1986.

139. Gerakis, Y., Quintero, M., Li, H., and Hetz, C. (2019). The UFMylation system in proteostasis and beyond. Trends Cell Biol *29*, 974-986.

140. Wu, J., Lei, G., Mei, M., Tang, Y., and Li, H. (2010). A novel C53/LZAP-interacting protein regulates stability of C53/LZAP and DDRGK domain-containing Protein 1 (DDRGK1) and modulates NF-κB signaling. J Biol Chem *285*, 15126-15136.
141. Tatsumi, K., Sou, Y.S., Tada, N., Nakamura, E., Iemura, S., Natsume, T., Kang, S.H., Chung, C.H., Kasahara, M., Kominami, E., et al. (2010). A novel type of E3 ligase for the UFM1 conjugation system. J Biol Chem *285*, 5417-5427.
142. Cai, Y., Pi, W., Sivaprakasam, S., Zhu, X., Zhang, M., Chen, J., Makala, L., Lu, C., Wu, J., Teng, Y., et al. (2015). UFBP1, a key component of the UFM1 conjugation system, is essential for ufmylation-mediated regulation of erythroid development. PLoS Genet *11*, e1005643.
143. Lemaire, K., Moura, R.F., Granvik, M., Igoillo-Esteve, M., Hohmeier, H.E., Hendrickx, N., Newgard, C.B., Waelkens, E., Cnop, M., and Schuit, F. (2011). Ubiquitin fold modifier 1 (UFM1) and its target UFBP1 protect pancreatic beta cells from ER stress-induced apoptosis. PLoS One *6*, e18517.
144. Zhu, H., Bhatt, B., Sivaprakasam, S., Cai, Y., Liu, S., Kodeboyina, S.K., Patel, N., Savage, N.M., Sharma, A., Kaufman, R.J., et al. (2019). UFBP1 promotes plasma cell development and ER expansion by modulating distinct branches of UPR. Nat Commun *10*, 1084.
145. Yang, R., Wang, H., Kang, B., Chen, B., Shi, Y., Yang, S., Sun, L., Liu, Y., Xiao, W., Zhang, T., et al. (2019). CDK5RAP3, a UFL1 substrate adaptor, is crucial for liver development. Development *146,* dev169235.
146. Jiang, H., Luo, S., and Li, H. (2005). Cdk5 activator-binding protein C53 regulates apoptosis induced by genotoxic stress via modulating the G2/M DNA damage checkpoint. J Biol Chem *280*, 20651-20659.
147. Jiang, H., Wu, J., He, C., Yang, W., and Li, H. (2009). Tumor suppressor protein C53 antagonizes checkpoint kinases to promote cyclin-dependent kinase 1 activation. Cell Res *19*, 458-468.
148. Kwon, J., Cho, H.J., Han, S.H., No, J.G., Kwon, J.Y., and Kim, H. (2010). A novel LZAP-binding protein, NLBP, inhibits cell invasion. J Biol Chem *285*, 12232-12240.
149. Wang, J., An, H., Mayo, M.W., Baldwin, A.S., and Yarbrough, W.G. (2007). LZAP, a putative tumor suppressor, selectively inhibits NF-κB. Cancer Cell *12*, 239-251.
150. Zhang, Y., Zhang, M., Wu, J., Lei, G., and Li, H. (2012). Transcriptional regulation of the UFM1 conjugation system in response to disturbance of the endoplasmic reticulum homeostasis and inhibition of vesicle trafficking. PLoS One *7*, e48587.
151. Andersen, J.S., Wilkinson, C.J., Mayor, T., Mortensen, P., Nigg, E.A., and Mann, M. (2003). Proteomic characterization of the human centrosome by protein correlation profiling. Nature *426*, 570-574.
152. Hubert, T., Vandekerckhove, J., and Gettemans, J. (2011). Actin and Arp2/3 localize at the centrosome of interphase cells. Biochem Biophys Res Commun *404*, 153-158.
153. Plessner, M., Knerr, J., and Grosse, R. (2019). Centrosomal actin assembly is required for proper mitotic spindle formation and chromosome congression. iScience *15*, 274-281.
154. Chesarone, M.A., DuPage, A.G., and Goode, B.L. (2010). Unleashing formins to remodel the actin and microtubule cytoskeletons. Nat Rev Mol Cell Biol *11*, 62-74.
155. Nejedlá, M., Sadi, S., Sulimenko, V., de Almeida, F.N., Blom, H., Dráber, P., Aspenstrom, P., and Karlsson, R. (2016). Profilin connects actin assembly with microtubule dynamics. Mol Biol Cell *27*, 2381-2393.
156. Pimm, M.L., Hotaling, J., and Henty-Ridilla, J.L. (2020). Profilin choreographs actin and microtubules in cells and cancer. Int Rev Cell Mol Biol *355*, 155-204.
157. Nejedlá, M., Klebanovych, A., Sulimenko, V., Sulimenko, T., Dráberova, E., Dráber, P., and Karlsson, R. (2021). The actin regulator profilin 1 is functionally associated with the mammalian centrosome. Life Sci Alliance *4,* e202000655.
158. Galli, S.J., Grimbaldeston, M., and Tsai, M. (2008). Immunomodulatory mast cells: negative, as well as positive, regulators of immunity. Nat Rev Immunol *8*, 478-486.

159.   Gilfillan, A.M., Austin, S.J., and Metcalfe, D.D. (2011). Mast cell biology: introduction and overview. Adv Exp Med Biol *716*, 2-12.

160.   Silver, R., and Curley, J.P. (2013). Mast cells on the mind: new insights and opportunities. Trends Neurosci *36*, 513-521.

161.   Kitamura, Y. (1989). Heterogeneity of mast cells and phenotypic change between subpopulations. Annu Rev Immunol *7*, 59-76.

162.   Miller, H.R., Wright, S.H., Knight, P.A., and Thornton, E.M. (1999). A novel function for transforming growth factor-β1: upregulation of the expression and the IgE-independent extracellular release of a mucosal mast cell granule-specific β-chymase, mouse mast cell protease-1. Blood *93*, 3473-3486.

163.   Theoharides, T.C., Alysandratos, K.D., Angelidou, A., Delivanis, D.A., Sismanopoulos, N., Zhang, B., Asadi, S., Vasiadi, M., Weng, Z., Miniati, A., et al. (2012). Mast cells and inflammation. Biochim Biophys Acta *1822*, 21-33.

164.   Wernersson, S., and Pejler, G. (2014). Mast cell secretory granules: armed for battle. Nat Rev Immunol *14*, 478-494.

165.   Migalovich-Sheikhet, H., Friedman, S., Mankuta, D., and Levi-Schaffer, F. (2012). Novel identified receptors on mast cells. Front Immunol *3*, 238.

166.   Dráber, P., Sulimenko, V., and Dráberova, E. (2012). Cytoskeleton in mast cell signaling. Front Immunol *3*, 130.

167.   Paolini, R., Jouvin, M.H., and Kinet, J.P. (1991). Phosphorylation and dephosphorylation of the high-affinity receptor for immunoglobulin E immediately after receptor engagement and disengagement. Nature *353*, 855-858.

168.   Pribluda, V.S., Pribluda, C., and Metzger, H. (1994). Transphosphorylation as the mechanism by which the high-affinity receptor for IgE is phosphorylated upon aggregation. Proc Natl Acad Sci U S A *91*, 11246-11250.

169.   Dráber, Pe., Halova, I., Polakovicova, I., and Kawakami, T. (2016). Signal transduction and chemotaxis in mast cells. Eur J Pharmacol *778*, 11-23.

170.   Kovarova, M., Tolar, P., Arudchandran, R., Dráberova, L., Rivera, J., and Dráber, P. (2001). Structure-function analysis of Lyn kinase association with lipid rafts and initiation of early signaling events after Fcε receptor I aggregation. Mol Cell Biol *21*, 8318-8328.

171.   Chen, T., Repetto, B., Chizzonite, R., Pullar, C., Burghardt, C., Dharm, E., Zhao, Z., Carroll, R., Nunes, P., Basu, M., et al. (1996). Interaction of phosphorylated FcεRIγ immunoglobulin receptor tyrosine activation motif-based peptides with dual and single SH2 domains of p72syk. Assessment of binding parameters and real time binding kinetics. J Biol Chem *271*, 25308-25315.

172.   Brdicka, T., Imrich, M., Angelisová, P., Brdicková, N., Horváth, O., Spicka, J., Hilgert, I., Lusková, P., Dráber, Pe., Novák, P., et al. (2002). Non-T cell activation linker (NTAL): a transmembrane adaptor protein involved in immunoreceptor signaling. J Exp Med *196*, 1617-1626.

173.   Rivera, J. (2002). Molecular adapters in FcεRI signaling and the allergic response. Curr Opin Immunol *14*, 688-693.

174.   Teramoto, H., Salem, P., Robbins, K.C., Bustelo, X.R., and Gutkind, J.S. (1997). Tyrosine phosphorylation of the vav proto-oncogene product links FcεRI to the Rac1-JNK pathway. J Biol Chem *272*, 10751-10755.

175.   Parravicini, V., Gadina, M., Kovarova, M., Odom, S., Gonzalez-Espinosa, C., Furumoto, Y., Saitoh, S., Samelson, L.E., O'Shea, J.J., and Rivera, J. (2002). Fyn kinase initiates complementary signals required for IgE-dependent mast cell degranulation. Nat Immunol *3*, 741-748.

176.   Thastrup, O., Cullen, P.J., Drobak, B.K., Hanley, M.R., and Dawson, A.P. (1990). Thapsigargin, a tumor promoter, discharges intracellular Ca^{2+} stores by specific inhibition of the endoplasmic reticulum Ca2(+)-ATPase. Proc Natl Acad Sci USA *87*, 2466-2470.

177. Teshima, R., Ikebuchi, H., Nakanishi, M., and Sawada, J. (1994). Stimulatory effect of pervanadate on calcium signals and histamine secretion of RBL-2H3 cells. Biochem J *302 (Pt 3)*, 867-874.

178. Holst, J., Sim, A.T., and Ludowyke, R.I. (2002). Protein phosphatases 1 and 2A transiently associate with myosin during the peak rate of secretion from mast cells. Mol Biol Cell *13*, 1083-1098.

179. Wang, J., and Richards, D.A. (2011). Spatial regulation of exocytic site and vesicle mobilization by the actin cytoskeleton. PLoS One *6*, e29162.

180. Hájková, Z., Bugajev, V., Dráberova, E., Vinopal, S., Dráberova, L., Janáček, J., Dráber, Pe., and Dráber, P. (2011). STIM1-directed reorganization of microtubules in activated mast cells. J Immunol *186*, 913-923.

181. Nishida, K., Yamasaki, S., Ito, Y., Kabu, K., Hattori, K., Tezuka, T., Nishizumi, H., Kitamura, D., Goitsuka, R., Geha, R.S., et al. (2005). FcεRI-mediated mast cell degranulation requires calcium-independent microtubule-dependent translocation of granules to the plasma membrane. J Cell Biol *170*, 115-126.

182. Smith, A.J., Pfeiffer, J.R., Zhang, J., Martinez, A.M., Griffiths, G.M., and Wilson, B.S. (2003). Microtubule-dependent transport of secretory vesicles in RBL-2H3 cells. Traffic *4*, 302-312.

183. Sulimenko, V., Dráberova, E., Sulimenko, T., Macůrek, L., Richterová, V., Dráber, Pe., and Dráber, P. (2006). Regulation of microtubule formation in activated mast cells by complexes of γ-tubulin with Fyn and Syk kinases. J Immunol *176*, 7243-7253.

184. Efergan, A., Azouz, N.P., Klein, O., Noguchi, K., Rothenberg, M.E., Fukuda, M., and Sagi-Eisenberg, R. (2016). Rab12 regulates retrograde transport of mast cell secretory granules by interacting with the RILP-dynein complex. J Immunol *196*, 1091-1101.

185. Ang, W.X., Church, A.M., Kulis, M., Choi, H.W., Burks, A.W., and Abraham, S.N. (2016). Mast cell desensitization inhibits calcium flux and aberrantly remodels actin. J Clin Invest *126*, 4103-4118.

186. Merrifield, C.J., Moss, S.E., Ballestrem, C., Imhof, B.A., Giese, G., Wunderlich, I., and Almers, W. (1999). Endocytic vesicles move at the tips of actin tails in cultured mast cells. Nat Cell Biol *1*, 72-74.

187. Dráberova, L., Dráberova, E., Surviladze, Z., Dráber, P., and Dráber, P. (1999). Protein tyrosine kinase p53/p56(lyn) forms complexes with γ-tubulin in rat basophilic leukemia cells. Int Immunol *11*, 1829-1839.

188. Rubíková, Z., Sulimenko, V., Paulenda, T., and Dráber, P. (2018). Mast cell activation and microtubule organization are modulated by miltefosine through protein kinase C inhibition. Front Immunol *9*, 1563.

189. Mohseny, A.B., Machado, I., Cai, Y., Schaefer, K.L., Serra, M., Hogendoorn, P.C., Llombart-Bosch, A., and Cleton-Jansen, A.M. (2011). Functional characterization of osteosarcoma cell lines provides representative models to study the human disease. Lab Invest *91*, 1195-1205.

190. Gaillard, J., Neumann, E., Van Damme, D., Stoppin-Mellet, V., Ebel, C., Barbier, E., Geelen, D., and Vantard, M. (2008). Two microtubule-associated proteins of *Arabidopsis* MAP65s promote antiparallel microtubule bundling. Mol Biol Cell *19*, 4534-4544.

191. Dryková, D., Cenklová V., Sulimenko, V., Volc, J., Dráber, P., and Binarová, P. (2003). Plant γ-tubulin interacts with αβ-tubulin dimers and forms membrane-associated complexes. Plant Cell *15*, 465-480.

192. Inclan, Y.F., and Nogales, E. (2001). Structural models for the self-assembly and microtubule interactions of γ-, δ- and ε-tubulin. J Cell Sci *114*, 413-422.

193. Detraves, C., Mazarguil, H., Lajoie-Mazenc, I., Julian, M., Raynaud-Messina, B., and Wright, M. (1997). Protein complexes containing γ-tubulin are present in mammalian brain microtubule protein preparations. Cell Motil Cytoskeleton *36*, 179-189.

194. Chiba, Y., Takei, S., Kawamura, N., Kawaguchi, Y., Sasaki, K., Hasegawa-Ishii, S., Furukawa, A., Hosokawa, M., and Shimada, A. (2012). Immunohistochemical localization of aggresomal

proteins in glial cytoplasmic inclusions in multiple system atrophy. Neuropathol Appl Neurobiol *38*, 559-571.

195. Pilhofer, M., and Jensen, G.J. (2013). The bacterial cytoskeleton: more than twisted filaments. Curr Opin Cell Biol *25*, 125-133.

196. Metzger, H. (1992). The receptor with high affinity for IgE. Immunol Rev *125*, 37-48.

197. Eiseman, E., and Bolen, J.B. (1992). Engagement of the high-affinity IgE receptor activates Src protein-related tyrosine kinases. Nature *355*, 78-80.

198. Munoz, I., Danelli, L., Claver, J., Goudin, N., Kurowska, M., Madera-Salcedo, I.K., Huang, J.D., Fischer, A., Gonzalez-Espinosa, C., de Saint Basile, G., et al. (2016). Kinesin-1 controls mast cell degranulation and anaphylaxis through PI3K-dependent recruitment to the granular Slp3/Rab27b complex. J Cell Biol *215*, 203-216.

199. Gilfillan, A.M., and Rivera, J. (2009). The tyrosine kinase network regulating mast cell activation. Immunol Rev *228*, 149-169.

200. Fargier, G., Favard, C., Parmeggiani, A., Sahuquet, A., Merezegue, F., Morel, A., Denis, M., Molinari, N., Mangeat, P.H., Coopman, P.J., et al. (2013). Centrosomal targeting of Syk kinase is controlled by its catalytic activity and depends on microtubules and the dynein motor. FASEB J *27*, 109-122.

201. Zyss, D., Montcourrier, P., Vidal, B., Anguille, C., Merezegue, F., Sahuquet, A., Mangeat, P.H., and Coopman, P.J. (2005). The Syk tyrosine kinase localizes to the centrosomes and negatively affects mitotic progression. Cancer Res *65*, 10872-10880.

202. Hornbeck, P.V., Chabra, I., Kornhauser, J.M., Skrzypek, E., and Zhang, B. (2004). PhosphoSite: a bioinformatics resource dedicated to physiological protein phosphorylation. Proteomics *4*, 1551-1561.

203. Colin, A., Singaravelu, P., Thery, M., Blanchoin, L., and Gueroui, Z. (2018). Actin-network architecture regulates microtubule dynamics. Curr Biol *28*, 2647-2656.

204. Obino, D., Farina, F., Malbec, O., Saez, P.J., Maurin, M., Gaillard, J., Dingli, F., Loew, D., Gautreau, A., Yuseff, M.I., et al. (2016). Actin nucleation at the centrosome controls lymphocyte polarity. Nat Commun *7*, 10969.

205. Gomez, T.S., Kumar, K., Medeiros, R.B., Shimizu, Y., Leibson, P.J., and Billadeau, D.D. (2007). Formins regulate the actin-related protein 2/3 complex-independent polarization of the centrosome to the immunological synapse. Immunity *26*, 177-190.

206. Hubert, T., Perdu, S., Vandekerckhove, J., and Gettemans, J. (2011). γ-Tubulin localizes at actin-based membrane protrusions and inhibits formation of stress-fibers. Biochem Biophys Res Commun *408*, 248-252.

207. Karlsson, R., and Lindberg, U. (2007). Profilin, an essential control element for actin polymerization. In Actin-Monomer-Binding Proteins. (New York, NY: Springer New York), pp. 29-44.

208. Carlier, M.F., and Shekhar, S. (2017). Global treadmilling coordinates actin turnover and controls the size of actin networks. Nat Rev Mol Cell Biol *18*, 389-401.

209. Witke, W. (2004). The role of profilin complexes in cell motility and other cellular processes. Trends Cell Biol *14*, 461-469.

210. Henty-Ridilla, J.L., Juanes, M.A., and Goode, B.L. (2017). Profilin directly promotes microtubule growth through residues mutated in amyotrophic lateral sclerosis. Curr Biol *27*, 3535-3543.

211. Nejedlá, M., Li, Z., Masser, A.E., Biancospino, M., Spiess, M., Mackowiak, S.D., Friedlander, M.R., and Karlsson, R. (2017). A Fluorophore fusion construct of human profilin 1 with non-compromised poly(L-proline) binding capacity suitable for imaging. J Mol Biol *429*, 964-976.

212. Akhmanova, A., and Steinmetz, M.O. (2008). Tracking the ends: a dynamic protein network controls the fate of microtubule tips. Nat Rev Mol Cell Biol *9*, 309-322.

213. Dogterom, M., and Koenderink, G.H. (2019). Actin-microtubule crosstalk in cell biology. Nat Rev Mol Cell Biol *20*, 38-54.

214. Vale, R.D. (2003). The molecular motor toolbox for intracellular transport. Cell *112*, 467-480.

215. Grishchuk, E.L., Molodtsov, M.I., Ataullakhanov, F.I., and McIntosh, J.R. (2005). Force production by disassembling microtubules. Nature *438*, 384-388.

216. Grigoriev, I., Gouveia, S.M., van der Vaart, B., Demmers, J., Smyth, J.T., Honnappa, S., Splinter, D., Steinmetz, M.O., Putney, J.W., Jr., Hoogenraad, C.C., et al. (2008). STIM1 is a MT-plus-end-tracking protein involved in remodeling of the ER. Curr Biol *18*, 177-182.

217. Waterman-Storer, C.M., Gregory, J., Parsons, S.F., and Salmon, E.D. (1995). Membrane/microtubule tip attachment complexes (TACs) allow the assembly dynamics of plus ends to push and pull membranes into tubulovesicular networks in interphase *Xenopus* egg extracts. J Cell Biol *130*, 1161-1169.

218. Schuck, S., Prinz, W.A., Thorn, K.S., Voss, C., and Walter, P. (2009). Membrane expansion alleviates endoplasmic reticulum stress independently of the unfolded protein response. J Cell Biol *187*, 525-536.

219. Ron, D., and Walter, P. (2007). Signal integration in the endoplasmic reticulum unfolded protein response. Nat Rev Mol Cell Biol *8*, 519-529.

220. Terasaki, M., Chen, L.B., and Fujiwara, K. (1986). Microtubules and the endoplasmic reticulum are highly interdependent structures. J Cell Biol *103*, 1557-1568.

221. Ding, W.X., Ni, H.M., Gao, W., Hou, Y.F., Melan, M.A., Chen, X., Stolz, D.B., Shao, Z.M., and Yin, X.M. (2007). Differential effects of endoplasmic reticulum stress-induced autophagy on cell survival. J Biol Chem *282*, 4702-4710.

222. Schindelin, J., Arganda-Carreras, I., Frise, E., Kaynig, V., Longair, M., Pietzsch, T., Preibisch, S., Rueden, C., Saalfeld, S., Schmid, B., et al. (2012). Fiji: an open-source platform for biological-image analysis. Nat Methods *9*, 676-682.

223. Nováková, M., Dráberova, E., Schürmann, W., Czihak, G., Viklický, V., and Dráber, P. (1996). γ-Tubulin redistribution in taxol-treated mitotic cells probed by monoclonal antibodies. Cell Motil Cytoskeleton *33*, 38-51.

224. Deacon, S.W., Beeser, A., Fukui, J.A., Rennefahrt, U.E., Myers, C., Chernoff, J., and Peterson, J.R. (2008). An isoform-selective, small-molecule inhibitor targets the autoregulatory mechanism of p21-activated kinase. Chem Biol *15*, 322-331.

225. Havelka, D., Chafai, D.E., Krivosudský, O., Klebanovych, A., Vostárek, F., Kubínová, L., Dráber, P., and Cifra, M. (2020). Nanosecond pulsed electric field lab-on-chip integrated in super-resolution microscope for cytoskeleton imaging. Advanced Materials Technologies *5*, 1900669.

VII   PRESENTED PUBLICATIONS

VII.1   Sulimenko, V., Hájková, Z., **Klebanovych, A.,** & Dráber, P. (2017) Regulation of microtubule nucleation mediated by γ-tubulin complexes. Protoplasma *254(3)*:1187-1199.

REVIEW ARTICLE

Regulation of microtubule nucleation mediated by γ-tubulin complexes

Vadym Sulimenko[1] & Zuzana Hájková[1] & Anastasiya Klebanovych[1] & Pavel Dráber[1]

Abstract The microtubule cytoskeleton is critically important for spatio-temporal organization of eukaryotic cells. The nucleation of new microtubules is typically restricted to microtubule organizing centers (MTOCs) and requires γ-tubulin that assembles into multisubunit complexes of various sizes. γ-Tubulin ring complexes (TuRCs) are efficient microtubule nucleators and are associated with large number of targeting, activating and modulating proteins. γ-Tubulin-dependent nucleation of microtubules occurs both from canonical MTOCs, such as spindle pole bodies and centrosomes, and additional sites such as Golgi apparatus, nuclear envelope, plasma membrane-associated sites, chromatin and surface of pre-existing microtubules. Despite many advances in structure of γ-tubulin complexes and characterization of γTuRC interacting factors, regulatory mechanisms of microtubule nucleation are not fully understood. Here, we review re- cent work on the factors and regulatory mechanisms that are involved in centrosomal and non-centrosomal micro- tubule nucleation.

Handling Editor: Reimer Stick

* Pavel Dráber
  paveldra@img.cas.cz

[1] Department of Biology of Cytoskeleton, Institute of Molecular Genetics, Academy of Sciences of the Czech Republic, Vídeňská 1083, 142 20 Prague 4, Czech Republic

Abbreviations

AKAP450	A-kinase anchor protein 450
Cdk1	Cyclin-dependent kinase 1
CDK5RAP2	Cyclin-dependent kinase 5 regulatory subunit-associated protein 2
CLASP	Cytoplasmic linker associated protein
CM1	Centrosomin (Cnn) motif 1
EBs	End-binding proteins
γTuRC	γ-Tubulin ring complex
γTuSC	γ-Tubulin small complex
GCPs	γ-Tubulin complex proteins
GIPs	γ-Tubulin complex protein 3-interacting proteins
GM130	Golgin subfamily A member 2 protein
GRIPs	γ-Tubulin ring proteins
Mozart	Mitotic spindle-organizing protein
MTOC	Microtubule-organizing center
NEDD1	Neural precursor cell expressed, developmentally down-regulated protein 1
NME7	Nucleoside-diphosphate kinase 7
PCM	Pericentriolar material
Plk1	Polo-like kinase 1
Ran	Ras-related nuclear protein
SAFs	Spindle assembly factors
SPB	Spindle pole body
+TIPs	Microtubule plus-end tracking proteins
TPX2	Targeting protein for Xklp2

Introduction

Microtubules, 25-nm cylindrical cytoskeletal polymers, play an essential role in many vital cellular activities as maintenance of cell shape and polarity, division, migration and positioning of cellular organelles. They also serve as roads for ordered motor-

driven cargo transport and signal transduction. Microtubules can be organized into microtubule-based organelles with a specialized function, including the radial cytoplasmic network, axonemes, centrioles, midbodies and the mitotic/meiotic spindles. Singlet microtubules are the most ubiquitous forms of the polymer; however, microtubules can also form doublets (in cilia) or triplets (in centrioles and basal bodies) (Verhey and Gaertig 2007). Microtubules are assembled from globular α-tubulin–β-tubulin (αβ-tubulin) heterodimers in a GTP-dependent manner. Both α- and β-tubulins are encoded by multiple phylogenetically conserved genes (Ludueña and Banerjee 2008). Tubulins are arranged in a head-to-tail fashion to form protofilaments. A left-handed helical microtubule wall typically comprises 13 protofilaments. Microtubules are thus inherently polar and contain two structurally distinct ends: a slow-growing minus end, exposing α-tubulin subunits, and a fast-growing plus end, exposing β-tubulin subunits (Nogales and Wang 2006). In cells, microtubules are typically anchored by their minus end in microtubule organizing centers (MTOCs), whereas the plus ends are highly dynamic and switch between phases of growth and shrinkage. Microtubule dynamics helps remodel the microtubular network during the cell cycle. Microtubules can be adapted to highly divergent tasks by mechanisms that are not yet fully understood. Incorporation of alternative tubulin isotypes and post-translational modification of tubulin subunits can regulate microtubule properties. Intracellular microtubule organization is further controlled by the activity of microtubule-regulatory proteins and distribution of nucleation sites (Dráber and Dráberová 2012).

Nucleation, a de novo formation of microtubule polymer from αβ-tubulin dimers, plays the key role in microtubule organization. Microtubule assembly occurs spontaneously in vitro when the concentration of pure αβ-tubulin dimers exceeds a critical concentration. Besides that, the concentration of αβ-tubulin dimers in cells is subcritical and therefore requires a nucleating factor(s) to initiate polymerization. The canonical MTOCs are laminar spindle pole bodies (SPBs) in yeast and centrosomes in higher eukaryotes. Mitotic SPBs are embedded in the nuclearenvelopewith geometrically separated nuclear and cytoplasmic microtubule sites. In mammalian cells, microtubules are nucleated from centrosomes (Fig. 1), composed of two barrel-shaped orthogonally arranged centrioles wrapped in a multicomponent protein matrix called pericentriolar material (PCM). However, microtubule nucleation also takes place in other cellular locations. During interphase, microtubules are nucleated at the Golgi apparatus, the nuclear envelope, the plasma membrane-associated sites and pre-existing microtubules. During cell division, microtubules originate from spindle microtubules and the vicinity of chromatin. These non-centrosomal sites play an important role in the cell architecture (Lin et al. 2015; Petry and Vale 2015). The essential microtubule nucleation components are protein complexes formed by γ-tubulin and γ-tubulin complex proteins (GCPs) or γ-tubulin ring proteins (GRIPs).

This review will focus on the latest research and emerging questions concerning the microtubule nucleation by γ-tubulin complexes and their activating, docking and modulating factors. Specific attention will be given to centrosomal and non-centrosomal nucleation.

γ-Tubulin complexes

Microtubule nucleation is mediated in vivo by γ-tubulin protein complexes, which allow spatio-temporal control of new microtubule growth. γ-Tubulin is a highly conserved but minor member of the tubulin superfamily that is not incorporated into the microtubule polymer (Oakley and Oakley 1989). In contrast to α- and β-tubulins, there are only one to three γ-tubulin genes in eukaryotic genomes (Findeisen et al. 2014). Two human γ-tubulins are nucleation competent (Vinopal et al. 2012). γ-Tubulin is capable to form oligomers (Sulimenko et al. 2002), but it usually forms two distinct well characterized complexes. γ-Tubulin small complex (γTuSC) and the larger γ-tubulin ring complex (γTuRC), named for its characteristic ring-shaped structure. Multiple γTuSCs

Fig. 1 Centrosomal nucleation of microtubules during the cell cycle. Human osteosarcoma U2OS cells in interphase (a), metaphase (b), anaphase (c) and telophase (d) were fixed and stained for microtubules with polyclonal antibody to α-tubulin (*green*) and for centrosomes with monoclonal antibody TU-30 (Nováková et al. 1996) to γ-tubulin (*red*). DNA is stained by DAPI (*blue*). *Bars*, 10 μm
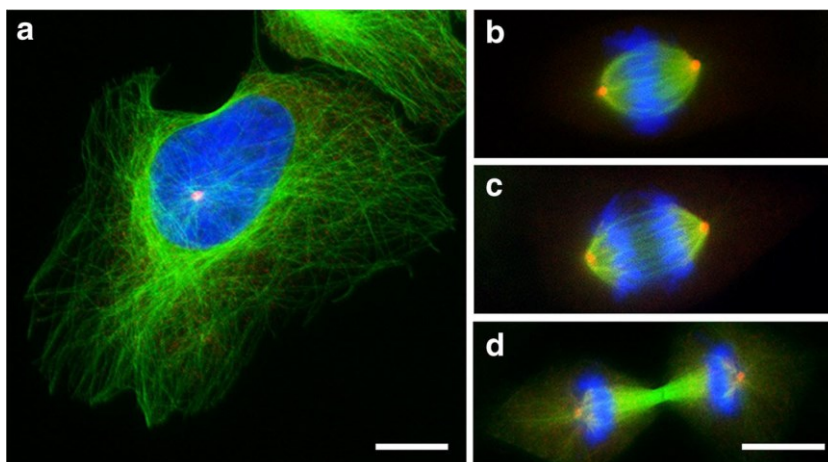
assemble with GCP4, GCP5 and GCP6 into the conical oligomer γTuRC that is recruited to various MTOCs and serves as a template by presenting a γ-tubulin ring that mimics microtubule geometry (Kollman et al. 2011). The GCPs share regions of homology, although with very low levels of sequence identity. Two short homologous regions, N-terminal GRIP1 and C-terminal GRIP2, are unique for the GCPs (Gunawardane et al. 2000). Designations for γ-tubulins and GCPs in various organisms in which they have been studied extensively, such as *Homo sapiens*, *Xenopus laevis*, *Drosophila melanogaster*, *Arabidopsis thaliana*, *Aspergillus nidulans*, *Schizosaccharomyces pombe* and *Sacharomyces cerevisiae*, are shown in Table 1.

In budding yeast *S. cerevisiae*, which lacks the γTuRC-specific GCPs (Table 1), microtubules are nucleated from γTuSC oligomers. The γTuSC, a 300-kDa V-shaped structure, consists of two molecules of γ-tubulin molecules and one molecule each of GCP2 and GCP3. The GCPs 2 and 3 constitute elongated arms of the V shape, interacting laterally via their N-terminal domains. The C-terminal domains are located at the two tips of the V, each binding one molecule of γ-tubulin. The complex is flexible, with a hinge-like motion near the center of the GCP3 arm. The movement about this hinge alters position of γ-tubulin molecules (Kollman et al. 2008). In budding yeast, γTuSCs are driven to form γTuSC ring structure after binding to anchoraging coiled-coil protein Spc110 concentrated at SPB. In such γTuSC ring structure, resembling γTuRC, the γ-tubulin molecules are almost in the correct position to directly contact the base of the

microtubule (Kollman et al. 2010). γTuRC assembly is critically dependent on the oligomerization state of Spc110, with higher-order oligomers dramatically enhancing the stability of assembled γTuRC (Lyon et al. 2016). When a hinge region in GCP3 is moved, the γ-tubulin ring precisely matches microtubule symmetry and the nucleating ability of the γTuSC ring structure is greatly enhanced. Conformation of GCP3 could therefore regulate the ability of the γTuRC to nucleate microtubules (Kollman et al. 2015). Further studies are necessary to elucidate what controls the rotation of GCP3 around its hinge.

In contrast, less is known about the architecture of a large ~2.1 MDa γTuRC. Based on the crystal structure of GCP4 and sequence similarity between GCPs, all members of GCPs were predicted to have the same elongated shape. It was confirmed that GCP4 interacts with γ-tubulin via its C-terminal domain (Guillet et al. 2011). According to the current model, GCP2-GCP6 each bind directly to γ-tubulin, and γTuSC-like structures can be formed. Replacement of one of GCP2/GCP3 with GCP4, GCP5 or GCP6 generates hybrid γTuSC. A novel γTuSC can be composed by two molecules of γ-tubulin and any combination of two molecules from GCP4-GCP6 proteins. Half complexes can be composed of a single molecule of GCP4, GCP5 or GCP6 interacting with γ-tubulin. The precise stoichiometry of GCP4–GCP6 within γTuRC remains unknown. γTuRC could be formed by five γTuSC and one molecule each of GCP4–GCP6 bound to γ-tubulin. The γTuRC then contains 13 γ-tubulin molecules, the arrangement of which matches microtubule symmetry. The flexibility of the GCP3 hinge is essential to close the γTuRC in a

Table 1 Building components of γ-tubulin complexes in different model systems

Homo sapiens	*Xenopus laevis*	*Drosophila melanogaster*	*Arabidopsis thaliana*	*Aspergillus nidulans*	*Schizosaccharomyces pombe*	*Saccharomyces cerevisiae*
TUBG1	*tubg1*	*gammaTub23C*	*TUBG1*	*mipA*	*tug1*	*TUB4*
γ-tubulin 1	γ-tubulin	γ-tubulin 1	γ-tubulin 1	γ-tubulin	γ-tubulin	γ-tubulin
TUBG2		*gammaTub37C*	*TUBG2*			
γ-tubulin 2		γ-tubulin 2	γ-tubulin 2			
TUBGCP2	*tubgcp2*	*Grip84*	*GCP2*	*gcpB*	*alp4*	*SPC97*
GCP2	Xgrip110	Dgrip84	AtGCP2	GCPB	Alp4	Spc97
TUBGCP3	*tubgcp3*	*Grip91*	*GCP3*	*gcpC*	*alp6*	*SPC98*
GCP3	Xgrip109	Dgrip91	AtGCP3	GCPC	Alp6	Spc98
TUBGCP4	*tubgcp4*	*Grip75*	*GCP4*	*gcpD*	*gfh1*	
GCP4	Xgrip75	Dgrip75	AtGCP4	GCPD	Gfh1	
TUBGCP5	*tubgcp5*	*Grip128*	*At1g80260*	*gcpE*	*mod21*	
GCP5	Xgrip113	Dgrip128	AtGCP5	GCPE	Mod21	
TUBGCP6	*tubgcp6*	*Grip163*	*At3g43610*	*gcpF*	*alp16*	
GCP6	Xgrip210	Dgrip163	AtGCP6	GCPF	Alp16	

Gene identifiers (in italics) and protein names are shown for *Homo sapiens*, *Xenopus laevis*, *Drosophila melanogaster*, *Arabidopsis thaliana*, *Aspergillus nidulans*, *Schizosaccharomyces pombe* and *Saccharomyces cerevisiae*. Adapted from Teixidó-Travesa et al. (2012) and Oakley et al. (2015)

conformation compatible with the geometry of the microtubule, increasing its nucleation capacity. In this template-based nucleation model, γTuRC provides platform for the assembly of αβ-tubulin heterodimers (Kollman et al. 2011; Moritz et al. 2000). It was proposed that GCP4, GCP5 and GCP6 position together at the ends of the helix, which would allow them either to initiate or terminate the self-assembly of γTuSCs and/or to stabilize the structure by bridging the two ends (Farache et al. 2016). Although GCP4-6-dependent γTuRC assembly is not essential for spindle formation in *S. pombe*, *A. nidulans* and *D. melanogaster*, it may be important for the targeting of γTuRCs to specific cellular structures. In contrast, in human cells, γTuRCs are required for mitotic spindle formation (Lin et al. 2015). As GCPs are phosphorylated (Teixidó-Travesa et al. 2010), phosphorylation can regulate conformational changes that might be required for γTuRC activation (Kollman et al. 2011). Organization of proteins in γ-tubulin complexes is depicted in Fig. 2.

Nucleation from templates is itself a kinetically unfavourable process that is limited by the formation of a plus end capable of persistent growth. Anti-catastrophe factor targeting protein for Xklp2 (TPX2) and microtubulepolymerase xenopus microtubule-associated protein 215 kDa (XMAP215), that belongs to microtubule plus end tracking proteins (+TIPs), help to transform nascent microtubule with a blunt end into microtubule with an actively growing plus end, which is splayed and outwardly curved. On the other

hand, GTP hydrolysis inhibits microtubule nucleation by destabilizing the nascent plus ends (Wieczorek et al. 2015).

In cells, γ-tubulin complexes are soluble in the cytoplasm. However, their nucleating activity seems to be limited to specific locations in the cell. Various associated proteins are involved in regulation of γ-tubulin complexes. Theseproteins are not essential for assembly of γTuSCs or TuRCs but target them to specific sites or activate their nucleation activity. An important role in microtubule nucleation at specific sites is also played by anchoring proteins that can affect recruitment of complexes as well as modulating proteins that have a less obvious role. Microtubule nucleation can be roughly categorized into three groups, from SPBs, centrosomes and from additional sites.

Nucleation from SPB

The SPB in budding yeast *S. cerevisiae* represents the simplest microtubulenucleation system of any model. Thenuclear side of SPB nucleates microtubules for spindle formation, while the cytoplasmic side nucleates microtubules for proper nucleus and spindle positioning. Two targeting factors, Spc110 and Spc72, recruit γTuSCs to the nuclear and cytoplasmic side of the SPB, respectively (Kilmartin and Goh 1996; Soues and Adams 1998). The Spc110 directly interacts with Spc98/GCP3 and recruits γTuSCs to the nuclear side of SPB (Knop and Schiebel 1997). Spc110 contains two conserved elements, centrosomin [Cnn] motif 1 (CM1) and Spc110-Pcp1 motif (SPM), that are essential for γTuSC oligomerization and microtubule nucleation (Lin et al. 2014). Phosphorylation of Spc110 plays an important role in the regulation of its activity and γTuSC oligomerization. While phosphorylation of Spc110 by S-phase Cdk1-Clb5 kinase and Mps1 kinase promotes γTuSC oligomerization, subsequent phosphorylation by mitotic Cdk1-Clb2 kinase counteracts the activity of S-phase phosphorylation (Lin et al. 2015). Concerningmicrotubule nucleation on the cytoplasmic side of SPB, the targeting factor Spc72 possesses the CM1 element but lacks the SPM, suggesting a different form of interaction with γTuSC. Interestingly, Spc72 acts together with TOG domain Stu2 to anchor microtubules at the cytoplasmic side of SPB (Usui et al. 2003).

Protein Pcp1 is a homolog of Spc110 in fission yeast *S. pombe*. It contains both CM1 and SPM elements and targets γTuRCs and polo-like kinase (Plo1) to the nuclear side of SPBs and supports spindle formation (Fong et al. 2010). Mto1, containing the CM1 element, is the *S. cerevisiae* Spc72 ortholog and enables γTuRC binding on the cytoplasmic side of SPB during mitosis (Samejima et al. 2008). Targeting of γTuRCs to SPB is also supported by Mzt1/Tam4 that directly interacts with Alp6/GCP3 (Dhani et al. 2013). In addition to SPBs, *S. cerevisiae* employsadditional
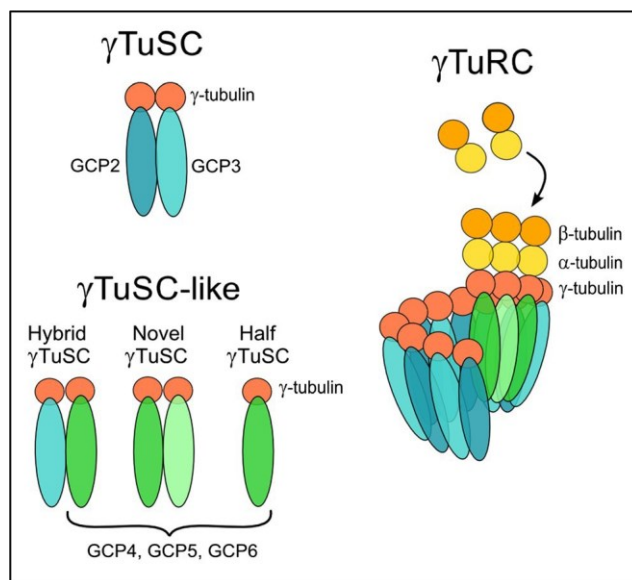

Fig. 2 Composition of γ-tubulin complexes and model of γTuRC assembly. γTuSC are composed of GCP2 and GCP3 and two molecules of γ-tubulin. Different γTuSC-like structures (hybrid γTuSC, novel γTuSC, half γTuSC) can be formed by replacement of GCP2 or GCP3 with GCP4, GCP5 or GCP6. All complexes participate in the formation of the γTuRC ring structure. Nucleation of microtubule polymerization involves longitudinal interactions of αβ-tubulin heterodimers with γ-tubulin in the γTuRC (template nucleation model)

nucleation sites, termed interphase MTOCs (Sawin and Tran 2006), and both Mto1 with Mto2 and Mzt1/Tam4 are required for the non-SPB-derived microtubules. Mto1 and Mto2 cooperate to efficiently interact with γ-tubulin complexes (Samejima et al. 2008). Nucleation of microtubules from both SPB and additional nucleation sites has also been well described in *A. nidulans* (Lin et al. 2015).

Centrosomal nucleation

The relationship between the PCM and the microtubule nucleation capacity is well established and is observed during the cell cycle, whereby the centrosome recruits large amounts of γ-tubulin during mitosis concomitant with an increase in microtubule nucleation (Khodjakov and Rieder 1999). In contrast to the conventional view of the PCM as an amorphous protein network, advances in superresolution microscopy have revealed that it is highly structured with consecutive layers of proteins responsible for microtubule nucleation and γTuRC anchorage (Lawo et al. 2012).

In vertebrates centrosomal proteins neural precursor cell expressed, developmentally down-regulated protein 1 (NEDD1/GCP-WD) (Lüders et al. 2006), Mozart1 (mitotic spindle-organizing protein 1/Mzt1/GCP9), Mozart2 (mitotic spindle-organizing protein 2/Mzt2/GCP8)(Teixidó-Travesa et al. 2010) and CDK5RAP2 (cyclin-dependent kinase 5 regulatory subunit-associated protein 2/Cep215/centrosomin) (Choi et al. 2010) are implicated in γTuRCs targeting. NEDD1 is the attachment factor that lies most proximal to the γTuRC and is important for centrosomal localization of γTuRC in interphase and mitotic cells. Differential phosphorylation of NEDD1 controls the sites to which NEDD1 recruits γTuRCs (Pinyol et al. 2013). Mozart1 seems to be involved in γTuRC recruitment to centrosomes in mitotic cells, while Mozart2 plays this role in interphase cells (Teixidó-Travesa et al. 2010). Additional proteins AKAP450 (A-kinase anchor protein 450/AKAP9/CG-NAP) (Takahashi et al. 2002), pericentrin (PCNT/kendrin) (Zimmerman et al. 2004), ninein (GSK3B-interacting protein) (Delgehyr et al. 2005) and Cep192 (Centrosomal protein 192) (Gomez-Ferreria et al. 2007) are also important for localization of γTuRC to centrosomes. However, as these proteins are incorporated in PCM, they can also indirectly affect γTuRC anchoraging.

The best-characterized activator for γTuRC is CDK5RAP2 that contains activating ~5.5 kDa γ-tubulin complex binding domain (γ-TuNA; γTuRC-mediated nucleation activator 1/ centrosomin motif 1/CM1). CDK5RAP2 contains also a centrosome-targeting domain (centrosomin motif 2/CM2). In vitro CDK5RAP2 activates γTuRC-mediated nucleation by ~7-fold (Choi et al. 2010; Wang et al. 2010). It is currently unclear how γ-TuNA activates γTuRCs. Another nucleation activator is nucleoside-diphosphate kinase 7 (NME7) that

increases the nucleation capacity of γTuRC by ~2.5-fold (Choi et al. 2010; Liu et al. 2014). The association of NME7 with γTuRCs promotes centrosomal nucleation in kinase-dependent manner, but a corresponding target for NME7 was not identified. The molecular basis of γTuRC activation is currently unknown but may involve a conformation switch described for activation of γTuSC.

It is currently unclear whether multiple γTuRC recruitment factors interact with γTuRC simultaneously or whether the various factors function independently of each other. Recently, two functionally distinct γ-TuRC pools were identified in keratinocytes. CDK5RAP2-γTuRCs are potent nucleators, while NEDD1-γTuRCs do not nucleate microtubules but are required for microtubule anchoring (Muroyama et al. 2016). Future studies are necessary to find out if γ-TuRC heterogeneity is more widespread both in terms of γTuRC composition and generation of different microtubule arrays.

Several proteins are implicated in modulation of centrosomal microtubule nucleation, but the precise mechanism of their action remains to be defined. Protein lectin galactoside-binding soluble 3 binding protein (LGALS3BP) plays an essential role in centriolar integrity and biogenesis. In addition, LGALS3BP levels are critical for overall centrosome structure and function, as the increase or decrease of its protein level leads to PCM dispersion with enhanced γ-tubulin recruitment and defective microtubule easter formation, respectively (Fogeron et al. 2013). Nucleolin (C23), a nucleolar phosphoprotein involved in the synthesis and maturation of ribosomes, is associated with centrosomes, and its absence leads to defects in microtubule nucleation. It was suggested that nucleolin might act as an activator of microtubule nucleation when bound to centrosomal γTuRC (Gaume et al. 2015). Interestingly, several centrosomal proteins including γ-tubulin (Hořejší et al. 2012) and GCP2/GCP3 (Dráberová et al. 2015) have been observed in the nucleoli. On the other hand, nucleolar protein HCA66 (U3 small nucleolar RNA-associated protein 6 homolog) has been detected in the centrosome and it was proposed to play a role in stabilizing components of γTuSC (Fant et al. 2009). A molecular communication between the two cellular compartments may be essential to coordinate nucleolar and centrosomal functions (Gaume et al. 2015). In addition, it was reported that protein transforming acidic coiled-coil containing protein 3 (TACC3) is involved in the regulation of the centrosomal microtubule nucleation through the stabilization of the γTuRC assembly from γTuSCs (Singh et al. 2014). Centrobin (centriole duplication and spindle assembly protein), daughter centriole-specific protein participating in duplication and elongation of the centriole, regulates also microtubule nucleation from the centrosome. Centrobin depletion results in the increased recruitment of pericentriolar matrix proteins to the centrosome, including γ-tubulin, AKAP450 and pericentrin. It was proposed that centrobin might regulate

microtubule nucleation and organization by controlling the amount of pericentriolar matrix (Jeffery et al. 2013).

The regulatory role in centrosomal microtubule nucleation can also be played by signalling proteins. It was described recently that protein kinase D3 (PKD3) modulates microtubule nucleation, but a corresponding substrate in PCM is unknown (Zhang et al. 2016). Several other signalling proteins, such as G protein-coupled receptor kinase-interacting protein 1 (GIT1), p21-activated kinase interacting exchange factor (βPIX) and p21 protein [Cdc42/Rac]-activated kinase 1 (PAK1) were identified as regulators of microtubule nucleation. It was reported that GIT1 with PAK1 act as positive regulators, and βPIX is a negative regulator of microtubule nucleation from the interphase centrosomes. The regulatory roles of GIT1, βPIX and PAK1 correlated with recruitment of γ-tubulin to the centrosome (Černohorská et al. 2016; Sulimenko et al. 2015). It was shown that Aurora A phosphorylation of TACC3 is required for γ-tubulin accumulation and centrosome-dependent microtubule assembly in mitosis (Kinoshita et al. 2005) and that sequential phosphorylation of NEDD1 by Cyclin-dependent kinase 1 (Cdk1, Cdc2) and Polo-like kinase 1 (Plk1) is required for targeting of the γTuRC to the centrosome (Zhang et al. 2009).

Non-centrosomal nucleation

The majority of work on microtubule nucleation was performed on SPBs and centrosomes. However, non-centrosomal microtubule nucleation plays also a very important role in creation and maintenance of cellular architecture (Petry and Vale 2015). It can operate next to centrosomal nucleation or function independently. Non-centrosomal MTOCs were first described in higher plants that do not contain centrosome-like microtubule organizer at all (Lüders and Stearns 2007). Since then, many more non-centrosomal MTOCs have been described in different organisms and some of them appear to be functional only in specialized cell types. In differentiated animal cells, like polarized epithelial cells, myotubes or matured neurons, a substantial number of microtubules is not attached to centrosomes but forms parallel arrays with free plus and minus ends (Bartolini and Gundersen 2006). Non-centrosomal microtubules could be formed by nucleation and release from the centrosome, by assembly in the cytoplasm or by nucleation from non-centrosomal MTOC (Lüders and Stearns 2007).

Golgi apparatus

Golgi apparatus works as an MTOC and nucleates a subset of microtubules. Todate, Golgi-derived microtubules have been characterized only in animal cells. Generally, there arethree

steps of microtubule formation: recruitment of γTuRC to the Golgimembrane, template-based nucleation and stabilization of Golgi-derived microtubules (Sanders and Kaverina 2015). It was proposed that Golgi apparatus shares the same anchoring and microtubule-nucleating components with centrosomes (Rivero et al. 2009).

The γTuRCs are recruited to the Golgi membrane by proteins possessing γTuRC-scaffolding capacity (Sanders and Kaverina 2015). Current model proposes that cis-Golgi protein GM130 (Golgin subfamily A member 2 protein) recruits AKAP450 (Rivero et al. 2009), which in turn binds CDK5RAP2 (Wang et al. 2010) or myomegalin (MMG/phosphodiesterase 4D interacting protein/PDE4DIP) isoform CM-MMG (centrosomin motif-myomegalin), that associates also with centrosome (Roubin et al. 2013). CDK5RAP2 can also bind to pericentrin to attach γTuRCs to Golgi apparatus (Wang et al. 2010). Both myomegalin and CDK5RAP2promote microtubule nucleation at the cis-Golgi using GM130-AKAP450-CDK5RAP2/myomegalin-γTuRC axis, and they might play a redundant or complementary role in the microtubule nucleation (Roubin et al. 2013). Securin (pituitary tumour-transforming gene 1 (PTTG1)) was also reported to form a complex with GM130, AKAP450 and γ-tubulin at the cis face of the Golgi and its depletion results in a delay in microtubule nucleation (Moreno-Mateos et al. 2011). Moreover, it was shown that dynein/dynactin complexes retain microtubule seeds at the Golgi apparatus and function as other scaffolding proteins (Rivero et al. 2009).

Microtubule nucleation from Golgi membrane needs some additional factors to make the template nucleation kinetically favourable (Sanders and Kaverina 2015). Among them belong +TIP proteins cytoplasmic linker associated proteins (CLASPs; CLASP1 and CLASP2) that are recruited to and associate specifically with the trans-Golgi scaffold protein GCC185 (GRIP and coiled-coil domain-containing protein 2) at the Golgi periphery. It was suggested that newly nucleated Golgi-derived short microtubules are coated and stabilized with CLASPs, which were relocalized from the Golgi membrane (Efimov et al. 2007). However, CLASPs are also known to directly modify polymerizing microtubules (Grimaldi et al. 2014) and could therefore modulate the initial polymerization steps of Golgi-derived microtubules rather than simply stabilize already assembled polymers (Sanders and Kaverina 2015). Moreover, +TIP protein EB1 can associate with myomegalin isoform EB1-myomegalin (EB-MMG) and this affects EB1 loading on microtubules and microtubule growth (Roubin et al. 2013). Because of low γTuRC abundance at the Golgi, nucleation of microtubules from these γTuRCs templates requires high local concentration of functional tubulin dimers. This could be achieved by tubulin chaperone tubulin-specific chaperone E (TBCE) concentrating at the Golgi membrane in an ADP ribosylation factor 1 (Arf1) manner (Bellouze et al. 2014) and reviving tubulin in the vicinity of nucleation sites.

Nuclear envelope

Nuclear membrane serves as a microtubule nucleation site in several cell types among which skeletal muscle belongs to the well-characterized ones. During skeletal muscle differentiation, undifferentiated myoblasts fuse into multinucleated myotubes. It was reported that nuclei of undifferentiated cells have a dormant potential to bind centrosome proteins which becomes activated during the myoblast differentiation(Fant et al. 2009). Moreover, early after the fusion, the microtubule network is completely reorganized from radial array into parallel fibres which also involves redistribution of proteins of pericentriolar material from centrosome to the nuclear membrane (Dyachuk et al. 2016). During myogenesis in *D. melanogaster*, Rac GTPase activating protein 50C (RacGap50C) is necessary for binding γ-tubulin to various foci associated with the nuclear periphery. It was found that proper localization of RacGAP50C in nuclear periphery depends on Pavarotti kinesin-like protein (Pav) (Guerin and Kramer 2009). In mouse, muscle cells γ-tubulin as well as pericentrin and ninein are associated with nuclear membrane and γ-tubulin-dependent nucleation takes place along the nuclear membrane of myotubes (Bugnard et al. 2005).

Nuclear surface of higher plant cells also functions as a microtubule-nucleating site and proteins involved in this process are localized at the nuclear periphery. Besides the γ-tubulin (Binarová et al. 2000) and GCP3 (Erhardt et al. 2002), the whole γTuSCs were identified in the nuclear periphery of plant cells (Seltzer et al. 2007). Moreover, proteins GCP3-interacting protein 1 (GIP1) and GCP3-interacting protein2 (GIP2), which are homologous to vertebrate Mozart1, localize at the nuclear periphery with γ-tubulin, GCP3 and/or GCP4 and stabilize γ-tubulin complexes (Janski et al. 2012). GIPs may have a dual function, both as components of microtubule nucleation complexes and as adaptors or modulators of nuclear envelope associated proteins (Batzenschlager et al. 2013). It was shown that the activity and positioning of the plant nuclear MTOC can influence cortical microtubule orientation and polarity along the long axis of the cell (Ambrose and Wasteneys 2014).

Chromatin and kinetochores

Chromatin-mediated microtubule nucleation occurs after the breakdown of nuclear envelope. The key player in the molecular mechanism is the small GTPase Ran (Ras-related nuclear protein). Theassociation of Ran-guaninenucleotideexchange factor (GEF) regulator of chromosome condensation 1 (RCC1) with chromosomes produces a gradient of RanGTP which promotes dissociation of spindle assembly factors (SAFs) from importins. The released SAFs promote microtubule nucleation, stabilization and organization around the chromosomes(Meunier and Vernos2016). SAFs also localize to microtubules, and this interaction leads to feedback based on spatial localization (Oh et al. 2016b). The most studied SAF is a nuclear protein TPX2. Interaction of TPX2 with Aurora A leads to Aurora A activation by its autophosphorylation in a RanGTP-dependent manner (Tsai and Zheng 2005). TPX2 also form complexes with γTuRC and microtubule-associated protein receptor for hyaluronan-mediated motility (RHAMM) (Groen et al. 2004). The TPX2-Aurora A complex associates with specific complex containing RHAMM-NEDD1-γTuRC (Scrofani et al. 2015). In this macro-complex, the activated Aurora A phosphorylates NEDD1 that is an essential prerequisite for microtubule nucleation in the proximity of chromosomes (Pinyol et al. 2013). The association of γ-tubulin with the mitotic spindle requires another specific NEDD1 phosphorylation (Lüders et al. 2006). The precise roles of NEDD1 phosphorylations are not known. Besides the regulation of the chromatin-mediated microtubule nucleation and γTuRCs scaffolding, TPX2 also promotes microtubule nucleation by stabilizing early nucleation intermediates. For faster and more efficient microtubule nucleation, TPX2 cooperates with microtubule polymerase XMAP215 (chTOG), which has only weak nucleation activity on its own (Roostalu et al. 2015). Moreover, other proteins are involved in RanGTP-dependent, chromatin-mediated nucleation. Hepatoma upregulated protein (HURP) was found to drive RanGTP-dependent, chromatin-induced microtubule assembly in a TPX2-independent manner and may be also involved in other steps of RanGTP-mediated microtubule nucleation (Casanova et al. 2008). Maternal effect lethal-28 protein (MEL-28) promotes RanGTP-dependent recruitment of γTuRC and microtubule nucleation (Yokoyama et al. 2014). In general, the RanGTP pathway was described in animal and plant cells and seems to be highly conserved. Nevertheless, its key player TPX2 is not highly conserved in organisms such as *D. melanogaster* and *Caenorhabditis elegans.* Although related proteins were described in both systems, they are fairly distant in terms of sequence and function (Meunier and Vernos 2016).

RanGTP gradient on mitotic chromatin favours microtubule nucleation in the vicinity of the chromosome rather than from γTuRCs localized at kinetochores as suggested previously (Mishra et al. 2010). However, kinetochores provide an environment for microtubule stabilization. The major role in microtubule stabilization is played by the kinetochore-associatedchromosomalpassengercomplex(CPC) that localizes to centromeres (Meunier and Vernos 2016). Observation of γTuRC components at the kinetochores in microtubule regrowth experiments in plants (Binarová et al. 1998) may result from the presence of short microtubules connected to the kinetochores by their plus ends. It was suggested that after chromosomal RanGTP-dependent microtubule nucleation, microtubules are stabilized in the kinetochore area and amplified throughmicrotubule nucleation by the augmin-dependent pathway (Meunier and Vernos 2016).

Surface of other microtubules

One of the possible mechanisms of non-centrosomal nucleation is the formation of new microtubules from the lateral surface of pre-existing Bmother^ microtubules. This γ-tubulin-dependent branching was initially observed in higher plantinterphasecells (Murata et al. 2005). Theessentialrole in this process is played by a hetero-octameric protein complex termed augmin. Augmin functions by recruiting NEDD1 and its associated γTuRC to preexisting microtubules (Goshima et al. 2008). Augmin-dependent nucleation of microtubules is phylogenetically conserved as it was described in plants (Hotta et al. 2012), *D. melanogaster* (Goshima et al. 2008), *X. laevis* (Petry et al. 2013) and human cells (Uehara et al. 2009). It is usually connected with formation of branching microtubules in bipolar metaphase spindle, but it also promotes central spindle assembly in anaphase and cytokinesis (Uehara et al. 2016). The augmin-γTuRC module organizes

microtubules in post-mitotic neurons and controls axonal microtubule polarity (Sánchez-Huertas et al. 2016). In plants, augmin complex plays an important role not only in the formation of the acentrosomal spindle and microtubule-rich phragmoplast (Hotta et al. 2012) but also in triggering microtubule nucleation at the plant cortex (Liu et al. 2014). In *A. thaliana*, mutation of the augmin six subunit disturbs both mitotic and meiotic divisions due to malformation of the microtubular network (Oh et al. 2016a). Within the cortical array, microtubules are nucleated either along the mother microtubules as branches at angles ranging from 20° (= 20° angle) to 60° (~40° on average) or in parallel mode (0° angle). Microtubule-dependent microtubule nucleation thus provides an effective mean of quick amplification of microtubules with the same polarity (Sánchez-Huertas and Lüders 2015). An augmin-like protein complex was identified in *A. nidulans*. Although its subunits have significant homology to animal and plant proteins, it seems that the *A. nidulans* augmin

Table 2   Proteinsregulatingmicrotubulenucleation fromcentrosomal and non-centrosomal sites in animals

Location	Protein	Role	Reference
Centrosome	NEDD1[1], Mozart1[2], Mozart2[2], CDK5RAP2[3]	γTuRC targeting	[1] Lüders et al. 2006; [2] Teixidó-Travesa et al. 2010; [3] Choi et al. 2010; [4] Liu et al. 2014;
	CDK5RAP2[3], NME7[4]	γTuRC activation	[3] Choi et al. 2010; [4] Liu et al. 2014;
	AKAP450[5], Pericentrin[6], Ninein[7], Cep192[8]	Anchoring	[5] Takahashi et al. 2002; [6] Zimmerman et al. 2004;[7] Delgehyr et al. 2005; [8] Gomez-Ferreria et al. 2007;
	PDK3[9], Nucleolin[10], TACC3[11], Centrobin[12], LGALS3BP[13], GIT1[14,15], βPIX[14,15], PAK1[15], Aurora A[16], PLK1[17], myomegalin CM-MMG[18]	Modulating	[9] Zhang et al. 2016; [10] Gaume et al. 2015; [11] Singh et al. 2014; [12] Jeffery et al. 2013; [13] Fogeron et al. 2013; [14] Sulimenko et al. 2015; [15] Černohorská et al. 2016; [16] Kinoshita et al. 2005; [17] Zhang et al. 2009; [18] Roubin et al. 2013;
Golgi apparatus	myomegalin CM-MMG[18], CDK5RAP2[19]	γ-TuRC targeting	[18] Roubin et al. 2013; [19] Wang et al. 2010;
	Pericentrin[19], GM130[20], AKAP450[19], GCC185[21]	Anchoring	[19] Wang et al. 2010; [20] Chabin-Brion et al. 2001; [21] Efimov et al. 2007;
	Myomegalin EB-MMG[18], dynein/dynactin[22], CLASP1−2[23,24], Securin[25], TBCE[26], Arf[26]	Modulating	[18] Roubin et al. 2013; [22] Rivero et al. 2009; [23] Efimov et al. 2007; [24] Grimaldi et al. 2014; [25] Moreno-Mateos et al. 2011; [26] Bellouze et al. 2014;
Nuclear envelope	RacGAP50C[27], GIP1−2[28,29]	γ-TuRC targeting	[27] Guerin and Kramer 2009; [28] Janski et al. 2012; [29] Batzenschlager et al. 2013;
	Pav[27], pericentrin[30], ninein[30]	Anchoring	[27] Guerin and Kramer 2009; [30] Bugnard et al. 2005;
Chromatin	NEDD1[31]	γ-TuRC targeting	[31] Pinyol et al. 2013;
	TPX2[32], RHAMM[33]	Anchoring	[32] Tsai and Zheng 2005; [33] Groen et al. 2004;
	TPX2[32], Aurora A[32], RCC1[33], Ran GTPase[34], HURP[35], XMAP215[36], MEL-28[37]	Modulating	[32] Tsai and Zheng 2005; [33] Carazo-Salas et al. 1999; [34] Kalab et al. 2006; [35] Casanova et al. 2008; [36] Roostalu et al. 2015; [37] Yokoyama et al. 2014;
Pre-existing microtubules	NEDD1[38]	γ-TuRC targeting	[38] Johmura et al. 2011;
	Augmin complex[39]	Anchoring	[39] Goshima et al. 2008;
	Plk1[38], Cdk1[38]	Modulating	[38] Johmura et al. 2011;
Plasma membrane	Ninein[40], keratin[41], NOCA-1[42]	Anchoring	[40] Mogensen et al. 2000; [41] Oriolo et al. 2007; [42] Wang et al. 2015;
	Fyn[43], PI3K[43,44]	Modulating	[43] Macurek et al. 2008; [44] Inukai et al.2000.

complex is dispensable for spindle formation in fungi. Interestingly, Aug6-like genes were identified in several other fungal species but not in yeast (Edzuka et al.2014).

Reconstitution of human augmin revealed that it is a Y-shaped complex that can adopt multiple conformations. Augmin subunit HAUS8 (Hice1) is responsible for binding of the complex to microtubules, but the whole complex binds to microtubules with more than 10-fold higher affinity than Hice1 alone (Hsia et al. 2014). The binding of augmin to microtubules is promoted by phosphorylation of the Hice1 by Plk1. This phosphorylation depends on Plk1-NEDD1 interaction that is induced by Cdk1 phosphorylation of NEDD1 (Johmura et al. 2011). In plant cells, microtubule branching is regulated by protein phosphatase 2A (PP2A). The PP2A signalling pathway plays an important role in the organization of interphase microtubule arrays through regulatingnucleation geometry (Kirik et al. 2012).

Plasma membrane-associated sites

In differentiated cells of many tissues, PCM proteins lose their association with the centrosome and can redistribute to cellular cortex. Plasma membrane-associated sites can thus functionally replace the centrosomal MTOCs (Dyachuk et al. 2016). In polarized epithelial cells, microtubules are anchored in aregion underlying the apical plasma membrane where ninein is concentrated. It was proposed that initial microtubule nucleation at the centrosome is followed by release, translocation and anchorage of microtubule minus ends to the apical membrane by ninein (Mogensen et al. 2000). The maintenance of such microtubule network may be further supported by minus end-targeting proteins (–TIPs), such ascalmodulin-regulated spectrin-associated proteins 1–3 (CAMSAPs 1–3) in mammals or patronin in invertebrates (Akhmanova and Steinmetz 2015). It was reported that a ninein-related protein in the nematode *C. elegans*, non-centrosomal array protein 1 (NOCA-1) regulates together with γ-tubulin the assembly of non-centrosomal microtubules. Moreover, in epidermal cells, NOCA-1 has functional redundancy with patronin. This indicates that the functional roles of ninein and patronin families overlap (Wang et al. 2015). It has also been shown that keratin binds directly to GCP6 and mediates γTuRC localization to the apical domain of epithelial cells. Interaction with GCP6 was disrupted by Cdk1 phosphorylation of GCP6 phosphorylation (Oriolo et al. 2007).

Interestingly, in animal cells, protein tyrosinekinases of Src family, which are associated with cell surface receptors, form complexes with γ-tubulin and phosphorylates γ-tubulin associated proteins(Dráberová et al. 1999; Sulimenko et al. 2006). A direct interaction of γ-tubulin with regulatory subunit of

Fig. 3 Models of non-centrosomal microtubule nucleation. Schematic representation of microtubule nucleation from Golgi apparatus (a), nuclear envelope (b) chromatin (c) and surface of pre-existing microtubule (d). Regulatory proteins are distinguished according to their role in the nucleation: γTuRC targeting (*yellow*), anchoring (*red*) and modulating proteins (*green*). γTuRCs with nucleated microtubules are in *blue*. Not all regulatory proteins are depicted. Proteins are not in scale
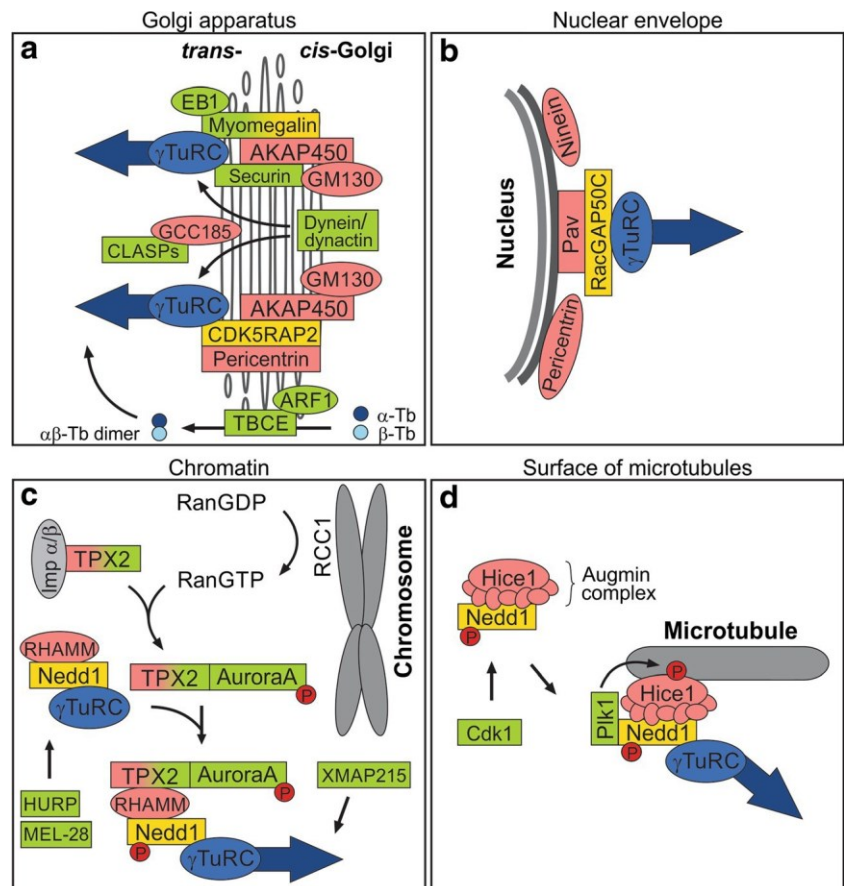
phosphoinositide 3-kinase (PI3K) was also reported (Inukai et al. 2000). It was shown that microtubules are nucleated from detergent-resistant membranes containing γ-tubulin, and nucleation from membranes is dependent on the activity of tyrosine kinase Fyn (p59-FYN) and PI3K (Macurek et al. 2008). Fyn phosphorylates its substrate PI3K, which might then regulate γ-tubulin through direct interaction. The precise mechanism of kinase actions remains to bedefined.

In higher plants, the nucleation activity of membrane-bound large γ-tubulin complexes has been shown in vitro (Dryková et al. 2003). Moreover, γ-tubulin, GCP2 and GCP3 were found at the plasma membrane in plants (Erhardt et al. 2002; Seltzer et al. 2007). γ-TuSC proteins arealso enriched in post-cytokinetic, newly formed crosswalls of *A. thaliana,* where they nucleate microtubules (Ambrose and Wasteneys 2011). An important role in the formation of nucleation of microtubules at the plant cell cortex is played by augmin (see above) (Liu et al. 2014).

Proteins involved in the regulation of microtubule nucleation in animal cells are summarized in Table 2. Models of non-centrosomalnucleationfromtheGolgiapparatus,nuclear envelope, chromatin and surface of microtubules aredepicted in Fig. 3.

Conclusions and future directions

Two decades of research on γ-tubulin complexes led to the conclusion that they are almost universally involved in microtubule nucleation. γ-Tubulin complexes have been shown to form microtubule templates that nucleate microtubules through longitudinal contacts with αβ-tubulin dimers. However, different mechanisms ensuring proper spatio-temporal regulation of microtubule nucleation are applied at specific locations in the cell. It seems that the γTuRC attachment to both centrosomal and non-centrosomal sites is correlated with an increase in its nucleating activity.

The recent structural studies on γTuSC have been highly illustrative, but a high-resolution structure of the γTuRC both before and after nucleation will be neces- sary to understand how GCP4, GCP5 and GCP6 are located in the complex and what are the specific interac- tions they make with each other and with the γTuSC. The transition from an open to a closed state of γTuSC provides an allosteric mechanism for modulating γTuSC activity. It remains to be determined what factors are involved in promoting this transition. Elucidation of pre- cise mechanism of γTuRC activation also remains a pressing question in understanding γTuRC regulation. Many proteins interacting with γTuRCs, highlighted in this review, have been implicated in activation, targeting and modulation of γTuRCs. However, little is known

about the upstream signalling pathways ensuring that these proteins initiate microtubule nucleation at the cor- rect location and time. The importance of kinases and phosphatases in regulation of nucleation is emerging, but the details are only partially understood. Future stud- ies are also necessary to find out if distinct γTuRCs may be independently used by different tissues to generate cell type-specific non-centrosomal microtubule arrays. Further studies are needed to assess microtubule branch angles during cell cycle stages and in different cell types. Finally, a thorough understanding of microtubule nucle-ation should clarify the relevance of γTuRC dysregula- tion in cancer cells and neurodevelopmental diseases.

Together, these studies will help us comprehend how mi-crotubulenucleation is initiated and regulated in vivo to create microtubule arrays essential to various cell activities.

Compliance with ethical standards

Conflict of interest The authors declare that they have no conflict of interest.

References

Akhmanova A, Steinmetz MO (2015) Control of microtubule organiza-tion and dynamics: two ends in the limelight. Nat Rev Mol Cell Biol 16:711–726

Ambrose C, Wasteneys GO (2011) Cell edges accumulate gamma tubulin complex components and nucleate microtubules following cytoki-nesis in *Arabidopsis thaliana*. PLoS One 6:e27423

Ambrose C, Wasteneys GO (2014) Microtubule initiation from the nu-clear surface controls cortical microtubule growth polarity and ori-entation in *Arabidopsis thaliana*. Plant Cell Physiol 55:1636–1645

Bartolini F, Gundersen GG (2006) Generation of noncentrosomalmicro-tubule arrays. J Cell Sci 119:4155–4163

Batzenschlager M, Masoud K, Janski N, Houlné G, Herzog E, Evrard JL, Baumberger N, Erhardt M, Nominé Y, Kieffer B, Schmit AC, Chabouté ME (2013) The GIP γ-tubulin complex-associated pro-teins are involved in nuclear architecture in *Arabidopsis thaliana*. Front Plant Sci 4:480

Bellouze S, Schäfer MK, Buttigieg D, Baillat G, Rabouille C, Haase G (2014) Golgifragmentation in pmn mice is due to a defective ARF1/TBCE cross-talk that coordinates COPI vesicleformation and tubu-lin polymerization. Hum Mol Genet 23:5961–5975

Binarová P, Doležel J, Dráber P, Heberle-Bors E, Strnad M, Bögre L (1998) Treatment of *Vicia faba* root tip cells with specific inhibitors to cyclin-dependent kinases leads to abnormal spindle formation. Plant J 16:697–707

Binarová P, Cenklová V, Hause B, Kubátová E, Lysák M, Doležel J, Bögre L, Dráber P (2000) Nuclear γ-tubulin duringacentriolarplant mitosis. Plant Cell 12:433–442

Bugnard E, Zaal KJ, Ralston E (2005) Reorganization of microtubule nucleation during muscle differentiation. Cell Motil Cytoskeleton 60:1–13

Carazo-SalasRE,GuarguagliniG, GrussOJ,Segref A, Karsenti E,Mattaj IW (1999) Generation of GTP-bound ran by RCC1 is required for chromatin-induced mitotic spindleformation. Nature 400:178–181

Casanova CM, Rybina S, Yokoyama H, Karsenti E, Mattaj IW (2008) Hepatoma up-regulated protein is required for chromatin-induced microtubule assembly independently of TPX2. Mol Biol Cell 19: 4900–4908

Černohorská M, Sulimenko V, Hájková Z, Sulimenko T, Sládková V, Vinopal S, Dráberová E, Dráber P (2016) GIT1/βPIX signaling proteins and PAK1 kinase regulate microtubule nucleation. BBA Mol Cell Res 1863:1282–1297

Chabin-Brion K, Marceiller J, Perez F, Settegrana C, Drechou A, Durand G, Poüs C (2001) The Golgi complex is a microtubule-organizing organelle. Mol Biol Cell 12:2047–2060

Choi YK, Liu P, Sze SK, Dai C, Qi RZ (2010) CDK5RAP2 stimulates microtubule nucleation by the γ-tubulin ring complex. J Cell Biol 191:1089–1095

Delgehyr N, Sillibourne J, Bornens M (2005) Microtubulenucleation and anchoring at the centrosome are independent processes linked by ninein function. J Cell Sci 118:1565–1575

Dhani DK, Goult BT, George GM, Rogerson DT, Bitton DA, Miller CJ, Schwabe JW, Tanaka K (2013) Mzt1/Tam4, a fission yeast MOZART1 homologue, is an essential component of the γ-tubulin complexand directly interacts with GCP3(Alp6). Mol Biol Cell 24: 3337–3349

Dráber P, Dráberová E (2012) Microtubules. In: Kavallaris M (ed) Cytoskeleton and human disease. Humana Press, New York, pp 29–55

Dráberová L, Dráberová E, Surviladze Z, Dráber P, Dráber P (1999) Protein tyrosine kinase p53/p56(lyn) forms complexes with γ- tubulin in rat basophilic leukemia cells. Int Immunol 11:1829–1839

Dráberová E, D'Agostino L, Caracciolo V, Sládková V, Sulimenko T, Sulimenko V, Sobol M, Maounis NF, Tzelepis E, Mahera E, Křen L, Legido A, Giordano A, Mörk S, Hozák P, Dráber P, Katsetos CD (2015) Overexpression and nucleolar localization of γ-tubulin small complex proteins GCP2 and GCP3 in glioblastoma. J Neuropathol Exp Neurol 74:723–742

Dryková D, Cenklová V, Sulimenko V, Volc J, Dráber P, Binarová P (2003) Plant gamma-tubulin interacts with alphabeta-tubulin dimers and forms membrane-associated complexes. Plant Cell 15:465–480

Dyachuk V,Bierkamp C, Merdes A(2016)Non-centrosomalmicrotubule organization in differentiated cells. In: Lüders J (ed) Themicrotubule cytoskeleton. Springer-Verlag, Wien, pp 27–42

Edzuka T, Yamada L, Kanamaru K, Sawada H, Goshima G (2014) Identification of the augmin complex in the filamentous fungus *Aspergillus nidulans*. PLoS One 9:e101471

Efimov A, Kharitonov A, Efimova N, Loncarek J, Miller PM, Andreyeva N, Gleeson P, Galjart N, Maia AR, McLeod IX, Yates JR 3rd, Maiato H, Khodjakov A, Akhmanova A, Kaverina I (2007) Asymmetric CLASP-dependent nucleation of noncentrosomal microtubules at the trans-Golgi network. Dev Cell 12:917–930

Erhardt M, Stoppin-Mellet V,Campagne S, Canaday J, Mutterer J, Fabian T,Sauter M, Muller T,Peter C, Lambert AM, Schmit AC (2002) The plant Spc98p homologue colocalizes with γ-tubulin at microtubule nucleationsites and is required for microtubulenucleation. J Cell Sci 115:2423–2431

Fant X, Gnadt N, Haren L, Merdes A (2009) Stability of the small γ-tubulin complex requires HCA66, a protein of the centrosome and the nucleolus. J Cell Sci 122:1134–1144

Farache D, Jauneau A, Chemin C, Chartrain M, Rémy MH, Merdes A, Haren L (2016) Functional analysis of γ-tubulin complex proteins indicatesspecific lateral associationvia their N-terminal domains. J Biol Chem 291:23112–23125

Findeisen P, Mühlhausen S, Dempewolf S, Hertzog J, Zietlow A, Carlomagno T, Kollmar M (2014) Six subgroups and extensive recent duplications characterize the evolution of the eukaryotic tubulin protein family. Genome Biol Evol 6:2274–2288

Fogeron ML, Müller H, Schade S, Dreher F, Lehmann V, Kühnel A, Scholz AK, Kashofer K, Zerck A, Fauler B, Lurz R, Herwig R, Zatloukal K, Lehrach H, Gobom J, Nordhoff E, Lange BM (2013) LGALS3BP regulates centriole biogenesis and centrosome hypertrophy in cancer cells. Nat Commun 4:1531

Fong CS, Sato M, Toda T (2010) Fission yeast Pcp1 links polo kinase-mediated mitotic entry to γ-tubulin-dependent spindle formation. EMBO J 29:120–130

Gaume X, Tassin AM, Ugrinova I, Mongelard F, Monier K, Bouvet P (2015) Centrosomal nucleolin is required for microtubule network organization. Cell Cycle 14:902–919

Gomez-Ferreria MA, Rath U, Buster DW, Chanda SK, Caldwell JS, Rines DR, Sharp DJ (2007) Human Cep192 is required for mitotic centrosome and spindle assembly. Curr Biol 17:1960–1966

Goshima G, Mayer M, Zhang N, Stuurman N, Vale RD (2008) Augmin: a protein complex required for centrosome-independent microtubule generation within the spindle. J Cell Biol 181:421–429

Grimaldi AD, Maki T, Fitton BP, Roth D, Yampolsky D, Davidson MW, Svitkina T, Straube A, Hayashi I, Kaverina I (2014) CLASPs are required for proper microtubule localization of end-binding proteins. Dev Cell 30:343–352

Groen AC, Cameron LA, Coughlin M, Miyamoto DT, Mitchison TJ, Ohi R(2004) XRHAMMfunctions in ran-dependentmicrotubulenucleationand pole formation during anastral spindle assembly. Curr Biol 14:1801–1811

Guerin CM, Kramer SG (2009) RacGAP50C directs perinuclear Akhmanova A and Steinmetz MO (2015) Control of microtubule organization and dynamics: two ends in the limelight. Nat Rev Mol Cell Biol 16:711–726

Guillet V, Knibiehler M, Gregory-Pauron L, Remy MH, Chemin C, Raynaud-Messina B, Bon C, Kollman JM, Agard DA, Merdes A, Mourey L (2011) Crystal structure of γ-tubulin complex protein GCP4 provides insight into microtubule nucleation. Nat Struct Mol Biol 18:915–919

Gunawardane RN, Lizarraga SB, Wiese C, Wilde A, Zheng Y (2000) γ-Tubulin complexes and their role in microtubule nucleation. Curr Top Dev Biol 49:55–73

Hořejší B, VinopalS, Sládková V,Dráberová E, Sulimenko V,Sulimenko T, Vosecká V, Philimonenko A, Hozák P, Katsetos CD, Dráber P (2012) Nuclear γ-tubulin associates withnucleoli and interactswith tumor suppressor protein C53. J Cell Physiol 227:367–382

Hotta T, Kong Z, Ho CM, Zeng CJ, Horio T, Fong S, Vuong T, Lee YR, Liu B (2012) Characterization of the *Arabidopsis* augmin complex uncovers its critical function in the assembly of the acentrosomal spindle and phragmoplast microtubule arrays. Plant Cell 24:1494–1509

Hsia KC, Wilson-Kubalek EM, Dottore A, Hao Q, Tsai KL, Forth S, Shimamoto Y, Milligan RA, Kapoor TM (2014) Reconstitution of theaugmin complex providesinsights into its architecture and function. Nat Cell Biol 16:852–863

Inukai K, Funaki M, Nawano M, Katagiri H, Ogihara T, Anai M, Onishi Y, Sakoda H, Ono H, Fukushima Y, Kikuchi M, Oka Y, Asano T (2000) The N-terminal 34 residues ofthe 55 kDa regulatory subunits of phosphoinositide 3-kinase interact with tubulin. Biochem J 346(Pt 2):483–489

Janski N, Masoud K, Batzenschlager M, Herzog E, Evrard JL, Houlné G, Bourge M, Chabouté ME, Schmit AC (2012) The GCP3-interacting proteins GIP1 and GIP2 are required forγ-tubulin complex protein

localization, spindle integrity, and chromosomal stability. Plant Cell 24:1171–1187

Jeffery JM, Grigoriev I, Poser I, van der Horst A, Hamilton N, Waterhouse N, Bleier J, Subramaniam VN, Maly IV, Akhmanova A, Khanna KK (2013) Centrobin regulates centrosome function in interphase cells by limiting pericentriolar matrix recruitment. Cell Cycle 12:899–906

Johmura Y, Soung NK, Park JE, Yu LR, Zhou M, Bang JK, Kim BY, Veenstra TD, Erikson RL, Lee KS (2011) Regulation of microtubule-based microtubule nucleation by mammalian polo-like kinase 1. Proc Natl Acad Sci U S A 108:11446–11451

Kalab P, Pralle A, Isacoff EY, Heald R, Weis K (2006) Analysis of a RanGTP-regulated gradient in mitotic somatic cells. Nature 440: 697–701

Khodjakov A, Rieder CL (1999) The sudden recruitment of γ-tubulin to the centrosome at the onset of mitosis and its dynamic exchange throughout the cell cycle, do not require microtubules. J Cell Biol 146:585–596

Kilmartin JV, Goh PY (1996) Spc110p: assembly properties and role in the connection of nuclear microtubules to the yeast spindle pole body. EMBO J 15:4592–4602

Kinoshita K, Noetzel TL, Pelletier L, Mechtler K, Drechsel DN, Schwager A, Lee M, Raff JW, Hyman AA (2005) Aurora A phosphorylation of TACC3/maskin is required for centrosome-dependent microtubule assembly in mitosis. J Cell Biol 170:1047–1055

Kirik A, Ehrhardt DW, Kirik V (2012) TONNEAU2/FASS regulates the geometry of microtubule nucleation and cortical array organization in interphase *Arabidopsis* cells. Plant Cell 24:1158–1170

Knop M, Schiebel E (1997) Spc98p and Spc97p of the yeast γ-tubulin complex mediate binding to the spindle pole body via their interaction with Spc110p. EMBO J 16:6985–6995

Kollman JM, Zelter A, Muller EG, Fox B, Rice LM, Davis TN, Agard DA (2008) The structure of the γ-tubulin small complex: implications of its architecture and flexibility for microtubule nucleation. Mol Biol Cell 19:207–215

Kollman JM, Polka JK, Zelter A, Davis TN, Agard DA (2010) Microtubule nucleating γ-TuSC assembles structures with 13-fold microtubule-like symmetry. Nature 466:879–882

Kollman JM, Merdes A, Mourey L, Agard DA (2011) Microtubule nucleation by γ-tubulin complexes. Nat Rev Mol Cell Biol 12:709–721

Kollman JM, Greenberg CH, Li S, Moritz M, Zelter A, Fong KK, Fernandez JJ, Sali A, Kilmartin J, Davis TN, Agard DA (2015) Ring closure activates yeast γ-TuRC for species-specific microtubule nucleation. Nat Struct Mol Biol 22:132–137

Lawo S, Hasegan M, Gupta GD, Pelletier L (2012) Subdiffraction imaging of centrosomes reveals higher-order organizational features of pericentriolar material. Nat Cell Biol 14:1148–1158

Lin TC, Neuner A, Schlosser YT, Scharf AN, Weber L, Schiebel E (2014) Cell-cycle dependent phosphorylation of yeast pericentrin regulates γ-TuSC-mediated microtubule nucleation. Elife 3:e02208

Lin TC, Neuner A, Schiebel E (2015) Targeting of γ-tubulin complexes to microtubule organizing centers: conservation and divergence. Trends Cell Biol 25:296–307

Liu T, Tian J, Wang G, Yu Y, Wang C, Ma Y, Zhang X, Xia G, Liu B, Kong Z (2014) Augmin triggers microtubule-dependent microtubule nucleation in interphase plant cells. Curr Biol 24:2708–2713

Lüders J, Stearns T (2007) Microtubule-organizing centres: a re-evaluation. Nat Rev Mol Cell Biol 8:161–167

Lüders J, Patel UK, Stearns T (2006) GCP-WD is a γ-tubulin targeting factor required for centrosomal and chromatin-mediated microtubule nucleation. Nat Cell Biol 8:137–147

Ludueña RF, Banerjee A (2008) The isotypes of tubulin: distribution and functional significance. In: Fojo T (ed) The role of microtubules in

cell biology, neurobiology and oncology. Humana Press, Totowa, pp 123–175

Lyon AS, Morin G, Moritz M, Yabut KC, Vojnar T, Zelter A, Muller E, Davis TN, Agard DA (2016) Higher-order oligomerization of Spc110p drives γ-tubulin ring complex assembly. Mol Biol Cell 27:2245–2258

Macurek L, Dráberová E, Richterová V, Sulimenko V, Sulimenko T, Dráberová L, Marková V, Dráber P (2008) Regulation of microtubule nucleation from membranes by complexes of membrane-bound γ-tubulin with Fyn kinase and phosphoinositide 3-kinase. Biochem J 416:421–430

Meunier S, Vernos I (2016) Acentrosomal microtubule assembly in mitosis: the where, when, and how. Trends Cell Biol 26:80–87

Mishra RK, Chakraborty P, Arnaoutov A, Fontoura BM, Dasso M (2010) The Nup107-160 complex and γ-TuRC regulate microtubule polymerization at kinetochores. Nat Cell Biol 12:164–169

Mogensen MM, Malik A, Piel M, Bouckson-Castaing V, Bornens M (2000) Microtubule minus-end anchorage at centrosomal and non-centrosomal sites: the role of ninein. J Cell Sci 113(Pt 17):3013–3023

Moreno-Mateos MA, Espina AG, Torres B, Gámez del Estal MM, Romero-Franco A, Ríos RM, Pintor-Toro JA (2011) PTTG1/securin modulates microtubule nucleation and cell migration. Mol Biol Cell 22:4302–4311

Moritz M, Braunfeld MB, Guénebaut V, Heuser J, Agard DA (2000) Structure of the γ-tubulin ring complex: a template for microtubule nucleation. Nat Cell Biol 2:365–370

Murata T, Sonobe S, Baskin TI, Hyodo S, Hasezawa S, Nagata T, Horio T, Hasebe M (2005) Microtubule-dependent microtubule nucleation based on recruitment of γ-tubulin in higher plants. Nat Cell Biol 7: 961–968

Muroyama A, Seldin L, Lechler T (2016) Divergent regulation of functionally distinct γ-tubulin complexes during differentiation. J Cell Biol 213:679–692

Nogales E, Wang HW (2006) Structural intermediates in microtubule assembly and disassembly: how and why? Curr Opin Cell Biol 18: 179–184

Nováková M, Dráberová E, Schürmann W, Czihak G, Viklický V, Dráber P (1996) γ-tubulin redistribution in taxol-treated mitotic cells probed by monoclonal antibodies. Cell Motil Cytoskeleton 33:38–51

Oakley CE, Oakley BR (1989) Identification of γ-tubulin, a new member of the tubulin superfamily encoded by mipA gene of *Aspergillus nidulans*. Nature 338:662–664

Oakley BR, Paolillo V, Zheng Y (2015) γ-Tubulin complexes in microtubule nucleation and beyond. Mol Biol Cell 26:2957–2962

Oh SA, Jeon J, Park HJ, Grini PE, Twell D, Park SK (2016a) Analysis of gemini pollen 3 mutant suggests a broad function of AUGMIN in microtubule organization during sexual reproduction in *Arabidopsis*. Plant J 87:188–201

Oh D, Yu CH, Needleman DJ (2016b) Spatial organization of the Ran pathway by microtubules in mitosis. Proc Natl Acad Sci U S A 113: 8729–8734

Oriolo AS, Wald FA, Canessa G, Salas PJ (2007) GCP6 binds to intermediate filaments: a novel function of keratins in the organization of microtubules in epithelial cells. Mol Biol Cell 18:781–794

Petry S, Vale RD (2015) Microtubule nucleation at the centrosome and beyond. Nat Cell Biol 17:1089–1093

Petry S, Groen AC, Ishihara K, Mitchison TJ, Vale RD (2013) Branching microtubule nucleation in *Xenopus* egg extracts mediated by augmin and TPX2. Cell 152:768–777

Pinyol R, Scrofani J, Vernos I (2013) The role of NEDD1 phosphorylation by aurora a in chromosomal microtubule nucleation and spindle function. Curr Biol 23:143–149

Rivero S, Cardenas J, Bornens M, Rios RM (2009) Microtubule nucleation at the cis-side of the Golgi apparatus requires AKAP450 and GM130. EMBO J 28:1016–1028

Roostalu J, Cade NI, Surrey T (2015) Complementary activities of TPX2 and chTOG constitute an efficient importin-regulated microtubule nucleation module. Nat Cell Biol 17:1422–1434

Roubin R, Acquaviva C, Chevrier V, Sedjaï F, Zyss D, Birnbaum D, Rosnet O (2013) Myomegalin is necessary for the formation of centrosomal and Golgi-derived microtubules. Biol Open 2:238–250

Samejima I, Miller VJ, Groocock LM, Sawin KE (2008) Two distinct regions of Mto1 are required for normal microtubule nucleation and efficient association with the γ-tubulin complex *in vivo*. J Cell Sci 121:3971–3980

Sánchez-Huertas C, Lüders J (2015) The augmin connection in the geometry of microtubule networks. Curr Biol 25:R294–R299

Sánchez-Huertas C, Freixo F, Viais R, Lacasa C, Soriano E, Lüders J (2016) Non-centrosomal nucleation mediated by augmin organizes microtubules in post-mitotic neurons and controls axonal microtubule polarity. Nat Commun 7:12187

Sanders AA, Kaverina I (2015) Nucleation and dynamics of Golgi-derived microtubules. Front Neurosci 9:431

Sawin KE, Tran PT (2006) Cytoplasmic microtubule organization in fission yeast. Yeast 23:1001–1014

Scrofani J, Sardon T, Meunier S, Vernos I (2015) Microtubule nucleation in mitosis by a RanGTP-dependent protein complex. Curr Biol 25:131–140

Seltzer V, Janski N, Canaday J, Herzog E, Erhardt M, Evrard JL, Schmit AC (2007) *Arabidopsis* GCP2 and GCP3 are part of a soluble γ-tubulincomplexandhavenuclearenvelope targetingdomains. Plant J 52:322–331

Singh P, Thomas GE, Gireesh KK, Manna TK (2014) TACC3 protein regulates microtubule nucleation by affecting γ-tubulin ring complexes. J Biol Chem 289:31719–31735

Soues S, Adams IR (1998) SPC72: a spindle pole component required for spindle orientation in the yeast *Saccharomyces cerevisiae*. J Cell Sci 111:2809–2818

Sulimenko V, Sulimenko T, Poznanovic S, Nechiporuk-Zloy V, Böhm KJ, Macurek L, Unger E, Dráber P (2002) Association of brain γ-tubulins with αβ-tubulin dimers. Biochem J 365:889–895

Sulimenko V, Dráberová E, Sulimenko T, Macurek L, Richterová V, Dráber P, Dráber P (2006) Regulation of microtubule formation in activated mast cells by complexes of γ-tubulin with Fyn and Syk kinases. J Immunol 176:7243–7253

Sulimenko V, Hájková Z, Černohorská M, Sulimenko T, Sládková V, Dráberová L, Vinopal S, Dráberová E, Dráber P (2015) Microtubule nucleation in mouse bone marrow-derived mast cells is regulated by the concerted action of GIT1/βPIX proteins and calcium. J Immunol 194:4099–4111

Takahashi M, Yamagiwa A, Nishimura T, Mukai H, Ono Y (2002) Centrosomal proteins CG-NAP and kendrin provide microtubule nucleation sites by anchoring γ-tubulin ring complex. Mol Biol Cell 13:3235–3245

Teixidó-Travesa N, Villén J, Lacasa C, Bertran MT, Archinti M, Gygi SP, Caelles C, Roig J, Lüders J (2010) The γ-TuRC revisited: a comparative analysis of interphase and mitotic human γ-TuRCredefines the set of core components and identifies the novel subunit GCP8. Mol Biol Cell 21:3963–3972

Teixidó-Travesa N, Roig J, Lüders J (2012) The where, when and how of microtubule nucleation - one ring to rule them all. J Cell Sci 125:4445–4456

Tsai MY, Zheng Y (2005) Aurora a kinase-coated beads function as microtubule-organizing centers and enhance RanGTP-induced spindle assembly. Curr Biol 15:2156–2163

Uehara R, Nozawa RS, Tomioka A, Petry S, Vale RD, Obuse C, Goshima G (2009) The augmin complex plays a critical role in spindle microtubule generation for mitotic progression and cytokinesis in human cells. Proc Natl Acad Sci U S A106:6998–7003

Uehara R, Kamasaki T, Hiruma S, Poser I, Yoda K, Yajima J, Gerlich DW, Goshima G (2016) Augmin shapes the anaphase spindle for efficientcytokineticfurrowingressionandabscission.MolBiolCell 27:812–827

Usui T, Maekawa H, Pereira G, Schiebel E (2003) The XMAP215 homologue Stu2 at yeast spindle pole bodies regulates microtubule dynamics and anchorage. EMBO J 22:4779–4793

Verhey KJ, Gaertig J (2007) The tubulin code. Cell Cycle 6:2152–2160

Vinopal S, Černohorská M, Sulimenko V, Sulimenko T, Vosecká V, Flemr M, Dráberová E, Dráber P (2012) γ-Tubulin 2 nucleates microtubules and is downregulated in mouse early embryogenesis. PLoS One 7:e29919

Wang Z, Wu T, Shi L, Zhang L, Zheng W, Qu JY, Niu R, Qi RZ (2010) Conserved motif of CDK5RAP2 mediates its localization to centrosomes and the Golgi complex. J Biol Chem 285:22658–22665

Wang S, Wu D, Quintin S, Green RA, Cheerambathur DK, Ochoa SD, Desai A, Oegema K (2015) NOCA-1 functions with γ-tubulin and in parallel to Patronin to assemble non-centrosomal microtubule arrays in *C. elegans*. Elife 4:e08649

Wieczorek M, Bechstedt S, Chaaban S, Brouhard GJ (2015) Microtubule-associated proteins control the kinetics of microtubule nucleation. Nat Cell Biol 17:907–916

Yokoyama H, Koch B, Walczak R, Ciray-Duygu F, González-Sánchez JC, Devos DP, Mattaj IW, Gruss OJ (2014) The nucleoporin MEL-28 promotes RanGTP-dependent γ-tubulin recruitment and microtubulenucleationinmitoticspindleformation. NatCommun5:3270

Zhang X, Chen Q, Feng J, Hou J, Yang F, Liu J, Jiang Q, Zhang C (2009) Sequential phosphorylation of Nedd1 by Cdk1 and Plk1 is required for targeting of the γ-TuRC to the centrosome. J Cell Sci 122:2240–2251

Zhang T, Braun U, Leitges M (2016) PKD3 deficiency causesalterations in microtubule dynamics during the cell cycle. Cell Cycle 15:1844–1854

Zimmerman WC, Sillibourne J, Rosa J, Doxsey SJ (2004) Mitosis-specific anchoring of γ-tubulin complexes by pericentrin controls spindleorganizationand mitotic entry. MolBiolCell15:3642–3657

VII.2   Chumová, J., Trögelová, L., Kourová, H., Volc, J., Sulimenko, V., Halada, P., Kučera, O., Benada, O., Kuchařová, A., **Klebanovych, A.,** Dráber, P., Daniel, G., Binarová, P. (2018) γ-Tubulin has a conserved intrinsic property of self-polymerization into double stranded filaments and fibrillar networks. Biochim Biophys Acta Mol Cell Res *1865(5)*:734-748

γ-Tubulin has a conserved intrinsic property of self-polymerization into double stranded filaments and fibrillar networks

Jana Chumová[a,1], Lucie Trögelová[a,1], Hana Kourová[a], Jindřich Volc[a], Vadym Sulimenko[c], Petr Halada[a], Ondřej Kučera[b], Oldřich Benada[a], Anna Kuchařová[a], Anastasiya Klebanovych[c], Pavel Dráber[c], Geoffrey Daniel[d], Pavla Binarová[a,*]

[a] *Institute of Microbiology of the Czech Academy of Sciences, Vídeňská 1083, 142 20 Prague 4, Czech Republic*
[b] *Institute of Photonics and Electronics of the Czech Academy of Sciences, Chaberská 57, 182 00 Prague 8, Czech Republic*
[c] *Institute of Molecular Genetics of the Czech Academy of Sciences, Vídeňská 1083, 142 20 Prague 4, Czech Republic*
[d] *Department of Forest Biomaterials Technology, Swedish University of Agricultural Sciences, Box 7008, Uppsala SE-75007, Sweden*

ARTICLE INFO

ABSTRACT

γ-Tubulin is essential for microtubule nucleation and also plays less understood roles in nuclear and cell-cycle-related functions. High abundancy of γ-tubulin in acentrosomal *Arabidopsis* cells facilitated purification and biochemical characterization of large molecular species of γ-tubulin. TEM, fluorescence, and atomic force microscopy of purified high molecular γ-tubulin forms revealed the presence of linear filaments with a double protofilament substructure, filament bundles and aggregates. Filament formation from highly purified γ-tubulin free of γ-tubulin complex proteins (GCPs) was demonstrated for both plant and human γ-tubulin. Moreover, γ-tubulin associated with porcine brain microtubules formed oligomers. Experimental evidence on the intrinsic ability of γ-tubulin to oligomerize/polymerize was supported by conservation of α- and β-tubulin interfaces for longitudinal and lateral interactions for γ-tubulins. STED (stimulated emission depletion) microscopy of *Arabidopsis* cells revealed fine, short γ-tubulin fibrillar structures enriched on mitotic microtubular arrays that accumulated at polar regions of acentrosomal spindles and the outer nuclear envelope before mitosis, and were also present in nuclei. Fine fibrillar structures of γ-tubulin representing assemblies of higher order were localized in cell-cycle-dependent manner at sites of dispersed γ-tubulin location in acentrosomal plant cells as well as at sites of local γ-tubulin enrichment after drug treatment. Our findings that γ-tubulin preserves the capability of prokaryotic tubulins to self-organize into filaments assembling by lateral interaction into bundles/clusters help understanding of the relationship between structure and multiple cellular functions of this protein species and suggest that besides microtubule nucleation and organization, γ-tubulin may also have scaffolding or sequestration functions.

1. Introduction

Prokaryotic and eukaryotic tubulins diverge in their primary sequences, but share a common ability to assemble into filaments. While the bacterial FtsZ and TubZ are known to form homopolymeric single or double protofilaments, eukaryotic α- and β-tubulins and bacterial BtubA and BtubB tubulins evolved an ability to form heterodimers that assemble into protofilaments and microtubules. γ-Tubulin phylogenetically belongs to the eukaryotic clade of the tubulin family [1] and

was first described as a suppressor of β-tubulin mutation in *Aspergillus* [2]. Later, γ-tubulin was shown to have a specialized function in microtubule nucleation [3]. Complexes of γ-tubulin with γ-tubulin complex proteins (GCPs) represent well-established microtubule nucleators from spindle pole bodies, centrosomes or from non-centrosomal nucleation sites in eukaryotes. The small γ-tubulin complexes (γ-TuSCs) and large γ-tubulin ring complexes (γ-TuRCs) of animal cells are the best characterized. However, there are organism-specific differences in size and composition of γ-tubulin complexes and a variety of

attachment and regulatory factors recruit such complexes to sites of microtubule nucleation [4]. Self-oligomerization of budding yeast γ-TuSCs *in vitro* [5] and higher order assemblies of γ-TuSCs with GCP 4/5/6 proteins and pericentrin in mammalian cells [6] suggest that spatial arrangement of γ-tubulin complexes with attachment factors may play a role in formation and turnover of nucleation templates [7]. γ-Tubulin is also essential for microtubule nucleation in plant cells [8,9]. While presence of plant γ-TuRC-like complexes and their role in acentrosomal microtubule organization is suggested [10,11], plant homologues of centrosomal nucleation components such as pericentrin are absent.

Centrosomal γ-tubulin represents only a minor part of the γ-tubulin cellular pool [12] and large heterogeneous molecular forms of γ-tubulin showing different characteristics from γ-TuSCs or γ-TuRCs are reported in animal and plant cells [13–15]. γ-Tubulin interacts with components of the cytoskeleton and forms complexes with α- and β-tubulins and actin [16,17], and large γ-tubulin assemblies also associate with lamin B3 during nuclei formation [18]. Large molecular forms of γ-tubulin are also membrane-associated [15,19,20]. Like other eukaryotic tubulins, several γ-tubulin isoelectric variants have been demonstrated [13,21], for example, the brain specific isoform of γ-tubulin is bound to mitochondrial membranes and upregulated under oxidative stress [22].

Our previous data on the presence of γ-tubulin in nuclei and in kinetochore regions of chromosomes in plant cells indicated its interaction with DNA [23,24]. There is also a growing body of evidence for the interaction of γ-tubulin with proteins associated with DNA damage response [25,26], tumor suppressors [27] and with transcription factors [28]. γ-Tubulin also plays a role in cell cycle regulation [29], interacts with mitogen-activated protein kinases [30] and is recognized as a marker of aggresomes [31]. Thus in addition to its well-defined role in microtubule nucleation, γ-tubulin may play an important role in other cellular processes, although corresponding molecular mechanisms are poorly understood.

Substantially larger amounts of γ-tubulin are found in acentrosomal plant cells compared with animal cells. Plant γ-tubulin is also widely distributed in cells and forms heterogeneous high-molecular-mass complexes [15]. Here we report the molecular and structural characterization of large γ-tubulin forms purified from both *Arabidopsis* and human cells. We found large assemblies of γ-tubulin formed by short double-stranded filaments exhibiting prominent clustering *in vitro*. Organization of γ-tubulin into fibrillar structures was shown by STED microscopy in *Arabidopsis* cells. The ability of γ-tubulin to form filaments, demonstrated experimentally here for both plant and animal γ-tubulins is in agreement with model-derived predictions of human γ-tubulin oligomerization.

2. Materials and methods

2.1. Cells and gene constructs

Arabidopsis thaliana cell suspension cultures of ecotype Landsberg erecta (Ler) derived by [32] and cell cultures of ecotype Columbia (Col) [33] were grown under continuous darkness at 25 °C.

The N-terminal GFP or C-terminal GFP fusion of complete coding region of *Arabidopsis* γ-tubulin1 was prepared by Gateway cloning using pDONR207 and destination vector pK7WGF2 or pK7FWG2, respectively [34]. The constructs were transformed into Ler cell cultures using *Agrobacterium tumefaciens* GV3101 strain.

Human osteogenic sarcoma cells U2OS stably expressing TagRFP-tagged human γ-tubulin1 (γ-tubulin-RFP) or TagRFP-tagged human p21 protein (Cdc42/Rac)-activated kinase 1 (PAK1-RFP) were described previously [35]. Cells were cultured in Dulbecco's modified Eagle's medium (DMEM) containing 10% FCS, penicillin (100 units ml^{-1}) and streptomycin (0.1 mg ml^{-1}). Cells were grown at 37 °C in 5% CO_2 in air and passaged every 2 days.

2.2. Cell fractionation methods

3-day-old cultured *Arabidopsis* cells were harvested, ground in liquid nitrogen, and extracted at a biomass to buffer ratio of 1:1.5 in extraction buffer E (50 mM Hepes pH 7.5 (NaOH), 75 mM NaCl, 1 mM $MgCl_2$, 1 mM EGTA) supplemented with protease (1 mM DTT, 1 mM Pefablock, 5 µg ml^{-1} each of aprotinin, leupeptin, pepstatin, antipain, and soyabean trypsin inhibitor) and phosphatase (1 mM NaF, 0.5 mM Na_3VO_4, 60 mM β-glycerophosphate, 5 mM *p*-nitrophenylphosphate) inhibitors. For differential centrifugation, the homogenates were centrifuged at 10,000 ×*g* for 10 min at 4 °C and the resulting supernatants (S10) spun subsequently at 25,000 ×*g* for 1 h or at 20,000 ×*g* for 30 min when indicated. Supernatants S25 (~3 mg ml^{-1}) were treated for 60 min at 4 °C with 1% non-ionic detergent NP-40 (Roche Diagnostics, Mannheim, Germany) and spun at 100,000 ×*g* for 1 h to provide detergent-soluble S100 supernatant and the "detergent-insoluble" P100 pellet. P100 pellets were thoroughly resuspended under ice cooling in buffer E supplemented with 0.1% NP-40, ground in glass homogenizer and clarified at 10,000 ×*g* for 15 min before further analysis. To obtain microsomal P100, detergent non-treated S25 supernatant was spun at 100,000 ×*g* for 1 h.

To fractionate human U2OS cells expressing Tag-RFP-tagged proteins, cells from four 9-cm diameter Petri dishes (cell confluence 80–90%) were rinsed twice in cold PBS buffer and scraped to HEPES buffer supplemented with protease (Roche; Complete EDTA-free protease mixture) and phosphatase (1 mM Na_3VO_4, 1 mM NaF) inhibitors. Suspension of cells (~2,8 ml) was homogenized in 7 ml Dounce homogenizer on ice. Fractionation was performed by differential centrifugation as described for plant cells providing the detergent-soluble (S100) and detergent-insoluble (P100) fractions.

Protein gel filtrations were performed on a Superose 6 10/300 GL column (GE Healthcare Bio-Sciences, Little Chalfont, UK) equilibrated with buffer E containing 150 mM NaCl unless specified otherwise. 200-µl aliquots of resuspended P100 pellet (6–8 mg protein ml^{-1}) were loaded on the column and proteins size separated into 0.5-ml fractions collected at a flow rate of 0.2 ml min^{-1}.

Protein fractionation was alternatively done in sucrose gradient. Solubilised S20 (1 ml) or detergent-insoluble P100 (from 20 ml of S20, resuspended in 1 ml) was loaded on a four-step 10–40% sucrose gradient and centrifuged at 100,000 ×*g* for 16 h. Fractions (500 µl each) were collected from the top (fraction 1) to the bottom (fraction 17) and 40-µl samples were electrophoretically separated and Western blotted. Aldolase and Thyroglobulin (GE Healthcare), and Blue Dextran 2000 (Amersham Biosciences) were used as Mw standards.

2.3. Immunopurification of γ-tubulin

In standard endogenous γ-tubulin immunoprecipitations (Procedure *a*), the detergent-insoluble P100 pellets obtained from *Arabidopsis* cell extracts containing 30–40 mg of total proteins (10–15 ml S25) were resuspended in 1.8 ml to give an input sample. The sample was incubated with affinity purified anti-γ-tubulin antibody AthTU (3 µg ml^{-1}) on a rotator for 1 h at 4 °C and immuno-complexes bound to 60 µl Protein A-agarose beads (Roche) upon additional 1-h incubation. Beads were washed with 1 × 2 ml buffer E supplemented with 0.1% NP-40, 3 × 2 ml 50 mM Tris HCl (pH 8.0) plus 150 mM NaCl and 1 × 2 ml 50 mM Tris HCl pH 8.0, and γ-tubulin complexes sequentially eluted by 3 × 100 µl 0.1% immunogenic peptide in the 50 mM Tris buffer for 30 min each time at room temperature under gentle rocking. The combined peptide eluates were diafiltered into 50 mM Tris HCl (pH 8.0) in a Microcon-30 kDa Centrifugal Filter Unit (Millipore) to remove the elution peptide and concentrated to ~100 µl prior to negative staining TEM or, alternatively, to the column dead volume (50 µl) prior to sample analyses by LC MALDI-TOF MS/MS (direct tryptic digestion on the diafiltration column) and SDS–PAGE Western blot/silver staining (direct transfer in 2× Laemmli sample buffer).

Immunoprecipitation of γ-tubulin(-GFP) used in parallel to anti-γ-tubulin antibody also a GFP-TrapA (Chromo-Tek, Planegg-Martinsried, Germany) with slightly modified elution buffer (0.1 M glycine pH 2.5). pH of acidic eluates was instantly adjusted to 8.0 by 1 M Tris.

To prepare extracts for immunoprecipitation from human U2OS cells, the detergent-resistant P100 fraction was resuspended in 0.4 ml ice-cold 0.1% NP-40 in HEPES buffer, ground in a Teflon/glass homogenizer and clarified at 10,000 ×g for 15 min. When indicated, 0.08% SDS was added to the extract. Immunoprecipitation was performed as previously described [14] for 60 min at room temperature. Extracts were incubated with beads of protein A saturated with: (i) rabbit anti-tRFP (Evrogen AB234) antibody, (ii) negative control rabbit antibody to non-muscle myosin H chain (Biomedical Technologies, BT-561) or with (iii) immobilized protein A alone. Antibody to tRFP was used at Ig concentrations of 2 μg ml^{-1} and antibody to myosin was used at a dilution of 1:100. Beads were washed five-times with TBST (10 mM Tris-HCl, 150 mM NaCl, 0.05% Tween-20, pH 7.4), and bound proteins were eluted by low pH as described above.

For isolation of γ-tubulin from porcine brain microtubule proteins, prepared by two cycles of polymerization/depolymerization (MTP-2) [36], a mouse monoclonal anti-γ-tubulin antibody TU-31 directed to peptide from C-terminal domain of molecule was applied [37]. MTP-2 at concentration 5 mg ml^{-1} in BRB80 buffer (80 mM Pipes, pH 6.8, 1 mM EGTA, 1 mM MgCl$_2$) was incubated with TU-31 antibody immobilized on protein A-Sepharose. After extensive washing, protein A with bound proteins was loaded onto the column and eluted with immunizing peptide at a concentration 300 μg ml^{-1} in water. Fractions containing γ-tubulin were collected and used for analysis.

To enrich higher molecular forms of γ-tubulin for immunopurification we used La^{3+}-PEG precipitation of *Arabidopsis* extract. S25 cell extracts (16 ml) were under stirring on ice supplemented dropwise with 100 mM LaCl$_3$ (Sigma-Aldrich) in H$_2$O to 1–2 mM La^{3+} until turbidity appeared. The suspensions were incubated on ice for 10 min and centrifuged at 2600 ×g for 10 min at 4 °C. Pellets were dissolved in 1.7 ml ice-cold 50 mM EDTA in 200 mM Tris·HCl (pH 7.5) and treated for 90 min on a rotator at 4 °C with ~1% NP-40. Subsequently, powdered polyethylene glycol 6000 (PEG, Fluka) was added to 3.3% (w/v). The mixture was incubated on ice for 15 min and spun at 10,000 ×g for 15 min. The pellet was extracted in 0.5 ml of buffer E containing 350 mM NaCl and centrifuged at 10,000 ×g for 15 min. Prior to immunoprecipitation, the clarified supernatant was diluted 1:2 with 50 mM Tris·HCl pH 7.5.

To obtain γ-tubulin-GFP free of associated proteins, immunoprecipitations were performed under high stringency conditions from S25 extracts pre-treated with 0.3% SDS (Sigma) for 60 min at RT (Procedure *b*).

Ultrafiltration of eluates was performed using Microcon YM-100 spin columns (Millipore, Darmstadt, Germany) and Ultrafree-MC microcentrifuge filter units 300 kDa NMWL (M-1286 Sigma, St. Louis, Missouri) centrifuged at 10 °C at 10,000 ×g. Protein concentration was assayed using a Bradford colorimetric method and NanoDrop (Protein A280 module).

We performed independent experiments at least three times with exception of isolation of high molecular forms of γ-tubulin which were performed at least fifty times for TEM, AFM and IF microscopic analyses.

2.4. Electrophoresis and Western blot analyses

Proteins were separated on 8% SDS − PAGE gels or under non-denaturing conditions using 3–14% gradient native PAGE, and silver stained or Western blotted as described previously [15]. Alternatively, 7.5% native PAGE was used. Molecular-mass markers for native electrophoresis were from Amersham Biosciences (Uppsala, Sweden). List of antibodies and dilutions are given in Supplemental methods. Detection was performed using SuperSignal West Pico ECL kit (Pierce,

Dallas, Texas).

2.5. Mass spectrometry

Silver-stained protein bands were washed, in-gel trypsin-digested and identified by MALDI-TOF peptide mass mapping [38]. LC MALDI-TOF MS/MS (abbr. LC-MS/MS) was employed for identification of proteins co-immunoprecipitated with γ-tubulin. For details see Supplemental methods. Mass spectra were acquired on an Ultraflex III instrument (Bruker Daltonics, Bremen, Germany) and searched against *A. thaliana* subset of SwissProt or NCBI database using in-house Mascot search engine (Matrix Science).

2.6. Transmission electron microscopy (TEM)

For negative staining, 2 μl samples of the immunopurified γ-tubulin were applied onto glow-discharged carbon coated 400 mesh copper grids for 2 min, then washed 5× for 1 min with a drop of 50 mM Tris·HCl (pH 7.5), blotted and stained with 1% w/v uranyl acetate for 2 min. For immunogold labelling, 5 μl samples were applied onto glow-discharged activated Formvar/carbon coated nickel grids for 30 s and fixed in 4% paraformaldehyde (PFA) and 0.1% glutaraldehyde in PBS (pH 7.4) for 10 min. After blocking with 1% BSA in PBS plus 0.05% Tween, anti-GFP primary antibody diluted 1:100 in the blocking buffer was applied for 2 h. Anti-rabbit antibody conjugated with 5-nm gold particles (BBInternational, Cardiff, UK) was used. Grids were stained using 2% ammonium molybdate in ddH$_2$O (pH 6.5).

Observations were made at 120 kV using a Philips CM12 (FEI systems, Hillsboro, Oregon) TEM fitted with a LaB$_6$ electron source. Images were recorded on Kodak 4489 negative film and films subsequently scanned using an Epson Perfection Pro 750 film scanner. Some protein samples were viewed under a Philips CM100 microscope equipped with MegaViewII slow scan camera and operated at 80 kV and magnification of 46,000×.

2.7. Atomic Force Microscopy (AFM)

Atomic Force Microscopy (AFM) is described in Supplemental methods.

2.8. Fluorescence microscopy of isolated γ-tubulin

Fluorescence imaging of γ-tubulin high-molecular-mass species was performed with Protein A-agarose or GFP-TrapA immunosorbent eluates (see Immunopurification of γ-tubulin) containing γ-tubulin(-GFP). Samples (0.3–0.4 mg protein ml^{-1}) in a polymerization buffer (50 mM Tris·HCl pH 8.0 or 100 mM Tris/glycine pH 7.5–8.0 for GFP-Trap eluate) were applied to uncoated and poly-L-lysine-coated microscope slides and before inspection incubated at room temperature for 5–20 min in a moist chamber. GFP Trap eluates were renatured for 20 min before placing on slides. To determine conditions favorable for filament formation, the sample buffers were supplemented separately with 1 or 2 mM GTP, 1 mM MgCl$_2$, 10 mM CaCl$_2$, and up to 500 mM KCl, or transferred by diafiltration into the microtubule polymerization buffer BrB80. For details of fluorescence microscopy and of confocal laser scanning microscopy see Supplemental methods.

Immunopurified γ-tubulin-RFP or PAK1-RFP were renatured at room temperature for 20 min before 5 μl samples were applied on clean cover glasses and incubated at room temperature in a moist chamber for 10–15 min. Cover glasses with samples were placed on microscopic slides and preparations examined using a Delta Vision Core System (Applied precision) or on Olympus fluorescence microscope AX-70 Provis.
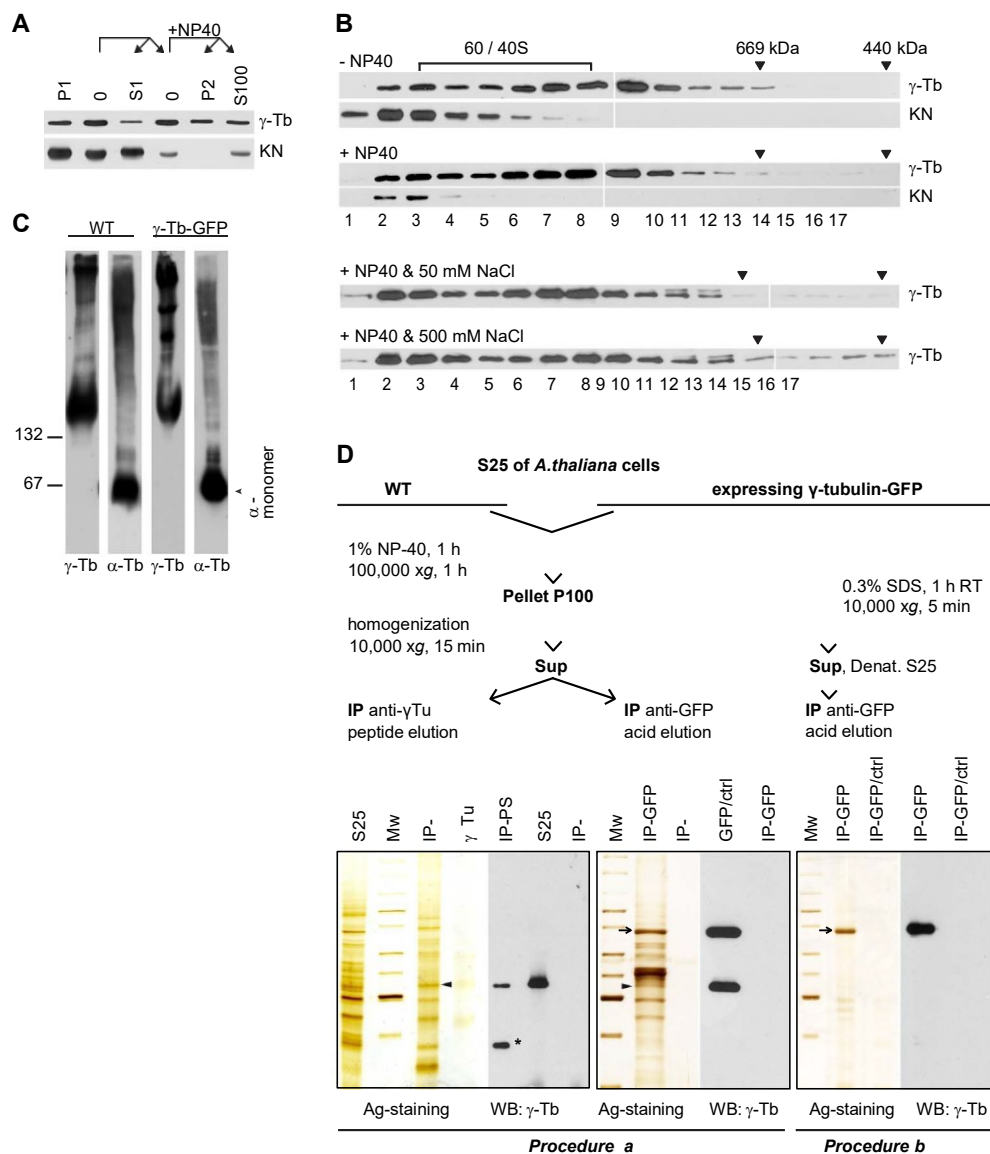
Fig. 1. *Arabidopsis* γ-tubulin heterogeneous high molecular weight forms and their purification from cell extracts.

(A) Differential centrifugation of *Arabidopsis thaliana* extracts. Western blot (WB) after SDS-PAGE, with anti-γ-tubulin (γ-Tb) and anti-KNOLLE (KN) antibodies. (B) Gel filtration profiles of P100 obtained from detergent-untreated (-NP40) or detergent-treated (+NP40) S25 samples. Alternatively P100 fractions obtained from detergent-treated samples were resuspended and fractionated in the presence of 50 mM NaCl (+NP40 & 50 mM NaCl) or 500 mM NaCl (+NP40 & 500 mM NaCl). WB with anti-γ-tubulin and anti-KNOLLE antibodies. Apparent molecular size markers are indicated by arrowheads; 60S/40S denotes position of ribosomal subunits. (C) Analysis of S20 cell extracts of WT or γ-tubulin-GFP expressing cells by native PAGE. Immunostaining with anti-γ-tubulin and anti-α-tubulin antibodies. Molecular weight standards in kDa are on the left.

(D) Left panel: γ-Tubulin was immunoprecipitated (IP) with anti-γ-tubulin (IP-γTu) and eluted from the immunosorbent beads using an immunogenic peptide. Pre-immune serum (IP-PS) was used as a negative control.

Proteins in eluates were separated by SDS-PAGE, silver stained (Ag) and Western blotted (WB)

with anti-γ-tubulin antibody. Endogenous γ-tubulin (arrowhead), an unspecific band recognized in the S25 input (asterisk). Central panel: γ-Tubulin-GFP was purified with anti-GFP antibody (IP-GFP) followed by acid elution. Immunoprecipitations from extracts of untransformed cells (IP-GFP/ctrl) was used as a negative control. γ-Tubulin-GFP (arrow), copurified endogenous γ-tubulin (arrowhead). Right panel: Endogenous γ-tubulin dissociated when γ-tubulin-GFP was purified under high stringency conditions (0.3% SDS).

MW standards (from bottom to top): 40, 50, 60, 70, 85, 100, 120, 150, and 200 kDa.

2.9. Fluorescence microscopy of cells

Immunofluorescence labelling of *Arabidopsis* cells was performed as described earlier [15] and cells were analyzed by confocal laser scanning microscopy (for details of CLSM and list of antibodies, dilutions and drug treatments see Supplemental methods).

For STED microscopy immunofluorescence labelling protocol was modified as followed: cells were prepared onto high precision cover glasses (thickness No. 1,5H, 170 μm, Marienfeld). Final wash after secondary antibody was in distilled water followed by air-drying. Dry samples were mounted in 90% glycerol with 5% anti-fade *N*-propyl gallate (Sigma Aldrich) or TDE (2,2-thiodiethanol). Rabbit polyclonal peptide purified anti-γ-tubulin antibody AthTU was tested in dilutions ranging from 1:500 to 1:6000 and dilution 1:1500 was used. Mouse monoclonal anti-γ-tubulin antibody TU32 was used in dilution 1: 4. For continuous 660 nm depletion laser, secondary antibody anti-rabbit Alexa Fluor 555 conjugated F(ab)2 in dilution 1:250 was used with anti-mouse Alexa Fluor 488 conjugated F(ab)2. Secondary antibodies, anti-mouse Abberior STAR 580 (1:200) or anti-mouse Alexa Fluor 594 (1:600) were used with anti-rabbit Abberior STAR RED (1:200) in case of 775 nm pulsed depletion laser.

Time-gated continuous wave stimulated emission depletion (gCW-

STED, 660 nm depletion laser) and pulsed stimulated emission (pulse-STED, 775 nm depletion laser) super-resolution microscopy was performed with Leica TCS SP8 STED 3X microscope. For 0% 3D-STED and 20% 3D-STED, z stacks were taken with 0.15 μm, 0.13 μm and 0.09 μm z-step, respectively. Time-gating was set between 0.2 and 6.0 ns according to sample life-time properties. For the stimulated depletion, 80% of intensity of 660 nm depletion laser and 80% or 90% intensity of 775 depletion laser was used.

Deconvolution was done using Huygens Professional version 16.05 (Scientific Volume Imaging, The Netherlands, http://svi.nl).Segmentation using auto local threshold with Bernsen method [39] and measurements of full width at half maximum of the intensity profile were done using an open source software Fiji. Images were prepared using Fiji, Adobe Photoshop CS4, and Adobe Illustrator CS4.

2.10. Sequence/structural analyses

For protein alignment, either BLAST (with BLOSUM62) [40] or T-Coffee [41] was used. Protein structures were compared using the DALI program [42]. Homology modelling was done by SwissModel [43] in Alignment Mode. Alignment was prepared in T-Coffee and further modified by us; input sequences were P38557 from SwissProt and
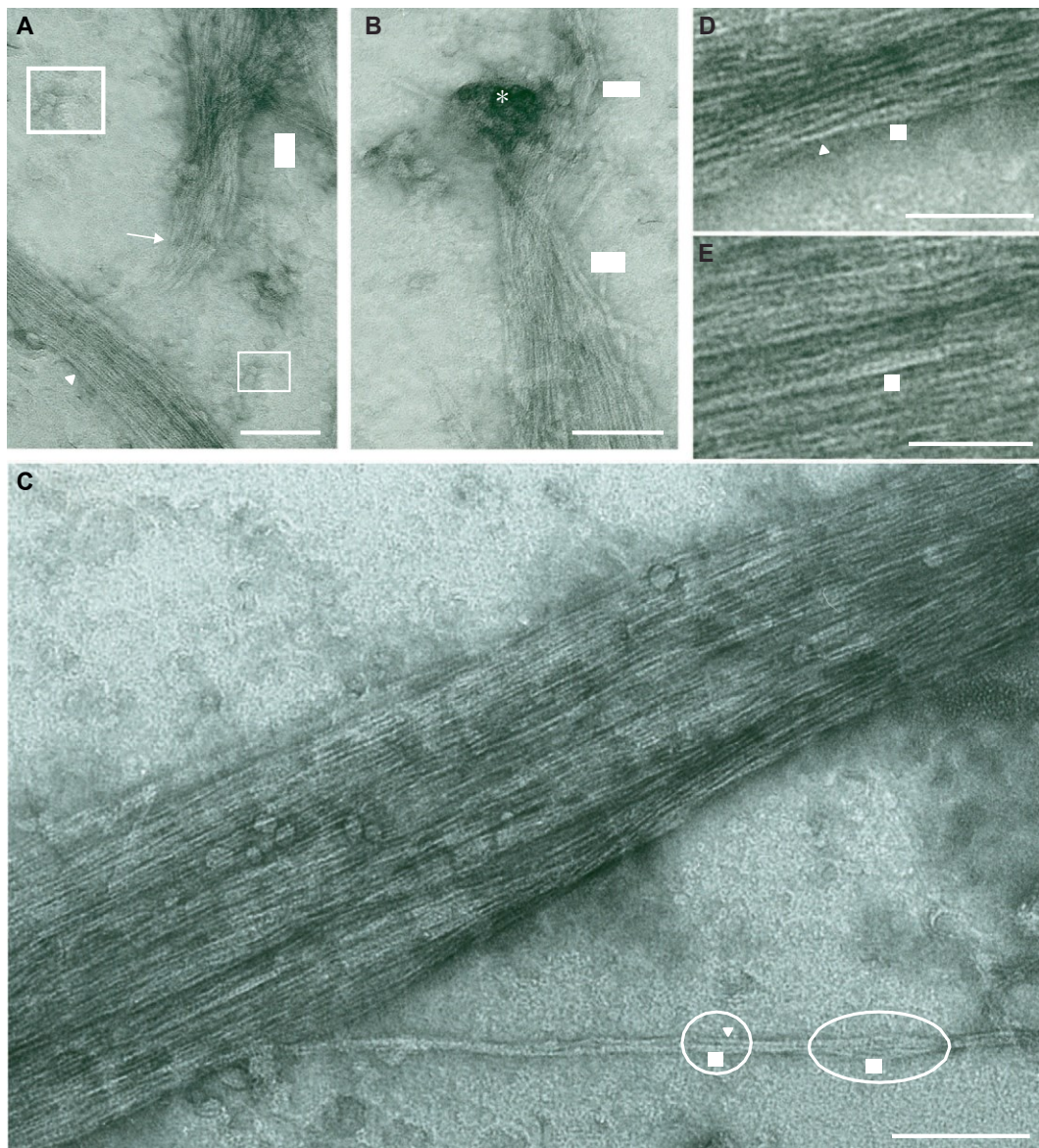
Fig. 2. TEM analyses of purified endogenous large *Arabidopsis* γ-tubulin forms revealed presence of filaments.

(A) Partially ordered bundles of filaments (arrows) and long straight bundle of filaments (arrowhead) are present together with unincorporated short double filaments (insets). (B) Loose bundles of filaments (arrows) and aggregate (asterisk). (C) High resolution image of a tightly packed bundle of straight, occasionally twisted γ-tubulin filaments. (D, E) Close-up views show ribbon-like morphology of loosely aligned double-stranded filaments of repeating homotypic subunits. The open arrowheads in D and E show the front view of a double filament and closed arrowhead in D a side view at the crossover point. The substructure can also be seen in the circle- and ellipse-marked areas of the thin protofilament split from the bundle (C). Scale bars 100 nm (A–C); Scale bars 50 nm (D, E).

12,653,673 from NCBI; a template PDB ID 3cb2a [44] was used. Phyre 2 [45] was used in One to one threading mode with PDB ID 3cb2a as a template and P38557 as an input sequence. For I-TASSER [46], input sequence was P38557 with PDB ID 3cb2a as a template. Molecular graphics and analyses were performed with the UCSF Chimera package [47].

2.11. Accession numbers

3. Results

3.1. Characterization of size-heterogeneous high-molecular-mass assemblies of γ-tubulin and their purification from Arabidopsis extracts

To characterize γ-tubulin forms in *Arabidopsis*, we performed differential centrifugation of non-ionic detergent NP-40-treated cell extracts. We found, that substantial amounts of γ-tubulin were pelleted into high speed detergent-insoluble P100 pellets (Fig. 1A). An efficient solubilization of microsomal membranes was shown by immunodetection of membrane marker syntaxin KNOLLE. When either the microsomal P100 pellets or detergent NP-40-resistant P100 pellets were size-fractionated by gel filtration, γ-tubulin was detected in fractions 2–10 corresponding to molecular masses > 1 MDa (Fig. 1B). This indicates that the high molecular mass of the γ-tubulin forms was not due to association of γ-tubulin with microsomal membranes. The size-
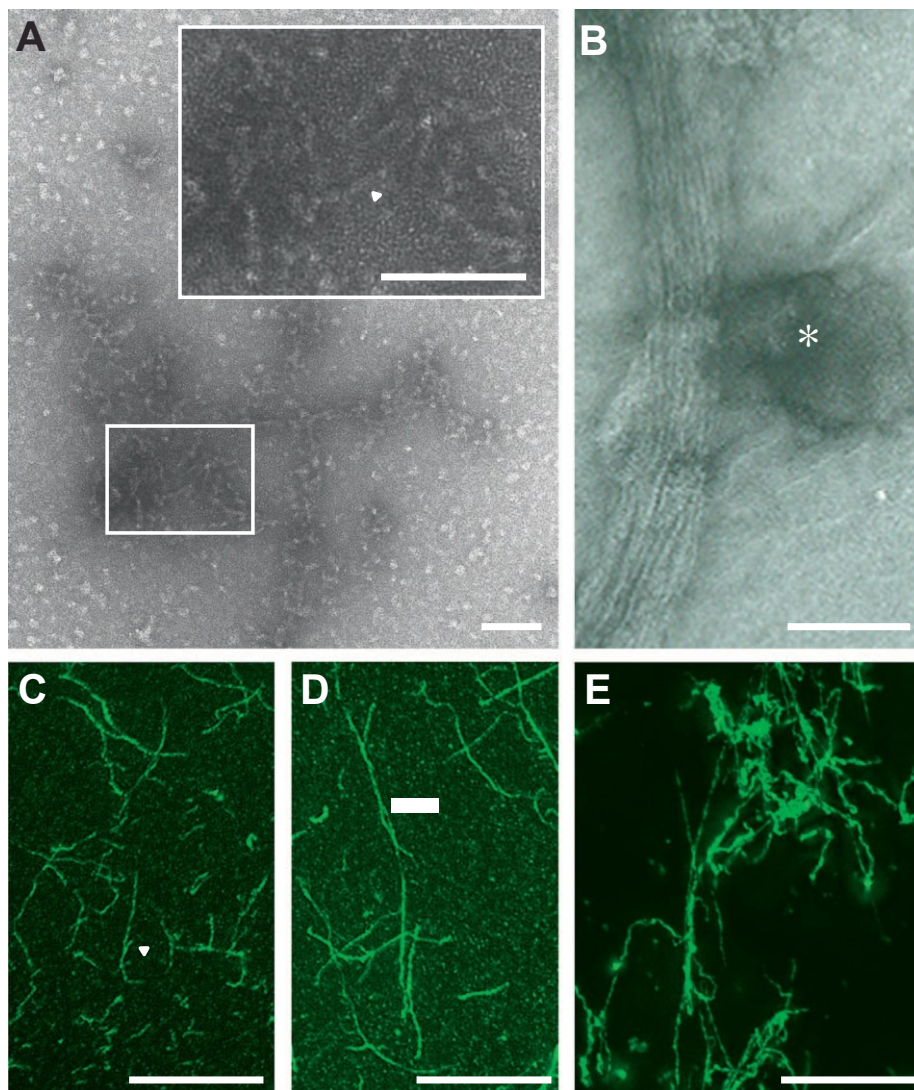
Fig. 3. γ-Tubulin(-GFP) purified from *Arabidopsis* cells preserves filament-forming capacity.

(A) γ-Tubulin(-GFP) immunopurified from detergent-resistant P100, visualized by negative stain TEM. Inset: higher magnification of the framed area. (B) Bundle of tightly aligned filaments and aggregate (asterisk) of γ-tubulin(-GFP). (C–E) Filament bundles and aggregates assembled from γ-tubulin(-GFP) visualized by fluorescence microscopy. (C, D) γ-Tubulin(-GFP) immunopurified from P100. Filaments aligned (C arrowhead) or interwined (D arrow). (E) γ-tubulin(-GFP) immunopurified from fraction enriched in high molecular proteins by La³⁺-PEG precipitation (see Supplemental Fig. 2). Maximal projection of two sections after deconvolution are shown in C and D. Scale bars 100 nm (A, B); scale bars 10 μm (C–E).

distribution pattern for the γ-tubulin high molecular weight forms was preserved when the detergent-insoluble pellets were pre-treated and subsequently fractionated under high ionic strength conditions with 500 mM NaCl (Fig. 1B).

When the cell extracts were analyzed by native PAGE, multiple bands were immunodetected using antibodies to γ-tubulin or α-tubulin (Fig. 1C). Oligomers of α,β -tubulins were observed under conditions of native PAGE with the most rapid migrating species corresponding to monomers [48] while γ-tubulin in position corresponding to MW of monomers was not detected (Fig. 1C). Similar multiple bands and absence of monomers (Fig. 1C) were shown by native PAGE in the cell extracts of *Arabidopsis* cells expressing *TubG1-GFP* fusion.

To purify high-molecular endogenous *Arabidopsis* γ-tubulin forms, we applied immunoprecipitation with affinity-purified polyclonal anti-γ-tubulin antibody. The detergent-insoluble P100 pellet served as input and a γ-tubulin-derived immunogenic peptide was used for elution (Fig. 1D, Procedure *a*). Immunopurified endogenous γ-tubulin was detected on Western blot (Fig. 1D, left panel) and identified by MALDI-TOF mass spectrometry (MS). γ-Tubulin was also immunopurified from cells expressing *TubG1-GFP* fusion (Supplemental Fig. 1) using either anti-γ-tubulin antibody with peptide elution or anti-GFP-antibody with acid elution. As shown in Fig. 1D, central panel, endogenous γ-tubulin co-purified with γ-tubulin-GFP in approx. ratio of 1:1.

Immunoprecipitation of GFP-tagged γ-tubulin followed by acid elution was also performed under high stringency conditions (Fig. 1D,

Procedure *b*). We found that treatment of the cell extracts with 0.3% SDS resulted in dissociation of endogenous γ-tubulin while the binding capacity of γ-tubulin-GFP to immunosorbent was still preserved (Fig. 1D, right panel).

To enrich large molecular forms of γ-tubulin as input for immunoprecipitation, we used La³⁺-PEG protein precipitation from S25 extracts (Supplemental Fig. 2A, 2B). Anti-γ-tubulin antibody precipitated endogenous γ-tubulin from wild-type cells (Supplemental Fig. 2C), as well as endogenous γ-tubulin with GFP-tagged γ-tubulin from cells expressing γ-tubulin-GFP (Supplemental Fig. 2D).

Altogether these data suggest that in *Arabidopsis* extracts, a substantial proportion of γ-tubulin was present in large molecular forms. The protocols established for immunopurification of γ-tubulin enabled us to obtain sufficient amounts of endogenous γ-tubulin or γ-tubulin-GFP with copurified endogenous γ-tubulin (in the following text denoted as γ-tubulin(-GFP)) for further analyses.

3.2. γ-Tubulin forms double protofilaments that cluster and self-assemble in vitro into filament bundles

γ-Tubulin samples immunopurified with anti-γ-tubulin antibody from resuspended detergent-insoluble P100 (Fig. 1D, Procedure *a*) were subsequently analyzed by TEM (Fig. 2). When concentrated immunogenic peptide eluates were applied to carbon coated TEM grids at concentration ~0.5 mg protein ml⁻¹, partially ordered bundles (Fig. 2A

arrows) and long straight bundles of filaments (Fig. 2A arrowhead) were present together with short double filaments (Fig. 2A insets). Amorphous aggregates (Fig. 2B asterisk) were also observed together with loose filament bundles (Fig. 2B arrows). Filament bundling was strictly favoured over the presence of individual long filaments. The tight bundles showed almost parallel aligned and straight filaments that occasionally appeared helically interwined, especially with loosely aligned γ-tubulin filaments (Fig. 2C). Due to the irregular twist, the filaments were revealed as double filaments presumably consisting of two protofilaments as shown at higher magnification in Fig. 2D and E (open arrowheads). From side-view at the crossover point they were visualized as single protofilaments (Fig. 2D, closed arrowhead). The bundle composition of elemental filaments of two parallel protofilament substructures (~6 × 9 nm in a cross section) was also evident on filaments loosen from thick bundles (Fig. 2C, ellipse and circle) showing the double protofilament from front (Fig. 2C, open arrowhead) and side views (Fig. 2C, closed arrowhead).

Endogenous γ-tubulin copurified with γ-tubulin-GFP from detergent insoluble P100 (Fig. 1D, central panel). TEM analyses of γ-tubulin (-GFP) samples applied to grids immediately after elution also showed fibrillar structures (Fig. 3A) exhibiting a substructure of double protofilaments (arrowhead). γ-Tubulin(-GFP) filaments aligned forming longer filament bundles (Fig. 3B) associated with aggregates (Fig. 3B, asterisk).

The characteristic clustering and bundling ability of γ-tubulin filaments observed by TEM enabled visualization by fluorescence microscopy (Figs. 3C–E). Samples of purified γ-tubulin(-GFP) in Tris buffer (pH 7.5–8.0) were applied to microscope slides and observed after incubation at room temperature for 5–20 min. Based on TEM analyses, the visualized filaments of variable thickness represented bundles of multiple (> 10) double protofilaments of γ-tubulin(-GFP). Assembly of filaments and their bundling were not affected by supplementation with 1 mM or 2 mM GTP, 1 mM MgCl₂, 10 mM CaCl₂ or by BRB80 buffer. The morphological heterogeneity of the γ-tubulin(-GFP) supramolecular forms most probably reflected the physical surface properties of the substrate and local protein concentrations. Deconvolved images showed fluorescence maxima of the γ-tubulin(-GFP) signal along filaments (Figs. 3C–D). Short, thinner filament bundles aligned to form long thick bundles (Fig. 3C, arrowhead). The filament bundles were often interwined (Fig. 3D, arrow). Bundled filaments and aggregates were also formed from γ-tubulin(-GFP) immunopurified from high molecular fractions obtained after La³⁺-PEG precipitation of cell extracts (Supplemental Fig. 2A, Fig. 3E).

Collectively, TEM analyses of purified high-molecular-mass γ-tubulin forms showed presence of short filaments and double stranded filaments exhibiting a strong tendency *in vitro* to cluster and self-assemble into long filament bundles or condense into tightly packed or amorphous aggregates. The expressed γ-tubulin-GFP *co*-polymerized with endogenous γ-tubulin and self-organized into high-order filament bundles and aggregates that could also be visualized by fluorescence microscopy.

3.3. Arabidopsis γ-tubulin forms dimers and filaments in the absence of γ-tubulin-associated proteins

Fractionation of cell extracts and detergent-insoluble P100 pellets by size exclusion chromatography and sucrose gradient centrifugation showed that GCP3, GCP4 and GCP6 co-distributed with γ-tubulin in fractions corresponding to large γ-tubulin complexes > 1 MDa. However, large molecular forms of γ-tubulin without detectable GCPs were also present (Supplemental Fig. 3).

The endogenous γ-tubulin coprecipitated with γ-tubulin-GFP from control NP-40 treated extracts (Fig. 4A, lane 2). GCP3, GCP4, α-tubulin and actin were also detected when sample loading was increased ten times compared to that used for γ-tubulin detection (Fig. 4A, lane 2). LC-MS/MS analyses of immunopurified γ-tubulin-GFP samples

confirmed coprecipitation of endogenous γ-tubulin, composed of both γ-tubulin1 and γ-tubulin2 (genes *TubG1* and *TubG2*) and presence of GCPs and associated proteins (Supplemental Table 1A). To evaluate possible effects of γ-tubulin associated proteins on γ-tubulin(-GFP) filament formation, we analyzed γ-tubulin preparations immunopurified from cell extracts under high stringency conditions. When γ-tubulin-GFP was purified in the presence of 0.3% SDS (Fig. 1D, Procedure *b*), endogenous γ-tubulin, GCPs, α-tubulin and actin were not detected in eluates (Fig. 4A, lane 3). Dissociation of co-purified proteins from γ-tubulin1-GFP in the presence of SDS was also confirmed by LC-MS/MS analyses (Supplemental Table 1B). These results indicated that assemblies of γ-tubulin(-GFP) dissociated into monomers of γ-tubulin and γ-tubulin-GFP during SDS treatment which was also confirmed by ultra-filtration using molecular weight cut-off 100 kDa or 300 kDa. Immediately after acid elution of γ-tubulin-GFP immunopurified from SDS-treated extracts, a significant portion of γ-tubulin-GFP was detected in the filtrate (Fig. 4B, lanes 7–8), while in neutralized eluates incubated for 30 min at room temperature only γ-tubulin-GFP was found in the retentate (Fig. 4B, lanes 1–2). This presumably reflects polymerization and aggregation of γ-tubulin-GFP during neutralization.

When samples of highly purified γ-tubulin-GFP were negatively stained immediately after application to grids, short linear oligomers were distinguishable from the background of purified γ-tubulin-GFP protein (Fig. 4C). As shown for endogenous γ-tubulin (Fig. 2) and for γ-tubulin(-GFP) in Fig. 3B we observed that the filaments of purified γ-tubulin-GFP protein clustered and assembled into bundles (Fig. 4D) that could be stained with anti-GFP antibody (Fig. 4E). Filament bundles of variable length and thickness as well as abundant γ-tubulin-GFP aggregates were visualized by fluorescence microscopy (Fig. 4F). These results demonstrate that γ-tubulin-GFP without any detectable associated proteins has the ability to assemble *in vitro* into linear filaments that form bundles.

We further analyzed assemblies of endogenous γ-tubulin by atomic force microscopy in the tapping mode (TM-AFM). When endogenous γ-tubulin purified with the antibody and peptide elution from P100 (Fig. 1D, Procedure *a*) was applied on mica slides, bundles of tightly aligned filaments with a double protofilament structure were imaged (Fig. 5A). Tight alignment of filaments enabled estimation of the average width of filaments due to the suppressed convolution of the tip with the sample in this geometry, compared to unaligned filaments [49]. The most frequent width of 8.5 nm measured (Fig. 5B) was consistent with the double-stranded filament width estimated from TEM analyses. Clusters composed of short linear fibrils with paired protofilament substructure (Fig. 5C and D, arrows) were also observed in preparations of γ-tubulin isolated from extracts containing 0.3% SDS (Fig. 1D, Procedure *b*). AFM imaging thus confirmed γ-tubulin forms linear bundles and aggregates composed of double-stranded fibrils.

3.4. Human and porcine γ-tubulins form oligomers

To determine whether formation of γ-tubulin oligomers/polymers is limited to plant γ-tubulins or can be also observed in other species, experiments were also performed with RFP-tagged human γ-tubulin. Functionality of γ-tubulin-RFP in cells was confirmed by phenotypic rescue experiments [21]. Detergent-insoluble fraction P100 was prepared from human osteosarcoma cell line U2OS expressing human γ-tubulin-RFP or PAK1-RFP (negative control). Extracts from P100 fractions were clarified and RFP-tagged proteins were bound to anti-RFP antibody immobilized on protein A. While endogenous γ-tubulin, GCP2 and GCP4 proteins co-purified with γ-tubulin-RFP, α-tubulin was not detected in γ-tubulin-RFP complexes (Fig. 6, Panel I-A, − SDS). When 0.08% SDS was added to extracts only γ-tubulin-RFP but not endogenous γ-tubulin, GCP2 and GCP4 were stained on Western blots (Fig. 6, Panel I-A, + SDS). RFP-tagged proteins were neither bound to the protein A carrier without antibody nor to immobilized negative control anti-myosin antibody (data not shown). Both γ-tubulin-RFP and
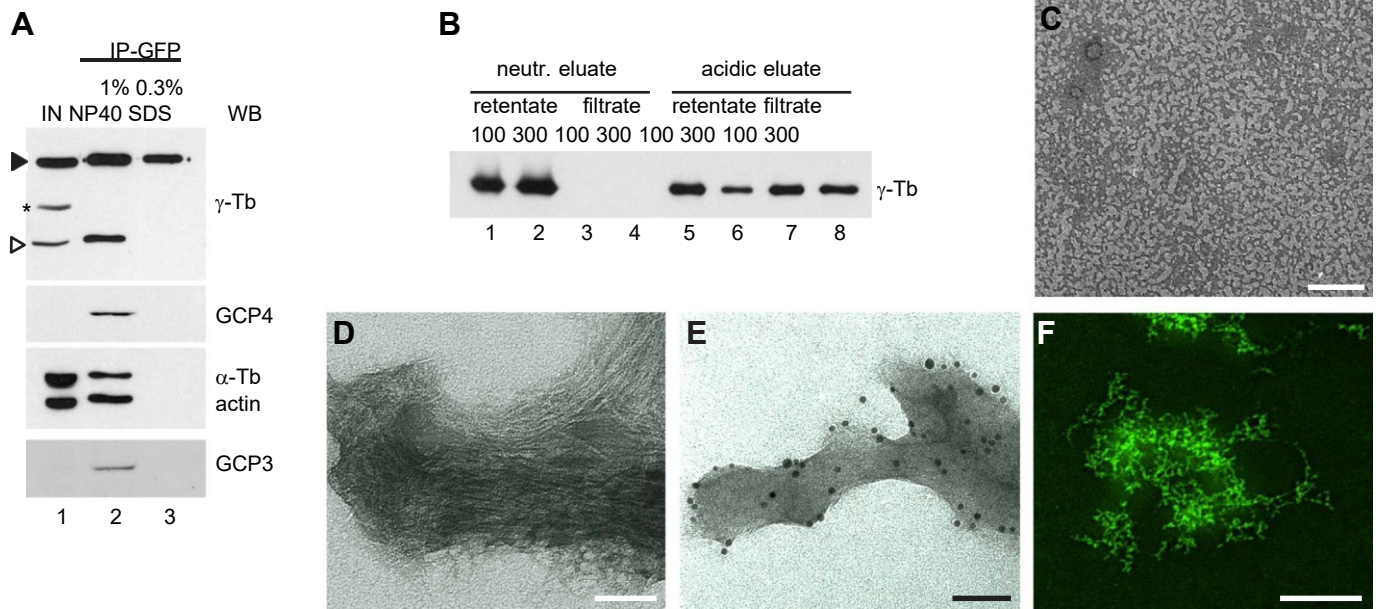
Fig. 4. Filaments assemble from monomers/dimers of *Arabidopsis* γ-tubulin-GFP free of associated proteins.
(A) Western blot analysis of γ-tubulin(-GFP) immunopurified from control 1% NP40- or 0.3% SDS-treated S25 extracts. Loadings were 1.8 μL for detection of γ-tubulin and 20 μL for detection of GCP4, actin and α-tubulin. Black arrowhead, γ-tubulin-GFP; empty arrowhead, endogenous γ-tubulin. Asterisk, an unspecific anti-γ-tubulin antibody-positive band (IN). (B) Significant amounts of γ-tubulin-GFP monomer/dimers were detected in filtrates of the acidic eluates after ultrafiltration while γ-tubulin-GFP was completely retained in retentate of the neutralized eluate. (C–E) TEM images (C) Oligomers of γ-tubulin-GFP immunopurified from SDS-treated samples. (D) Bundle of partially aligned long filaments. (E) Bundle of filaments immunogold labelled with anti-GFP antibody. (F) Network of filament bundles and clusters assembled from γ-tubulin-GFP immunopurified from SDS-treated sample visualized by fluorescence microscopy. Scale bars 50 nm (C, D, E, F).
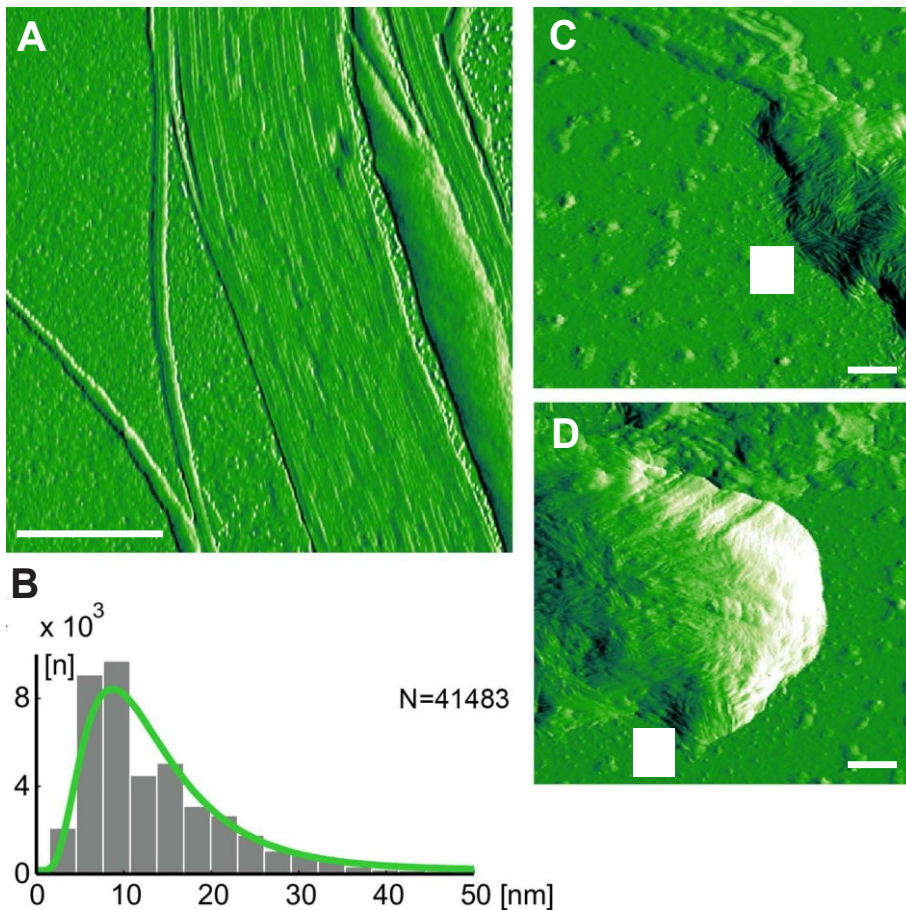
Fig. 5. AFM analyses of *Arabidopsis* high-molecular-weight γ-tubulins.
(A) AFM amplitude imaging of a filament bundle of endogenous γ-tubulin immunopurified from P100 by peptide elution. Visualization of double-protofilament substructure. (B) Histogram of distances in height maxima of adjacent protofilaments in the bundle presented in A. (C, D) Dense clusters of short filaments (arrows) in γ-tubulin-GFP immunopurified from SDS-treated samples (TM deflection image). Scale bars 300 nm.
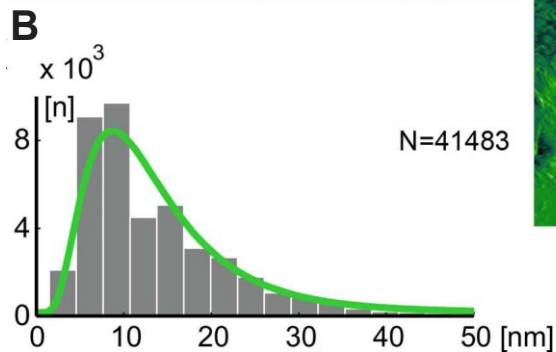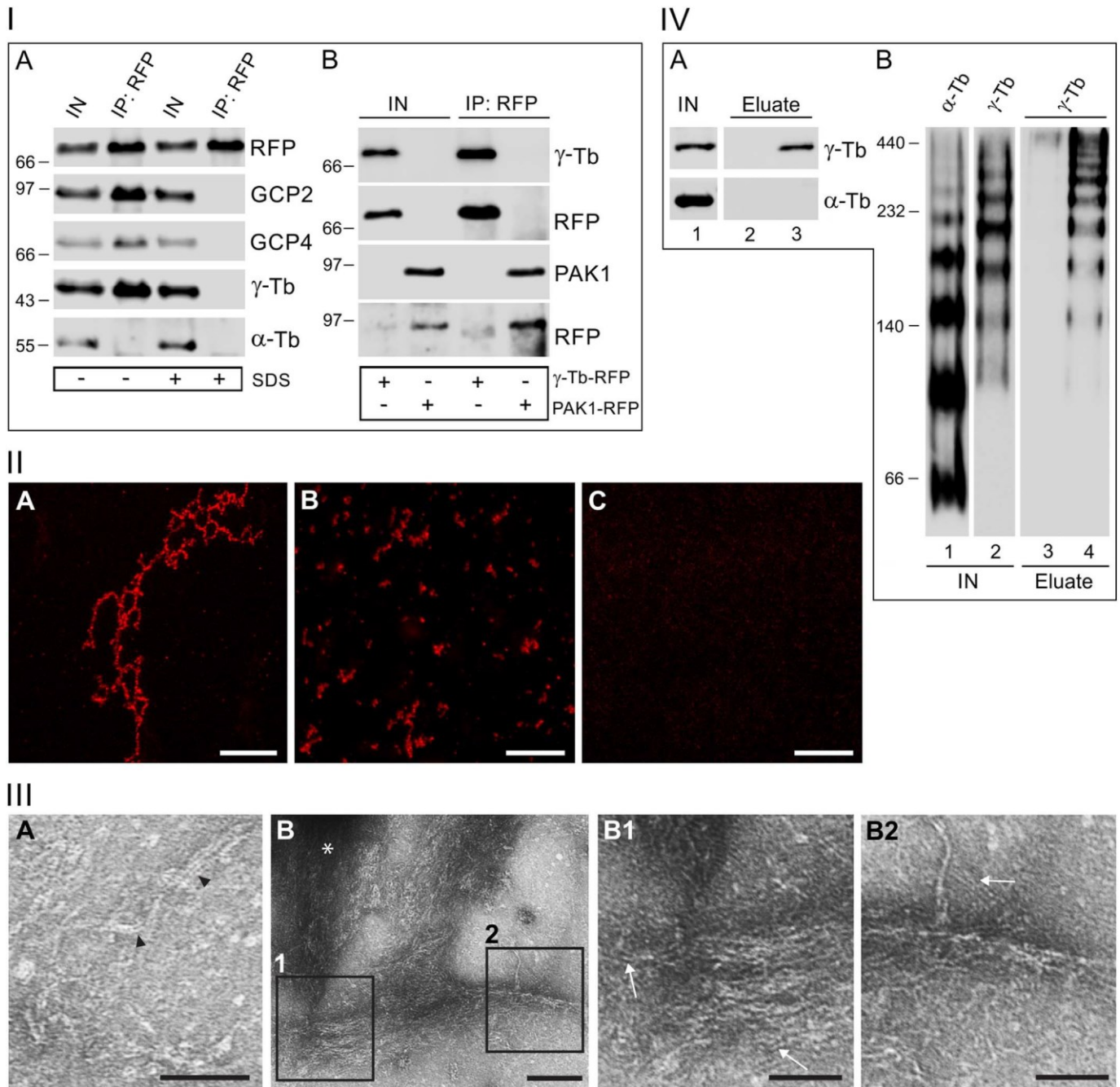
Fig. 6. Human and porcine γ-tubulins form oligomers.

Panel I. Isolation of human γ-tubulin-RFP by immunoprecipitation. (A-B) Western blot analysis of immunopurified γ-tubulin-RFP protein complexes. Detergent-resistant P100 fractions, prepared from U2OS cells expressing human γ-tubulin-RFP or PAK1-RFP (Control), were extracted in the presence or absence of 0.08% SDS (IN, Input). Extracts were precipitated with Protein A-immobilized antibody to RFP (IP: RFP). Blots were probed with antibodies to tRFP (RFP), GCP2, GCP4, γ-tubulin, α-tubulin or PAK1. (A) Immunoprecipitation of γ-tubulin-RFP protein complexes. (B) Isolation of γ-tubulin-RFP or PAK1-RFP from the immunosorbent beads using acid elution.

Panel II. Formation of filaments from human γ-tubulin-RFP. (A-C) Fluorescence microscopy of RFP-tagged proteins immunopurified from P100 extracts by acid elution in the absence or presence of SDS. (A) γ-Tubulin-RFP, -SDS. (B) γ-Tubulin-RFP, +SDS. (C) PAK1-RFP, -SDS. Scale bars 10 μm.

Panel III. TEM analyses of negatively stained purified γ-tubulin forms. γ-Tubulin-RFP was immunopurified from P100 extracts by acid elution in the presence of SDS. (A) Short γ-tubulin filaments with double filament structure (arrowheads). (B) γ-Tubulin aggregate (asterisk) composed of numerous loosely aligned and/or associated filaments. Insets 1 and 2 are shown at higher magnification in B1 and B2. Arrows point to individual γ-tubulin filaments. Scale bars 50 nm (A, B1, B2); 100 nm (B).

Panel IV. Porcine brain γ-tubulin is capable of forming oligomers. γ-Tubulin was isolated from porcine brain microtubule protein MTP-2 by means of anti-γ-tubulin peptide antibody and elution with specific peptide. (A) Western blot after SDS-PAGE of MTP-2 proteins (IN, Input; lane 1), eluate from immobilized antibody not incubated with MTP-2 (lane 2) and isolated γ-tubulin (lane 3). Blots were probed with antibodies to γ-tubulin and α-tubulin. (B) Western blot after native PAGE of MTP-2 proteins (IN, Input; lanes 1–2), eluate from immobilized antibody not incubated with MTP-2 (lane 3) and isolated γ-tubulin (lane 4). Blots were probed with antibodies to γ-tubulin and α-tubulin.

PAK1-RFP were efficiently eluted by low pH (Fig. 6, Panel I-B).

Fluorescence microscopy of γ-tubulin-RFP immunopurified from P100 extracts by acid elution in the absence of SDS revealed fibrillar structures (Fig. 6, Panel II-A). However, in the presence of SDS only short filaments were detected (Fig. 6, Panel II-B). When PAK1-RFP (negative control) was immunopurified in the same way and evaluated by fluorescence microscopy, elongated structures were absent (Fig. 6, Panel II-C). This indicated that generation of fibrillar structures was not

due to aggregation of RFP-tagged proteins.

When γ-tubulin-RFP samples immunopurified in the presence of SDS were examined by TEM, short γ-tubulin filaments with double filament structure were detected (Fig. 6, Panel III-A, arrowheads). Preparations also contained γ-tubulin aggregates (Fig. 6, Panel III-B, asterisk) composed of numerous loosely aligned filaments. Individual γ-tubulin filaments were also imaged as documented in Fig. 6, Panel III-B, B1 and B2 (arrows).

To examine whether purified γ-tubulin can form oligomers, γ-tubulin was isolated from porcine brain microtubule proteins, prepared by two cycles of polymerization depolymerization (MTP-2), using anti-γ-tubulin peptide antibody and elution with specific peptide. Although MTP-2 are composed mainly from αβ-tubulin heterodimers, these were not detected in eluted fractions containing γ-tubulin (Fig. 6, Panel IV-A, lane 3). When MTP-2 proteins were separated under non-denaturing conditions, multiple oligomers were detected with antibody to α-tubulin (Fig. 6, Panel IV-B, lane 1). Multiple resolvable bands were also detected in MTP-2 using the antibody to γ-tubulin (Fig. 6, Panel IV-B, lane 2). In contrast with the tubulin oligomer "ladder" stained with anti-α-tubulin antibody, γ-tubulin was not detected at the position corresponding to the most rapid migrating species of tubulin subunits which are primarily monomers [48]. The "ladder" of γ-tubulin oligomers was revealed in the eluate not containing αβ-tubulin heterodimers (Fig. 6, Panel IV-B, lane 4). Oligomers were also observed when γ-tubulin was immunoprecipitated from MTP-2 in the presence of low concentration of SDS that resulted in the depletion of GCPs, and then eluted with specific peptide (not shown). These data indicate that γ-tubulin alone has the ability to form oligomers under conditions of native electrophoresis.

Together, the results obtained with human γ-tubulin-RFP and porcine brain γ-tubulin support the data on intrinsic ability of γ-tubulin to oligomerize/polymerize as observed in plant cells. While in the case of purified plant γ-tubulin, long tightly bound filaments/bundles were assembled *in vitro* (Fig. 2), the filaments of human γ-tubulin formed loose bundles (Fig. 6, panel III). Whether the stronger lateral interaction of plant γ-tubulin filaments reflects specific features of *Arabidopsis* γ-tubulin or is due to higher amount of γ-tubulin in acentrosomal plant cells compared to animal cells remains to be elucidated.

3.5. γ-Tubulin is organized into fibrillar structures in Arabidopsis cells

To determine whether γ-tubulin filament bundles and clusters observed *in vitro* are present in cells, we studied the localization of γ-tubulin in *Arabidopsis* cells on a nanometer level using time-gated continuous wave (gCW-STED) and pulsed (pulse-STED) stimulated emission depletion microscopy. In the absence of centrosomes, plant γ-tubulin shows dispersed cellular localization and accumulates in a cell cycle-dependent manner in the vicinity of the nuclear envelope, with mitotic microtubular arrays and in nuclei [23,24,50]. γ-Tubulin signals in interphase cells (Fig. 7A) as well as in mitotic cells (Fig. 7B, C and D) were shown by STED as discrete elongate structures with bead-like fluorescence maxima interconnected by thinner fibrils. The bead-like maxima showed a mean diameter of 73 ± 21 nm (n = 60) when measured as full width at half maximum (FWHM) on raw data images obtained by pulse-STED with 775 nm depletion laser (Fig. 7A, inset 7A1, intensity profiles 7A2, 7A3). Distance between intensity peaks of two neighbouring fluorescence maxima in single z-stacks was 120 ± 31 nm (n = 55). Diameter of interconnecting fibrils estimated from intensity profiles across the fibrils and extracted from FWHM was 52 ± 12 nm (n = 56). γ-Tubulin fibril-like structures present with mitotic spindle (Fig. 7C, D) protruded from microtubules and interconnected microtubular bundles (Figures 7C1 and 7C2, arrowhead and arrows, respectively). On average, 42.0 ± 9.5% (n = 18) of γ-tubulin signal was associated with metaphase spindle microtubules as shown by measurement of segmented areas of γ-tubulin and α-tubulin on deconvolved single z-stacks after segmentation using auto local threshold

with Bernsen method [39]. The fibril-like assemblies showed parallel, oblique or perpendicular orientations to the plane of sectioning within the spindle, with the γ-tubulin dots representing fibrillar structures cross-sectioned in bead-like maxima (Fig. 7F). Enrichment of fibrillar γ-tubulin was observed with shortening kinetochore microtubules in polar area of anaphase spindles where 42.2 ± 4.5% (n = 19) of γ-tubulin signal was associated with microtubules, compared to the spindle midzones (35.8 ± 5.7%, n = 19) (Fig. 7D and E). γ-Tubulin frequently interlinked polar kinetochore microtubular bundles (Fig. 7D, insets 7D1, 7D2, arrows) while similar crosslinking was rarely observed in the spindle midzone.

γ-Tubulin associates with cortical microtubules and down regulation of γ-tubulin results in randomization of cortical microtubules [8]. STED analyses of the cell cortex showed elongated γ-tubulin structures partially localized with cortical microtubules (Fig. 7G, Figure 7G1, arrowhead).

γ-Tubulin accumulates on stable kinetochore stubs during recovery from drug induced microtubule depolymerization [23]. STED microscopy revealed such kinetochore stubs to contain γ-tubulin fibrillar structures with fluorescence maxima similar to that found for γ-tubulin with intact spindles (Fig. 8A, inset 8A1). The γ-tubulin fibrillar network associated with taxol stabilized microtubules was enriched in "centers of asters" (Fig. 8B, B1, B2) as shown in close-up views (Fig. 8B–B2, insets) where γ-tubulin fibrils crosslinked microtubular bundles.

Apart from its predominant localization with microtubules, γ-tubulin is also found in the cytoplasm and perinuclear area where it is enriched before nuclear envelope breakdown and is also present in the nuclear γ-tubulin pool [24]. STED analysis of interphase cells showed elongated structures of γ-tubulin (Figs. 8C, inset enlargements C1, C2 and C3). Fibrillar γ-tubulin was localized on the cytoplasmic side of the nuclear boundary and was also observed in the nuclear interior underlying inner nuclear envelope visualized by SUN protein immunodetection [51] (Supplemental Fig. 4). γ-Tubulin accumulated in the vicinity of nuclei before mitosis (Fig. 8D) and connected perinuclear microtubules with the nuclei (Figure 8D2, arrows) or interconnected microtubules (Figure 8D2, arrowhead). γ-Tubulin structures were also detected in lower amounts in the nuclei (Figure 8D2, asterisk). As described previously [52], γ-tubulin accumulates with persistent nuclear envelope in cells arrested at the G2/M interface after treatment with inhibitor of cyclin-dependent kinases roscovitine. We found that the patches of γ-tubulin accumulated with nuclei after roscovitine treatment were composed of fibrillar γ-tubulin structures (Fig. 8E).

In addition to fine fibrillar structures of γ-tubulin present in all known dispersed sites of cellular localization, we also observed sporadically in nuclei or in cytoplasm of non-dividing stationary grown cells robust γ-tubulin-positive rod-like structures. STED analyses suggested that ability of γ-tubulin to form clustered filaments may be reflected by formation of the rods (Supplemental Fig. 5A, B). Some rod-like structures were microtubular bundles heavily decorated with γ-tubulin (Supplemental Fig. 5C). Less often such rods were positive for actin (Supplemental Fig. 5D).

Together our data showed that organization of γ-tubulin in cells reflects the ability of the protein to assemble *in vitro* into filaments and filament bundles and clusters. Fine short fibril-like γ-tubulin structures with fluorescence maxima represents a basic structural form of the protein localized in cell-cycle dependent manner, with microtubules, mitotic microtubular arrays, membranes, nuclear envelope and interior of nuclei.

3.6. Sequence-structural analyses support experimental data on the filament-forming capacity of γ-tubulin

The recognition of sequence and structural features in α- and β-tubulins that are known to be important for longitudinal and lateral interaction interfaces within human γ-tubulin led to a prediction that γ-tubulin may form dimers and oligomers [53,54]. As the structure of
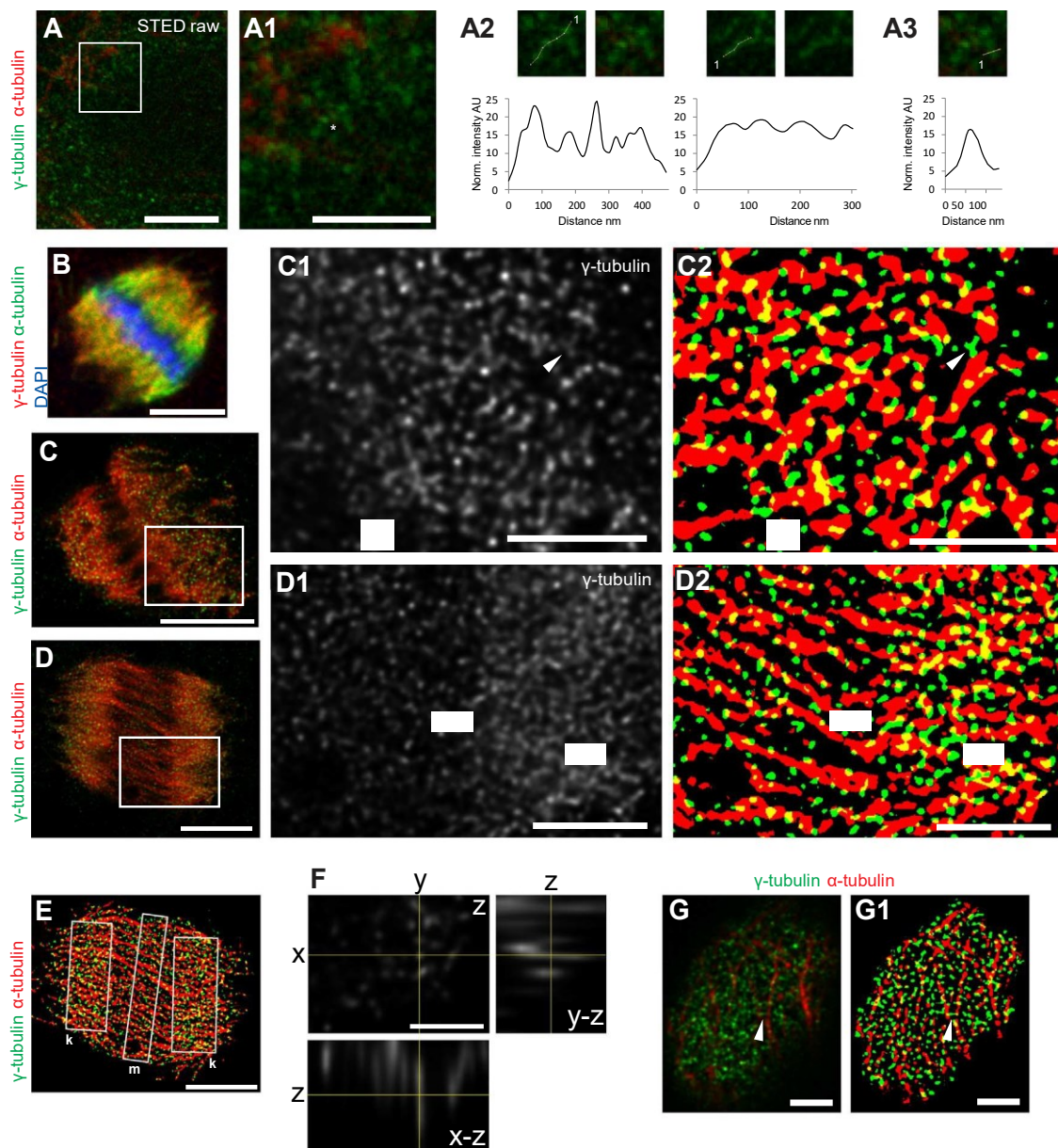
Fig. 7. STED super-resolution microscopy revealed fibrillar structures of γ-tubulin in *Arabidopsis* cells.
(A) Representative STED image of γ-tubulin (green) in interphase *Arabidopsis* cell, raw image (Abberior STAR RED for γ-tubulin, Abberior STAR 580 for α-tubulin, pulsed 775 nm depletion laser). (A1) Close-up view of inset area shows fibrillar structures with fluorescence maxima, intensity profile was measured for the structure marked by asterisk. (A2) Fluorescence intensity profiles of two representative γ-tubulin fibrillar structures. (A3) Normalized intensity signal measured across the fibrillar part interlinking fluorescence maxima. Normalized intensity signal was measured in the regions highlighted by the yellow lines from 1. (B) CLSM section of mitotic *Arabidopsis* cell shows punctate signal for γ-tubulin (red) associated with the metaphase spindle (green). (C) Representative STED image of γ-tubulin (green) with metaphase spindle (red), deconvolved using Huygens Professional version 16.05 (Scientific Volume Imaging, The Netherlands, http://svi.nl). (C1) Close-up view of γ-tubulin elongate fibrillar structures with bead-like maxima in inset area. (C2) γ-Tubulin and α-tubulin after segmentation using Bernsen method. γ-Tubulin protruding from the microtubules (arrowhead) or connecting the microtubules (arrow). (D, E) STED deconvolved image of γ-tubulin (green) localized with anaphase spindle (red). (D1 and D2) Close-up views of inset visualizing γ-tubulin (D1) and γ-tubulin and α-tubulin after segmentation (D2). γ-Tubulin fibrillar assemblies crosslinking kinetochore microtubular bundles in polar region of anaphase spindle (D2 arrows). (E) γ-Tubulin and α-tubulin after segmentation, polar area with shortening kinetochore microtubules (k) and spindle midzone (m). (F) STED close-up view of elongate structure cross-sectioned in bead-like maximum. The dots visible in the z-stack represent elongate filaments. Main panel *z* shows a single z-stack of the spindle; right panel *y-z* shows cross-section by *y* plane, lower panel *x-z* shows cross-section by *x* plane. (G) STED deconvolved image of cell cortex and (G1) segmentation showed fibrillar γ-tubulin structures partially localized with cortical microtubules (arrowhead). (C, D, F, G) Alexa Fluor 555 F(ab)2 for γ-tubulin, Alexa Fluor 488 F(ab)2 for α-tubulin, gCW-STED, 660 nm depletion laser. Scale bars 5 μm (B, C, E); Scale bars 2 μm (A, C1, C2, D1, D2, G, G1); Scale bars 1 μm (A1, F).

Arabidopsis γ-tubulin1 is unknown, we used homology modelling based on the X-ray crystallographic structure of human γ-tubulin1 [44]. Sequence identity of *Arabidopsis* γ-tubulin1 with human γ-tubulin1 is 74% and similarity 86% [40]. For manual adjustment of sequence alignments we used the Swiss-Model program [43] and PDB ID 3cb2A template [44] (Supplemental Fig. 6A). The models of *Arabidopsis* γ-tubulin1 achieved by program Phyre 2 and I-TASSER were generally similar to the Swiss-Model as revealed by UCSF Chimera analyses

(Supplemental Fig. 6B and 6C).

At sequence (BLAST) and structural level (DALI), *Arabidopsis* γ-tubulin1 showed like its human counterpart, highest similarity to *Arabidopsis* β-tubulins and bacterial BTubA and BTubB of *Prosthecobacter dejongeii*. We found the corresponding amino acids required for longitudinal interactions at the plus and minus end polymerization surfaces of molecule, [54] are almost identical between human and *Arabidopsis* γ-tubulins (Supplemental Fig. 7 and
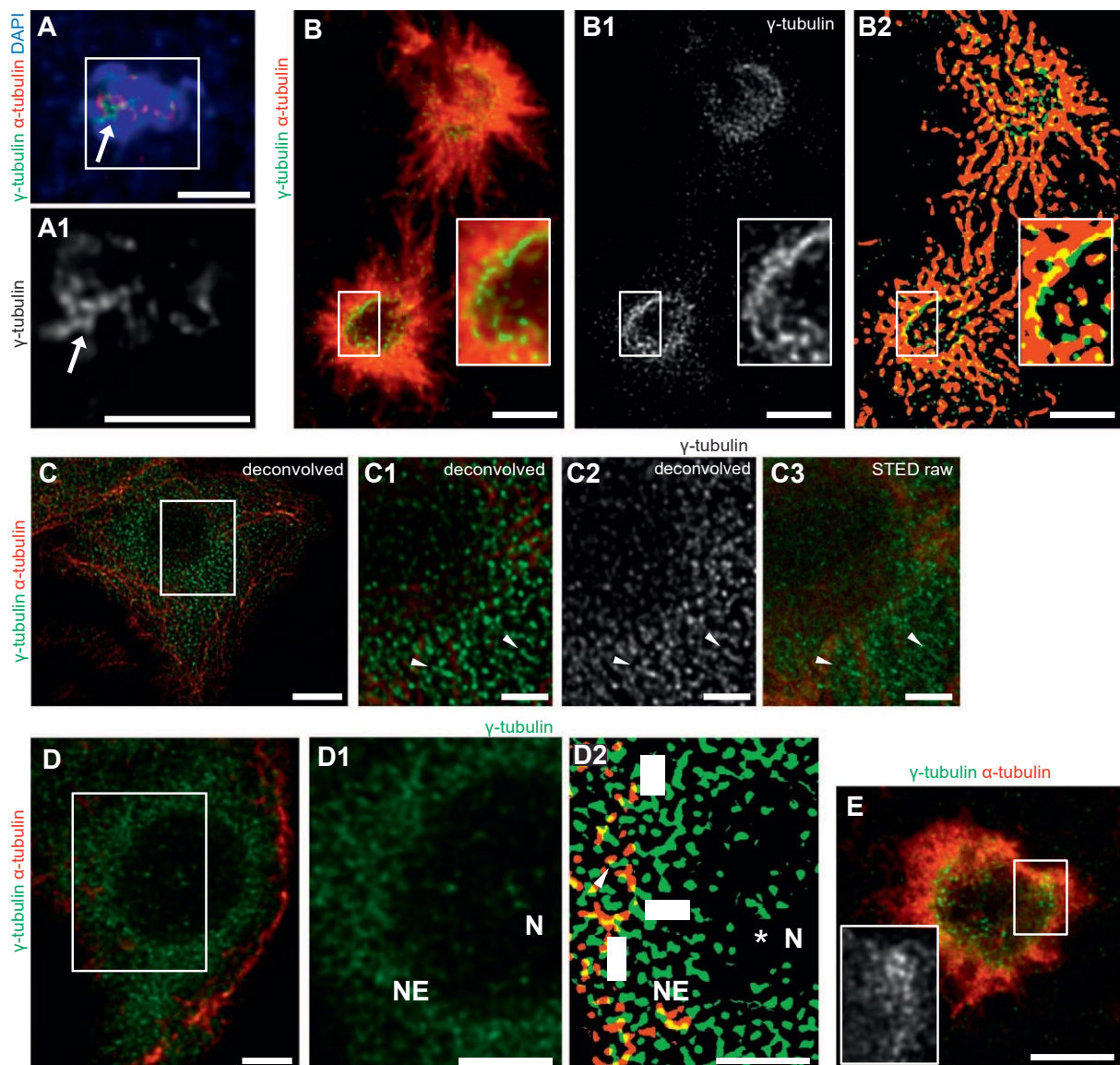
Fig. 8. γ-Tubulin fibrillar network is present in kinetochore stubs after APM treatment, with taxol induced asters as well as in perinuclear area and in nuclei of *Arabidopsis* cells. (A) Representative STED deconvolved image of the kinetochore stubs (arrow) after 30 min recovery from APM treatment, (experiment was performed three times). (Alexa Fluor 555 F(ab) 2 for γ-tubulin, Alexa Fluor 488 F(ab)2 for α-tubulin, 660 nm depletion laser). (A1) Close-up view of γ-tubulin in the inset area. (B) Representative STED deconvolved image of γ-tubulin (green) with taxol microtubular asters (α-tubulin red). Experiment was performed three times (Alexa Fluor 594 for γ-tubulin, Alexa Fluor 488 F(ab)2 for α-tubulin, 775 nm depletion laser). (B1) γ-Tubulin after deconvolution and (B2) γ-tubulin and α-tubulin after Bernsen segmentation. Close-up views of the inset area. (C) Representative STED deconvolved image of γ-tubulin (green) and microtubules (α-tubulin red) in interphase cell (Abberior STAR RED for γ-tubulin, Abberior STAR 580 for α-tubulin, 775 nm depletion laser). (C1-C3) Close-up views of the inset area. (C1,C2) STED deconvolved and (C3) STED raw images show γ-tubulin fibrillar structures (arowheads). (D) STED after deconvolution showed a network of γ-tubulin fibrillar structures accumulated in the vicinity of nuclei, γ-tubulin (green), microtubules (α-tubulin red). (D1) Close-up view of γ-tubulin in the inset area and (D2) γ-tubulin and α-tubulin after segmentation. γ-Tubulin accumulated at the nuclear envelope boundary (arrows); elongate structures were present in nuclei (asterisk). γ-Tubulin signal on perinuclear microtubules connecting the microtubules (arrowheads). N = nuclei, NE = nuclear envelope. (E) Representative STED deconvolved image of roscovitine and taxol treated cell, γ-tubulin (green), microtubules (α-tubulin red). Experiment was performed three times. Close-up view of the inset area shows cluster of γ-tubulin fibrillar structures accumulated at nuclear periphery. (D, E) Alexa Fluor 555 F(ab)2 for γ-tubulin, Alexa Fluor 488 F(ab)2 for α-tubulin, 660 nm depletion laser. Scale bars 3 μm (B, B1, B2, C); Scale bars 2 μm (A, A1, D, D1, D2, E); Scale bars 1 μm (C1, C2, C3).

Supplemental Fig. 8). Changes at the plus end surface motif HWY of αβ-tubulins were conserved for human and *Arabidopsis* γ-tubulins (Supplemental Fig. 8) suggesting changed geometry and/or curvature of the γ-tubulin protofilaments in comparison to αβ-protofilaments [54]. The interfaces H3 and ML responsible for lateral interactions are also similar, showing only 13 and 21% significant amino acid changes at the sequence level, respectively, between *Arabidopsis* and human γ-tubulin1 (Supplemental Fig. 8). However, there are some slight differences that may contribute to altered lateral interactions. The presence of His in *Arabidopsis* γ-tubulin1 in helix H3 (Supplemental Fig. 7, arrowhead, Supplemental Fig. 8,) suggests a preserved structural bulge in

Arabidopsis γ-tubulin1 which is similarly present in α- and β-tubulins but not in human γ-tubulin1 [55]. *Arabidopsis* γ-tubulin1 differs most from its human counterpart in the H9-S8 loop in helices H11 and H12 where insertion of variable length is found for different γ-tubulins [54]. While the C-terminus of the molecule is conserved for *Arabidopsis* and human γ-tubulin, there is a 20-amino acid C-terminal overhang in *Arabidopsis* γ-tubulin unique for plants (Supplemental Fig. 8). I-TASSER model of *Arabidopsis* γ-tubulin which also includes C-terminus showed a short β-strand (Chimera analysis).

We further found that residues at the plus and minus end surfaces involved in GTP binding and hydrolysis [54,55] are also conserved

between *Arabidopsis* γ-tubulin1 and human γ-tubulin1 including Gly in helix H8 instead of catalytic Glu or Asp present in α-tubulin or FtsZ, respectively (Supplemental Fig. 8). Since an acidic residue is required for GTP hydrolysis [54,56], we assume that *Arabidopsis* γ-tubulin1, like its human counterpart, does not have the ability to hydrolyze GTP [54]. In agreement, we did not observe enhanced assembly of γ-tubulin filaments under conditions favorable for polymerization of microtubules in the presence of GTP.

In conclusion, structural homology modelling and well-conserved sequences of α- and β-tubulin involved in longitudinal and lateral interactions with *Arabidopsis* and human γ-tubulin molecules provide further support to our experimental data on the ability of γ-tubulin to form dimers and assemble into filaments. Differences found on structural and sequence level between human and *Arabidopsis* γ-tubulin mainly at the C-terminal suggest specific protein interactions and also perhaps differences in protofilament bundling capacity [57].

4. Discussion

4.1. γ-Tubulin ability to oligomerize/polymerize in vitro

γ-Tubulin, originally defined as a microtubule nucleator has emerged as a multifunctional protein [58]. Characterization of heterogeneous high molecular forms of γ-tubulin is key for understanding the protein's versatile cellular functions. Studies in this direction have been hampered by difficulties in obtaining adequate amounts of native endogenous γ-tubulin. Recombinant eukaryotic tubulins, including γ-tubulin, are not fully functional due to their requirement for chaperone-assisted folding [59,60]. The higher abundance of γ-tubulin in acentrosomal plant cells compared to animal cells enabled us to uncover kinetochore and nuclear γ-tubulin [23,24]. We have also reported previously on heterogeneity of membrane-bound and cytoplasmic large γ-tubulin complexes in *Arabidopsis* [15]. This study provides evidence that the main source of heterogeneity in the abundant large molecular γ-tubulin forms lies in γ-tubulin ability to form oligomers/polymers.

Based on our TEM and AFM studies on isolated γ-tubulins from *Arabidopsis* we suggest that γ-tubulin forms filaments that the most commonly appear as double protofilaments that tend to cluster, lengthen and align by lateral contacts. This enables their assembly *in vitro* into long filament bundles and aggregates that can be detected by fluorescence microscopy. The same holds true for isolated γ-tubulin from human osteosarcoma cells. Oligomerization ability was also demonstrated for γ-tubulin isolated from microtubular fraction of porcine brain. The filaments formed from γ-tubulin resemble protofilaments formed by bacterial tubulins BTubA and BTubB, including straight double protofilaments that exhibit an irregular twist and form bundles [61]. Accordingly, we found highest similarity of *Arabidopsis* and human γ-tubulin with β-tubulins and *P. dejongeii* bacterial BTubA and BTubB both on sequence and structural levels. The observed plant and mammalian γ-tubulin filaments were structurally distinct from filaments with 13-fold symmetry assembled *in vitro* from the reconstituted small hetero-complexes of γ-tubulin with GCPs γTuSC of *Saccharomyces cerevisiae* [5] and also differed from γ-tubules made of γ-TuRC and pericentrin in mammalian cells [6]. We also found that GCPs were not necessary for neither plant nor mammalian γ-tubulin oligomerization. Moreover, pericentrin is not present in plant genomes. Thus, the ability to form fibrillar assemblies *in vitro* is apparently an intrinsic property of the γ-tubulin molecule. Our experimental data on the ability of γ-tubulin to form short filaments preferentially with double protofilament substructure are consistent with a comparative structural analysis of human γ-tubulin with α- and β-tubulins, that suggested dimer formation and polymerization of γ-tubulin [54]. Human and *Arabidopsis* γ-tubulins are on sequence and structural levels conserved, including structural features required for longitudinal and lateral interactions of α- and β-tubulins as well as conserved residues involved in GTP binding that differ from those found in GTP hydrolyzing prokaryotic tubulins

and α- and β-tubulins.

Our data show that *Arabidopsis* γ-tubulin preserves some characteristics of both eukaryotic and prokaryotic tubulins. Only properly folded endogenous plant and animal γ-tubulin form dimers while *in vitro* translated or baculovirus expressed γ-tubulins are monomeric [this study, 55,60,62]. Also the presence of CCT binding site and co-purification of CCT chaperones with *Arabidopsis* γ-tubulin suggest chaperone-assisted folding as shown for the human counterpart [12,59]. In contrary to requirements for chaperone-dependent folding of eukaryotic tubulins, we found that γ-tubulin tolerated a wide range of conditions for polymerization *in vitro*, characteristic for prokaryotic tubulins [61]. Similarly, the assembly of double stranded filaments with bundling capacity observed here for γ-tubulin, often occurs with prokaryotic tubulins where it offers a higher stability compared to single filaments. Assembly of paired filaments also minimizes requirements for supply of building subunits and energy compared to the more complex formation of eukaryotic microtubules [63].

4.2. γ-Tubulin assemblies in Arabidopsis cells

The tendency of short γ-tubulin filaments to form bundles *in vitro* may be employed in the formation of higher-order assemblies in cells. Indeed, our STED analyses showed on a nano-level that γ-tubulin signals with dispersed punctate pattern consist of elongate structures with bead-like fluorescence maxima. The fact that similar fluorescence maxima were observed with bundled γ-tubulin filaments *in vitro* suggests that the same filament building principles are applied in assembly of γ-tubulin supramolecular structures *in vitro* and in cells. γ-Tubulin may constitute a dynamic three dimensional arrangement consisting of more or less tightly packed laterally associated filaments. Similarly, short filaments of bacterial tubulin FtsZ are suggested to compose fluorescence maxima/clusters revealed in the division ring by super-resolution microscopy [64]. Notably, the concentration of FtsZ (5 μM) required for filament bundle formation [65] is comparable to what we assessed for assembly of γ-tubulin bundles *in vitro*. Our STED analyses suggest that a higher local concentration of γ-tubulin on microtubules or with nuclei promotes a shift from single filaments into bundles and higher-order assemblies like observed *in vitro*. A spatial-temporal regulation of γ-tubulin filament assembly through signaling proteins is expected. For example, mitotic CDK or Aurora 1 kinase/TPX2 has been localized at sites of cell cycle-specific accumulations of γ-tubulin at polar region of spindle or with nuclear envelope before mitosis [66].

While fine filaments of γ-tubulin were shown by super-resolution microscopy at all sites of dispersed cellular localization of γ-tubulin, the robust γ-tubulin-positive rod-like fibrils were observed sporadically in nuclei or in cytoplasm mostly in non-dividing cells of *Arabidopsis*. Some rods were shown by STED as microtubular bundles decorated with γ-tubulin most likely in form of clustered filament. High affinity of overproduced γ-tubulin with microtubules was previously shown [67]. Robust fibrillar structures of γ-tubulin, GCPs and pericentrin called γ-tubules were observed more frequently in non-dividing mammalian cells and often intertwined with microtubules [6]. However, the authors also showed interaction of γ-tubules with vimetin and actin microfilaments. Sporadic actin signal was also detected with some γ-tubulin rods by us. Linear inclusions positive for γ-tubulin and actin in nuclei and in perinuclear areas of mature neurons were suggested to serve as a supply of centrosomal material [68].

4.3. Is a capability to form filaments and higher order assemblies behind γ-tubulin multiple cellular functions?

The cellular fractions of *Arabidopsis* with large molecular forms of γ-tubulin reduced the critical level of α,β-tubulin dimers required for microtubule nucleation [15]. Our biochemical data suggested that only a subset of large molecular forms of γ-tubulin is represented by complexes with GCPs but whether and how γ-tubulin complexes containing

GCPs and γ-tubulin fibrillar structures free of GCPs interplay in the cell, remains to be addressed. Packing of γ-tubulin with GCPs into γ-TuRCs in which γ-tubulins interact laterally, provides the most efficient template for microtubule nucleation [69]. However, longitudinal interactions of γ-tubulin were proposed in a protofilament model where α,β-tubulin dimers are added laterally to the γ-tubulin protofilament template [70]. It is therefore tempting to speculate whether the short γ-tubulin filaments shown in this study could also function as seeds for microtubule nucleation as shown *in vitro* for double protofilaments of α,β-tubulin [71]. Moreover, γ-tubulin monomers were also shown to act as seeds for α,β-tubulin protofilament nucleation [62]. γ-Tubulin fibrillar assemblies were observed by us at kinetochore microtubular stubs during microtubule regrowth which is in accordance with nucleation function suggested for γ-tubulin that resides together with γ-TuRCs components, augmins in cell cycle dependent manner on plant spindle microtubules [72]. However, a function of the γ-tubulin in crosslinking of kinetochore microtubular bundles of acentrosomal spindles as suggested by our STED analyses should also be considered.

Ancient functions of filament-forming prokaryotic tubulins with DNA or membranes are partially preserved for eukaryotic tubulins [73] and most likely also for γ-tubulin. γ-Tubulin has been detected in the kinetochore region of chromosomes in both plant and animal cells [23,74]. A cytomotile function of filament forming γ-tubulin with DNA is speculative, as only GTP-binding but not GTPase activity has been demonstrated for γ-tubulins [55,75,76] which is consistent with sequence/structural analyses of human and *Arabidopsis* γ-tubulin [54; our data]. It is more likely that γ-tubulin assemblies have scaffolding or sequestration functions for signaling components or provide structural support for interacting proteins in complexes. A complex scaffolding function in cell division was suggested for filaments and clusters of FtsZ [77].

Fibrils of γ-tubulin were present with the outer nuclear envelope (NE) where a nucleation function is expected. However, we also observed intranuclear γ-tubulin fibrils. Filaments of 10 nm were previously shown by SEM to underly inner NE in tobacco cells with the term plamina (plant lamina) introduced [78]. Whether γ-tubulin can interconnect inner NE with chromatin is however a matter of speculation. Interactions with repair, transcription or chromatin remodelling complexes described for γ-tubulins (see Introduction) suggest a scaffolding or sequestration function either alone or in cooperation with other yet purely defined members of plant lamina. The meshwork of γ-tubulin interacts with lamin B3 in animal cells [18] and a function in organization of nuclei was also suggested. However, lamins are not present in plants.

The presence of larger molecular assemblies of γ-tubulin with brain microtubules was indicated previously [13,14] and similar large γ-tubulin forms were demonstrated in plants [15]. Here we provide evidence that both plant and animal γ-tubulins have the ability to oligomerize and to form filaments and we also clearly demonstrated oligomerization of isolated brain γ-tubulin. γ-Tubulin is a ubiquitous component of aggresomes and inclusion bodies in neurodegenerative diseases where it is detected together with other fibrillar proteins [31]. Further studies are necessary to elucidate whether the ability to oligomerize demonstrated here for γ-tubulin associated with brain microtubules is involved in aggresome generation and functions.

Overall, our results demonstrate the ability of γ-tubulins to form oligomers and filaments in plant and animal cells *in vitro*. γ-Tubulin fibrillar structures were demonstrated by STED microscopy at sites of local γ-tubulin enrichment with microtubules, with membranes and in nuclei of *Arabidopsis* cells. We suggest that a dual role may exist for oligomers/polymers forming γ-tubulin in microtubule nucleation and organization and in performing scaffolding or sequestration functions in analogy to prokaryotic bundling tubulin filaments.

Transparency document

The Transparency document associated with this article can be found, in online version.

Appendix A. Supplementary data

Supplementary data to this article can be found online at https://doi.org/10.1016/j.bbamcr.2018.02.009.

References

[1] M. Pilhofer, M.S. Ladinsky, A.W. McDowall, G. Petroni, G.J. Jensen, Microtubules in bacteria: ancient tubulins build a five-protofilament homolog of the eukaryotic cytoskeleton, PLoS Biol. 9 (2011) e1001213.
[2] C.E. Oakley, B.R. Oakley, Identification of gamma-tubulin, a new member of the tubulin superfamily encoded by mipA gene of *Aspergillus nidulans*, Nature 338 (1989) 662–664.
[3] B.R. Oakley, C.E. Oakley, Y. Yoon, M.K. Jung, Gamma-tubulin is a component of the spindle pole body that is essential for microtubule function in *Aspergillus nidulans*, Cell 61 (1990) 1289–1301.
[4] V. Sulimenko, Z. Hajkova, A. Klebanovych, P. Draber, Regulation of microtubule nucleation mediated by gamma-tubulin complexes, Protoplasma 254 (2017) 1187–1199.
[5] J.M. Kollman, J.K. Polka, A. Zelter, T.N. Davis, D.A. Agard, Microtubule nucleating gamma-TuSC assembles structures with 13-fold microtubule-like symmetry, Nature 466 (2010) 879–882.
[6] L. Lindström, M. Alvarado-Kristensson, Characterization of gamma-tubulin filaments in mammalian cells, Biochim. Biophys. Acta Mol. Cell Res. 1865 (2018) 158–171.
[7] T.C. Lin, A. Neuner, E. Schiebel, Targeting of gamma-tubulin complexes to microtubule organizing centers: conservation and divergence, Trends Cell Biol. 25 (2015) 296–307.
[8] P. Binarova, V. Cenklova, J. Prochazkova, A. Doskocilova, J. Volc, M. Vrlik, L. Bogre, Gamma-tubulin is essential for acentrosomal microtubule nucleation and coordination of late mitotic events in Arabidopsis, Plant Cell 18 (2006) 1199–1212.
[9] M. Pastuglia, J. Azimzadeh, M. Goussot, C. Camilleri, K. Belcram, J.L. Evrard, A.C. Schmit, P. Guerche, D. Bouchez, Gamma-tubulin is essential for microtubule organization and development in Arabidopsis, Plant Cell 18 (2006) 1412–1425.
[10] M. Nakamura, N. Yagi, T. Kato, S. Fujita, N. Kawashima, D.W. Ehrhardt, T. Hashimoto, Arabidopsis GCP3-interacting protein 1/MOZART 1 is an integral component of the gamma-tubulin-containing microtubule nucleating complex, Plant J. 71 (2012) 216–225.
[11] Z. Kong, T. Hotta, Y.R. Lee, T. Horio, B. Liu, The {gamma}-tubulin complex protein GCP4 is required for organizing functional microtubule arrays in *Arabidopsis thaliana*, Plant Cell 22 (2010) 191–204.
[12] M. Moudjou, N. Bordes, M. Paintrand, M. Bornens, Gamma-tubulin in mammalian cells: the centrosomal and the cytosolic forms, J. Cell Sci. 109 (1996) 875–887.
[13] C. Detraves, H. Mazarguil, I. Lajoie-Mazenc, M. Julian, B. Raynaud-Messina, M. Wright, Protein complexes containing gamma-tubulin are present in mammalian brain microtubule protein preparations, Cell Motil. Cytoskeleton 36 (1997) 179–189.
[14] V. Sulimenko, T. Sulimenko, S. Poznanovic, V. Nechiporuk-Zloy, K.J. Bohm, L. Macurek, E. Unger, P. Draber, Association of brain gamma-tubulins with alpha beta-tubulin dimers, Biochem. J. 365 (2002) 889–895.
[15] D. Drykova, V. Cenklova, V. Sulimenko, J. Volc, P. Draber, P. Binarova, Plant gamma-tubulin interacts with alphabeta-tubulin dimers and forms membrane-associated complexes, Plant Cell 15 (2003) 465–480.
[16] T. Hubert, S. Perdu, J. Vandekerckhove, J. Gettemans, Gamma-tubulin localizes at actin-based membrane protrusions and inhibits formation of stress-fibers, Biochem. Biophys. Res. Commun. 408 (2011) 248–252.
[17] V.T. Marchesi, N. Ngo, In vitro assembly of multiprotein complexes containing alpha, beta, and gamma tubulin, heat shock protein HSP70, and elongation factor 1 alpha, Proc. Natl. Acad. Sci. U. S. A. 90 (1993) 3028–3032.

[18] C.A. Rossello, L. Lindstrom, J. Glindre, G. Eklund, M. Alvarado-Kristensson, Gamma-tubulin coordinates nuclear envelope assembly around chromatin, Heliyon 2 (2016) e00166.

[19] L. Macurek, E. Draberova, V. Richterova, V. Sulimenko, T. Sulimenko, L. Draberova, V. Markova, P. Draber, Regulation of microtubule nucleation from membranes by complexes of membrane-bound gamma-tubulin with Fyn kinase and phosphoino-sitide 3-kinase, Biochem. J. 416 (2008) 421–430.

[20] R.M. Rios, A. Sanchis, A.M. Tassin, C. Fedriani, M. Bornens, GMAP-210 recruits gamma-tubulin complexes to cis-Golgi membranes and is required for Golgi ribbon formation, Cell 118 (2004) 323–335.

[21] S. Vinopal, M. Cernohorska, V. Sulimenko, T. Sulimenko, V. Vosecka, M. Flemr, E. Draberova, P. Draber, Gamma-tubulin 2 nucleates microtubules and is down-regulated in mouse early embryogenesis, PLoS One 7 (2012) e29919.

[22] E. Draberova, V. Sulimenko, S. Vinopal, T. Sulimenko, V. Sladkova, L. D'Agostino, M. Sobol, P. Hozak, L. Kren, C.D. Katsetos, P. Draber, Differential expression of human gamma-tubulin isotypes during neuronal development and oxidative stress points to a gamma-tubulin-2 prosurvival function, FASEB J. 31 (2017) 1828–1846.

[23] P. Binarova, B. Hause, J. Dolezel, P. Draber, Association of gamma-tubulin with kinetochore/centromeric region of plant chromosomes, Plant J. 14 (1998) 751–757.

[24] P. Binarova, V. Cenklova, B. Hause, E. Kubatova, M. Lysak, J. Dolezel, L. Bogre, P. Draber, Nuclear gamma-tubulin during acentriolar plant mitosis, Plant Cell 12 (2000) 433–442.

[25] C. Lesca, M. Germanier, B. Raynaud-Messina, C. Pichereaux, C. Etievant, S. Emond, O. Burlet-Schiltz, B. Monsarrat, M. Wright, M. Defais, DNA damage induce gamma-tubulin-RAD51 nuclear complexes in mammalian cells, Oncogene 24 (2005) 5165–5172.

[26] S. Sankaran, D.E. Crone, R.E. Palazzo, J.D. Parvin, BRCA1 regulates gamma-tubulin binding to centrosomes, Cancer Biol. Ther. 6 (2007) 1853–1857.

[27] B. Horejsi, S. Vinopal, V. Sladkova, E. Draberova, V. Sulimenko, T. Sulimenko, V. Vosecka, A. Philimonenko, P. Hozak, C.D. Katsetos, P. Draber, Nuclear gamma-tubulin associates with nucleoli and interacts with tumor suppressor protein C53, J. Cell. Physiol. 227 (2012) 367–382.

[28] G. Hoog, R. Zarrizi, K. von Stedingk, K. Jonsson, M. Alvarado-Kristensson, Nuclear localization of gamma-tubulin affects E2F transcriptional activity and S-phase progression, FASEB J. 25 (2011) 3815–3827.

[29] N.L. Prigozhina, C.E. Oakley, A.M. Lewis, T. Nayak, S.A. Osmani, B.R. Oakley, Gamma-tubulin plays an essential role in the coordination of mitotic events, Mol. Biol. Cell 15 (2004) 1374–1386.

[30] L. Kohoutova, H. Kourova, S.K. Nagy, J. Volc, P. Halada, T. Meszaros, I. Meskiene, L. Bogre, P. Binarova, The Arabidopsis mitogen-activated protein kinase 6 is asso-ciated with gamma-tubulin on microtubules, phosphorylates EB1c and maintains spindle orientation under nitrosative stress, New Phytol. 207 (2015) 1061–1074.

[31] Y. Chiba, S. Takei, N. Kawamura, Y. Kawaguchi, K. Sasaki, S. Hasegawa-Ishii, A. Furukawa, M. Hosokawa, A. Shimada, Immunohistochemical localization of aggresomal proteins in glial cytoplasmic inclusions in multiple system atrophy, Neuropathol. Appl. Neurobiol. 38 (2012) 559–571.

[32] M.J. May, C.J. Leaver, Oxidative stimulation of glutathione synthesis in Arabidopsis thaliana suspension cultures, Plant Physiol. 103 (1993) 621–627.

[33] A.L. Contento, S.J. Kim, D.C. Bassham, Transcriptome profiling of the response of Arabidopsis suspension culture cells to Suc starvation, Plant Physiol. 135 (2004) 2330–2347.

[34] M. Karimi, D. Inze, A. Depicker, GATEWAY vectors for Agrobacterium-mediated plant transformation, Trends Plant Sci. 7 (2002) 193–195.

[35] M. Cernohorska, V. Sulimenko, Z. Hajkova, T. Sulimenko, V. Sladkova, S. Vinopal, E. Draberova, P. Draber, GIT1/betaPIX signaling proteins and PAK1 kinase regulate microtubule nucleation, Biochim. Biophys. Acta 1863 (2016) 1282–1297.

[36] M.L. Shelanski, F. Gaskin, C.R. Cantor, Microtubule assembly in the absence of added nucleotides, Proc. Natl. Acad. Sci. U. S. A. 70 (1973) 765–768.

[37] M. Novakova, E. Draberova, W. Schurmann, G. Czihak, V. Viklicky, P. Dr-aber, Gamma-tubulin redistribution in taxol-treated mitotic cells probed by monoclonal antibodies, Cell Motil. Cytoskeleton 33 (1996) 38–51.

[38] P. Halada, P. Man, D. Grebenova, Z. Hrkal, V. Havlicek, Identification of HL60 proteins affected by 5-Aminolevulinic acid-based photodynamic therapy using mass spectrometric approach, Collect. Czechoslov. Chem. Commun. 66 (2001) 1720–1728.

[39] J. Bernsen, Dynamic Thresholding of Gray Level Images, Proceedings of the 8th International Conference on Pattern Recognition, Paris, France, (1986), pp. 1251–1255.

[40] S.F. Altschul, W. Gish, W. Miller, E.W. Myers, D.J. Lipman, Basic local alignment search tool, J. Mol. Biol. 215 (1990) 403–410.

[41] H. McWilliam, W. Li, M. Uludag, S. Squizzato, Y.M. Park, N. Buso, A.P. Cowley, R. Lopez, Analysis tool web services from the EMBL-EBI, Nucleic Acids Res. 41 (2013) W597–600.

[42] L. Holm, P. Rosenstrom, Dali server: conservation mapping in 3D, Nucleic Acids Res. 38 (2010) W545–549.

[43] M. Biasini, S. Bienert, A. Waterhouse, K. Arnold, G. Studer, T. Schmidt, F. Kiefer, T.G. Cassarino, M. Bertoni, L. Bordoli, T. Schwede, SWISS-MODEL: modelling protein tertiary and quaternary structure using evolutionary information, Nucleic Acids Res. 42 (2014) W252–258.

[44] L.M. Rice, E.A. Montabana, D.A. Agard, The lattice as allosteric effector: structural studies of alphabeta- and gamma-tubulin clarify the role of GTP in microtubule assembly, Proc. Natl. Acad. Sci. U. S. A. 105 (2008) 5378–5383.

[45] L.A. Kelley, S. Mezulis, C.M. Yates, M.N. Wass, M.J. Sternberg, The Phyre2 web portal for protein modeling, prediction, and analysis, Nat. Protoc. 10 (2015) 845–858.

[46]

[47] J. Yang, R. Yan, A. Roy, D. Xu, J. Poisson, Y. Zhang, The I-TASSER suite: protein structure and function prediction, Nat. Methods 12 (2015) 7–8.

[47] E.F. Pettersen, T.D. Goddard, C.C. Huang, G.S. Couch, D.M. Greenblatt, E.C. Meng, T.E. Ferrin, UCSF chimera–a visualization system for exploratory research and analysis, J. Comput. Chem. 25 (2004) 1605–1612.

[48] J.J. Correia, R.C. Williams Jr., Characterization of oligomers of tubulin by two-dimensional native electrophoresis, Arch. Biochem. Biophys. 239 (1985) 120–129.

[49] E. Ukraintsev, A. Kromka, H. Kozak, Z. Remeš, B. Rezek, Artifacts in atomic force microscopy of biological samples, in: C.L. Frewin (Ed.), Atomic Force Microscopy Investigations Into Biology - From Cell to Protein, InTech, New York, 2012, pp.29–54.

[50] B. Liu, J. Marc, H.C. Joshi, B.A. Palevitz, A gamma-tubulin-related protein asso-ciated with the microtubule arrays of higher plants in a cell cycle-dependent manner, J. Cell Sci. 104 (1993) 1217–1228.

[51] K. Graumann, J. Runions, D.E. Evans, Characterization of SUN-domain proteins at the higher plant nuclear envelope, Plant J. 61 (2010) 134–144.

[52] P. Binarova, J. Dolezel, P. Draber, E. Heberle-Bors, M. Strnad, L. Bogre, Treatment of Vicia Faba root tip cells with specific inhibitors to cyclin-dependent kinases leads to abnormal spindle formation, Plant J. 16 (1998) 697–707.

[53] E. Nogales, M. Whittaker, R.A. Milligan, K.H. Downing, High-resolution model of the microtubule, Cell 96 (1999) 79–88.

[54] Y.F. Inclan, E. Nogales, Structural models for the self-assembly and microtubule interactions of gamma-, delta- and epsilon-tubulin, J. Cell Sci. 114 (2001) 413–422.

[55] H. Aldaz, L.M. Rice, T. Stearns, D.A. Agard, Insights into microtubule nucleation from the crystal structure of human gamma-tubulin, Nature 435 (2005) 523–527.

[56] K. Dai, A.A. Mukherjee, Y. Xu, J. Lutkenhaus, Mutations in ftsZ that confer resistance to SulA affect the interaction of FtsZ with GTP, J. Bacteriol. 176 (1994) 130–136.

[57] K. Sundararajan, E.D. Goley, The intrinsically disordered C-terminal linker of FtsZ regulates protofilament dynamics and superstructure in vitro, J. Biol. Chem. 292 (2017) 20509–20527.

[58] B.R. Oakley, V. Paolillo, Y. Zheng, Gamma-tubulin complexes in microtubule nu-cleation and beyond, Mol. Biol. Cell 26 (2015) 2957–2962.

[59] R. Melki, I.E. Vainberg, R.L. Chow, N.J. Cowan, Chaperonin-mediated folding of vertebrate actin-related protein and gamma-tubulin, J. Cell Biol. 122 (1993) 1301–1310.

[60] A. Vassilev, M. Kimble, C.D. Silflow, M. LaVoie, R. Kuriyama, Identification of in-trinsic dimer and overexpressed monomeric forms of gamma-tubulin in Sf9 cells infected with baculovirus containing the Chlamydomonas gamma-tubulin sequence, J. Cell Sci. 108 (1995) 1083–1092.

[61] M. Pilhofer, G.J. Jensen, The bacterial cytoskeleton: more than twisted filaments, Curr. Opin. Cell Biol. 25 (2013) 125–133.

[62] R. Leguy, R. Melki, D. Pantaloni, M.F. Carlier, Monomeric gamma-tubulin nucleates microtubules, J. Biol. Chem. 275 (2000) 21975–21980.

[63] D. Ghosal, J. Lowe, Collaborative protein filaments, EMBO J. 34 (2015) 2312–2320.

[64] M.P. Strauss, A.T. Liew, L. Turnbull, C.B. Whitchurch, L.G. Monahan, E.J. Harry, 3D-SIM super resolution microscopy reveals a bead-like arrangement for FtsZ and the division machinery: implications for triggering cytokinesis, PLoS Biol. 10 (2012) e1001389.

[65] A. Dajkovic, G. Lan, S.X. Sun, D. Wirtz, J. Lutkenhaus, MinC spatially controls bacterial cytokinesis by antagonizing the scaffolding function of FtsZ, Curr. Biol. 18 (2008) 235–244.

[66] M. Weingartner, P. Binarova, D. Drykova, A. Schweighofer, J.P. David, E. Heberle-Bors, J. Doonan, L. Bogre, Dynamic recruitment of Cdc2 to specific microtubule structures during mitosis, Plant Cell 13 (2001) 1929–1943.

[67] H.B. Shu, H.C. Joshi, Gamma-tubulin can both nucleate microtubule assembly and self-assemble into novel tubular structures in mammalian cells, J. Cell Biol. 130 (1995) 1137–1147.

[68] M.S. Ramer, M.A. Cruz Cabrera, N. Alan, A.L. Scott, J.A. Inskip, A new organellar complex in rat sympathetic neurons, PLoS One 5 (2010) e10872.

[69] Y. Zheng, M.L. Wong, B. Alberts, T. Mitchison, Nucleation of microtubule assembly by a gamma-tubulin-containing ring complex, Nature 378 (1995) 578–583.

[70] H.P. Erickson, D. Stoffler, Protofilaments and rings, two conformations of the tu-bulin family conserved from bacterial FtsZ to alpha/beta and gamma tubulin, J. Cell Biol. 135 (1996) 5–8.

[71] W.A. Voter, H.P. Erickson, The kinetics of microtubule assembly. Evidence for a two-stage nucleation mechanism, J. Biol. Chem. 259 (1984) 10430–10438.

[72] Y.J. Lee, Y. Hiwatashi, T. Hotta, T. Xie, J.H. Doonan, B. Liu, The mitotic function of augmin is dependent on its microtubule-associated protein subunit EDE1 in Arabidopsis thaliana, Curr. Biol. 27 (2017) 3891–3897 (e3894).

[73] R.F. Luduena, A hypothesis on the origin and evolution of tubulin, Int. Rev. Cell Mol. Biol. 302 (2013) 41–185.

[74] R.K. Mishra, P. Chakraborty, A. Arnaoutov, B.M. Fontoura, M. Dasso, The Nup107-160 complex and gamma-TuRC regulate microtubule polymerization at kine-tochores, Nat. Cell Biol. 12 (2010) 164–169.

[75] K. Oegema, C. Wiese, O.C. Martin, R.A. Milligan, A. Iwamatsu, T.J. Mitchison, Y. Zheng, Characterization of two related Drosophila gamma-tubulin complexes that differ in their ability to nucleate microtubules, J. Cell Biol. 144 (1999) 721–733.

[76] L. Gombos, A. Neuner, M. Berynskyy, L.L. Fava, R.C. Wade, C. Sachse, E. Schiebel, GTP regulates the microtubule nucleation activity of gamma-tubulin, Nat. Cell Biol. 15 (2013) 1317–1327.

[77] K. Sundararajan, A. Miguel, S.M. Desmarais, E.L. Meier, K. Casey Huang, E.D. Goley, The bacterial tubulin FtsZ requires its intrinsically disordered linker to direct robust cell wall construction, Nat. Commun. 6 (2015) 7281.

[78] J. Fiserova, E. Kiseleva, M.W. Goldberg, Nuclear envelope and nuclear pore com-plex structure and organization in tobacco BY-2 cells, Plant J. 59 (2009) 243–255.
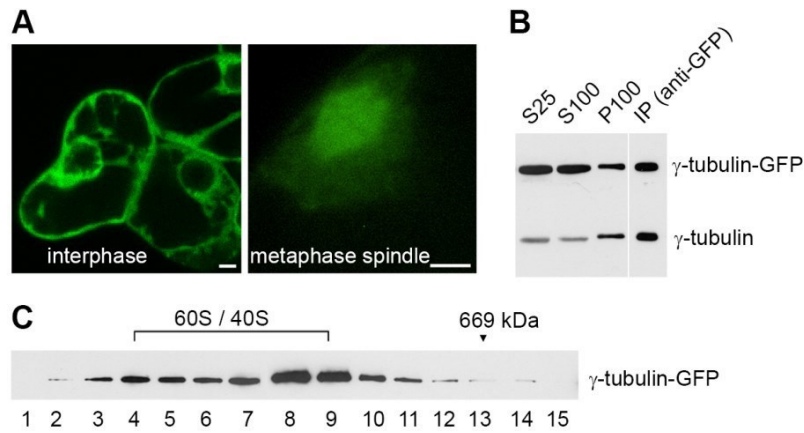
Supplemental Figure 1. Characterization of *Arabidopsis* cell lines with stable level of expression of γ-tubulin-GFP.

(A) CLSM analysis of cells expressing *TubG1-GFP.* γ-tubulin-GFP accumulated in perinuclear area and localized with metaphase mitotic spindle. Scale bars: 5 μm.

(B) γ-tubulin-GFP is pelleted to detergent-insoluble P100 together with endogenous γ-tubulin (P100). Endogenous γ-tubulin co-purified with γ-tubulin-GFP from detergent-insoluble P100 (IP anti-GFP) in aprox. ratio1:1. (C) A representative gel filtration profile of fractionated detergent-insoluble P100 derived from γ-tubulin-GFP expressing cells show presence of γ-tubulin-GFP in large molecular forms.
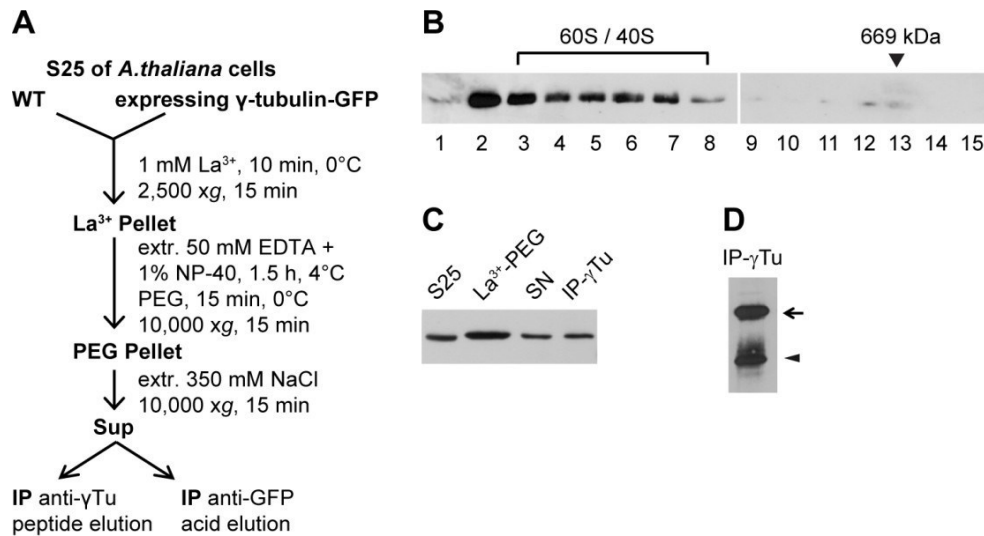
Supplemental Figure 2. Large molecular forms of γ-tubulin purified by La3+-PEG precipitation.

(A) Scheme for purification of large molecular forms of *Arabidopsis* γ-tubulin by La^{3+}-PEG. (B) Gel filtration of La^{3+}-PEG precipitated sample (Supernatant in A) showed presence of large molecular forms of γ-tubulin. (C, D) γ-tubulin immunopurification with anti-γ-tubulin antibody followed by peptide elution (IP-γTu) from La^{3+}-PEG precipitated extract S25 from (C) wildtype cells used as an input or from (D) cell line expressing a *TubG1-GFP* as an input. Western blots with anti-γ-tubulin antibody. SN, unbound supernatant after immunoprecipitation.
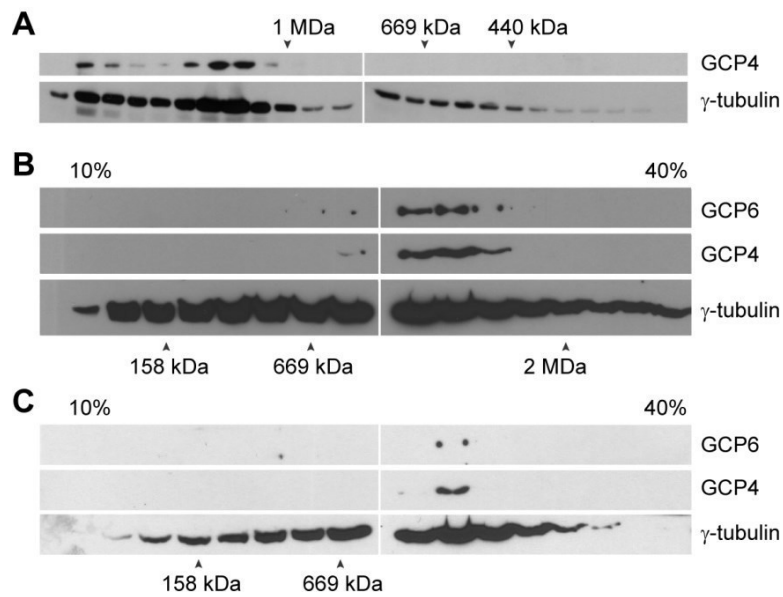
Supplemental Figure 3. Fractionations of *Arabidopsis* γ-tubulin and γ-tubulin complex proteins.

(A) Gel filtration profile of resuspended detergent-insoluble P100. (B) Sucrose gradient centrifugation of resuspended detergent-insoluble P100. (C) Sucrose gradient centrifugation of NP40-solubilised S20 supernatant. WB with anti-GCP4, anti-GCP6 and anti-γ-tubulin antibodies. Apparent molecular size markers are indicated by arrowheads.
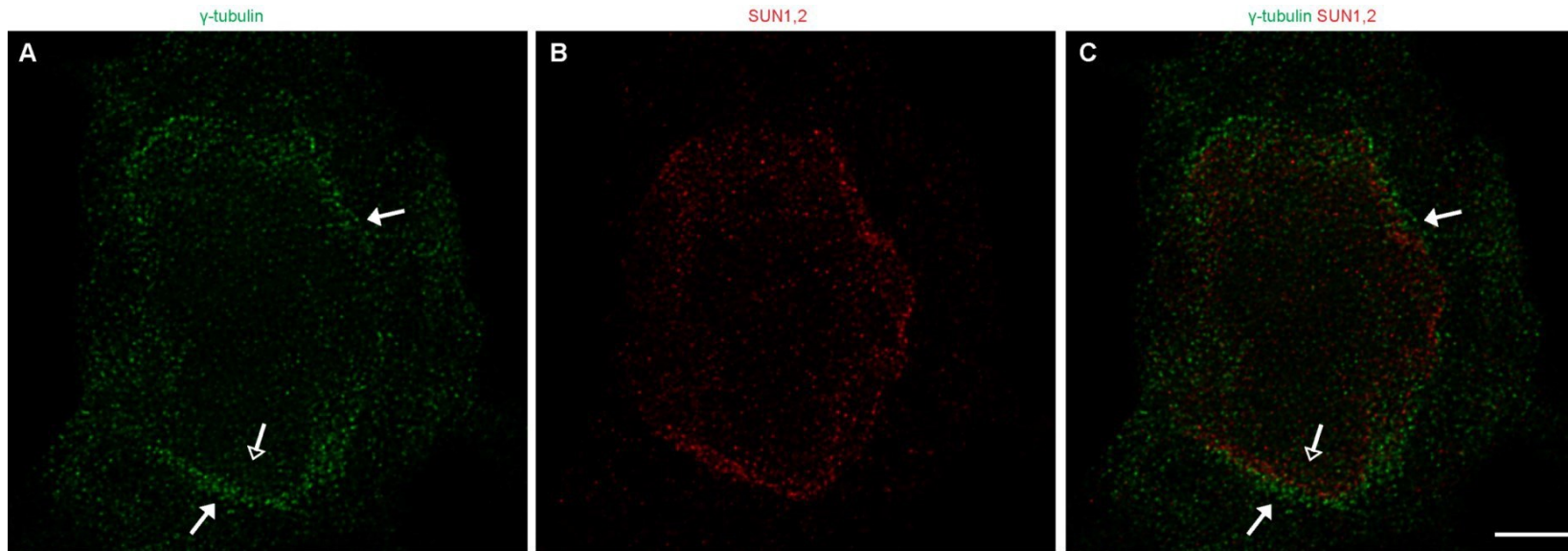
Supplemental Figure 4. γ-Tubulin fibrils are on cytoplasmic side of nucleus and also intranuclear.

STED deconvolved image of γ-tubulin and SUN1,2 protein showed that γ-tubulin fibrillar network is localized with outer nuclear envelope (arrow) and also with inner nuclear envelope (empty arrow) immunolabelled by antibody against SUN1,2 protein. Immunofluorescence staining: Alexa Fluor 594 for γ-tubulin, Abberior STAR RED for SUN1,2 protein, 775 nm depletion laser. Scale bar 3 μm.
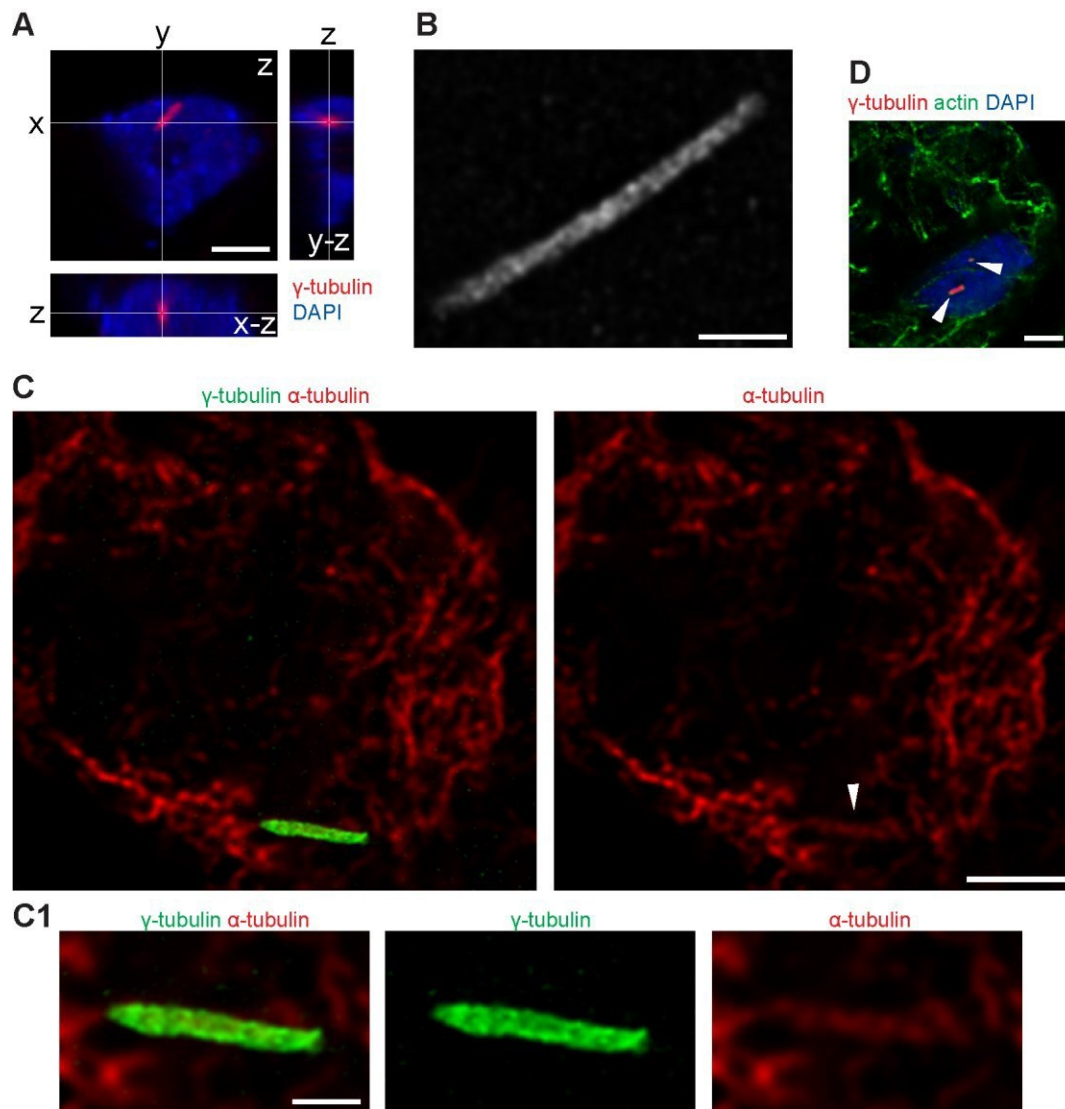
Supplemental Figure 5. γ-Tubulin positive rods in *Arabidopsis* cells.

(A) Representative confocal image of γ-tubulin rod in stationary grown *Arabidopsis* cell. Imaris sections of the nucleus with γ-tubulin rods (red), chromatin stained by DAPI (blue). Main panel *z* shows a single z-stack of the nucleus; right panel *y-z* shows cross-section by *y* plane perpendicular to *z* plane in the main panel; lower panel *x-z* shows cross-section by *x* plane perpendicular to *z* plane in the main panel. (B) Representative close-up view of STED deconvolved image of γ-tubulin rod indicated spiral-like pattern of globular fluorescent maxima. (C) Representative STED deconvolved image of γ-tubulin (green) and α-tubulin (red) positive rod. (D) Representative confocal image of γ-tubulin rods with signal for actin (arrowheads), γ-tubulin (red), actin (green). Immunofluorescence staining for STED: Alexa Fluor 555 F(ab)2, 660 nm depletion laser (B); Alexa Fluor 594 for γ-tubulin, Alexa Fluor 488 F(ab)2 for α-tubulin, 775 nm depletion laser (C, C1). Scale bars 1 µm (B, C1); Scale bars 3 µm (A, C); Scale bar 5 µm (D).
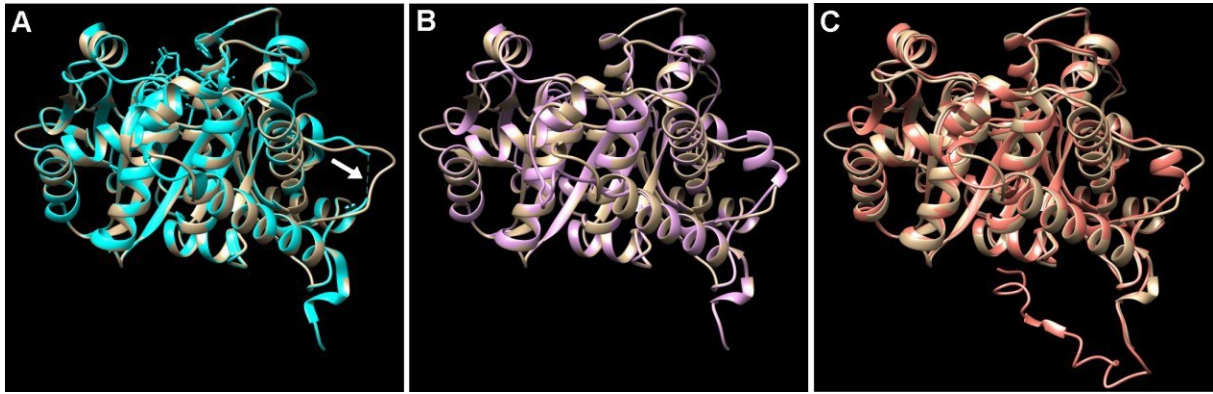
Supplemental Figure 6. Protein structure models of *Arabidopsis* γ-tubulin1.

(A) Cartoon representation of protein structure model of *A. thaliana* γ-tubulin1 gained from Swiss model (tan) aligned with PDB ID 3cb2a human γ-tubulin1 (cyan) using Chimera. GDP with its interacting amino acids from the plus end surface of PDB ID 3cb2a are shown in a stick representation (cyan). Dashed cyan line (arrow) marks amino acids not visible in PDB ID 3cb2a structure. (B, C) Structure of *Arabidopsis* γ-tubulin1 gained from Swiss model (tan) aligned with the model of *Arabidopsis* γ-tubulin1 either from Phyre 2 (violet) (B) or from I-TASSER (pink) (C). I-TASSER model includes C-terminus with β-strand (GEGNA).
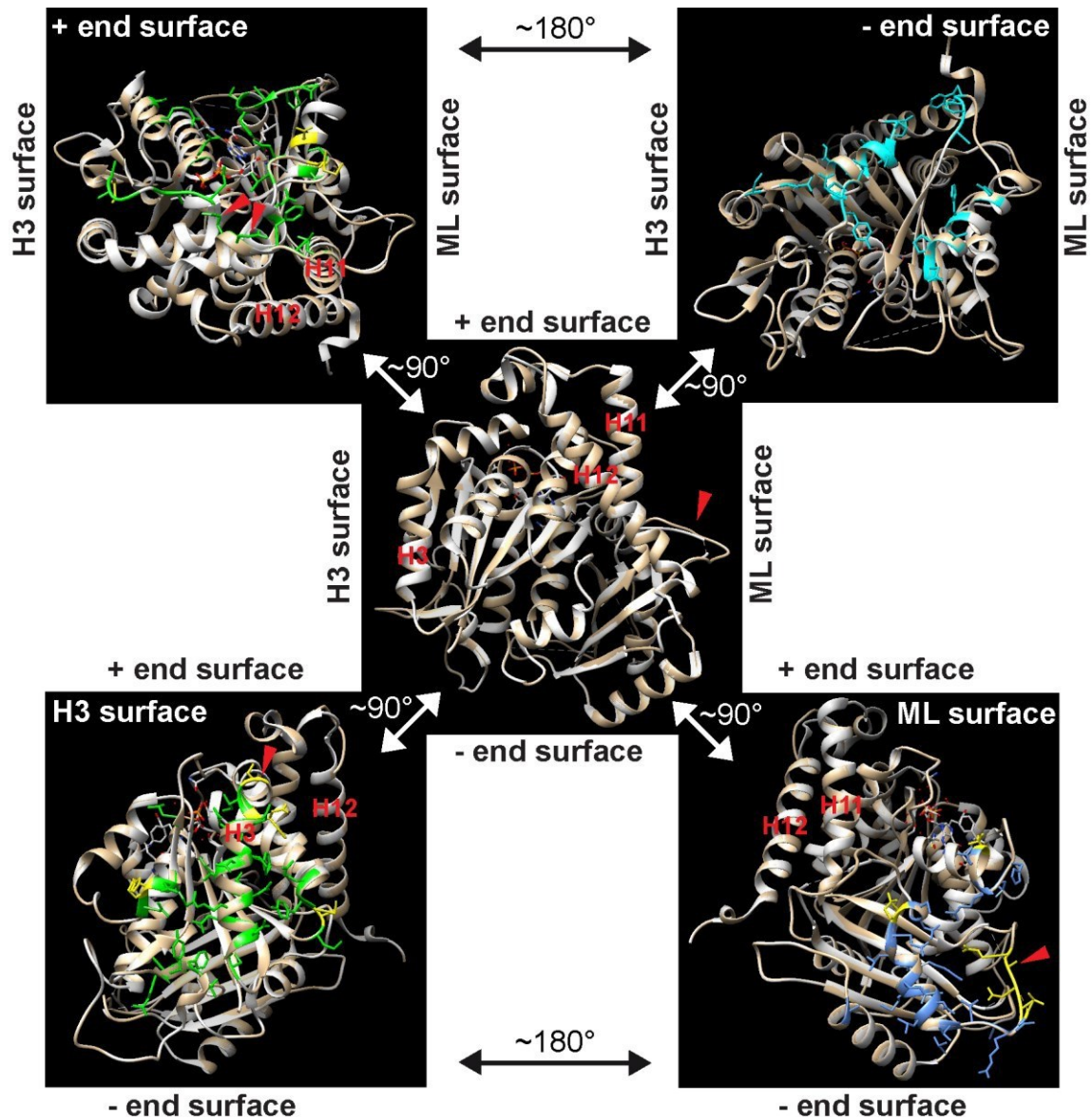
Supplemental Figure 7. Comparison of protein structures of *Arabidopsis* and human γ-tubulin1.

Cartoon representations of protein structure model of *Arabidopsis* γ-tubulin1 obtained from Swiss model (tan) aligned with PDB ID 3cb2a (Rice et al., 2008) human γ-tubulin1 (white) using Chimera. Amino acids that differed significantly between *Arabidopsis* and human γ-tubulin1 are marked in yellow (evaluated from T-Coffee as semi-and non-conservative, Supplemental Figure 8). In the centre, there is marked orientation of plus end and minus end surfaces, and H3 and ML surfaces needed for longitudinal and lateral interactions, respectively; helices H11 and H12 are seen from en face; H9-S8 loop (red arrowhead). The structural models around the centre, rotated 90° around horizontal or vertical axis, display in en face amino acids corresponding sequentially to amino acids involved directly in longitudinal and lateral interactions in α- and β-tubulin in microtubules or interacting with GDP. Upper left corner – amino acids involved in longitudinal interactions at plus end surface (green); changed amino acids are generally smaller and/or less polar than those of human γ-

tubulin1; change of HWY motif (red arrowheads); upper right corner – amino acids involved in longitudinal interactions at minus end surface (cyan) includes no significantly different amino acids; bottom left corner – amino acids involved in lateral interactions on H3 surface (green); His forming a bulge in helix H3 (red arrowhead) is present in *Arabidopsis* γ-tubulin1, while it is absent in human γ-tubulin; bottom right corner – amino acids involved in lateral interactions on ML surface (cornflower blue); changed amino acids in *Arabidopsis* γ-tubulin1 are larger with only one exception (red arrowhead). GDP is shown as an orange stick representation.

```
Ath    MPREIITLQVGQCGNQIGMEFWKQLCLEHGISKDGILEDFATQGGDRKDV          50
Hsa    MPREIITLQLGQCGNQIGFEFWKQLCAEHGISPEGIVEEFATEGTDRKDV          50
       ********* :********* ******* :**:*:***:* *****
                                                      T3
Ath    FFYQADDQHYIPRALLIDLEPRVINGIQNGDYRNLYNHENIFVADHGGGA         100
Hsa    FFYQADDEHYIPRAVLLDLEPRVIHSILNSPYAKLYNPENIYLSEHGGGA         100
       *******.*******.*:.*******:. .*  * :*** ***:::*****
                              H3
Ath    GNNWASGYHQGKGVEEEIMDMIDREADGSDSLEGFVLCHSIAGGTGSGMG         150
Hsa    GNNWASGFSQGEKIHEDIFDIIDREADGSDSLEGFVLCHSIAGGTGSGLG         150
       *******: **: :.*:*:*:*********************:*
                               T5
Ath    SYLLETLNDRYSKKLVQTYSVFPNQMETSDVVVQPYNSLLTLKRLTLNAD         200
Hsa    SYLLERLNDRYPKKLVQTYSVFPNQDEMSDVVVQPYNSLLTLKRLTQNAD         200
       ***** *****. *************  *  ****************  ***
                                                T7
Ath    CVVVLDNTALGRIAVERLHLTNPTFAQTNSLVSTVMSASTTTLRYPGYMN         250
Hsa    CVVVLDNTALNRIATDRLHIQNPSFSQINQLVSTIMSASTTTLRYPGYMN         250
       **********.*** .***.:.***: **.*.:* *.****:***********
              H8                S7           M              H9
Ath    NDLVGLLASLIPTPRCHFLMTGYTPLTVERQANVIRKTTVLDVMRRLLQT         300
Hsa    NDLIGLIASLIPTPRLHFLMTGYTPLTTDQSVASVRKTTVLDVMRRLLQP         300
       ***:**:********* **********:.::.  :*************.
                     S8              H10
Ath    KNIMVSSYARNKEASQAKYISILNIIQGEVDPTQVHESLQRIRERKLVNF         350
Hsa    KNVMVST-GRDRQ-TNHCYIAILNIIQGEVDPTQVHKSLQRIRERKLANF         348
       **:***: .*:: ::   **:***************:*********** **
                                              H11
Ath    IEWGPASIQVALSKKSPYVQTAHRVSGLMLASHTSIRHLFSKCLSQYDKL         400
Hsa    IPWGPASIQVALSRKSPYLPSAHRVSGLMMANHTSISSLFERTCRQYDKL         398
       * ***********:****: .*********:*. **** **.:    *****
                                  H12
Ath    RKKQAFLDNYRKFPMFADNDLSEFDESRDIIESLVDEYKACESPDYIKWG         450
Hsa    RKREAFLEQFRKEDMFKDN-FDEMDTSREIVQQLIDEYHAATRPDYISWG         447
       **::***::::**   ** ** :.*:* **:*::.*:***:*.  ****.**
Ath    MEDPEQLMTGEGNASGVVDPKLAF                                    474
Hsa    TQEQ-------------------                                     451
       ::
```

Supplemental Figure 8. Protein sequence alignment of *Arabidopsis* and human γ-tubulins.

Amino acids corresponding to those involved in longitudinal and lateral contacts in α- and β-tubulins are coloured; red – plus end surface; orange – minus end surface; green – H3 surface; azure – ML surface. Secondary structures or loops are marked with lines above sequences according to human γ-tubulin PDB ID 3cb2a; H – helix; S – β-sheet; T/M – loop. Identical amino acids are marked under sequences according to ClustalW (T-Coffee) with asterisk, conserved substitutions of the same size and

hydropathy with colon, and semi-conserved substitutions of similar size or hydropathy with dot. Underscore under sequences marks amino acids not visible in PDB ID 3cb2a structure. Ath, γ-tubulin1 from *Arabidopsis thaliana*; Hsa, γ-tubulin1 from *Homo sapiens*.

Supplemental Table 1A

IP_1% NP-40

Protein name		Accession No.	UniProt No.	TAIR No.	MW [kDa]	MASCOT Score	No. of peptides	SC [%]
Tubulin gamma-1 chain	TUBG1	NP_191724	P38557	At3g61650	53	2757	42	66
Tubulin gamma-2 chain	TUBG2	NP_196181	P38558	At5g05620	53	2118	32	49
Gamma-tubulin complex component 2	GCP2	NP_568346	Q9C5H9	At5g17410	77	227	6	8
Gamma-tubulin complex component 3	GCP3	NP_196286	Q9FG37	At5g06680	95	138	5	4
Gamma-tubulin complex component 4	GCP4	NP_190944	Q9M350	At3g53760	86	65	2	3
Spc97/Spc98 family of spindle pole body (SBP) component	GCP5	NP_565235	Q0WPZ0	At1g80260	111	48	1	1
Transducin/WD40 domain-containing protein GCP-WD	NEDD1	NP_196216	B3H5K9	At5g05970	85	178	5	6
GIP1 - Mitotic-spindle organizing protein 1B	GIP1/MZT1	NP_192693	Q9M0N8	At4g09550	8	44	1	11
Tubulin alpha-2/alpha-4	TUA4	NP_171974	Q0WV25	At1g04820	50	1442	17	43
Tubulin beta-4 chain	TUB4	NP_199247	P24636	At5g44340	50	1146	21	42
Actin-1	ACT1	NP_850284	P0CJ46	At2g37620	42	1149	18	51
Chaperonin hsp60, CPN60	HSP60	NP_189041	P29197	At3g23990	61	2283	28	44
Heat shock cognate 70 kDa protein 1	HSP70-1	NP_195870	P22953	At5g02500	71	1774	31	41
Heat shock protein 60-3A; chaperonin CPN60-like 2	HSP60-like 2	NP_566466	Q93ZM7	At3g13860	60	1120	16	26
Chaperonin 60 subunit alpha 1	CPN-60 alpha 1	NP_180367	P21238	At2g28000	62	680	10	18
T-complex protein 1 subunit alpha	TCP-1-alpha	NP_188640	P28769	At3g20050	59	1030	14	28
T-complex protein 1 epsilon subunit	TCP-1-epsilon	NP_173859	O04450	At1g24510	59	620	11	21

Supplemental Table 1B

IP_0.3 % SDS

Protein name		Accession No.	UniProt No.	TAIR No.	MW [kDa]	MASCOT Score	No. of peptides	SC [%]
Tubulin gamma-1 chain	TUBG1	NP_191724	P38557	At3g61650	53	3431	51	76
Actin-1	ACT1	NP_850284	P0CJ46	At2g37620	42	220	4	13
Heat shock cognate 70 kDa protein 3	HSP70-3	NP_187555	O65719	At3g09440	71	408	5	12
Heat shock protein 81-2	HSP90-3	NP_200412	P51818	At5g56010	80	100	2	4

Supplemental Table 1.

Comparative list of selected proteins co-immunopurified with γ-tubulin(-GFP). (A) 1% Nonidet-treated or (B) 0.3% SDS-treated (high stringency conditions, Procedure *b* in Figure 1D) S25 extract from *Arabidopsis* cells was immunoprecipitated with anti-GFP antibody. Precipitated material was analyzed by LC-MS/MS. SDS-treatment caused dissociation of endogenous γ-tubulin and majority of interacting proteins (demonstrated also on Western blots in Figure 4A).

Supplemental Methods.

Cell treatments

Compounds were applied at following final concentrations: 100 μM roscovitine (Sigma-Aldrich R7772), 20 μM taxol (Paclitaxel, Sigma T7402). To depolymerize microtubules, 10 μM aminoprophos-methyl (APM, A0185, Duchefa Biochemie, Haarlem, Netherlands) was applied for 2 h. Microtubule regrowth, after washing off APM, was for 0.5 h.

Western blot – list of antibodies

anti-γ-tubulin for detection in plant material (if not written otherwise), AthTU rabbit polyclonal raised against *Arabidopsis* γ-tubulin C-terminal peptide (Drykova et al., 2003) (diluted 1:2,000);

anti-γ-tubulin, TU-32 mouse monoclonal (Novakova et al., 1996) (hybridoma spent culture medium diluted 1:3);

anti-α-tubulin for detection in plant material, clone DM1A (T9026, Sigma, St. Louis, Missouri) (diluted 1:1,000);

anti-α-tubulin, TU-01 mouse monoclonal (Viklicky et al., 1982) (hybridoma spent culture medium diluted 1:5)

anti-actin (MA1-744, Thermo Scientific, Waltham, Massachusetts) (diluted 1:1,000);

anti-β-tubulin (Sigma T4026) (diluted 1:200);

anti-KNOLLE (Rose Biotechnology–Secant Chemicals, Winchendon, Massachusetts) (diluted 1:5,000);

anti-GCP2, GCP2-01 mouse monoclonal (Draberova et al., 2015) (hybridoma spent culture medium diluted 1:5);

anti-GCP3, custom polyclonal rabbit antibody against *Arabidopsis* GCP3-specific peptide (Clonestar, Brno, The Czech Republic; affinity-purified) (diluted 1:1000);

anti-GCP4 for detection in plant material, custom polyclonal rabbit antibody against *Arabidopsis* GCP4-specific peptide (GenScript, Piscataway, New Jersey; affinity-purified) (diluted 1:200);

anti-GCP4 for detection in animal material (Santa Cruz, sc-271876) (diluted 1:1,000);

anti-GCP6, custom polyclonal rabbit antibody against *Arabidopsis* GCP6-specific peptide (Clonestar, Brno, The Czech Republic; affinity-purified) (diluted 1:50);

anti-tRFP (Evrogen, AB234) (diluted 1:1,000);

anti-PAK1 (Sigma, HPA03565) (diluted 1:5,000).

Secondary anti-mouse Ig and anti-rabbit Ig antibodies conjugated with horseradish peroxidase (Amersham-GE Healthcare, Little Chalfont, UK) were diluted 1:10,000.

Immunofluorescence labelling – list of antibodies

anti-α-tubulin DM1A (T9026, Sigma) 1:2,000;

immunogenic peptide purified anti-γ-tubulin AthTU 1:2,000;

mouse monoclonal anti-γ-tubulin TU-32 (Novakova et al., 1996) (hybridoma spent culture medium) 1:4;

anti-SUN1,2 (AS15 2856, Agrisera) 1:1000;

Alexa Fluor 488-conjugated anti-mouse (111-585-146) or anti-rabbit (111-545-144) antibodies (Jackson ImmunoResearch Laboratories, West Grove, Pennsylvania) 1:600;

Alexa Fluor 594-conjugated anti-mouse (115-585-146) or anti-rabbit (111-585-144) antibodies (Jackson ImmunoResearch Laboratories, West Grove, Pennsylvania) 1:800;

Alexa Fluor 488 F(ab)2-conjugated anti-mouse antibody (A-11017, Invitrogen, ThermoFisher Scientific) 1:250;

Alexa Fluor 555 F(ab)2-conjugated anti-rabbit antibodies (A-21430 Invitrogen, Thermo Scientific) 1:250;

Abberior STAR 580 anti-mouse (2-0002-005-1, Abberior) 1:200;

Abberior STAR RED anti-rabbit (2-0012-011-9, Abberior) 1:200;

For STED: anti-γ-tubulin AthTU was diluted 1:1,500; Alexa Fluor 594-conjugated anti-mouse or anti-rabbit antibodies (Jackson ImmunoResearch Laboratories) was diluted 1:600;

Mass spectrometry analyses

For LC MALDI-TOF MS/MS, peptide-eluted proteins were pelleted at 100,000 x*g* or concentrated and washed on a 30-kDa ultrafiltration membrane as above denatured in 8 M urea, and digested overnight using trypsin. After desalting, the resulting peptides were separated using Ultimate LC Packings HPLC system on a Magic C18AQ column (0.2 x 150 mm, 5 μm, 200 Å). The eluent from the column was spotted directly onto MALDI target using a ProteineerFC spotting device (Bruker Daltonics, Bremen, Germany). Automatic MALDI MS/MS analyses were performed on an Ultraflex III TOF/TOF (Bruker Daltonics) and the proteins were identified by

searching MS/MS spectra against *A. thaliana* subset of SwissProt or NCBI database using Mascot program (Matrix Science).

MALDI spectra were also measured on an Apex-Q FTICR mass spectrometer (Bruker Daltonics) equipped with a 9.4T magnet. The spectrometer was calibrated externally using Peptide Calibration Mix II (Bruker Daltonics) resulting in the mass accuracy below 2 ppm.

Fluorescence microscopy and confocal laser scanning microscopy (CLSM)

Fluorescence microscopy observations were performed using an Olympus IX-81 with Olympus DSU (Disc Scan Confocal Unit) equipped with Hammamatsu Orca/ER digital camera and the Cell R^{TM} detection and analyzing system. A U-MGFPHQ filter (Olympus, Tokyo, Japan) was used with excitation 460-480 nm and emission 495-540 nm. Images were deconvolved using Wiener Filter algoritmus provided with CellR microscope, Olympus.

Alternatively preparations were imaged on Olympus fluorescence microscope AX-70 Provis equipped with 60x/1.20 NA water objective, SensiCam 12bit Cooled Imaging PCO CCD camera, filter Olympus U-MWIG, (Olympus, Tokyo, Japan) was used with excitation 520-550 nm, and emission 580 nm.

Confocal laser scanning microscopy was performed using an Olympus IX-81 FV-1000 imaging system with oil immersion objective 100x/1.45; DAPI: ex 405 nm, em 425-460 nm; Alexa 488: ex 473 nm, em 485-545 nm; Alexa 594: ex 559 nm, em 575-640 nm; TRITC: ex 559 nm; em 575-635 nm or 575-620 nm in combination with EGFP: ex 473 nm, em 485-535 nm. Sequential multitrack mode was used to avoid bleed-through. For cross-section views using Imaris software (Bitplane, Zurich, Schwitzerland), z-stacks were taken with 0.2 μm z-step. Images were analyzed using FV10-ASW (Olympus) and Fiji (Schindelin et al., 2012) and prepared in Adobe Photoshop CS4 and Adobe Illustrator CS4. Total Internal Reflection Fluorescence (TIRF) microscopy images were acquired using Olympus FV100-EVA modul equipped with CCD camera ImageEM C9100-23b (Hamamatsu).

Atomic Force Microscopy (AFM)

5-μl γ-Tubulin samples were applied to freshly cleaved mica (Grade V-4 Muscovite, SPI Supplies, West Chester, PA), incubated in a moist chamber for 30 min, washed twice with 50 mM Tris·HCl (pH 8.0), fixed with -20°C methanol for 10 min and dried.

Imaging was carried out in Tapping Mode (TM-AFM) in the air at room temperature using Veeco MultiMode IV Atomic Force Microscope (Veeco Instruments, Santa Barbara, CA) and NP-S10 silicon nitride probes (Bruker AFM Probes, Camarillo, CA) with nominal resonant frequency 56 and 18 kHz and nominal spring constants 0.24 and 0.06 N/m, respectively. Images show raw data without corrections. Images (TM deflection) are presented in adaptive non-linear color mapping (Gwyddion 2.30, Czech Metrology Institute, Brno, EU) which enhances the contrast. Analysis of the width of the filaments was performed using semi-automatic procedure developed in Matlab (MathWorks, Natick, MA). Data were leveled for this purpose using polynomial background subtraction. The width was approximated by the distance of the two subsequent height maxima in the cross-section perpendicular to the filament bundle. Histogram of the distance is supplemented with log-normal fit of the distribution and number of analyzed data points (N).

References for supplemental material

Draberova E., D'Agostino L., Caracciolo V., Sladkova V., Sulimenko T., Sulimenko V., Sobol M., Maounis N.F., Tzelepis E., Mahera E., Kren L., Legido A., Giordano A., Mork S., Hozak P., Draber P., and Katsetos C.D. (2015). Overexpression and Nucleolar Localization of gamma-Tubulin Small Complex Proteins GCP2 and GCP3 in Glioblastoma. *Journal of neuropathology and experimental neurology* **74**: 723-742.

Drykova D., Cenklova V., Sulimenko V., Volc J., Draber P., and Binarova P. (2003). Plant gamma-tubulin interacts with alphabeta-tubulin dimers and forms membrane-associated complexes. *Plant Cell* **15**: 465-480.

Novakova M., Draberova E., Schurmann W., Czihak G., Viklicky V., and Draber P. (1996). gamma-Tubulin redistribution in taxol-treated mitotic cells probed by monoclonal antibodies. *Cell Motil Cytoskeleton* **33**: 38-51.

Schindelin J., Arganda-Carreras I., Frise E., Kaynig V., Longair M., Pietzsch T., Preibisch S., Rueden C., Saalfeld S., Schmid B., Tinevez J.Y., White D.J., Hartenstein V., Eliceiri K., Tomancak P., and Cardona A. (2012). Fiji: an open-source platform for biological-image analysis. *Nature methods* **9**: 676-682.

Viklicky V., Draber P., Hasek J., and Bartek J. (1982). Production and characterization of a monoclonal antitubulin antibody. *Cell biology international reports* **6**: 725-731.

VII.3 **Klebanovych, A.,** Sládková, V., Sulimenko, T., Vosecká, V., Rubíková, Z., Čapek, M., Dráberová, E., Dráber, P., Sulimenko, V. (2019) Regulation of microtubule nucleation in mouse bone marrow-derived mast cells by protein tyrosine phosphatase SHP-1. Cells *8(4)*: e345.

Regulation of Microtubule Nucleation in Mouse Bone Marrow-Derived Mast Cells by Protein Tyrosine Phosphatase SHP-1

Anastasiya Klebanovych [1] , **Vladimíra Sládková** [1], **Tetyana Sulimenko** [1], **Věra Vosecká** [1], **Zuzana Rubíková** [1], **Martin Čapek** [2], **Eduarda Dráberová** [1], **Pavel Dráber** [1,*] and **Vadym Sulimenko** [1,*]

[1] Department of Biology of Cytoskeleton, Institute of Molecular Genetics, Czech Academy of Sciences, CZ-142 20 Prague, Czech Republic; Anastasiya.Klebanovych@img.cas.cz (A.K.); vladimira.sladkova@img.cas.cz (V.S.); tetyana.sulimenko@img.cas.cz (T.S.); vera.vosecka@img.cas.cz (V.V.); zuzana.rubikova@img.cas.cz (Z.R.); Eduarda.Draberova@img.cas.cz (E.D.)

[2] Light Microscopy Core Facility, Institute of Molecular Genetics, Czech Academy of Sciences, CZ-142 20 Prague, Czech Republic; martin.capek@img.cas.cz

* Correspondence: paveldra@img.cas.cz (P.D.); vadym.sulimenko@img.cas.cz (V.S.); Tel.: +420-241-062-632 (P.D.); +420-296-442-640 (V.S.); Fax: +420-241062758 (P.D. & V.S.)

Abstract: The antigen-mediated activation of mast cells initiates signaling events leading to their degranulation, to the release of inflammatory mediators, and to the synthesis of cytokines and chemokines. Although rapid and transient microtubule reorganization during activation has been described, the molecular mechanisms that control their rearrangement are largely unknown. Microtubule nucleation is mediated by γ-tubulin complexes. In this study, we report on the regulation of microtubule nucleation in bone marrow-derived mast cells (BMMCs) by Src homology 2 (SH2) domain-containing protein tyrosine phosphatase 1 (SHP-1; *Ptpn6*). Reciprocal immunoprecipitation experiments and pull-down assays revealed that SHP-1 is present in complexes containing γ-tubulin complex proteins and protein tyrosine kinase Syk. Microtubule regrowth experiments in cells with deleted SHP-1 showed a stimulation of microtubule nucleation, and phenotypic rescue experiments confirmed that SHP-1 represents a negative regulator of microtubule nucleation in BMMCs. Moreover, the inhibition of the SHP-1 activity by inhibitors TPI-1 and NSC87877 also augmented microtubule nucleation. The regulation was due to changes in γ-tubulin accumulation. Further experiments with antigen-activated cells showed that the deletion of SHP-1 stimulated the generation of microtubule protrusions, the activity of Syk kinase, and degranulation. Our data suggest a novel mechanism for the suppression of microtubule formation in the later stages of mast cell activation.

1. Introduction

Mast cells play a crucial role in allergies, as well as in innate and adaptive immune responses. They express plasma membrane-associated high-affinity IgE receptors (FcεRIs), the aggregation of which by a multivalent antigen (Ag)-IgE complex triggers mast cell activation, resulting in their degranulation; in the release of inflammatory mediators, proteases, and lipid mediators; and in the production of various cytokines [1]. FcεRI crosslinking initiates a tyrosine phosphorylation of the FcεRI β- and γ-subunits by the Src family non-receptor kinase Lyn. This is followed by an enhanced activity of tyrosine kinase Syk from the Syk/Zap family and the phosphorylation of transmembrane

adaptors, which organize and coordinate further signals, resulting in a Ca²⁺ efflux from the endoplasmic reticulum. A depletion of Ca²⁺ from the ER lumen induces a Ca²⁺ influx across the plasma membrane, leading to an enhancement of the free cytoplasmic Ca²⁺ concentration, a step which is substantial in further signaling events [2]. The tyrosine phosphorylation of numerous substrates is only transient and returns to baseline levels several minutes after receptor triggering. An important role in this process is played by protein tyrosine phosphatases [3].

Microtubules, built up from αβ-tubulin dimers, are important for mast cell degranulation since the movement of secretory granules depends on intact microtubules [4,5]. It has been reported that the activation of mast cells induces an increased formation of microtubules [5,6] and the transient generation of protrusions containing microtubules (microtubule protrusions) [7,8]. Moreover, the influx of Ca²⁺ plays a decisive role in microtubule remodeling [7,9]. The importance of motor proteins for the anterograde [8] and retrograde [10] transport of the granules along the microtubules of mast cells was also demonstrated. Although these data point to the necessity of the microtubule network for mast cell degranulation, the molecular mechanisms responsible for microtubule reorganization in activated mast cells are still largely unknown.

In mast cells, microtubules are dominantly nucleated from the centrosomes. One of the key components for microtubule nucleation is γ-tubulin, a highly conserved, albeit minor, member of the tubulin superfamily [11]. Together with other proteins named Gamma-tubulin Complex Proteins (GCPs), it assembles into γ-Tubulin Small Complex (γTuSC) and the γ-Tubulin Ring Complex (γ TuRC). γTuSC is composed of two molecules of γ-tubulin and one copy each of GCP2 and GCP3. In mammalian cells, γTuRCs comprise γTuSCs and additional GCPs, GCP4–6 [12,13].

Protein tyrosine kinases phosphorylate γ-tubulin or associated proteins and, in this way, could modulate γ-tubulin functions [6,14,15]. It has been reported that Src signaling, leading to the activation of the MEF/ERK pathway, regulates microtubule nucleation by the accumulation of γ-tubulin at the centrosome [16,17]. Recently, we have reported that tyrosine-phosphorylated proteins GIT1 and βPIX regulate microtubule nucleation in mast cells [18]. The identification of protein tyrosine phosphatases that regulate microtubule nucleation should help in the elucidation of the mechanisms involved in the transient microtubule formation during mast cell activation.

In this study, we examined the hypothesis that phosphotyrosine (P-Tyr) proteins associated with γ-tubulin could modulate microtubule nucleation in activated mast cells. We identified protein tyrosine phosphatase SHP-1, forming complexes with γ-tubulin complex proteins, as a negative regulator of microtubule nucleation from the centrosomes of bone marrow-derived mast cells (BMMCs). The regulation is due to changes in γ-tubulin accumulation. During an Ag-induced activation, SHP-1 modulates the activity of the Syk kinase and affects the organization of microtubules. Our data suggest a novel mechanism for the attenuation microtubule formation in the later stages of mast cell activation. In this way, Ag-induced signaling pathways leading to the degranulation could be regulated.

2. Materials and Methods

2.1. Reagents

Nocodazole, puromycin, dinitrophenyl-albumin (DNP-albumin), fibronectin, and 4-nitrophenyl N-acetyl-β-D-glucosaminide (4-NAG) were from Sigma-Aldrich (St. Louis, MO, USA). Hygromycin B and Fura-2-acetoxymethyl ester (Fura-2-AM) were purchased from Invitrogen (Carlsbad, CA, USA). Protein A Sepharose CL-4B and Glutathione Sepharose 4 Fast Flow were from GE Healthcare Life Sciences (Chicago, IL, USA). Protein G Plus Agarose and the SuperSignal WestPico Chemiluminescent reagents were from Pierce (Rockford, IL, USA). The protease-inhibitor mixture tablets (Complete EDTA-free) were from Roche Molecular Biochemicals (Mannheim, Germany), and polyethylenimine was from (Polysciences, Inc., Warrington, PA, USA). The SHP-1 inhibitors TPI-1 and NSC87877 were purchased from Axon Medchem BV (Groningen, The Netherlands) and Selleckchem (Munich,

Germany), respectively. The inhibitor stocks (10 mM) were prepared in DMSO. The restriction enzymes were from New England Biolabs (Ipswich, MA, USA). The oligonucleotides were synthesized by Sigma-Aldrich.

2.2. Antibodies

The catalog numbers for the primary commercial antibodies (Abs) are shown in parentheses. Mouse monoclonal Abs (mAb) TU-30 (IgG1) and TU-31 (IgG2b) to γ-tubulin sequence 434–449 were described previously [19,20]. Rabbit Ab (T3195) to γ-tubulin sequence 433–451 and rabbit Ab (T5192) and mouse mAb GTU-88 (IgG1; T6557) to γ-tubulin sequence 38–53 were from the Sigma-Aldrich. Rabbit Abs to SHP-1 (sc-287), SHP-2 (sc-280), and GIT1 (sc-13961) and mouse mAbs to GCP4 (IgG1, sc-271876), GCP5 (IgG2b, sc-365837), and GCP6 (IgG1, sc-374063) were purchased from Santa Cruz Biotechnology (Dallas, TX, USA). Mouse mAbs SPE-7 (IgE, D8406) specific for DNP; PY-20 (IgG2b, P4110) to P-Tyr; and rabbit Abs to actin (A2066), GFP (G1544), and βPIX (HPA004744) were from Sigma-Aldrich. Mouse mAb 4G10 (IgG2b) to P-Tyr was from Upstate Laboratories (Syracuse, NY, USA). Rabbit Abs to phospho-SHP-1 (Y^{564}) (8849) and phospho-Syk (Y^{352}) (2717) were from Cell Signaling (Danvers, MA, USA), to GCP3 (15719–1-AP) was from ProteinTech (Manchester, UK), and to α-tubulin (GTX15246) was from Genetex (Irvine, CA, USA). Mouse mAb to pericentrin (IgG1, 611815) was purchased from BD Transduction Laboratories (San Jose, CA, USA). Mouse mAbs GCP2–01 (IgG2b) and GCP2–02 (IgG1) to GCP2 were described previously [21]. Rabbit Ab to non-muscle myosin heavy chain (BT-561; Biomedical Technologies., Stoughton, MA, USA) and mAb NF-09 (IgG2a) to neurofilament NF-M protein [22] served as negative controls in the immunoprecipitation experiments. Mouse mAb Syk-01 (IgG1) [23] and rabbit Ab to Syk [24] were provided by Dr. Petr Dráber (Institute of Molecular Genetics CAS, Prague, Czech Republic).

Anti-mouse and anti-rabbit Abs conjugated with horseradish peroxidase (HRP) were from Promega Biotec (Madison, WI, USA). TrueBlot anti-rabbit IgG HRP was purchased from Rockland Immunochemicals (Limerick, PA, USA). Anti-mouse Ab conjugated with DyLight549 and anti-rabbit Ab conjugated with Cy3 or AF488 were from Jackson Immunoresearch Laboratories (West Grove, PA, USA).

2.3. Cell Cultures and Transfection

A stable cell line of mouse bone marrow-derived mast cells (BMMCs) was donated by Dr. Margaret Hibbs (Ludwig Institute for Cancer Research, Melbourne, Australia) [25]. The cells were cultured in freshly a prepared culture medium (RPMI-1640 supplemented with 100 U/mL penicillin, 100 μg/mL streptomycin, nonessential amino acids, 1 mM sodium pyruvate, 10% fetal calf serum, and 10% WEHI-3 cell supernatant as a source of IL-3). The cells were grown at 37 °C in 5% CO_2 in air and passaged every 2–3 days.

The human epithelial breast cancer cells MCF7 (Cat. No. ATTC HTB-22) were obtained from the American Type Culture Collection (Manassas, VA, USA), and the human embryonic kidney HEK 293FT cells (HEK; Cat. No. R70007) were from ThermoFisher Scientific (Waltham, MA, USA). The cells were grown at 37 °C in 5% CO_2 in Dulbecco's Modified Eagle Medium supplemented with 10% fetal calf serum and antibiotics. The HEK cells used for lentivirus production were at passages 4–15. In some cases, the cells were cultivated with 100 nM TPI-1, 500 nM NSC87877, or a DMSO carrier (Control) for 1 h to evaluate the effect of SHP-1 inhibitors.

The HEK cells were transfected with 17 μg of DNA per 9-cm tissue culture dish using 51 μg of polyethylenimine and serum-free DMEM. After 24 h, the transfection mixture was replaced with a fresh medium supplemented with serum, and the cells were incubated for an additional 24 h.

2.4. DNA Constructs

To prepare C-terminally enhanced green fluorescent protein (EGFP)-tagged mouse SHP-1 (gene *Ptpn6*; RefSeq ID: NM_013545.3), the coding sequence without a stop codon was amplified

from the C-terminally Myc-DDK-tagged Ptpn6 (tv1) (OriGene Technologies, Rockville, MD, USA; MR209258) by PCR using the forward 5 -GCTC<u>GAATTC</u>ATGGTGAGGTGGTTTC-3 and reverse 5 -AGC<u>GTCGAC</u>CTTCCTCTTGAGAGAACCT-3 primers. The PCR product was digested with *Eco*RI/*Sal*I and ligated to pEGFP-N3 (ClonTech Laboratories, Mountain View, CA, USA), resulting in plasmid pmSHP-1_EGFP.

To prepare a lentiviral vector for the phenotypic rescue experiment, the coding sequence of mouse SHP-1 was amplified from the Myc-DDK-tagged Ptpn6 (tv1) (OriGene Technologies, MR209258) by PCR using the forward 5 -AGA<u>GCTAGC</u>ATGGTGAGGTGGTTTCACCGG-3 and reverse 5 -AAT<u>GCGGCCGC</u>TTACTTCCTCTTGAGAGAAC-3 primers. The PCR product was digested with *Nhe*I/*Not*I and ligated into the pCDH-CMV-MCS-EF1-hygro vector (System Biosciences, Palo Alto, CA, USA), resulting in the lentiviral construct pmSHP-1-hygro.

To prepare N-terminally glutathione S-transferase (GST)-tagged mouse spleen-associated tyrosine kinase (gene *Syk*; RefSeq ID: NM_011418), the coding sequence was amplified from the C-terminally Myc-DDK-tagged Syk (tv1) (OriGene Technologies, MR209591) by PCR using the forward 5 -TCAC<u>GAATTC</u>ATGGCGGGAAGTGCTGTGGACA-3 and reverse 5 -GGCC<u>GTCGAC</u>TTAGTTAACCACGTCGTAGTAG-3 primers. The PCR product was digested with *Eco*RI/*Sal*I and ligated into pGEX-6P-1 (Amersham Biosciences, Freiburg, Germany), resulting in the plasmid pGST-mSyk.

CRISPR/Cas9 gene editing [26] was used to disrupt the expression of all mouse SHP-1 variants (Ensembl, Ptpn6 ENSMUSG00000004266). Plasmids SpCas9 and pU6-sgRNAnew-III (donated by Dr. R. Malík, Institute of Molecular Genetics CAS, Prague, Czech Republic) were used for an optimal production of Cas9 and single-guide RNA (sgRNA), respectively. The CRISPR tool (available from Dr. F. Zhang Laboratory, Broad Institute, Cambridge, MA, USA) was used to design the DNA oligonucleotides (for production of sgRNA) that were cloned into the *Bsm*BI sites of pU6-sgRNAnew-III. To enrich cells with a disrupted expression of SHP-1, we used the pRR-puro plasmid with multiple cloning sites that encode a nonfunctional puromycin resistance cassette [27]. Annealed sense and antisense oligonucleotides containing the sequences from the region of interest and overhangs with *Aat*II/*Sac*I restriction sites were ligated into pRR-puro digested with *Aat*II/*Sac*I, resulting in a reporter plasmid pRR-mSHP-1-puro. A co-transfection of the reporter plasmid with the plasmids encoding sgRNAs and Cas9 led to a CRISPR-induced double-strand break (DSB) in the reporter plasmid. When the DSB was repaired by a homologous recombination, puromycin resistance was restored.

2.5. Generation of SHP-1 Deficient Cell Lines

In order to delete part of the 5' region of the gene containing the canonical and alternative start codons, BMMCs were transfected with CRISPR/Cas9 vectors (sgRNA#1, sgRNA#2, SpCas9) together with the reporter plasmid pRR-mSHP-1-puro by nucleofection using a Mouse Macrophage Kit and program T-020 in Amaxa Nucleofector II (Lonza Cologne AG, Cologne, Germany) according to the manufacturer's instructions. After nucleofection, the cells were transferred into the culture media supplemented with 10% WEHI-3 cell supernatant (source of IL-3). Puromycin (5 µg/mL) was added into the culture media 48 h after nucleofection. A stable selection was achieved by culturing cells for 1 week in the presence of puromycin. The single-cell dilution protocol [28] was used to obtain cell clones that were thereafter analyzed by PCR and immunoblotting.

Single-cell clones were expanded, the genomic DNA was extracted with the QIAamp DNA Mini Kit (Qiagen, Gilden, Germany), and a deletion in the gene was determined by PCR amplification with primers flanking the deleted region: forward 5 -CAGAGTCCCATTGGTTTGACAGGCT-3 ; reverse 5'-GGACAGGGGATTGGTTAGATACA-3 . The amplified fragments were visualized in 2% agarose gels stained by GelRed Nucleic Acid Gel Stain (Biotium, Fremont, CA, USA). While an amplification of short fragments (approx. 560bp) was detected in SHP-1 deficient clones, no amplification was found in control BMMCs due to the large size of the deleted region (approx. 6 kb).

2.6. Reverse Transcription PCR (RT-PCR)

The total RNAs from BMMCs or mouse spleen, heart, brain, and liver was isolated with the RNeasy Mini kit (Qiagen) and converted to cDNAs using the SuperScript® VILO cDNA Synthesis Kit with random primers (ThermoFisher Scientific), according to the manufacturer's protocol. The PCRs were performed with gene-specific primers for mouse SHP-1 (*Ptpn6*, NCBI Ref. Seq.: NM_013545.3, NM_001077705.2; primers anneal to both transcript variants) and for mouse SHP-2 (*Ptpn11*, NCBI Ref. Seq.: NM_011202.3, NM_001109992.1; primers anneal to both transcript variants). All primers were tested in silico by Basic Local Alignment Search Tool from National Center for Biotechnology Information (BLAST NCBI; NIH, Bethesda, MD, USA) to amplify the specific targets. The primer sequences are summarized in Supplemental Table S1. The PCRs were performed as described [20]. The amplified fragments were visualized in 2% agarose gels.

2.7. Real-Time qRT-PCR

The total RNAs was extracted in three independent isolations from nonactivated and activated BMMCs or SHP-1_KO cells using the RNeasy Mini Kit (QIAGEN), according to the manufacturer's protocol. The RNAs were converted to cDNA with the High-Capacity cDNA Reverse Transcription Kit using random primers (Applied Biosystems, Waltham, MA, USA), according to the manufacturer's protocol. The quantitative PCRs were performed with gene-specific primers for mouse interleukin 13 (*Il13*, NCBI Ref. Seq.: NM_008355.3), tumor necrosis factor (*Tnf*, NCBI Ref. Seq.: NM_013693.3, NM_001278601.1; primers anneal to both transcript variants), prostaglandin-endoperoxide synthase 2 (*Ptgs2*, NCBI Ref. Seq.: NM_011198.4), and glyceraldehyde-3-phosphate dehydrogenase (*Gapdh*, NCBI Ref. Seq.: NM_001289726.1, NM_008084.3; primers anneal to both transcript variants). All primers were tested in silico by NCBI BLAST to amplify the specific targets. The primer sequences are summarized in Supplemental Table S1. The quantitative PCRs were performed in the LightCycler 480 System (Roche, Mannheim, Germany) as described previously [20]. Each sample was run in triplicate. The identity of the PCR products was verified by sequencing.

2.8. Lentiviral Infection

Lentiviral infections were done as described previously [7] using HEK 293FT packaging cells for virus preparation. Virus particles with the pmSHP-1-hygro construct were added to the cells and replaced after 3 days with a fresh complete medium containing 1 mg/mL hygromycin B. A stable selection was achieved by culturing the cells for 1–2 weeks.

2.9. Cell Activation

The cells were sensitized with DNP-specific IgE (mouse mAb SPE-7; 1 μg/mL) for 2 h in a culture medium without the 10% WEHI-3 cell supernatant and activated with Ag (DNP-albumin conjugate; 100 ng/mL; 30–40 mol DNP/mol albumin) for 1–30 min in a buffered saline solution (20 mM HEPES, pH 7.4, 135 mM NaCl, 5 mM KCl, 1.8 mM $CaCl_2$, 2 mM $MgCl_2$, 5.6 mM glucose) supplemented with 0.1% albumin as described [7]. For the immunofluorescence experiments, the BMMCs were sensitized in suspension, overlaid on fibronectin-coated coverslips, and then activated [7].

2.10. Degranulation Assay and Determination of Intracellular Ca^{2+} Concentration

The degree of degranulation was quantified as the release of β-hexosaminidase from Ag-activated cells, using 4-NAG as a substrate [5]. The extent of degranulation was calculated as follows: absorbance of culture supernatant ×100/absorbance of total cell lysate and normalized to control cells.

Changes in the level of free intracellular Ca^{2+} were measured using Fura-2-AM as a cell permeant calcium reporter following the protocol for sample handling as described [7]. The intracellular free Ca^{2+} was measured in a microplate reader Infinite M200 (Tecan, Männedorf, Switzerland) as a ratio of

Fura emissions at 510 nm after excitation with 340 nm and 380 nm (340/380) lasers at the indicated time points. After the measurement of the Ca^{2+} basic level, activation was triggered by the addition of Ag.

2.11. Evaluation of Cell Growth

Cell proliferation was assessed by the manual cell counting of control BMMCs or SHP-1_KO cells. A total of 2×10^5 cells diluted in the culture medium were plated into the wells of a 6-well plate. The cells were counted at one day intervals from one to six days. The samples were counted in doublets in a total of three independent experiments.

2.12. Preparation of Cell Extracts

Whole-cell extracts for SDS-PAGE were prepared by washing the cells in a cold HEPES buffer (50 mM HEPES pH 7.6, 75 mM NaCl, 1 mM $MgCl_2$, and 1 mM EGTA), solubilizing them in a hot SDS-sample buffer and boiling for 5 min. When preparing the extracts for immunoprecipitation and GST pull-down assays, the cells were rinsed twice in cold HEPES buffer and extracted at a concentration of 1×10^7 cells/mL for 10 min at 4 °C with a HEPES buffer supplemented with 1% NP-40 (extraction buffer) and protease inhibitor mixture. The suspension was then spun down (20,000 × g, 15 min, 4 °C), and the supernatant was collected. When preparing the extracts for gel filtration chromatography, the cells were extracted at a concentration of 14×10^7 cells/mL.

2.13. Immunoprecipitation, Kinase Assay, GST Pull-Down Assay, Gel Electrophoresis, and Immunoblotting

Immunoprecipitation was performed as previously described [29,30]. The cell extracts were incubated with beads of protein A saturated with mAbs to (i) γ-tubulin (TU-31; IgG2b), (ii) GCP2 (GCP2-01; IgG2b), or (iii) NF-M (NF-09; IgG2a, negative control); with rabbit Abs to (iv) γ-tubulin (T5192), (v) SHP-1, (vi) SHP-2, (vii) Syk, (viii) (GFP), (ix) GIT1, (x) βPIX, or (xi) non-muscle myosin (negative control); or with (xii) immobilized protein A alone. The extracts were also incubated with beads of protein G saturated with mAb to GCP4 (IgG1) or with immobilized protein G alone. The antibodies to γ-tubulin (T5192), SHP-1, SHP-2, GCP4, and GFP were used at Ig concentrations 2–5 µg/mL. Abs to Syk, in the form of ascitic fluid, and myosin were used at a dilution of 1:500 and 1:100, respectively. mAbs TU-31, GCP2-01, and NF-09, in the form of hybridoma supernatants, were diluted 1:2.

Alternatively, beads with immunoprecipitated material were used for the in vitro kinase assay as described previously [6]. The ^{32}P-labeled-immunocomplexes were separated by gel electrophoresis and blotted to membranes, and ^{32}P-labeled proteins were detected by autoradiography using the Amersham Typhoon scanner (GE Healthcare Europe GmbH, Freiburg, Germany). The preparation and purification of GST-tagged fusion proteins were described previously, as were the pull-down assays with whole-cell extracts [30].

Gel electrophoresis and immunoblotting were performed using standard protocols [31]. For immunoblotting, mAbs to γ-tubulin (GTU-88), P-Tyr (PY-20), GCP4, GCP5, and GCP6 were diluted 1:10,000, 1:2000, 1:1000, 1:1000, and 1:500, respectively. mAbs to GCP2 (GCP2-02), in the form of a spent culture supernatant, and Syk (Syk-01), in the form of ascitic fluid, were diluted 1:10 and 1:1000, respectively. Rabbit Abs to SHP-1, SHP-2, actin, GFP, GCP3, βPIX, and GIT1 were diluted 1:100,000, 1:50,000, 1:10,000, 1:5000, 1:3000, 1:3000, and 1:1000, respectively. Rabbit Abs to phospho-SHP-1 (Y^{564}) and phospho-Syk (Y^{352}) were diluted 1:2000 and 1:1000, respectively. Secondary anti-mouse and anti-rabbit Abs conjugated with HRP (Promega Biotec) were diluted 1:10,000. The TrueBlot anti-rabbit IgG HRP was diluted 1:100,000. The HRP signal was detected with SuperSignal WestPico Chemiluminescent reagents and the LAS 3000 imaging system (Fujifilm, Düsseldorf, Germany). The AIDA image analyzer v5 software (Raytest, Straubenhardt, Germany) was used for the quantification of signals from immunoblots.

2.14. Gel Filtration Chromatography

Gel filtration was performed using fast protein liquid chromatography (AKTA-FPLC system, Amersham) on a Superose 6 10/300 GL column (Amersham) as described previously [32]. The column equilibration and chromatography were performed in an extraction buffer.

2.15. Microtubule Regrowth

Microtubule regrowth from the centrosomes was followed in a nocodazole washout experiment. The cells growing in suspension were treated with nocodazole at a final concentration of 10 µM for 1 h at 37 ℃ to depolymerize microtubules. The cells were then washed with phosphate-buffered saline (PBS) precooled to 4 ℃ (3 times, 5 min each) to remove the drug and transferred to the complete medium tempered to 28 ℃, and microtubule regrowth was allowed for 1.5 min at 28 ℃. After that, the cells were fixed and immunostained in suspension. In the case of MCF7 growing on coverslips, the microtubules were depolymerized by 30 µM nocodazole for 1 h and regrowth was performed as described [33].

2.16. Immunofluorescence Microscopy

The cells were fixed and immunostained as described [34]. The samples were fixed in formaldehyde/Triton X-100 (F/Tx) and, for the double-label experiments with anti-γ-tubulin Ab, were postfixed in cold methanol (F/Tx/M). mAbs to P-Tyr (4G10) and pericentrin were diluted 1:1000 and 1:250, respectively. mAbs to γ-tubulin (TU-30), in the form of a spent culture supernatant, and Syk (Syk-01), in the form of ascitic fluid, were diluted 1:10 and 1:1000, respectively. Rabbit Abs to γ-tubulin (T3195) and α-tubulin were diluted 1:500 and 1:100, respectively. Secondary AF488- and Cy3-conjugated anti-rabbit Abs were diluted 1:200 and 1:1000, respectively. The DY549-conjugated anti-mouse Ab was diluted 1:1000. The preparations were mounted in MOWIOL 4–88 (Calbiochem, San Diego, CA, USA) and examined with an Olympus AX-70 Provis microscope (Olympus, Hamburg Germany) equipped with a 60×/1.0 NA water objective or with a Delta Vision Core system (AppliedPrecision, Issaquah, WA, USA) equipped with a 60×/1.42 NA oil objective. Some images were deconvoluted with Huygens Professional v18.10 (Scientific Volume Imaging, Hilversum, the Netherlands). To quantify the microtubule regrowth, different areas per sample were taken in both fluorescence channels. The sum of the γ-tubulin or α-tubulin immunofluorescence intensities was obtained from 11 (BMMCs) or 9 (MCF7) consecutive frames (0.2 µm steps), with the middle frame chosen with respect to the highest γ-tubulin intensity. The quantification of the microtubule regrowth assay was analyzed automatically in 1-µm regions of interest (ROIs) centered at the centrosomes, marked by γ-tubulin staining, using an in-house written macro (Supplemental Text 1) for Fiji processing program [35]. The determination of the number of cells that responded to the activation events by a generation of microtubule protrusions was done as described previously. Three experiments were performed, and in each experiment, 150–200 cells were examined [7].

2.17. Statistical Analysis

All data are presented as means ± SD or SE, as indicated. For the statistical analysis, the two-tailed, unpaired Student's *t*-test was applied. For the statistical analysis of cells with microtubule protrusions, the Chi-Square Goodness of Fit Test was applied.

3. Results

3.1. Protein Tyrosine Phosphatase SHP-1 Interacts with Proteins of γ-Tubulin Complexes

Ag-induced FcεRI aggregation results in a transient increase of the protein tyrosine phosphorylation level in mast cells isolated from different sources [36,37]. Similarly, in the BMMC line used in this study, the P-Tyr signal in Ag-activated cells substantially increased at the beginning of activation but

then gradually weakened to the original level (Figure 1A). When compared with nonactivated cells, a 3-min activation resulted in an approximate fivefold increase of P-Tyr proteins, but after 30 min, the level of protein tyrosine phosphorylation returned to that in nonactivated cells (Supplemental Figure S1). Transient changes in the P-Tyr level after Ag-induced activation were also detected by immunofluorescence in fixed BMMCs stained with anti-P-Tyr antibody (Figure 1Ba–c). Previously, we have shown that an Ag-induced activation of BMMCs resulted in the generation of protrusions containing microtubules (microtubule protrusions) [7]. We observed a time course correlation between the level of P-Tyr signal and the generation of protrusions containing microtubules. In nonactivated cells, microtubule protrusions were very rare, but after 3 min activation, they appeared in a large number of cells. In later stages of the activation, microtubule protrusions diminished (Figure 1Bd–f). A statistical evaluation of BMMCs with microtubule protrusions during the activation was documented by a histogram (Supplemental Figure S3E, Control). Altogether, these data on BMMCs support the previous findings that active tyrosine phosphatases are involved in the later stages of an Ag-induced activation [3]. Protein tyrosine phosphatases might also be important for the regulation of microtubule organization in BMMCs.
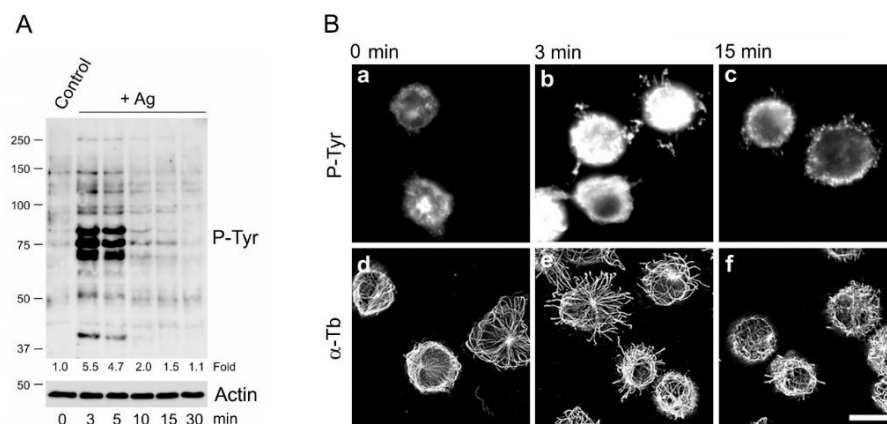
Figure 1. The antigen-induced activation of bone marrow-derived mast cells (BMMCs) results in a transient increase of the phosphorylation of proteins on tyrosine and the spatial redistribution of microtubules. (**A**) A comparison of the protein tyrosine phosphorylation level (P-Tyr) on blots from whole-cell lysates of controls and cells activated by FcεRI aggregation (**+**Ag) using an antigen (100 ng/mL) for various time intervals: Actin served as the loading control. Representative image, out of three repetitions, is shown. The numbers under the blot indicate the relative amounts of P-Tyr normalized to unstimulated control cells and the amount of actin in individual samples. (B) IgE-sensitized cells activated with antigen (100 ng/mL) for various time intervals were fixed and stained for tyrosine-phosphorylated proteins (**a–c**) and α-tubulin (**d–f**). Fixation F/Tx. Scale bar, 10 μm.

It is well established that non-transmembrane Src homology 2 (SH2) domain-containing protein tyrosine phosphatases (SH-PTPs; SHPs) are critical regulators of intracellular signaling in activated mast cells [3]. SHP-1 (gene *Ptpn6*) and SHP-2 (gene *Ptpn11*) are SHPs sharing many structural and regulatory features. These include the presence of two SH2 domains (N-SH2, C-SH2), a phosphatase domain, and a C-terminal domain containing conserved tyrosine phosphorylation sites that influence the function and activities of these phosphatases [38]. The expression of SHPs in BMMCs was determined by gel-based RT-PCR analysis using mouse spleen and heart as positive controls for SHP-1 and SHP-2, respectively. The brain and the liver were used as additional positive controls for SHP-2. We found that both SHP-1 and SHP-2 were abundant in BMMCs. In the tested tissue samples, SHP-1 was prominent only in the spleen, while SHP-2 was highly expressed in all four tested mouse tissues: spleen, heart, brain, and liver (Figure 2I), confirming that SHP-2 is more general than SHP-1, which is primarily expressed in hematopoietic cells [38]. The immunoprecipitation experiments with Abs to SHP-1 and SHP-2 revealed a coprecipitation of γ-tubulin with SHP-1 (Figure 2IIA, lane 3) but not

with SHP-2 (Figure 2IIB, lane 3). The reciprocal precipitation with mAb to γ-tubulin sequence 434–449 (TU-31) confirmed the interaction of SHP-1 (Figure 2IIF, lane 3) but not SHP-2 (Figure 2III, lane 3) with γ-tubulin. Similarly, when the Ab to γ-tubulin sequence 38–53 was used for the precipitation of the two SHP isotypes, only SHP-1 coprecipitated with γ-tubulin (Supplemental Figure S2A). In the following experiments, mAb TU-31 was used for the precipitation of γ-tubulin. The precipitation with Ab to SHP-1 did not coprecipitate SHP-2 (Figure 2IIG, lane 3) and with Ab to SHP2 did not coprecipitate SHP-1 (Figure 2IIE, lane 3). The results of these experiments suggested that SHP-1 might interact with γ-tubulin complexes and might modulate microtubule nucleation.
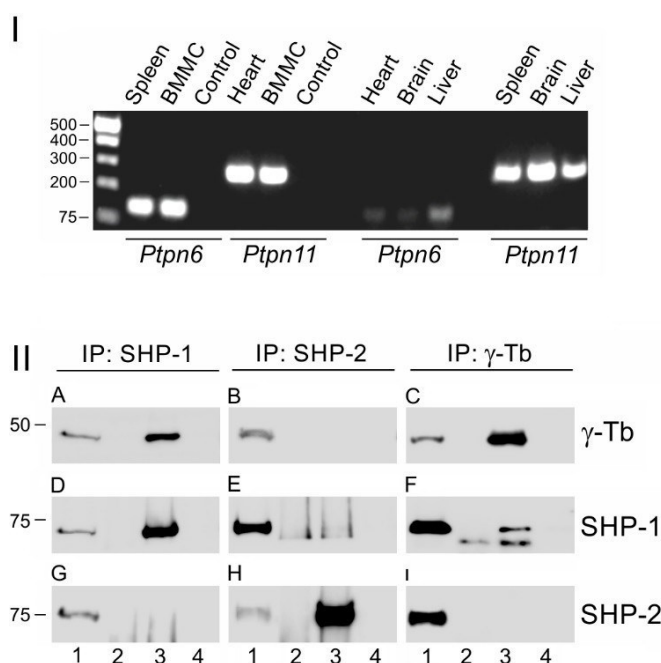
Figure 2. The SHP-1 and SHP-2 in complexes containing γ-tubulin. (**I**) The expression profile of SHP-1 and SHP-2 in selected mouse tissues and BMMCs: A gel-based RT-PCR analysis of mouse SHP-1 (*Ptpn6*) and SHP-2 (*Ptpn11*) is shown. Mouse spleen and heart served as positive controls for SHP-1 and SHP-2, respectively. (**II**) The extracts from BMMCs precipitated with immobilized Abs specific to SHP-1 (**A**,**D**,**G**), SHP-2 (**B**,**E**,**H**), or γ-tubulin sequence 434–449 (**C**,**F**,**I**): The blots were probed with Abs to γ-tubulin (γ-Tb), SHP-1, and SHP-2. The load (*lane 1*), the immobilized Abs not incubated with cell extracts (*lane 2*), the precipitated proteins (*lane 3*), and the carriers without Abs and incubated with cell extracts (*lane 4*).

To ascertain whether, besides γ-tubulin, SHP-1 interacts also with γ-tubulin complex proteins, immunoprecipitation experiments were performed with Abs to γ-tubulin, GCP2, and GCP4. The immunoblot analysis revealed a coprecipitation of SHP-1 with γ-tubulin (Figure 3IA, lane 3), GCP2 (Figure 3IB, lane 3), and GCP4 (Figure 3IC, lane 3). Also, the reciprocal precipitation with Ab to SHP-1 confirmed the interaction of GCP2 (Figure 3IH, lane 3), GCP4 (Figure 3IL, lane 3), and γ-tubulin (Figure 3IP, lane 3) with SHP-1. Moreover, SHP-1 formed complexes with GCP3, GCP5, and GCP6 (Supplemental Figure S2B). As expected, Ab to γ-tubulin coprecipitated GCP2 (Figure 3IE, lane 3) and GCP4 (Figure 3II, lane 3), Ab to GCP2 coprecipitated GCP4 (Figure 3IJ, lane 3) and γ-tubulin (Figure 3IN, lane 3), and finally, Ab to GCP4 coprecipitated GCP2 (Figure 3IG, lane 3) and γ-tubulin (Figure 3IO, lane 3).
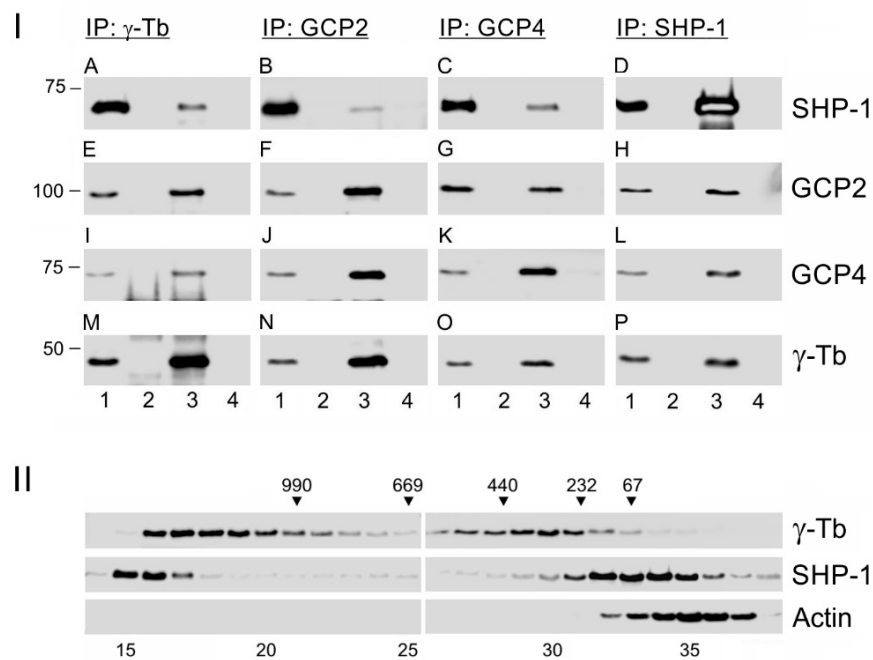
Figure 3. The SHP-1 associates with γ-tubulin complex proteins. (**I**) The immunoprecipitation experiments: Extracts from the BMMCs were precipitated with immobilized Abs specific to γ-tubulin (**A,E,I,M**), GCP2 (**B,F,J,N**), GCP4 (**C,G,K,O**), or SHP-1 (**D,H,L,P**). The blots were probed with Abs to SHP-1, GCP2, GCP4, and γ-tubulin (γ-Tb). The load (*lane 1*), the immobilized Abs not incubated with cell extracts (*lane 2*), the precipitated proteins (*lane 3*), and the carriers without Abs and incubated with cell extracts (*lane 4*). (**II**) The size distribution of the proteins fractionated on Superose 6: The blots of the collected fractions were probed with Abs to γ-tubulin (γ-Tb), SHP-1, and actin. The calibration standards (in kDa) are indicated on the top. The numbers at the bottom denote individual fractions.

To independently confirm the interaction of SHP-1 with γ-tubulin, we performed immunoprecipitation experiments using extracts from cells expressing EGFP tagged SHP-1 or EGFP alone. For this, we used HEK cells that could be easily transfected. The antibody to GFP coprecipitated γ-tubulin from HEK cells expressing mSHP-1_EGFP (Supplemental Figure S2C, lane 4) but not from cells expressing EGFP alone (Supplemental Figure S2C, lane 5). The isotype controls for the immunoprecipitation experiments with mouse and rabbit Abs are shown in Supplemental Figure S2D.

The combined data indicate that SHP-1 is capable of forming complexes with γ-TuRC proteins. This finding was further supported by a separation of the extracts from BMMCs on a Superose 6B column. SHP-1 was mainly distributed in low molecular weight fractions, but its part was also detected in high molecular weight pools, where γ-tubulin was present in the form of γTuRCs. On the other hand, the control actin was not detected in the high molecular fractions (Figure 3II).

3.2. Characterization of BMMCs Deficient in SHP-1

To evaluate the effect of SHP-1 on microtubule nucleation, we prepared BMMC lines lacking SHP-1. For this, we took advantage of CRISP/Cas 9 editing. To delete the gene region containing the canonical and alternative start codons, BMMCs were transfected with CRISPR/Cas9 vectors (sgRNA#1, sgRNA#2, SpCas9) together with reporter plasmid pRR-mSHP1-puro for an enrichment of the cells not expressing SHP-1. A schematic diagram of the mouse SHP-1 gene with sites targeted by sgRNA#1 and sgRNA#2 enabling an efficient depletion of SHP-1 is shown in Figure 4A. We established three independent cell lines (denoted SHP-1_KO1, SHP-1_KO2, and SHP-1_KO3) that have deletions in the targeted region (Figure 4B) and undetectable SHP-1 in immunoblotting (Figure 4C). If not mentioned otherwise, in the following figures, we documented the results with SHP-1_KO1 cells (abbreviated SHP-1_KO).
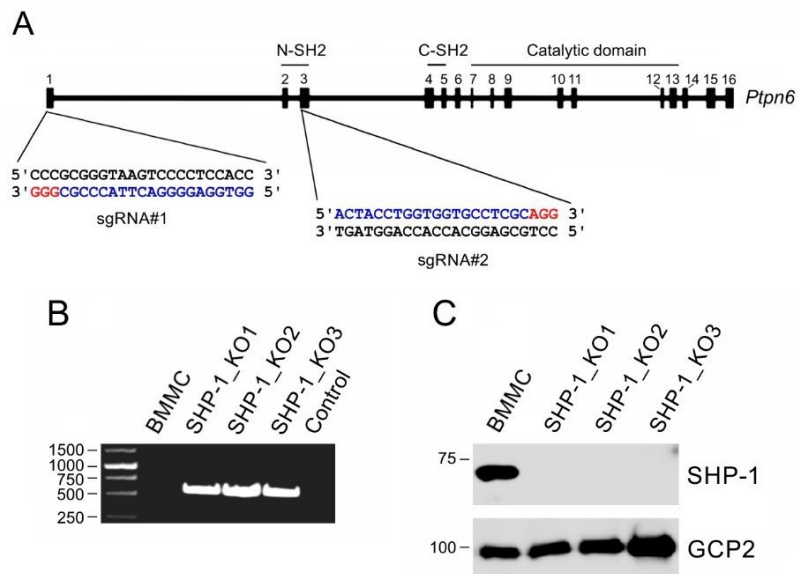
Figure 4. The generation of SHP-1 deficient cell lines. (**A**) A schematic diagram of *Ptpn6* with sites targeted by guide RNA (sgRNA) sequences: The targeted sites (blue) and protospacer-adjacent motifs (PAM; red) on the gene (18.01 kb) containing 16 exons are shown. The defined domains are indicated. (**B**) The PCR amplification of genomic DNA from the control cells (BMMC) and SHP-1-deficient cell lines (SHP-1_KO1, SHP-1_KO2, SHP-1_KO3) with primers flanking the deleted region: The template is not present in the control sample. Due to the large size of the deleted region (approx. 6 kb), no amplification was found in the control BMMCs. The amplification of short fragments (approx. 560 bp) was detected in SHP-1-deficient clones. (**C**) The SHP-1 protein levels in BMMCs and SHP-1-deficient cell lines analyzed by an immunoblotting of whole-cell lysates: GCP2 served as the loading control.

Compared to the control BMMCs, the absence of SHP-1 resulted in an increase of the P-Tyr protein level during the activation (Figure 5A; P-Tyr). Src family protein tyrosine kinases phosphorylate SHP-1 and the phosphorylation of Y^{564} on SHP-1 are critical to achieving a maximal phosphatase activity [39]. In the course of the control cell activation, a transient increase of the phosphorylation level on Y^{564} of SHP-1 was detected (Figure 5A, P-SHP-1[Y^{564}]). SHP-1 negatively regulates the tyrosine phosphorylation of the Syk kinase, which is important for the signal propagation in activated mast cells [3]. The phosphorylation of Syk on Y^{352} releases its autoinhibition and marks active kinase [40,41]. Here, we show that while the deficiency in SHP-1 (SHP-1_KO cells) did not affect the level of Syk (Figure 5A, Syk), the phosphorylation level on Y^{352} of Syk in the course of the activation was significantly higher (Figure 5A, P-Syk [Y^{352}]). An evaluation of all the data obtained by densitometry quantification of P-Syk Y^{352} in the control and SHP-1_KO cells is shown in Supplemental Figure S1B. Proliferation was hampered in SHP-1-deficient cells, as demonstrated in the growth curves (Figure 5B). Both the release of β-hexosaminidase (Figure 5C) and the Ca^{2+} influx (Figure 5D) increased in activated SHP-1_KO cells compared with the control BMMCs. The deficiency in SHP-1 also affected the expression of cytokines and prostaglandins. The levels of mRNA for cytokine tumor necrosis factor (TNFα; gene *Tnf*) and interleukin 13 (IL-13; gene *Il13*) increased in SHP-1_KO cells compared to control cells, and the same held true for prostaglandin-endoperoxidase synthase 2 (COX-2; gene *Ptgs2*) mRNA, essential for the production of prostaglandins (Figure 5E). A significantly higher number of cells with microtubule protrusions was observed in the course of Ag-induced activation in the SHP-1_KO cells compared to the controls (Supplemental Figure S3E, SHP-1_KO).
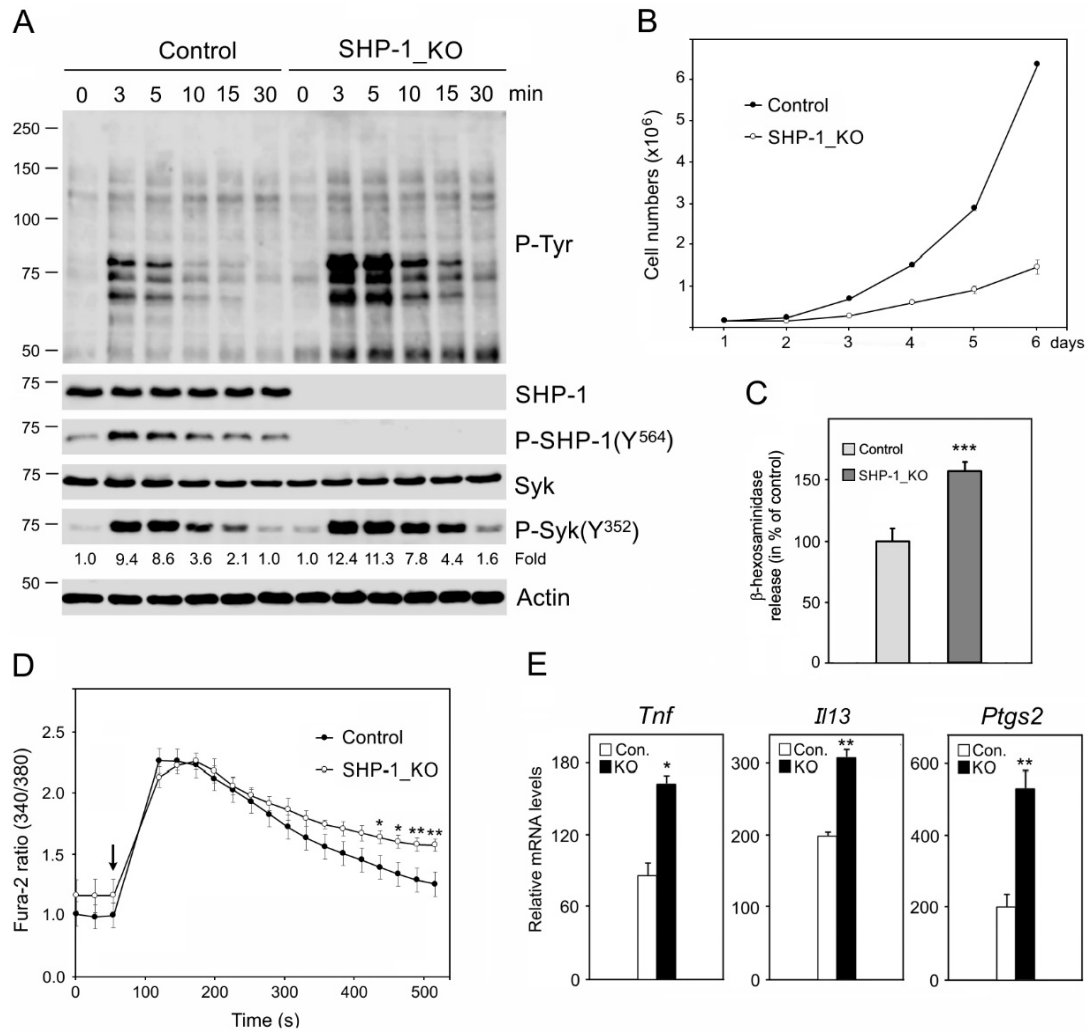
Figure 5. The characterization of cells lacking SHP-1. (**A**) The immunoblot characterization of control BMMCs and BMMCs without SHP-1 (SHP-1_KO): The cells were activated by FcεRI aggregation using an antigen (100 ng/mL) for various time intervals, and the blots from whole-cell lysates were probed with antibodies to phosphotyrosine (P-Tyr), SHP-1, phosphorylated SHP-1 (P-SHP-1[Y^{564}]), Syk, and phosphorylated Syk (P-Syk[Y^{352}]). Actin served as the loading control. Shown is a representative image out of three repetitions. The numbers under the P-Syk (Y^{352}) blot indicate relative amounts of phosphorylated Syk normalized to unstimulated cells and the amount of Syk in the individual samples. (**B**) The growth curves in the control BMMCs and SHP-1_KO cells: A total of 2×10^5 cells was plated in both cell lines. The values indicate the mean $\pm$ SD (*n* = 3). (**C**) The degranulation in the control BMMCs and SHP-1_KO cells: The cells were activated by Ag (100 ng/mL), and the degranulation was measured by β-hexosaminidase release. The data represent the mean $\pm$ SD (*n* = 3), *** $p < 0.00001$. (**D**) The intracellular Ca^{2+} mobilization during cell activation in the control BMMCs and SHP-1_KO cells: IgE-sensitized cells were loaded with Fura-2-acetoxymethyl ester and activated by a high-affinity IgE receptor aggregation with Ag (100 ng/mL). The arrow indicates the addition of Ag. The data represent the mean $\pm$ SD (n = 3) from the independent experiments performed in duplicates; * $p < 0.05$; ** $p < 0.01$. (**E**) The cytokine (TNFα and IL-13) and prostaglandin (COX-2) expressions in the control BMMCs and SHP-1_KO cells in a RT-PCR analysis: The cells were sensitized and either unstimulated or stimulated with Ag (100 ng/mL) for 30 min. The obtained values were normalized with an internal glyceraldehyde-3-phosphate dehydrogenase (GAPDH) control, and the fold increases were determined relative to the unstimulated BMMCs, which was arbitrarily designated a value of 1.0. The data represent the mean $\pm$ SEM (*n* = 3); * $p < 0.05$; ** $p < 0.01$.

3.3. The Absence of SHP-1 Affects Microtubule Regrowth

The de novo formation of microtubules from interphase centrosomes in BMMCs and SHP-1_KO cells was followed by microtubule regrowth in nocodazole-washout experiments as previously described [16,18]. The extent of microtubule regrowth could be modulated by mechanisms regulating either microtubule nucleation or microtubule dynamics. It has been previously reported that microtubule dynamics is regulated in the cell periphery [42]. Three independent experiments were performed with cells deficient in SHP-1 and control BMMCs. α-Tubulin and γ-tubulin immunofluorescence was measured 1.5 min after a washout in a 1.0-μm ROI. When compared with control BMMCs, an increase in microtubule regrowth was observed in both the SHP-1_KO1 (Figure 6A) and SHP-1_KO2 (Supplemental Figure S3A) cells. The typical staining of α-tubulin in the control and SHP-1_KO1 cells is shown in Figure 6Ca,b. The quantification of γ-tubulin immunofluorescence revealed that the amount of γ-tubulin in centrosomes increased in both SHP-1_KO1 (Figure 6B) and SHP-1_KO2 (Supplemental Figure S3B). In contrast to γ-tubulin, the amount of pericentriolar marker pericentrin [43] was not affected (Supplemental Figure S3C,D). The typical staining of γ-tubulin in the control and SHP-1_KO1 cells is shown in Figure 6Cc,d. The importance of SHP-1 in the modulation of proteins interacting with γ-tubulin during activation events was disclosed by an in vitro kinase assay after precipitation with Ab to γ-tubulin. The phosphorylation of proteins associated with γ-tubulin was higher in SHP-1_KO cells compared to the control BMMCs (Supplemental Figure S3G, 3 min).
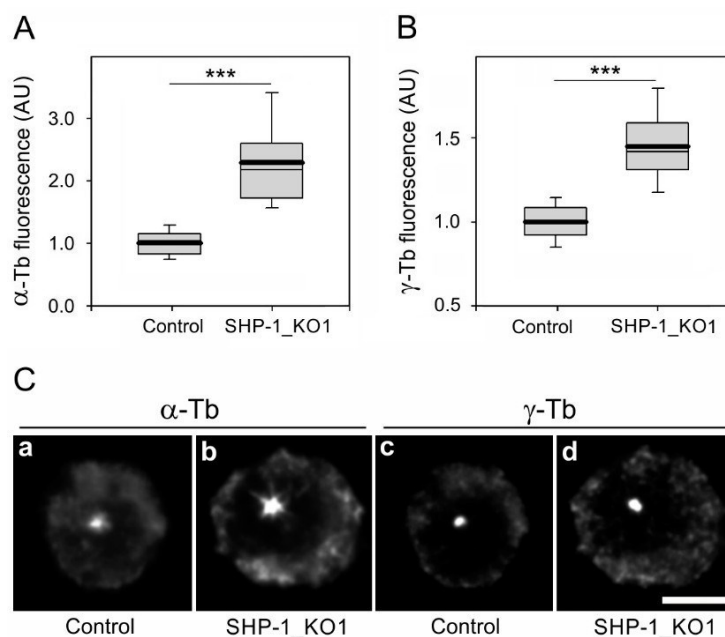
Figure 6. SHP-1 modifies microtubule regrowth. (**A**,**B**) The distribution of α-tubulin or γ-tubulin fluorescence intensities (arbitrary units (AU)) in 1-μm ROI at 1.5 min of regrowth in BMMCs (Control) and SHP-1 deficient BMMCs (SHP-1_KO1) is shown as box plots (three independent experiments, >30 cells counted for each experimental condition). (**A**) The box plot of α-tubulin fluorescence intensities in SHP-1_KO1 cells (n = 100) relative to the control cells (Control, n = 100). (**B**) The box plot of γ-tubulin fluorescence intensities in SHP-1_KO1 cells (n = 100) relative to the control cells (Control, n = 100). The bold and thin lines within the box represent the mean and median (the 50th percentile), respectively. The bottom and top of the box represent the 25th and 75th percentiles. The whiskers below and above the box indicate the 10th and 90th percentiles. *** p < 0.00001. (**C**) The labeling of α-tubulin and γ-tubulin in the microtubule regrowth experiment in the control cells (Control; **a**,**c**) and SHP-1_KO1 cells (**b**,**d**). The cells were fixed with F/Tx/M at 1.5 min of regrowth. The pairs of images Figure 6a,b and Figure 6c,d were collected and processed in exactly the same manner. Scale bar, 5 μm.

For the phenotypic rescue experiments, we prepared a lentiviral vector encoding mouse SHP-1. To rescue microtubule regrowth, SHP-1 in the vector or empty vector were expressed in SHP-1_KO cells. A typical result of an immunoblotting experiment is shown in Figure 7A. When compared with the control BMMCs, an increase in the microtubule regrowth was observed in SHP-1_KO cells with the empty vector, while the introduction of SHP-1 into these cells restored microtubule regrowth to that in control cells (Figure 7B). The quantification of γ-tubulin immunofluorescence revealed that the amount of γ-tubulin in centrosomes also increased in SHP-1_KO cells with the empty vector and was restored after the introduction of SHP-1 (Figure 7B). An introduction of SHP-1 into deficient cells also restored degranulation (Supplemental Figure S3F).
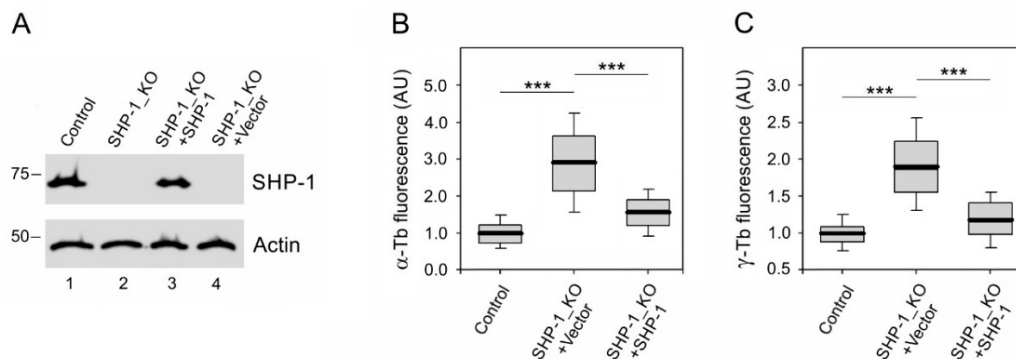
Figure 7. Microtubule regrowth in a phenotypic rescue experiment. (**A**) An immunoblot analysis of SHP-1 in whole-cell lysates from BMMCs (Control), SHP-1_KO cells, SHP-1_KO cells rescued by mSHP-1 in lentiviral vector (SHP-1_KO+SHP-1), and SHP-1_KO cells infected by empty vector (SHP-1_KO+Vector): The blots were probed by Abs to SHP-1 and Actin (loading control). (**B**,**C**) The distribution of α-tubulin or γ-tubulin fluorescence intensities (arbitrary units (AU)) in 1-µm ROI at 1.5 min of regrowth in BMMCs (Control), SHP-1_KO cells infected by empty vector (SHP-1_KO+Vector), and SHP-1_KO cells rescued by mSHP-1 in lentiviral vector (SHP-1_KO+SHP-1) is shown as box plots (three independent experiments, >50 cells counted for each experimental condition). (**B**) The box plot of α-tubulin fluorescence intensities in SHP-1_KO+Vector (n = 159) and SHP-1_KO+SHP-1 cells (n = 236) relative to the control cells (Control, n = 315). (**C**) The box plot of γ-tubulin fluorescence intensities in SHP-1_KO+Vector (n = 255) and SHP-1_KO+SHP-1 cells (n = 244) relative to the control cells (Control, n = 315). The bold and thin lines within the box represent the mean and median (the 50th percentile), respectively. The bottom and top of the box represent the 25th and 75th percentiles. The whiskers below and above the box indicate the 10th and 90th percentiles. *** p < 0.00001.

Altogether, these data suggest that SHP-1 negatively regulates microtubule nucleation from the centrosomes, and its regulatory role is conveyed by the amount of γ-tubulin/γTuRCs.

3.4. Inhibition of Enzymatic Activity of SHP-1 Modulates Microtubule Regrowth

To find out whether the SHP-1 enzymatic activity is essential for the regulatory role of phosphatase in microtubule nucleation, we performed microtubule regrowth experiments with SHP inhibitors. We used both a highly specific inhibitor TPI-1 at low concentrations, targeting only SHP-1 [44], and a less specific inhibitor NSC87877, targeting both SHP-1 and SHP-2 [45]. The cells were preincubated in the presence of 100 nM TPI-1, 500 nM NSC87877, or a DMSO carrier (Control) for 1 h before the nocodazole washout assay, and the inhibitors were present throughout the assay. The inhibition of phosphatase activity by both inhibitors resulted in an increase of the immunofluorescence signal for both α-tubulin (Figure 8A) and γ-tubulin (Figure 8B). The typical co-staining of α-tubulin and γ-tubulin in the control and NSC87877-treated cells is shown in Figure 8C. These results document that enzymatically active SHP-1 modulates the nucleation of microtubules in BMMCs.
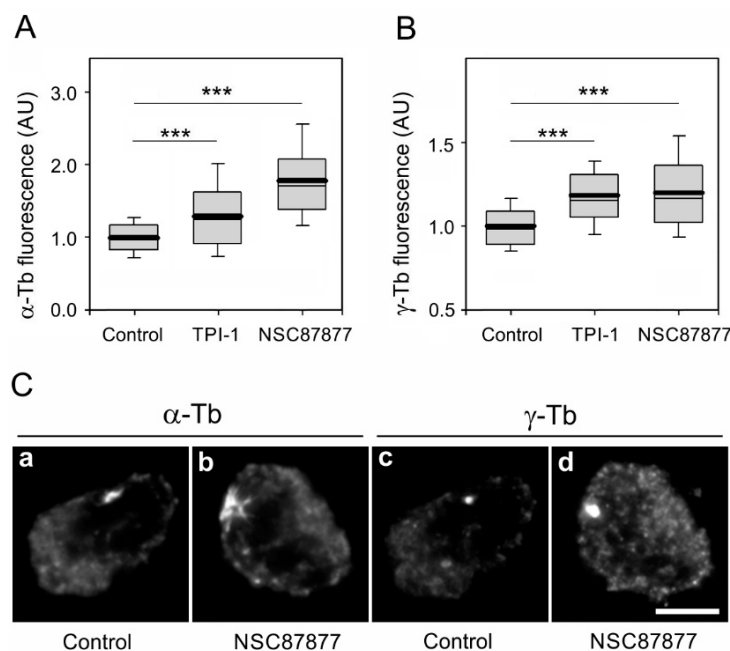
Figure 8. The inhibition of SHP-1 activity augments microtubule nucleation. (**A**,**B**) BMMCs were cultivated with 100 nM TPI-1, 500 nM NSC87877, or a DMSO carrier (Control) for 1 h before and during the microtubule regrowth assay. The distribution of α-tubulin or γ-tubulin fluorescence intensities (arbitrary units (AU)) in 1-μm ROI at 1.5 min of regrowth is shown as box plots (three independent experiments, >50 cells counted for each experimental condition). (**A**) The box plot of α-tubulin fluorescence intensities in TPI-1 (*n* = 158) or NSC87877 (*n* = 158) preincubated cells relative to the control cells (Control, n = 158). (**B**) The box plot of γ-tubulin fluorescence intensities in TPI-1 (*n* = 158) or NSC87877 (n = 158) preincubated cells relative to the control cells (Control, *n* = 158). The bold and thin lines within the box represent the mean and median (the 50th percentile), respectively. The bottom and top of the box represent the 25th and 75th percentiles. The whiskers below and above the box indicate the 10th and 90th percentiles. *** $p < 0.00001$. (**C**) The labeling of α-tubulin and γ-tubulin in the microtubule regrowth experiment in control cells with a DMSO carrier (Control; **a**,**c**) and cells pretreated with 500 nM NSC87877 for 1 h before and during the microtubule regrowth assay (**b**,**d**). The cells were fixed with F/Tx/M at 1.5 min of regrowth. The pairs of images Figure 8a,b and Figure 8c,d were collected and processed in exactly the same manner. Scale bar, 5 μm.

Although SHP-1 is mainly expressed in hematopoietic cells, it is also detected in some epithelial cells, e.g., human epithelial-like breast adenocarcinomas. This is demonstrated by an immunoblotting of the cell extracts from the MCF7 cell line (Supplemental Figure S4A). Precipitation experiments with MCF7 extracts showed that SHP-1 interacted with γ-tubulin, GCP2, and GCP-4 (Supplemental Figure S4A, left panel, IP: SHP-1 lane 3). A reciprocal precipitation with Ab to γ-tubulin confirmed the interaction of SHP-1 with γ-tubulin (Supplemental Figure S4A, right panel, lane 3). Altogether, these experiments suggest that the formation of complexes containing SHP-1 and γ-tubulin complex proteins is not limited to BMMCs. To evaluate whether an inhibition of the SHP-1 activity modulates microtubule regrowth in MCF7 cells, we performed microtubule regrowth assay in cells preincubated with TPI-1. Similarly, as in BMMCs, an inhibition of the SHP-1 activity resulted in an enhancement of microtubule regrowth (Supplemental Figure S4B) and the accumulation of γ-tubulin in centrosomes (Supplemental Figure S4C). These data suggest that active SHP-1 can regulate microtubule nucleation, by affecting the centrosomal accumulation of γ-tubulin in various cell types.

3.5. SHP-1 Interacts with Syk Protein Tyrosine Kinase Associating with γ-Tubulin Complex Proteins

Even though SHP-1 affected microtubule nucleation from centrosomes in BMMCs, we failed to localize the phosphatase to a centrosomal region, using a limited number of commercial Abs, both in

resting cells and cells activated by FcεRI aggregation. On the other hand, SHP-1 regulated the activity of the Syk kinase (Figure 5), which was reported to interact with γ-tubulin [6]. Moreover, in breast cancer cells, Syk localized to centrosomes [46,47]. We, therefore, investigated whether, in BMMCs, Syk forms complexes with SHP-1 and localizes to centrosomes.

Double-label immunofluorescence experiments with Abs to Syk and γ-tubulin revealed that, in BMMCs, Syk accumulated in a broad pericentrosomal region (Figure 9A, Syk), where centrosomal γ-tubulin was located (Figure 9A, γ-Tb). SHP-1 precipitated in the course of the activation Syk and γ-tubulin (Figure 9B, IP: SHP-1), and a reciprocal precipitation with Ab to Syk (Figure 9B, IP: Syk) corroborated the interaction of Syk with SHP-1 and γ-tubulin. SHP-1 precipitated less Syk in activated cells when compared to resting cells. Pull-down experiments with GST-tagged whole-length Syk confirmed that, in BMMCs, SHP-1, γ-tubulin, and GCP-2 associate with recombinant Syk (Figure 9C, lane 3) but not with GST alone (Figure 9C, lane 5). Immunocomplexes containing γ-tubulin and Syk were also detected when the antibody to γ-tubulin was used for precipitation (Figure 9D, lane 3). The activities of Syk and associated proteins during activation were modulated by SHP-1 as disclosed in vitro kinase assays after a precipitation with Ab to Syk. The phosphorylation of proteins associated with Syk was higher in SHP-1_KO cells compared to the control BMMCs (Supplemental Figure S3H).
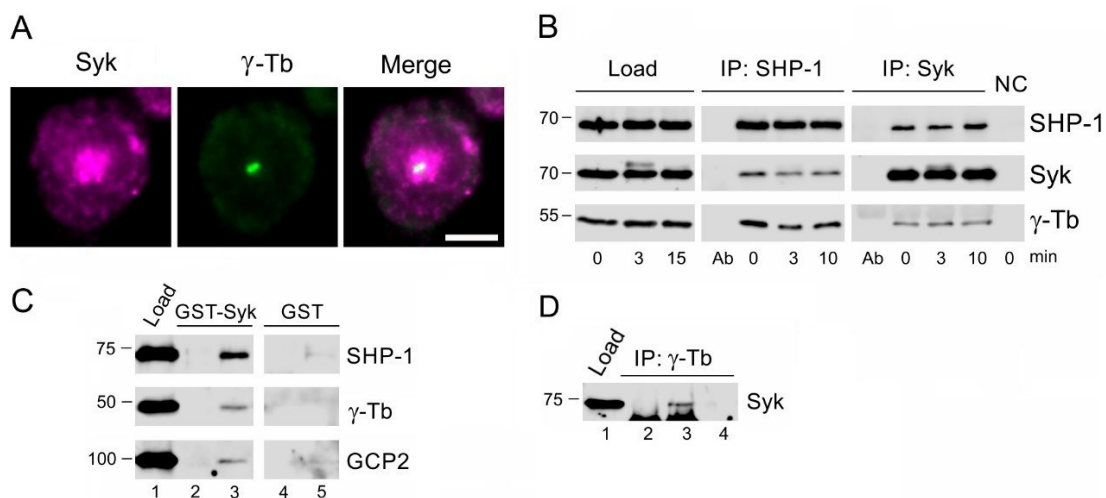
Figure 9. Syk kinase localizes to a centrosomal region and associates both with γ-tubulin complex proteins and SHP-1. (**A**) The double-label immunofluorescence staining of Syk and γ-tubulin: The cells were fixed with F/Tx/M and stained for Syk (**a**) in magenta and for γ-tubulin (**b**) in green. A superimposition of the images (Figure 9a,b) is also shown (**c**). Scale bar, 5 μm. (**B**) The immunoprecipitation experiments: Extracts from the nonactivated (0 min) or antigen-activated (3 min, 10 min) BMMCs were precipitated with the immobilized Abs specific to SHP-1 or Syk. The blots were probed with Abs to SHP-1, Syk, and γ-tubulin (γ-Tb). Ab, immobilized Ab not incubated with cell extract; NC, carrier without Ab, incubated with cell extract (negative control). (**C**) The pull-down assay: Extracts from BMMCs incubated with the GST-tagged whole-length Syk or GST alone were immobilized on glutathione-Sepharose beads. The blots of the bound proteins were probed with abs to SHP-1, γ-Tb, and GCP2. The load (*lane 1*), the immobilized GST-Syk not incubated with cell extracts (*lane 2*), the proteins bound to GST-Syk (*lane 3*), the immobilized GST alone not incubated with cell extracts (*lane 4*), and the proteins bound to GST alone (*lane 5*). (**D**) The immunoprecipitation experiment: Extracts from BMMCs were precipitated with immobilized Ab specific to γ-tubulin. The blot was probed with Ab to Syk. The load (*lane 1*), the immobilized Ab not incubated with cell extracts (*lane 2*), the precipitated proteins (*lane 3*), and the carrier without Ab and incubated with cell extracts (*lane 4*).

Collectively, these results suggest that SHP-1 is capable of forming complexes with Syk that interact with γ-tubulin complex proteins. Consequently, the regulatory role of SHP-1 on microtubule nucleation might be due to a modulation of the Syk activity.

4. Discussion

The Ag-induced activation of mast cells leads to rapid cytoskeleton rearrangements and degranulation. Accumulated data point to the importance of microtubules in this process [5,8–10,48]. We have shown previously that the stimulation of mast cells by FcεRI aggregation triggers the generation of complexes containing γ-tubulin, tyrosine-phosphorylated proteins, and tyrosine kinases [6,49]; a transient increase in the amount of polymerized tubulin [6]; and a reorganization of the microtubules [6,7,50]. The opposing actions of protein tyrosine kinases and protein tyrosine phosphatases determine the level of tyrosine phosphorylation during the activation events. It is well-accepted that protein tyrosine kinases are essential during mast cell signaling, but the exact function of protein tyrosine phosphatases is less understood. Here, we report on SHP-1 tyrosine phosphatase interacting with proteins of γ-tubulin complexes and modulating microtubule nucleation from the centrosomes of BMMCs. SHP-1 represents a negative regulator of microtubule nucleation. Our study provides a possible mechanism for the concerted action of tyrosine kinases and tyrosine phosphatases in the regulation of microtubule formation in activated mast cells.

Several lines of evidence indicate that the association of SHP-1 with γ-tubulin complex proteins is specific. First, reciprocal precipitation experiments confirmed an interaction between SHP-1 and proteins constituting γ-TuRCs. Second, two SHPs (SHP-1 and SHP-2) are expressed in BMMCs, but only SHP-1 interacted with the γ-tubulin complex proteins. Third, GFP-tagged SHP-1 interacted with γ-tubulin. Fourth, a gel filtration chromatography revealed that the high molecular weight pool of SHP-1 co-distributed with γ-TuRCs. Finally, the absence of SHP-1 in SHP-1_KO cells increased the phosphorylation of proteins in γ-tubulin immunocomplexes. Interestingly, such an association was not limited to BMMCs, as SHP-1 was also present in γ-tubulin immunocomplexes prepared from human epithelial breast cells MCF7. These findings suggest that the direct or indirect interactions between SHP-1 and γ-tubulin complex proteins might occur in various cell types.

Microtubule nucleation at the centrosome occurs from γ-TuRCs located in the pericentriolar material [13]. We, therefore, asked whether SHP-1 regulates microtubule nucleation in BMMCs by affecting the centrosomal γ-tubulin levels. Our data from measuring the γ-tubulin signal in regrowth experiments from cells lacking SHP-1 or cells with an inhibited SHP-1 enzymatic activity suggest that SHP-1 prevents γ-tubulin accumulation at the centrosome. Moreover, this SHP-1 function is not limited to BMMCs, as it was also found in epithelial MCF7 cells expressing SHP-1. On the other hand, no changes in the amount of pericentrin were detected, indicating that the pericentriolar matrix integrity was not affected. Although SHP-1 represents a negative regulator of microtubule nucleation, we did not locate SHP-1 into the centrosome using a limited number of commercial Abs. However, we cannot rule out that SHP-1 associates with the centrosomes only transiently. Alternatively, it could modulate cytosolic proteins before their interaction(s) with centrosomes. In principle, SHP-1 could affect tyrosine-phosphorylated γTuRCs proteins or tyrosine-phosphorylated proteins that target, anchor, or activate γ-TuRCs [43]. Alternatively, SHP-1 could regulate protein kinases modulated by tyrosine.

In contrast to αβ-tubulin dimers [51,52], the posttranslational modification of γ-tubulin is less prominent [53]. However, it has been repeatedly reported that γ-tubulin is phosphorylated [14,30,54]. The phosphorylation of γ-tubulin residue Tyr 445, which is invariably present in all γ-tubulins, was described, and a mutation of this residue changed the microtubule dynamics [14]. However, the precipitation of γ-tubulin from resting or activated BMMCs, followed by immunoblotting, did not reveal its phosphorylation on tyrosine [6]. Proteomic studies revealed the tyrosine phosphorylation sites on human GCP2, GCP3, GCP5, and GCP6 [55]. Collectively, these data suggest that tyrosine kinases could regulate γ-tubulin properties. Because GCPs coordinate the arrangement of γ-tubulin in γ-TuRCs, the phosphorylation of GCPs could also regulate the conformational changes that might be required for γ-TuRC activation [56].

Evidence suggests an important role for tyrosine kinases in the regulation of microtubule organization from centrosomes. The Fyn kinase was found on centrosomes in myelocytic leukemia cells HL-60 [57] and human T-lymphocytes [58]. The JAK2 tyrosine kinase specifically associates

with centrioles and regulates microtubule anchoring [59]. Androgen and Src signaling modulated the microtubule nucleation during interphase by promoting the centrosomal localization of γ-tubulin [16] via the activation of the MAPK/Erk signaling pathway [17]. It has also been shown that Syk is catalytically active at the centrosome [46,47]. In the early stages of BMMCs activation, when microtubule formation is stimulated, tyrosine-phosphorylated proteins concentrate in the centrosomal region. Inhibitors of Src or Syk kinases inhibited the phosphorylation of proteins interacting with γ-tubulin in activated BMMCs [6]. An association of Src family kinases with γ-tubulin complexes was also reported in activated rat basophilic leukemia cell line RBL-2H3 [49] and in differentiating mouse P19 embryonic carcinoma cells [30,60].

Although several protein tyrosine phosphatases co-localize with γ-tubulin on the centrosome, e.g., PTB-BL (PTPN13) [61] or PRL-1 (PTP4A1) [62], our knowledge of their involvement in the regulation of microtubule nucleation from centrosomes is very limited. In the case of dual-specificity phosphatase CDC25B, essential for the regulation of the cell cycle, it was reported that the inhibition of its activity suppressed an assembly of interphase microtubules and the centrosomal localization of γ-tubulin [63]. This indicates that different protein tyrosine phosphatases might be involved in distinct signaling pathways with respect to the regulation of microtubule nucleation. SHP-1 in BMMCs might balance the stimulating effect of the Src and Syk/ZAP families on microtubule formation.

The signaling pathway leading to an inhibition of microtubule nucleation via the activation of SHP-1 is currently unknown. Interestingly, multidomain G protein-coupled receptor kinase-interacting protein 1 (GIT1) [64] and p21-activated kinase interacting exchange factor (βPIX) [65] are substrates for tyrosine kinases and associate with centrosomes of fibroblasts [66]. Previously, we have shown that, in BMMCs, these signaling proteins also located at the centrosomes and formed complexes with γ-tubulin and the Ag-induced cell activation stimulates their phosphorylation on tyrosines [18]. Moreover, γ-tubulin binds directly to the N-terminal ARF GTPase-activating protein (ARF-GAP) domain (aa 1–124) of GIT1 in vitro [33]. GIT1 has been shown to be phosphorylated in cells in a Src kinase-dependent manner [67], and different studies have pointed to the relevance of tyrosine phosphorylation in the regulation of GIT1 functions. It has been shown that the tyrosine phosphorylation of GIT1 is required for intramolecular conformational changes in GIT1 and the release of its auto-inhibitory interaction [68]. The tyrosine phosphorylation of GIT1 in stimulated mast cells might, thus, lead to its activation. On the other hand, the tyrosine phosphorylation of βPIX, in a Src kinase-dependent manner weakens its ability to bind GIT1 [69]. We have shown that GIT1 and βPIX regulate microtubule nucleation from interphase centrosomes in various cell types [18,33]. We have found that the tyrosine phosphorylation level on GIT1 increased during BMMCs activation and was higher in SHP-1_KO cells. On the other hand, we did not detect the tyrosine phosphorylation of βPIX (Supplemental Figure S3I). SHP-1 could, thus, affect activated BMMC in both the activity of Syk kinase and the conformational state of GIT1. Deciphering the role of SHP-1 in the modulation of GIT1/βPIX complexes warrants further investigation. Other proteins essential for microtubule nucleation might be potentially modulated by SHP-1. Proteomic studies revealed that the tyrosine phosphorylation of proteins is important for targeting or anchoring γ-TuRCs to centrosomes; e.g., CDK5RAP2, NEDD1, ninein, and pericentrin [70].

An increased degranulation was reported in BMMCs isolated from mew mice deficient in SHP-1 [71]. On the other hand, a decreased degranulation was found in another study using BMMC from SHP-1 deficient me mice [72]. The discrepancy between studies was explained by different experimental setups [71]. In this study, the increased microtubule nucleation in established BMMC line lacking SHP-1 correlated with an increased degranulation. The degranulation returned to the level in wild-type cells when SHP-1 was introduced into the deficient cells. Our data, thus, suggest that SHP-1 negatively regulates Ag-induced degranulation.

In conclusion, our data suggest a novel mechanism of microtubule modulation in mast cells with SHP-1 tyrosine phosphatase as a negative regulator of microtubule nucleation. Presumably, also through this action, SHP-1 is involved in the spatiotemporal regulation of degranulation. An interference with

the microtubular network via specific regulators of microtubule nucleation in mast cells could open up new rational approaches to the treatment of inflammatory and allergic diseases.

Abbreviations

Ab(s)	Antibody(ies)
Ag	Antigen
BMMC(s)	Bone marrow-derived mast cell(s)
GCP	γ-tubulin complex protein
mAb	Monoclonal antibody
P-Tyr	Phosphotyrosine
ROI	Region of interest
γTuRC	γ-tubulin ring complex
γTuSC	γ-tubulin small complex

References

1. Kalesnikoff, J.; Galli, S.J. New developments in mast cell biology. *Nat. Immunol.* **2008**, *9*, 1215–1223. [CrossRef]

2. Blank, U.; Rivera, J. The ins and outs of IgE-dependent mast-cell exocytosis. *Trends Immunol.* **2004**, *25*, 266–273. [CrossRef]

3. Gilfillan, A.M.; Rivera, J. The tyrosine kinase network regulating mast cell activation. *Immunol. Rev.* **2009**, *228*, 149–169. [CrossRef]

4. Smith, A.J.; Pfeiffer, J.R.; Zhang, J.; Martinez, A.M.; Griffiths, G.M.; Wilson, B.S. Microtubule-dependent transport of secretory vesicles in RBL-2H3 cells. *Traffic* **2003**, *4*, 302–312. [CrossRef]

5. Nishida, K.; Yamasaki, S.; Ito, Y.; Kabu, K.; Hattori, K.; Tezuka, T.; Nishizumi, H.; Kitamura, D.; Goitsuka, R.; Geha, R.S.; et al. FcεRI-mediated mast cell degranulation requires calcium-independent microtubule-dependent translocation of granules to the plasma membrane. *J. Cell Biol.* **2005**, *170*, 115–126. [CrossRef]

6. Sulimenko, V.; Dráberová, E.; Sulimenko, T.; Macurek, L.; Richterová, V.; Dráber, P.; Dráber, P. Regulation of microtubule formation in activated mast cells by complexes of γ-tubulin with Fyn and Syk kinases. *J. Immunol.* **2006**, *176*, 7243–7253. [CrossRef]

7. Hájková, Z.; Bugajev, V.; Dráberová, E.; Vinopal, S.; Dráberová, L.; Janáček, J.; Dráber, P.; Dráber, P. STIM1-directed reorganization of microtubules in activated cells. *J. Immunol.* **2011**, *186*, 913–923. [CrossRef]

8. Munoz, I.; Danelli, L.; Claver, J.; Goudin, N.; Kurowska, M.; Madera-Salcedo, I.K.; Huang, J.D.; Fischer, A.; Gonzalez-Espinosa, C.; de Saint, B.G.; et al. Kinesin-1 controls mast cell degranulation and anaphylaxis through PI3K-dependent recruitment to the granular Slp3/Rab27b complex. *J. Cell Biol.* **2016**, *215*, 203–216. [CrossRef]

9. Cruse, G.; Beaven, M.A.; Ashmole, I.; Bradding, P.; Gilfillan, A.M.; Metcalfe, D.D. A truncated splice-variant of the FcεRIβ receptor subunit is critical for microtubule formation and degranulation in mast cells. *Immunity* **2013**, *38*, 906–917. [CrossRef]

10. Efergan, A.; Azouz, N.P.; Klein, O.; Noguchi, K.; Rothenberg, M.E.; Fukuda, M.; Sagi-Eisenberg, R. Rab12 regulates retrograde transport of mast cell secretory granules by interacting with the RILP-dynein complex. *J. Immunol.* **2016**, *196*, 1091–1101. [CrossRef]

11. Oakley, C.E.; Oakley, B.R. Identification of γ-tubulin, a new member of the tubulin superfamily encoded by mipa gene of *Aspergillus nidulans*. *Nature* **1989**, *338*, 662–664. [CrossRef] [PubMed]

12. Oegema, K.; Wiese, C.; Martin, O.C.; Milligan, R.A.; Iwamatsu, A.; Mitchison, T.J.; Zheng, Y. Characterization of two related *Drosophila* γ-tubulin complexes that differ in their ability to nucleate microtubules. *J. Cell Biol.* **1999**, *144*, 721–733. [CrossRef] [PubMed]

13. Oakley, B.R.; Paolillo, V.; Zheng, Y. γ-Tubulin complexes in microtubule nucleation and beyond. *Mol. Biol. Cell* **2015**, *26*, 2957–2962. [CrossRef]

14. Vogel, J.; Drapkin, B.; Oomen, J.; Beach, D.; Bloom, K.; Snyder, M. Phosphorylation of γ-tubulin regulates microtubule organization in budding yeast. *Dev. Cell* **2001**, *1*, 621–631. [CrossRef]

15. Keck, J.M.; Jones, M.H.; Wong, C.C.; Binkley, J.; Chen, D.; Jaspersen, S.L.; Holinger, E.P.; Xu, T.; Niepel, M.; Rout, M.P.; et al. A cell cycle phosphoproteome of the yeast centrosome. *Science* **2011**, *332*, 1557–1561. [CrossRef]

16. Colello, D.; Reverte, C.G.; Ward, R.; Jones, C.W.; Magidson, V.; Khodjakov, A.; LaFlamme, S.E. Androgen and Src signaling regulate centrosome activity. *J. Cell Sci.* **2010**, *123*, 2094–2102. [CrossRef]

17. Colello, D.; Mathew, S.; Ward, R.; Pumiglia, K.; LaFlamme, S.E. Integrins regulate microtubule nucleating activity of centrosome through mitogen-activated protein kinase/extracellular signal-regulated kinase kinase/extracellular signal-regulated kinase (MEK/ERK) signaling. *J. Biol. Chem.* **2012**, *287*, 2520–2530. [CrossRef]

18. Sulimenko, V.; Hájková, Z.; Černohorská, M.; Sulimenko, T.; Sládková, V.; Dráberová, L.; Vinopal, S.; Dráberová, E.; Dráber, P. Microtubule nucleation in mouse bone marrow-derived mast cells is regulated by the concerted action of GIT1/βPIX proteins and calcium. *J. Immunol.* **2015**, *194*, 4099–4111. [CrossRef]

19. Nováková, M.; Dráberová, E.; Schürmann, W.; Czihak, G.; Viklický, V.; Dráber, P. γ-Tubulin redistribution in taxol-treated mitotic cells probed by monoclonal antibodies. *Cell Motil. Cytoskel.* **1996**, *33*, 38–51. [CrossRef]

20. Dráberová, E.; Sulimenko, V.; Vinopal, S.; Sulimenko, T.; Sládková, V.; D'Agostino, L.; Sobol, M.; Hozák, P.; Krˇen, L.; Katsetos, C.D.; et al. Differential expression of human γ-tubulin isotypes during neuronal development and oxidative stress points to a γ-tubulin-2 prosurvival function. *FASEB J.* **2017**, *31*, 1828–1846. [CrossRef]

21. Dráberová, E.; D'Agostino, L.; Caracciolo, V.; Sládková, V.; Sulimenko, T.; Sulimenko, V.; Sobol, M.; Maounis, N.F.; Tzelepis, E.; Mahera, E.; et al. Overexpression and nucleolar localization of γ-tubulin small complex proteins GCP2 and GCP3 in glioblastoma. *J. Neuropathol. Exp. Neurol.* **2015**, *74*, 723–742. [CrossRef]

22. Dráberová, E.; Sulimenko, V.; Kukharskyy, V.; Dráber, P. Monoclonal antibody NF-09 specific for neurofilament protein NF-M. *Folia Biol.* **1999**, *45*, 163–165.

23. Tolar, P.; Dráberová, L.; Dráber, P. Protein tyrosine kinase Syk is involved in Thy-1 signaling in rat basophilic leukemia cells. *Eur. J. Immunol.* **1997**, *27*, 3389–3397. [CrossRef]

24. Amoui, M.; Dráberová, L.; Tolar, P.; Dráber, P. Direct interaction of Syk and Lyn protein tyrosine kinases in rat basophilic leukemia cells activated via type I Fcεreceptors. *Eur. J. Immunol.* **1997**, *27*, 321–328. [CrossRef]

25. Hibbs, M.L.; Tarlinton, D.M.; Armes, J.; Grail, D.; Hodgson, G.; Maglitto, R.; Stacker, S.A.; Dunn, A.R.R. Multiple defects in the immune-system of Lyn-deficient mice, culminating in autoimmune-disease. *Cell* **1995**, *83*, 301–311. [CrossRef]

26. Sander, J.D.; Joung, J.K. CRISPR-Cas systems for editing, regulating and targeting genomes. *Nature Biotechnol.* **2014**, *32*, 347–355. [CrossRef] [PubMed]

27. Flemr, M.; Buhler, M. Single-step generation of conditional knockout mouse embryonic stem cells. *Cell Rep.* **2015**, *12*, 709–716. [CrossRef]

28. Green, M.R.; Sambrook, J. *Molecular Cloning; A Laboratory Manual*, 4th ed.; Cold Spring Harbor Laboratory Press: Cold Spring Harbor, NY, USA, 2012; pp. 1378–1380, ISBN 978-1-936113-42-2.

29. Blume, Y.; Yemets, A.; Sulimenko, V.; Sulimenko, T.; Chan, J.; Lloyd, C.; Dráber, P. Tyrosine phosphorylation of plant tubulin. *Planta* **2008**, *229*, 143–150. [CrossRef]

30. Kukharskyy, V.; Sulimenko, V.; Macurek, L.; Sulimenko, T.; Dráberová, E.; Dráber, P. Complexes of γ-tubulin with non-receptor protein tyrosine kinases Src and Fyn in differentiating p19 embryonal carcinoma cells. *Exp. Cell Res.* **2004**, *298*, 218–228. [CrossRef]

31. Dráber, P.; Lagunowich, L.A.; Dráberová, E.; Viklický, V.; Damjanov, I. Heterogeneity of tubulin epitopes in mouse fetal tissues. *Histochemistry* **1988**, *89*, 485–492. [CrossRef]

32. Horˇejší, B.; Vinopal, S.; Sládková, V.; Dráberová, E.; Sulimenko, V.; Sulimenko, T.; Vosecká, V.; Philimonenko, A.; Hozák, P.; Katsetos, C.D.; et al. Nuclear γ-tubulin associates with nucleoli and interacts with tumor suppressor protein C53. *J. Cell Physiol.* **2012**, *227*, 367–382. [CrossRef]

33. Černohorská, M.; Sulimenko, V.; Hájková, Z.; Sulimenko, T.; Sládková, V.; Vinopal, S.; Dráberová, E.; Dráber, P. GIT1/βPIX signaling proteins and PAK1 kinase regulate microtubule nucleation. *BBA Mol. Cell. Res.* **2016**, *1863*, 1282–1297. [CrossRef] [PubMed]

34. Dráberová, E.; Dráber, P. A microtubule-interacting protein involved in coalignment of vimentin intermediate filaments with microtubules. *J. Cell Sci.* **1993**, *106*, 1263–1273. [PubMed]

35. Schindelin, J.; Arganda-Carreras, I.; Frise, E.; Kaynig, V.; Longair, M.; Pietzsch, T.; Preibisch, S.; Rueden, C.; Saalfeld, S.; Schmid, B.; et al. Fiji: An open-source platform for biological-image analysis. *Nat. Methods* **2012**, *9*, 676–682. [CrossRef]

36. Rivera, J.; Fierro, N.A.; Olivera, A.; Suzuki, R. New insights on mast cell activation via the high affinity receptor for IgE. *Adv. Immunol.* **2008**, *98*, 85–120. [CrossRef]

37. Ruschmann, J.; Antignano, F.; Lam, V.; Snyder, K.; Kim, C.; Essak, M.; Zhang, A.; Lin, A.H.; Mali, R.S.; Kapur, R.; et al. The role of SHIP in the development and activation of mouse mucosal and connective tissue mast cells. *J. Immunol.* **2012**, *188*, 3839–3850. [CrossRef] [PubMed]

38. Lorenz, U. SHP-1 and SHP-2 in T cells: Two phosphatases functioning at many levels. *Immunol. Rev.* **2009**, *228*, 342–359. [CrossRef]

39. Xiao, W.; Ando, T.; Wang, H.Y.; Kawakami, Y.; Kawakami, T. Lyn- and PLC-β3-dependent regulation of SHP-1 phosphorylation controls Stat5 activity and myelomonocytic leukemia-like disease. *Blood* **2010**, *116*, 6003–6013. [CrossRef] [PubMed]

40. Bohnenberger, H.; Oellerich, T.; Engelke, M.; Hsiao, H.H.; Urlaub, H.; Wienands, J. Complex phosphorylation dynamics control the composition of the Syk interactome in B cells. *Eur. J. Immunol.* **2011**, *41*, 1550–1562. [CrossRef] [PubMed]

41. Kulathu, Y.; Grothe, G.; Reth, M. Autoinhibition and adapter function of Syk. *Immunol. Rev.* **2009**, *232*, 286–299. [CrossRef]

42. Komarova, Y.A.; Vorobjev, I.A.; Borisy, G.G. Life cycle of MTts: Persistent growth in the cell interior, asymmetric transition frequencies and effects of the cell boundary. *J. Cell Sci.* **2002**, *115*, 3527–3539.

43. Sulimenko, V.; Hájková, Z.; Klebanovych, A.; Dráber, P. Regulation of microtubule nucleation mediated by γ-tubulin complexes. *Protoplasma* **2017**, *254*, 1187–1199. [CrossRef] [PubMed]

44. Kundu, S.; Fan, K.; Cao, M.; Lindner, D.J.; Zhao, Z.J.; Borden, E.; Yi, T. Novel SHP-1 inhibitors tyrosine phosphatase inhibitor-1 and analogs with preclinical anti-tumor activities as tolerated oral agents. *J. Immunol.* **2010**, *184*, 6529–6536. [CrossRef] [PubMed]

45. Chen, L.; Sung, S.S.; Yip, M.L.; Lawrence, H.R.; Ren, Y.; Guida, W.C.; Sebti, S.M.; Lawrence, N.J.; Wu, J. Discovery of a novel SHP2 protein tyrosine phosphatase inhibitor. *Mol. Pharmacol.* **2006**, *70*, 562–570. [CrossRef] [PubMed]

46. Zyss, D.; Montcourrier, P.; Vidal, B.; Anguille, C.; Merezegue, F.; Sahuquet, A.; Mangeat, P.H.; Coopman, P.J. The Syk tyrosine kinase localizes to the centrosomes and negatively affects mitotic progression. *Cancer Res.* **2005**, *65*, 10872–10880. [CrossRef]

47. Fargier, G.; Favard, C.; Parmeggiani, A.; Sahuquet, A.; Merezegue, F.; Morel, A.; Denis, M.; Molinari, N.; Mangeat, P.H.; Coopman, P.J.; et al. Centrosomal targeting of Syk kinase is controlled by its catalytic activity and depends on microtubules and the dynein motor. *FASEB J.* **2013**, *27*, 109–122. [CrossRef] [PubMed]

48. Martin-Verdeaux, S.; Pombo, I.; Iannascoli, B.; Roa, M.; Varin-Blank, N.; Rivera, J.; Blank, U. Evidence of a role for Munc18-2 and microtubules in mast cell granule exocytosis. *J. Cell Sci.* **2003**, *116*, 325–334. [CrossRef] [PubMed]

49. Dráberová, L.; Dráberová, E.; Surviladze, Z.; Dráber, P.; Dráber, P. Protein tyrosine kinase p53/p56^{lyn} form complexes with γ-tubulin in rat basophilic leukemia cells. *Int. Immunol.* **1999**, *11*, 1829–1839. [CrossRef] [PubMed]

50. Rubíková, Z.; Sulimenko, V.; Paulenda, T.; Dráber, P. Mast cell activation and microtubule organization are modulated by miltefosine through protein kinase C inhibition. *Front. Immunol.* **2018**, *9*. [CrossRef]

51. Linhartová, I.; Dráber, P.; Dráberová, E.; Viklický, V. Immunological discrimination of β-tubulin isoforms in developing mouse brain. Posttranslational modification of non-class III β-tubulins. *Biochem. J.* **1992**, *288*, 919–924. [CrossRef] [PubMed]

52. Janke, C.; Bulinski, J.C. Post-translational regulation of the microtubule cytoskeleton: Mechanisms and functions. *Nat. Rev. Mol. Cell Biol.* **2011**, *12*, 773–786. [CrossRef] [PubMed]

53. Katsetos, C.D.; Dráberová, E.; Legido, A.; Dráber, P. Tubulin targets in the pathobiology and therapy of glioblastoma multiforme. II. γ-Tubulin. *J. Cell Physiol* **2009**, *221*, 514–520. [CrossRef] [PubMed]

54. Harris, J.; Shadrina, M.; Oliver, C.; Vogel, J.; Mittermaier, A. Concerted millisecond timescale dynamics in the intrinsically disordered carboxyl terminus of γ-tubulin induced by mutation of a conserved tyrosine residue. *Protein Sci.* **2018**, *27*, 531–545. [CrossRef] [PubMed]

55. Teixidó-Travesa, N.; Roig, J.; Lüders, J. The where, when and how of microtubule nucleation - one ring to rule them all. *J. Cell Sci.* **2012**, *125*, 4445–4456. [CrossRef]

56. Kollman, J.M.; Merdes, A.; Mourey, L.; Agard, D.A. Microtubule nucleation by γ-tubulin complexes. *Nat. Rev. Mol. Cell Biol.* **2011**, *12*, 709–721. [CrossRef]

57. Katagiri, K.; Katagiri, T.; Kajiyama, K.; Yamamoto, T.; Yoshida, T. Tyrosine-phosphorylation of tubulin during monocytic differentiation of HL-60 cells. *J. Immunol.* **1993**, *150*, 585–593. [PubMed]

58. Ley, S.C.; Marsh, M.; Bebbington, C.R.; Proudfoot, K.; Jordan, P. Distinct intracellular-localization of Lck and Fyn protein-tyrosine kinases in human T-lymphocytes. *J. Cell Biol.* **1994**, *125*, 639–649. [CrossRef]

59. Jay, J.; Hammer, A.; Nestor-Kalinoski, A.; Diakonova, M. JAK2 tyrosine kinase phosphorylates and is negatively regulated by centrosomal protein ninein. *Mol. Cell Biol.* **2015**, *35*, 111–131. [CrossRef]

60. Macurek, L.; Dráberová, E.; Richterová, V.; Sulimenko, V.; Sulimenko, T.; Dráberová, L.; Marková, V.; Dráber, P. Regulation of microtubule nucleation from membranes by complexes of membrane-bound γ-tubulin with Fyn kinase and phosphoinositide 3-kinase. *Biochem. J.* **2008**, *416*, 421–430. [CrossRef]

61. Herrmann, L.; Dittmar, T.; Erdmann, K.S. The protein tyrosine phosphatase PTP-BL associates with the midbody and is involved in the regulation of cytokinesis. *Mol. Biol. Cell* **2003**, *14*, 230–240. [CrossRef]

62. Wang, J.; Kirby, C.E.; Herbst, R. The tyrosine phosphatase PRL-1 localizes to the endoplasmic reticulum and the mitotic spindle and is required for normal mitosis. *J. Biol. Chem.* **2002**, *277*, 46659–46668. [CrossRef] [PubMed]

63. Boutros, R.; Lobjois, V.; Ducommun, B. CDC25B involvement in the centrosome duplication cycle and in microtubule nucleation. *Cancer Res.* **2007**, *67*, 11557–11564. [CrossRef]

64. Webb, D.J.; Mayhew, M.W.; Kovalenko, M.; Schroeder, M.J.; Jeffery, E.D.; Whitmore, L.; Shabanowitz, J.; Hunt, D.F.; Horwitz, A.F. Identification of phosphorylation sites in GIT1. *J. Cell Sci.* **2006**, *119*, 2847–2850. [CrossRef]

65. Manser, E.; Loo, T.H.; Koh, C.G.; Zhao, Z.S.; Chen, X.Q.; Tan, L.; Tan, I.; Leung, T.; Lim, L. PAK kinases are directly coupled to the PIX family of nucleotide exchange factors. *Mol. Cell* **1998**, *1*, 183–192. [CrossRef]

66. Zhao, Z.S.; Lim, J.P.; Ng, Y.W.; Lim, L.; Manser, E. The GITt-associated kinase PAK targets to the centrosome and regulates Aurora-A. *Mol. Cell* **2005**, *20*, 237–249. [CrossRef] [PubMed]

67. Bagrodia, S.; Bailey, D.; Lenard, Z.; Hart, M.; Guan, J.L.; Premont, R.T.; Taylor, S.J.; Cerione, R.A. A tyrosine-phosphorylated protein that binds to an important regulatory region on the cool family of p21-activated kinase-binding proteins. *J. Biol. Chem.* **1999**, *274*, 22393–22400. [CrossRef]

68. Totaro, A.; Astro, V.; Tonoli, D.; de Curtis, I. Identification of two tyrosine residues required for the intramolecular mechanism implicated in GIT1 activation. *PLoS ONE* **2014**, *9*, e93199. [CrossRef]

69. Feng, Q.; Baird, D.; Yoo, S.; Antonyak, M.; Cerione, R.A. Phosphorylation of the cool-1/β-Pix protein serves as a regulatory signal for the migration and invasive activity of Src-transformed cells. *J. Biol. Chem.* **2010**, *285*, 18806–18816. [CrossRef] [PubMed]

70. Hornbeck, P.V.; Chabra, I.; Kornhauser, J.M.; Skrzypek, E.; Zhang, B. Phosphosite: A bioinformatics resource dedicated to physiological protein phosphorylation. *Proteomics* **2004**, *4*, 1551–1561. [CrossRef] [PubMed]

71. Zhang, L.; Oh, S.Y.; Wu, X.; Oh, M.H.; Wu, F.; Schroeder, J.T.; Takemoto, C.M.; Zheng, T.; Zhu, Z. SHP-1 deficient mast cells are hyperresponsive to stimulation and critical in initiating allergic inflammation in the lung. *J. Immunol.* **2010**, *184*, 1180–1190. [CrossRef]

72. Nakata, K.; Yoshimaru, T.; Suzuki, Y.; Inoue, T.; Ra, C.; Yakura, H.; Mizuno, K. Positive and negative regulation of high affinity IgE receptor signaling by Src homology region 2 domain-containing phosphatase 1. *J. Immunol* **2008**, *181*, 5414–5424. [CrossRef] [PubMed]
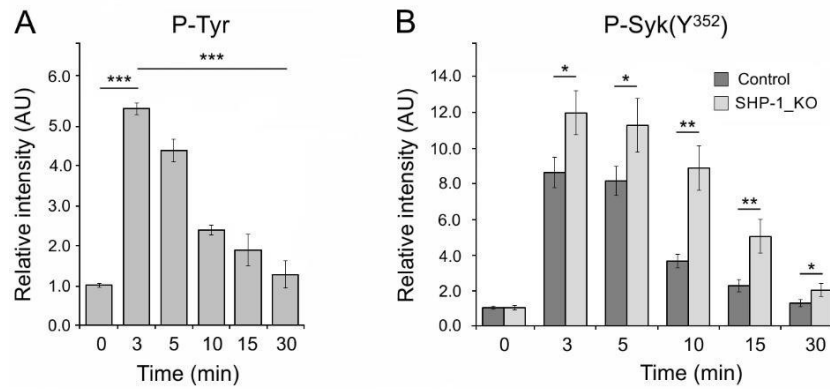
Figure S1. Quantitative analysis of overall tyrosine phosphorylation and tyrosine phosphorylation of Syk in the course of BMMCs activation. **(A)** Densitometric quantification of overall protein tyrosine phosphorylation level shown in Figure 1A. Relative intensities of P-Tyr normalized to non-activated cells and the amount of actin in individual samples. **(B)** Densitometric quantification of Syk kinase Y^{352} phosphorylation level shown in Figure 5A. Relative intensities of P-Syk(Y^{352}) in control BMMCs and SHP-1_KO cells normalized to non-activated cells and the amount of actin in individual samples. (A-B) Values indicate mean ± SD (n=3), *$p < 0.05$, **$p < 0.01$, ***$p < 0.001$.
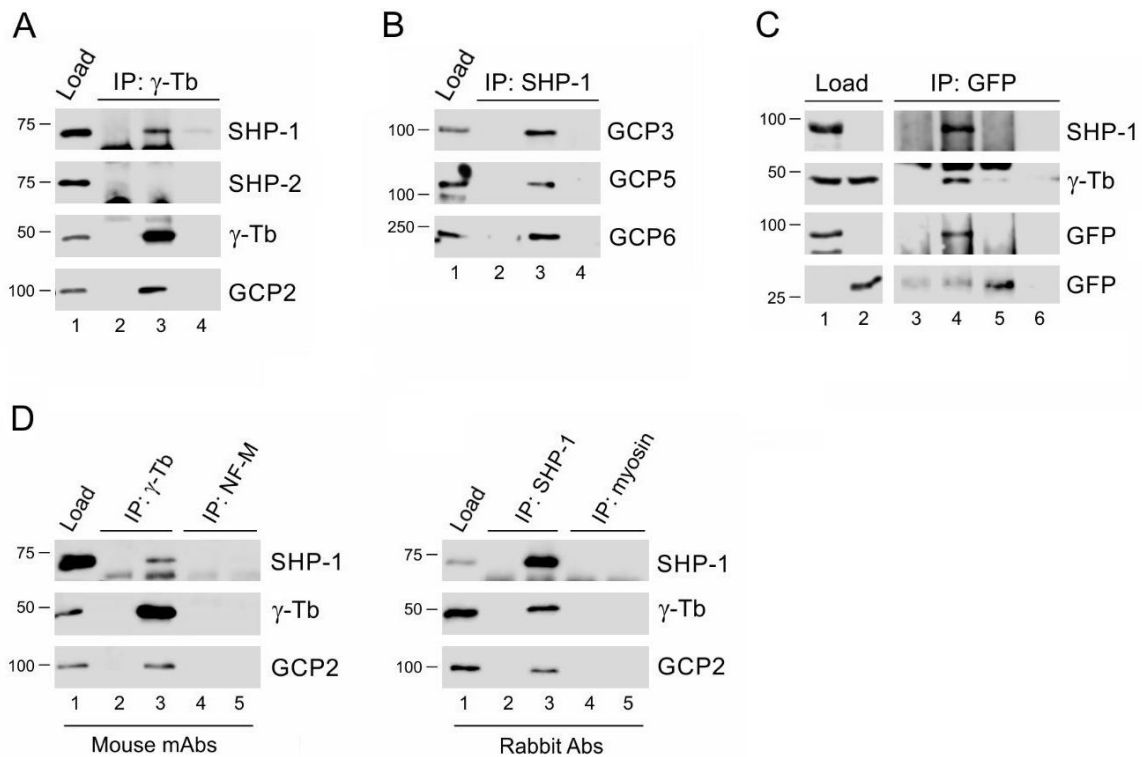
Figure S2. Association of SHP-1 with γ-tubulin complex proteins, and isotype controls for immunoprecipitation experiments. Immunoprecipitation from BMMCs (**A-B, D**) or HEK (**C**) extracts. (**A**) Precipitation with immobilized Ab to γ-tubulin sequence 38-53. Blots probed with Abs to SHP-1, SHP-2, γ-tubulin (γ-Tb) and GCP2. Load (*lane 1*), immobilized Ab not incubated with cell extract (*lane 2*), precipitated proteins (*lane 3*), and carrier without Ab, incubated with cell extracts (*lane 4*). (**B**) Precipitation with immobilized Ab to SHP-1. Blots probed with Abs to GCP3, GCP5 and GCP6. Load (*lane 1*), immobilized Ab not incubated with cell extract (*lane 2*), precipitated proteins (*lane 3*), and carrier without Ab, incubated with cell extracts (*lane 4*). (**C**) Precipitation with immobilized Ab to GFP. Blots probed with Abs to SHP-1, γ-tubulin (γ-Tb) and GFP. Load, HEK cells expressing SHP-1_EGFP (*lane 1*), Load, cells expressing EGFP (*lane 2*), immobilized Ab not incubated with cell extract (*lane 3*), precipitated proteins from cells expressing SHP-1_EGFP (*lane 4*), cells expressing EGFP (*lane 5*), and carrier without Ab, incubated with cell SHP-1_EGFP cell extract (*lane 6*). (**D**) Isotype controls for immunoprecipitation experiments. Extracts were precipitated with immobilized mouse mAb to γ-tubulin (IgG2b), mouse mAb to NF-M (IgG2a), rabbit Ab to SHP-1, or rabbit Ab to myosin. Blots were probed with Abs to SHP-1, γ-tubulin (γ-Tb) and GCP2. Load (*lane 1*), immobilized Abs not incubated with cell extracts (*lanes 2 and 4*), precipitated proteins (*lanes 3 and 5*).
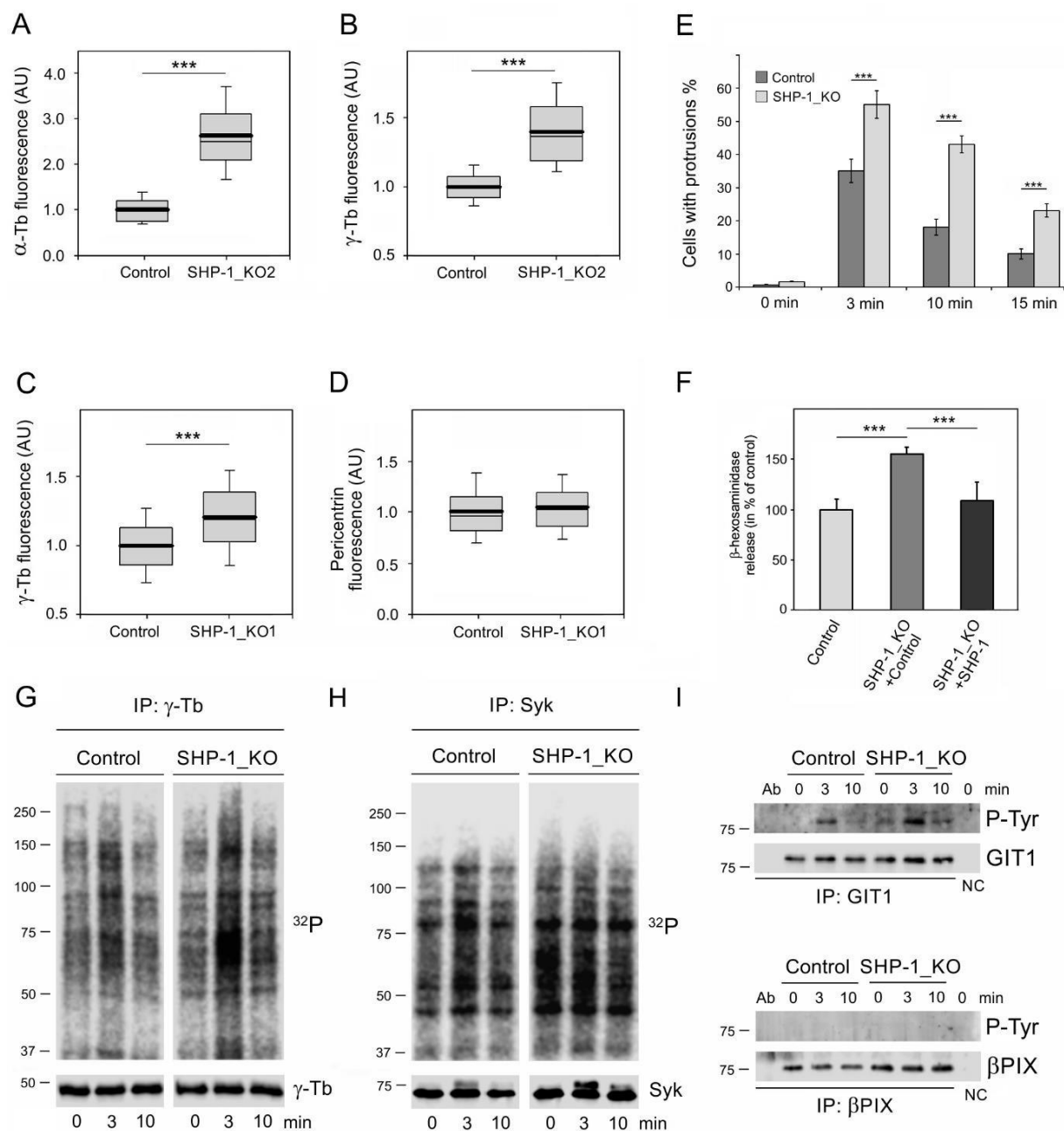
Figure S3. Characterization of SHP-1 deficient BMMCs, and microtubule regrowth. (**A-B**) Distribution of α-tubulin or γ-tubulin fluorescence intensities (arbitrary units [AU]) in 1-μm ROI at 1.5 min of regrowth in BMMCs (Control) and SHP-1 deficient cells (SHP-1_KO2) is shown as box plots (three independent experiments, > 50 cells counted for each experimental condition). (**A**) Box plot of α-tubulin fluorescence intensities in SHP-1_KO2 cells (n = 155) relative to control cells (Control, n = 155). (**B**) Box plot of γ-tubulin fluorescence intensities in SHP-1_KO2 cells (n = 154) relative to control cells (Control, n = 154). Bold and thin lines within the box represent mean and median (the 50th percentile), respectively. The bottom and top of the box represent the 25th and 75th percentiles. Whiskers below and above the box indicate the 10th and 90th percentiles. ***, p < 1 x 10^{-5}. (**C-D**) Distribution of γ-tubulin or pericentrin fluorescence intensities (arbitrary units [AU]) in 1-μm ROI at 1.5 min of regrowth in BMMCs (Control) and SHP-1 deficient cells (SHP-1_KO1) is shown as box plots (three independent experiments, > 80 cells counted for each experimental condition). (**C**)

Box plot of γ-tubulin fluorescence intensities in SHP-1_KO1 cells (n = 248) relative to control cells (Control, n = 272). (**D**) Box plot of pericentrin fluorescence intensities in SHP-1_KO1 cells (n = 225) relative to control cells (Control, n = 272). Bold and thin lines within the box represent mean and median (the 50th percentile), respectively. The bottom and top of the box represent the 25th and 75th percentiles. Whiskers below and above the box indicate the 10th and 90th percentiles. ***, p < 1 x 10^{-5}. (**E**) Quantitative analysis of number of cells with microtubule protrusions in the course of activation in control BMMCs and SHP-1_KO cells. Values indicate mean ± SD (n=3), ***p < 0.001. (**F**) Degranulation in control BMMCs, SHP-1_KO cells infected by empty lentiviral vector (SHP-1_KO+Vector) and SHP-1_KO cells rescued by mSHP-1 in lentiviral vector (SHP-1_KO+SHP-1). Cells were activated by Ag (100 ng/ml) and degranulation was measure by β-hexosaminidase release. Data represent the mean ± SD (n=3), ***p < 1 x 10^{-5}. (**G-H**) The kinase activity in γ-tubulin and Syk immunocomplexes. Non-activated (0 min) or antigen-activated (3 min, 10 min) control BMMCs and SHP-1_KO cells were precipitated with Abs to γ-tubulin (G) or Syk (H). Immunocomplexes were subjected to *in vitro* kinase assay, electrophoretically separated, and detected by autoradiography (^{32}P). (**I**) Tyrosine phosphorylation of GIT1 and βPIX in control and SHP-1_KO cells during activation by FcεRI aggregation. Extracts from BMMCs precipitated with immobilized Abs specific to GIT1 or βPIX. Blots were first probed with mouse Ab to phosphotyrosine (P-Tyr). The same blots were after that probed with Abs to GIT1 or βPIX, respectively. Ab, immobilized Abs not incubated with cell extract; NC, negative control, carriers without Ab, incubated with cell extracts.
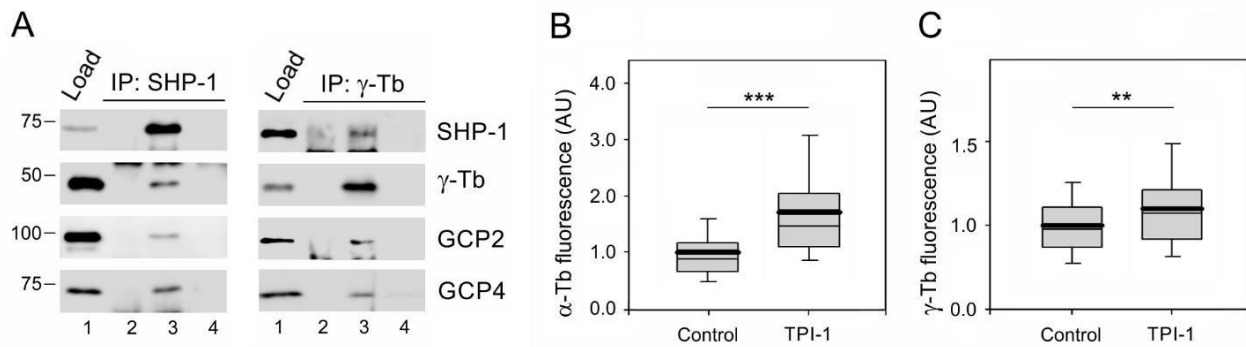
Figure S4. SHP-1 modifies microtubule regrowth, and associates both with γ-tubulin complex proteins in epithelial MCF7 cells. **(A)** Immunoprecipitation experiments. Extracts from MCF7 cells precipitated with immobilized Abs specific to γ-tubulin or SHP-1. Blots probed with Abs to SHP-1, γ-tubulin (γ-Tb), GCP2 and GCP4. Load (*lane 1*), immobilized Abs not incubated with cell extracts (*lane 2*), precipitated proteins (*lane 3*), and carriers without Abs, incubated with cell extracts (*lane 4*). **(B-C)** Cells were cultivated with 100 nM TPI-1 or DMSO carrier (Control) for 1 h before and during microtubule regrowth assay. Distribution of α-tubulin or γ-tubulin fluorescence intensities (arbitrary units [AU]) in 1-μm ROI at 1.5 min of regrowth is shown as box plots (three independent experiments, > 30 cells counted for each experimental condition). **(B)** Box plot of α-tubulin fluorescence intensities in TPI-1 (n = 108) pre-incubated cells relative to control cells (Control, n = 143). **(C)** Box plot of γ-tubulin fluorescence intensities in TPI-1 (n = 90) pre-incubated cells relative to control cells (Control, n = 142). Bold and thin lines within the box represent mean and median (the 50th percentile), respectively. The bottom and top of the box represent the 25th and 75th percentiles. Whiskers below and above the box indicate the 10th and 90th percentiles. **, p < 0.001; ***, p < 1 x 10^{-5}.

Table S1   **Sequences of primers used for RT-qPCR analysis of mouse genes**

Name	Sequence	Amplicon length
Ptpn6, fwd	5'- GAACATTCTTCCCTTTGACC-3'	127 bp
Ptpn6, rev	5'- TCTTAGAGTTCTCATCTGGAC-3'	
Ptpn11, rev	5'- AACATCACTGGTGTGGAGGC-3'	287 bp
Ptpn11, rev	5' – TGCACAGTTCAGCGGGTA-3'	
Il13, fwd	5'- CTTAAGGAGCTTATTGAGGAG-3'	144 bp
Il13, rev	5'- CATTGCAATTGGAGATGTTG-3'	
Tnf, fwd	5'- CTATGTCTCAGCCTCTTCTC-3'	108 bp
Tnf, rev	5'- CATTTGGGAACTTCTCATCC-3'	
Ptgs2, fwd	5'- ACTCATAGGAGAGACTATCAAG-3'	147 bp
Ptgs2, rev	5'- GAGTGTGTTGAATTCAGAGG-3'	
Gapdh, fwd	5'- AACTTTGGCATTGTGGAAGG-3'	68 bp
Gapdh, rev	5'- ATCCACAGTCTTCTGGGTGG-3'	

Supplementary Text S1

Features of in-house written macro for processing images from microtubule regrowth experiment

Images of γ-tubulin (centrosomal marker, 1st channel) and α-tubulin (microtubule asters, 2nd channel) were stored separately as z-stacks in tif format. The size of the image matrix was 256 × 256 pixels, using 16-bit depth. The size of voxel was 0.106 μm × 0.106 μm × 200 μm. Macro written in ImageJ macro language using Fiji works under a directory with files in tif format to process automatically all contained images.

Tasks for individual channels

1st channel: Creating Maximum Intensity projection from a z-stack data. Smoothing the resulting picture by a 5x5 mean filter to remove high-intensity noise particles. Finding the brightest point in the smoothed picture corresponding to a center of a centrosome. Creating a circle 1 μm in a diameter as a ROI around this center. Measuring a mean intensity in this circle in original non-smoothed data.

2nd channel: Creating Maximum Intensity projection from a z-stack data. Removing non-homogenous background from this picture. Creating a circle 1 μm in a diameter as a ROI around the center point position found in the 1st channel. Measuring a mean intensity in this circle.

For checking the quality of analysis after the computation, an image pair of both channels is stored with overlays of found ROIs for each original picture. Computed mean image intensities are stored in an Excel file.

VII.4   Nejedlá, M., **Klebanovych, A.,** Sulimenko, V., Sulimenko, T., Dráberová, E., Dráber, P., Karlsson, R. (2021) The actin regulator profilin 1 is functionally associated with the mammalian centrosome. Life Sci Alliance *4(1)*: e202000655.

Research Article

Check for updates

The actin regulator profilin 1 is functionally associated with the mammalian centrosome

Michaela Nejedlá[1],*, Anastasiya Klebanovych[2],* ⓘ Vadym Sulimenko[2], Tetyana Sulimenko[2] ⓘ Eduarda Dráberová[2] ⓘ
Pavel Dráber[2] ⓘ, Roger Karlsson[1] ⓘ

Profilin 1 is a crucial actin regulator, interacting with monomeric actin and several actin-binding proteins controlling actin polymerization. Recently, it has become evident that this profilin isoform associates with microtubules via formins and interferes with microtubule elongation at the cell periphery. Recruitment of microtubule-associated profilin upon extensive actin polymerizations, for example, at the cell edge, enhances microtubule growth, indicating that profilin contributes to the coordination of actin and microtubule organization. Here, we provide further evidence for the profilin-microtubule connection by demonstrating that it also functions in centrosomes where it impacts on microtubule nucleation.

Introduction

The centrosome is the major microtubule-organizing structure in eukaryotic cells and as such crucial for intracellular architecture, cell polarity, and directional migration; consequently it has intrigued scientists for decades (1). Studies of the complex protein composition of mammalian centrosomes (2, 3, 4) combined with high-resolution imaging of centrosome behavior in cultured cells have led to the realization that in addition to being intimately linked with the microtubule system they are also closely connected to the actin microfilament system (2, 5, 6, 7, 8, 9, 10), reflecting the tight coordination and polarization of microtubule and actin organization (11, 12, 13). Several actin regulatory components such as WASH, Arp2/3, cofilin, and members of the formin family (2, 7, 14) have been found to be associated with the centrosome and likely to govern centrosome-linked actin reorganization. Examples of such activities are for instance the alteration of actin organization during synapse formation in immune cells with subsequent centrosome relocation and changes in microtubule distribution (9) and the centrosomal actin polymerization linked to

spindle formation during mitosis in somatic mouse and human cells (15). Moreover, centrosomal proteins also have been reported to promote actin polymerization-driven cell protrusions at the cell cortex in cancer cells (16).

The γ-tubulin ring complex (γTuRC) is crucial to centrosome-derived microtubule nucleation (17). It consists of 14 γ-tubulin (γ-Tb) molecules (18) arranged together with γ-tubulin complex proteins (GCP) 2-6 (4, 19) into a cone-shaped structure designed to nucleate microtubules (20, 21). In addition, recent cryo-electron microscopy revealed that the lumen of γTuRC contains an actin-like molecule associated with both the GCPs and γ-Tbs (22, 23, 24), which appears to be important for γTuRC-dependent microtubule nucleation (23). Although, currently unclear whether it is β- or γ-actin, the observation unveils a direct association between key components of the γTuRC and the microfilament system. The connection between actin and γ-Tb is further emphasized by reports of the latter localizing to the actin-rich cell periphery and influencing stress fiber formation (25).

Profilin is a principal control component of actin polymerization; it brings polymerization-competent, ATP-bound actin monomers to sites where polymerization is called for by activated actin nucleation and elongation factors such as members of the Ena/Vasp, formins, WASP, and WAVE families of actin binding proteins whose interaction with profilin is established via poly(L-proline)-sequences, reviewed by references 26, 27, 28, and 29.

Here, we have continued our studies of the interplay between actin and microtubules which were initiated by the identification of profilin as a control component of microtubule elongation at the cell periphery (30), and report that regulation of microtubules by profilin also extends to the centrosome. It is found that its occurrence in the centrosome impacts on centrosomal accumulation of γ-Tb and microtubule nucleation. Unless otherwise stated, "profilin" refers to profilin 1 throughout this text.

[1]Department of Molecular Biosciences, The Wenner-Gren Institute, Stockholm University, Stockholm, Sweden [2]Department of Biology of Cytoskeleton, Institute of Molecular Genetics of the Czech Academy of Sciences, Prague, Czech Republic

Correspondence: roger.karlsson@su.se; paveldra@img.cas.cz
Michaela Nejedlá's present address is Institute of Botany, Czech Academy of Sciences, Průhonice, Czech Republic
*Michaela Nejedlá´ and Anastasiya Klebanovych contributed equally to this work

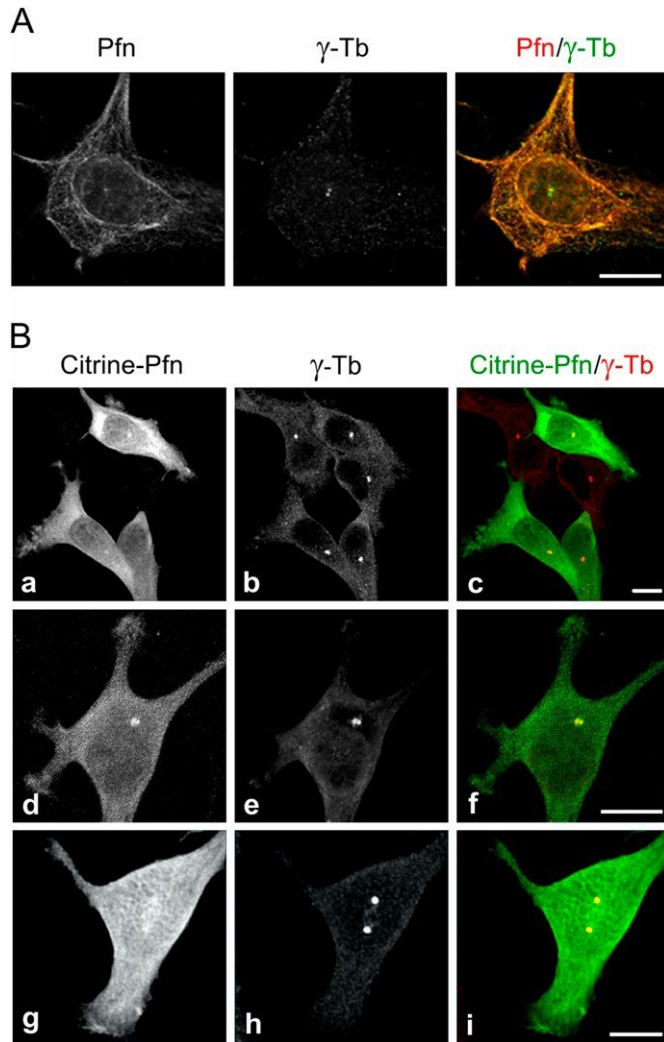Figure 1. Profilin is present in centrosomes throughout the cell cycle. Fluorescence microscopy revealed the co-localization of profilin and γ-tubulin. (A) Ab staining of profilin and γ-Tb in B16 cells after a brief pretreatment with 0.1% Triton X-100 before fixation (see text). High-resolution confocal microscopy (AiryScan). (B) B16 cells expressing citrine-profilin (a, d, g; green) were captured at different cell cycle stages. Cells were permeabilized with 10 μM digitonin, fixed, and stained for γ-tubulin (b, e, h; red). Superposition of images in (c, f, i). The cell in (d, e, f) was captured at an early G2-stage of the cell cycle and the one in (g, h, i) at late G2/prophase. Micrographs were obtained by spinning disk microscopy. Scale bars (A) and (B): 10 μm.

Results

To learn more about the microtubule association of profilin in the perinuclear region and its possible association with the centrosome we applied a brief washout in accordance with our previous study (30) to reduce accumulation of profilin in this region and unveil possible distinct features of its distribution by immunofluorescence microscopy of mouse melanoma B16 cells. Strikingly enough, this approach enabled visualization of a prominent fluorescence in one or two discrete spots of size, character and position suggesting they represented centrosomes. Co-labeling of γ-tubulin verified that this

indeed was the case (Fig 1A) in agreement with earlier mass spectroscopy data identifying profilin as a component of isolated centrosomes (2). Moreover, the fluorescence intensity emanating from the centrosome after profilin Ab staining increased 1.6 times in cells during mitosis (Fig S1A–C).

To further investigate the centrosomal distribution of profilin and to exclude the risk that the Ab used either cross-reacted with profilin 2, whose expression is up-regulated in B16 profilin 1 knock-out cells (KO27) (31) or contained autoantibodies recognizing the centrosome (32), a fluorescent variant of profilin with citrine fused intra-molecularly was expressed in B16 cells. This chimeric citrine-profilin molecule binds actin and poly(L-proline) (31); the two principal interaction properties of profilin (27, 33, 34). After digitonin extraction, fixation, labeling of γ-tubulin with Ab and microscopy, the distribution of citrine-profilin to centrosomes as identified by the γ-tubulin staining was obvious, and a fine reticular profilin fluorescence juxtaposed to centrosomes was often particularly prominent (Fig 1B). Altogether, this demonstrates that profilin associates with mammalian centrosomes.

Based on these microscopy results and our previous observations of profilin operating as a regulator of microtubule elongation (30), we decided to test if profilin interacts with the γ-tubulin ring complex (γTuRC), which is essential for nucleation of microtubules from centrosomes. Therefore, a series of immunoprecipitation (IP)-experiments of extracts of B16 cells was performed using Abs to profilin, γ-tubulin (γ-Tb), and γ-Tb complex protein (GCP)-2 (Fig 2A–C). The material precipitated with the anti-profilin Ab was then found to contain γ-Tb, GCP2 and GCP4, and reciprocal IPs of γ-Tb and GCP2, respectively, revealed co-precipitation of profilin, indicating interaction of profilin with γTuRC. To further validate the obtained data, we performed IP experiments using extracts of B16 wild-type and KO27 cells. Congruent with a profilin-γTuRC interaction, the profilin Abs co-precipitated γ-tubulin, GCP2, GCP4 and actin from wild-type B16 cells but not from the profilin 1-lacking KO27 (Fig 2D). Moreover, the profilin-γTuRC association was not limited to B16 cells, as similar observations also were made with extracts of human colorectal adenocarcinoma Caco-2 cells (Fig S2A and B). Isotype controls for the IP experiments are shown in (Fig S2C and D). Together these results provide strong evidence for profilin being a partner to one or more components of γTuRC. To test whether the association of profilin to γTuRC was due to a direct interaction with γ-tubulin, different GST-fusions of γ-tubulin were used in pull-down experiments. However, an interaction could not be established (data not shown), suggesting that the association of profilin with γTuRC requires one or more additional components. Next we again took advantage of the KO27 cells, to determine de novo formation of microtubules from interphase centrosomes. To that end, nocodazole-washout experiments were performed as described previously (35, 36). As demonstrated by immunofluorescence microscopy of α-tubulin after drug removal and 2 min of recovery in fresh medium at 37°C, the microtubule array reformed more rapidly in KO27 than in the profilin-expressing control cells (Fig 3A). Quantification of the α-tubulin immunofluorescence revealed approximately three times more intensive signal in the profilin-depleted cells than in the control (Fig 3B), and, interestingly, a similar quantification of γ-tubulin immunofluorescence unveiled that also γ-tubulin accumulates above wild-type level at
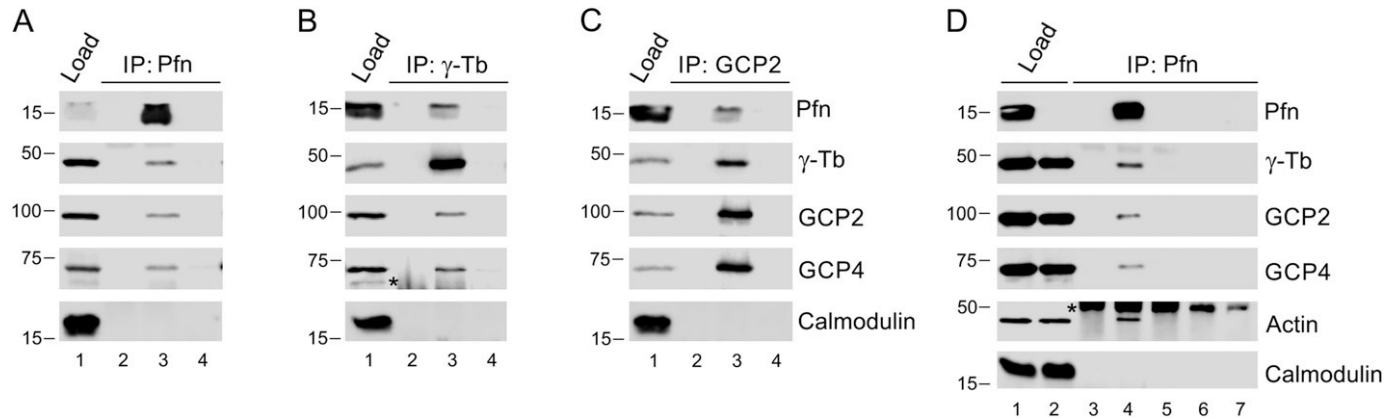
Figure 2. Profilin interacts with γ-TuRC.

(A, B, C) Extracts of B16 cells were precipitated with immobilized Abs to profilin (A), γ-tubulin (B) or GCP2 (C), followed by Western blotting and probing with Abs against profilin (Pfn), γ-tubulin (γ-Tb), GCP2, GCP4, and calmodulin (negative control) as indicated (C). In each blot (A, B, C), the sample lanes denoted 1—4 show: total cell extract, gel load (1); no cell extract (2); precipitated proteins (3); and Ab-free carrier (4). Note reciprocal precipitation in all three cases. (D) Extracts of B16 control (1, 4, 6) and profilin knock-out KO27 (2, 5, 7) cells were precipitated with immobilized Abs to profilin, followed by Western blotting and probing with Abs against profilin (Pfn), γ-tubulin (γ-Tb), GCP2, GCP4, actin, and calmodulin (negative control) as indicated. The sample lanes denoted 1—7 show: total cell extract, gel load (1, 2); no cell extract (3); precipitated proteins (4—5); and Ab-free carrier (6—7). Note co-precipitation of γ-tubulin, GCP2, GCP4, and actin with profilin Ab occurs in B16 cells solely. (B, D) Asterisks (*) in panels (B) and (D), lanes 2 and 3, and 3—5, respectively, denote cut off bands reflecting precipitating Abs.

centrosomes in KO27 cells (Fig 3C). To exclude a possible risk that the enhanced microtubule nucleation in the KO27 cells reflected an increase in nocodazole-resistant microtubules, B16 wild-type and KO27 cells were fixed in the presence of nocodazole and further processed for fluorescence microscopy using Abs to α-tubulin and γ-tubulin. The subsequent microscopy analysis revealed no difference in amount of nocodazole-resistant microtubules in B16 and KO27 cells (Fig S3A). We, therefore, conclude that microtubule nucleation from the centrosome is increased in absence of profilin. Consistently and in agreement with our earlier study (30), non-drug-treated KO27 cells displayed vastly more microtubules than wild-type cells (Fig S3B and C).

Because these observations pointed to the possibility that profilin in addition to its previously shown effect on microtubule elongation also may modulate de novo nucleation of microtubules from the centrosome, we decided to compare the nucleation rate of centrosomal microtubules in control and KO27 cells. To that end time-lapse imaging of cells expressing mNeonGreen-tagged microtubule end-binding protein 3 (EB3), decorating plus ends of the growing microtubules (37), was performed and followed by determination of the number of EB3 comets leaving the centrosomes per unit time, that is, the nucleation rate. Data analysis demonstrated a significantly augmented nucleation rate (2.2 times) in profilin-lacking cells (Fig 3D), which was consistent with the observation above of more microtubules in KO27 cells than in the control. The difference was particularly notable by comparing 10-frame projections of B16 control and KO27 cells expressing EB3 (Fig 3E).

Hence, it appeared that profilin is not only interfering with microtubule elongation as previously determined but is also a regulator of microtubule formation de novo. To provide further evidence for this conclusion, we performed phenotypic rescue experiments by co-expressing citrine-profilin or citrine-cathepsin B

(control) with EB1-tdTomato in KO27 cells, and citrine-cathepsin B with EB1-tdTomato in B16 wild-type cells. The expression of tagged proteins was documented by immunoblotting of whole-cell lysates (Fig 4A). As mentioned above, comparing the nucleation rate of microtubules from the centrosome in control and KO27 cells expressing citrine-cathepsin B revealed a significant increase (2.2 times) in the profilin-depleted cells, whereas the presence of citrine-profilin restored the nucleation rate in the KO27 cells to the level observed for control cells (Fig 4B). Collectively these data support the results obtained by measurement of the α-tubulin signal after nocodazole washout and recovery (Fig 3B) and provide strong arguments for profilin as a regulator of centrosomal mi- crotubule nucleation. Furthermore, this puts profilin in a unique position as a coordinator of actin and microtubule organization in mammalian cells.

Discussion

In this study we have continued to explore the role of the actin regulatory protein profilin for microtubule organization in mammalian cells. Previously, we demonstrated that a brief exposure to detergent before fixation enables immunofluorescence visualization of microtubule-associated profilin without disturbing fluorescence from the large pool of more generally distributed profilin in the cell (30). Here we applied this protocol to study the perinuclear distribution of profilin in mouse melanoma B16 cells and were able to detect profilin by immunofluorescence microscopy in centrosomes identified by γ-tubulin. We then took advantage of the fluorescent citrine-profilin (31) to independently establish that profilin distributes to centrosomes. Furthermore, reciprocal immunoprecipitation experiments combined with Western blotting demonstrated that profilin is a binding partner to components of
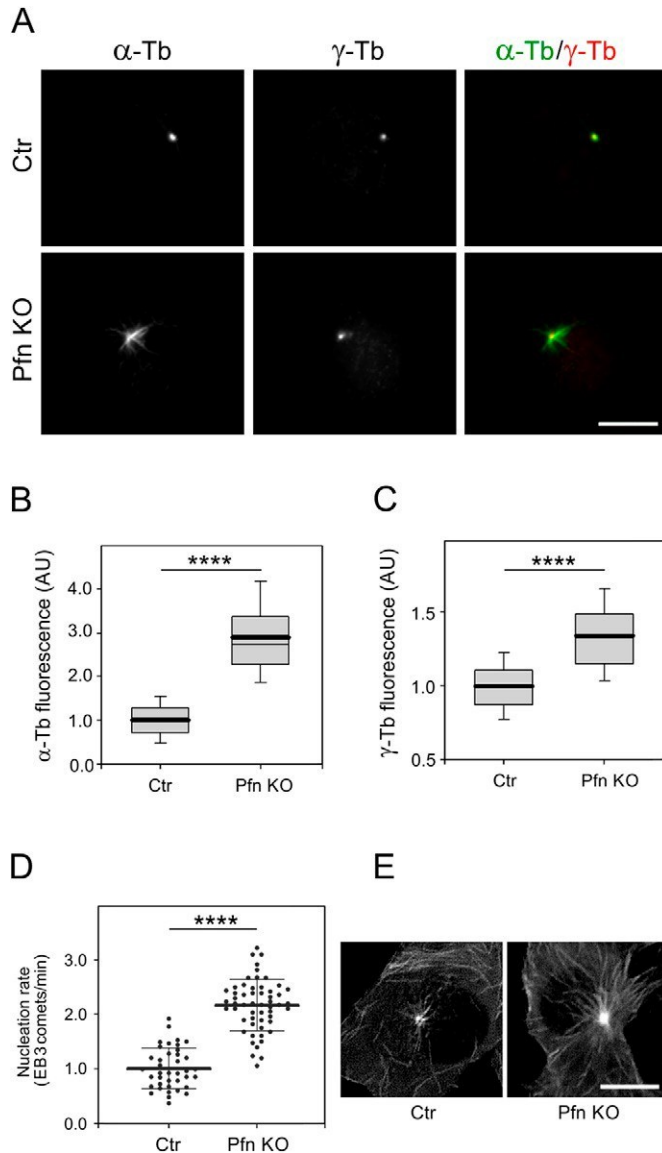
Figure 3. Profilin modulates microtubule regrowth.
(A) B16 control and profilin knock-out (KO27) cells visualized after nocodazole washout and 2 min of recovery in drug-free medium at 37°C followed by processing for fluorescence labeling of microtubules (α-tubulin; α-Tb) and centrosomes (γ-tubulin; γ-Tb). Note the more prominent array of nascent microtubules extending from the centrosome in the KO27 cells compared with the control. Scale bar: 10 μm. (B) Box plots illustrating the distribution of α-tubulin fluorescence intensity (arbitrary units, AU) determined 3 min after drug washout at 28°C within a 1.0-μm region of interest in B16 control and KO27 cells, respectively; n = 330 (control; Ctr) and 322 (KO27; Pfn KO). (C) As in (B), but γ-tubulin fluorescence intensity; n = 339 (control) and 284 (KO27). The data in (B, C) are based on three independent experiments and >90 cells for each experimental condition. The thick and thin lines within each box represent the mean and median (50th percentile), respectively, whereas bottom and top represent the 25th and 75th percentiles. The whiskers below and above the box indicate the 10th and 90th percentiles; ****P < 0.0001. (D) Microtubule nucleation rate in KO27 cells relative to control cells. Three independent experiments with at least 13 cells counted in each experiment, n = 39 (control) and 55 (KO27). The thick and thin lines within the dot box plots represent mean ± SD; ****P < 0.0001. (E) Time-lapse imaging of control and KO27 cells expressing EB3-mNeonGreen. Tracks of EB3 comets captured during 10 s are shown. Scale bar: 10 μm.
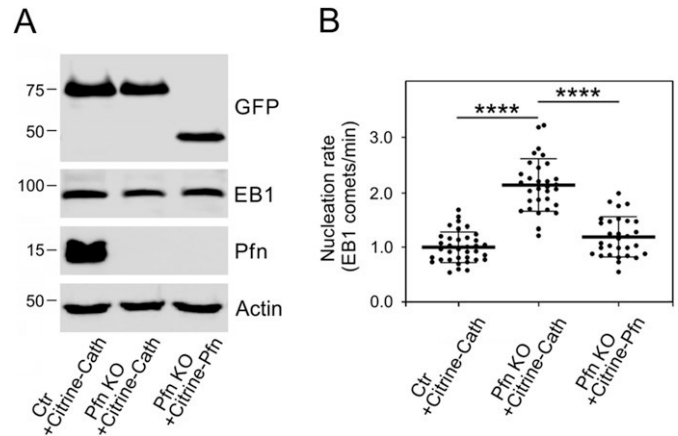

Figure 4. Phenotypic rescue of increased microtubule nucleation in KO27 cells. (A) Immunoblot analysis of whole-cell lysates of B16 control cells expressing citrine-cathepsin B (Ctr+Citrine-Cath), profilin knock-out KO27 cells expressing citrine-cathepsin B (Pfn KO+Citrine-Cath), and KO27 cells rescued by citrine-profilin (Pfn KO+Citrine-Pfn). Blots were probed with Abs to GFP to detect citrine-tagged proteins, to EB1 to detect co-expressed EB1-tdTomato, profilin (Pfn), and to actin (loading control). (B) Comparison of the microtubule nucleation rate observed in KO27 (Pfn KO) cells expressing Citrine-cathepsin B and Citrine-profilin, respectively, and in control cells (Ctr) expressing Citrine-cathepsin B. Three independent experiments and at least 10 cells analyzed in each experiment, n = 36 (Ctr+Citrine-Cath), n = 31 (Pfn KO+Citrine-Cath), and n = 30 (Pfn KO+Citrine-profilin); abbreviations as in left panel. The thick and thin lines within dot box plots represent mean ± SD; ****P < 0.0001.

the γ-tubulin ring complex. Finally, microtubule regrowth experiments and evaluation of de novo nucleation in wild-type B16 and the profilin-depleted B16 cells KO27 ([31]) disclosed that profilin is a negative regulator of microtubule nucleation.

We and others have shown that profilin interferes with microtubule elongation ([30], [38]). In our study by Nejedla et al ([30]), we presented data suggesting that the distribution of profilin along microtubules was dependent on formins. Because formins are well-known binding partners to profilin and have been demonstrated to attach to microtubules, we concluded that the association of profilin to microtubules was at least partially indirect via formins. Indeed, in support of an indirect interaction, in vitro experiments involving co-sedimentation and assembly assays did not reveal any interaction between purified profilin and polymerization-competent porcine brain tubulin in monomer or polymer form ([30]). However, in striking contrast, the subsequent study by Henty-Ridilla et al ([38]) reported that such a direct interaction in fact can occur. The reason for this discrepancy is unclear. Possibly it could be explained by variations of protein preparations or the different approaches used for analysis.

Combined with the current study, we have thus uncovered a dual role of profilin for microtubule organization in mammalian cells because it interferes with both centrosomal microtubule nucleation and microtubule elongation. Amazingly enough, profilin, therefore, operates in the molecular processes behind formation and growth of both actin filaments and microtubules; in the former case, it exert a positive role by providing actin as profilin-actin for polymer growth, whereas in the latter its function is to interfere with nucleation and elongation. Today, several proteins have been characterized as contributors to the connection and coordination of actin and microtubule organization ([12], [39]), but to our knowledge, the duality of profilin in this

respect is unique and puts profilin in a central position for the coupling of the actin and microtubule systems in mammalian cells. Tentatively, the role of profilin in the centrosome may be related to recent observations that also actin isa component of this organelle. Profilin-actin serves as source of actin for microfilament polymerization and as such co-operates with actin nucleation and elongation promoting proteins (26, 27, 28, 29, 33, 39, 40). A possible scenario is therefore that the loss of profilin results in less of actin polymerization in the centrosomal region in analogy with what was recently reported for the cell edge (41); as a consequence, less of steric hindrance (8, 42) would reduce a possible space constrain for enhanced de novo microtubule nucleation. Alternatively, because actin is a structural component of functional γTuRCs (22, 23, 24), centrosomal profilin may tune the availability of actin for γTuRC. Therefore, profilin deletion could increase formation of functional γTuRC because of more actin being accessible for association with γTuRC. This in turn would enable enhanced de novo microtubule nucleation from centrosomes.

With this study, we emphasize profilin as a critical mediator of actin and microtubule cross-talk and extend the view of its role as a crucial component for cell architecture and behavior by its coordinated maintenance of actin and microtubule homeostasis as was recently discussed (39). We expect future studies to be directed to understand whether the interaction of profilin with either actin or components carrying the typical profilin-binding poly(L-proline)-motif (26, 27, 28, 29), or both is required for its inhibitory effect on centrosomal microtubule nucleation.

Materials and Methods

Antibodies

Mouse mAb TU-31 (IgG2b; for precipitation hybridoma supernatant diluted 1:2) to γ-tubulin, GCP2-01 (IgG2b; for precipitation hybridoma supernatant diluted 1:2) and GCP2-02 (IgG1; for immunoblotting hybridoma supernatant diluted 1:5) to GCP2 were described previously (43, 44, 45). Rabbit Abs to actin (# A2066; 1:10,000) and profilin I N-terminal (# P7749; 1:3,000 for immunoblotting, and 1:100 for fluorescence microscopy (31), and mAb GTU-88 (IgG1; # T6557; 1:10,000 for immunoblotting, 1:1,000 for immunofluorescence) to γ-tubulin were from Sigma-Aldrich. Mouse mAb to GCP4 (IgG1, # sc-271876; 1:1,000) was purchased from Santa Cruz Biotechnology. Rabbit Abs to profilin (#ab50667; 1:200 for precipitation) and calmodulin (# ab45689; 1:5,000) were from Abcam. Rabbit Ab to α-tubulin (# 600-401-880; 1:100) was from Rockland. Rabbit Ab to non-muscle myosin heavy chain (# BT-561; 1:1,000; Biomedical Technologies) and mAbs NF-09 (IgG2a; hybridoma supernatant diluted 1:2) to neurofilament NF-M protein (46) served as negative controls in immunoprecipitation experiments. Antimouse and antirabbit Abs conjugated with HRP were from Promega Biotec (1:10,000). Antimouse Ab conjugated with DyLight 549 (1:1,000) or DyLight 649 (1:500) and antirabbit Ab conjugated with Alexa Fluor 488 were from Jackson Immunoresearch Laboratories (1:200).

Cell cultures and transfection

Mouse melanoma B16-F1, control clone, and profilin KO clone 27 (B16 Pfn1, KO27) generated by Crispr/Cas9 (31) as well as human epithelial colorectal adenocarcinoma Caco-2 (HTB-37; ATCC) were cultured in DMEM (Thermo Fisher Scientific) supplemented with 10% FCS and antibiotics at 37°C in the presence of 5% CO_2. To prepare B16 cells expressing citrine-profilin 1 (31), citrine-cathepsin B (#56554; Addgene), or EB3-mNeonGreen (Allele Biotechnology), the cells were transfected with 2.5 μg plasmid DNA per 3-cm tissue culture dish using Lipofectamine LTX (Invitrogen) according to the manufacturer's instructions. The transfection mixture was replaced with fresh complete medium after 12 h followed by continued culturing for another 48 h after which fresh medium containing 1.2 mg/ml geneticin (G418; Sigma-Aldrich) was added, and the incubation was continued for 7 d.

For the phenotypic rescue experiment, B16 control or KO27 cells were co-transfected with two plasmids (total 2.5 μg DNA per 3-cm tissue culture dish, plasmid molar ratio 1:1) using Lipofectamine 3000 (Invitrogen) according to the manufacturer's instructions. After 24 h, the cells were seeded onto dishes for live cell imaging. B16 control cells were co-transfected with EB1-tdTomato (# 50825; Addgene) and citrine-cathepsin B (#56554; Addgene) plasmids. KO27 cells were co-transfected with EB1-tdTomato and citrine-cathepsin B plasmids or with EB1-tdTomato and citrine-profilin 1 plasmids.

Immunoprecipitation

For immunoprecipitation experiments, washed cells were incubated for 10 min at 4°C with RIPA buffer (50 mM Tris, pH 8.0, 150 mM NaCl, 1% NP-40, 0.5% sodium deoxycholate, and 0.1% SDS) supplemented with protease inhibitors (Complete EDTA-free; Roche) and phosphatase inhibitors (1 mM Na_3VO_4, 1 mM NaF). The suspension was then centrifuged (20,000g, 10 min, 4°C) and the supernatant subjected to immunoprecipitation as described previously (47, 48) by incubation with Protein A beads (Protein A Sepharose CL-4B; GE-Healthcare Life Sciences) saturated with Abs as indicated (Figs 2 and S2). Gel electrophoresis and immunoblotting were performed using standard protocols (49). The HRP signal was detected with SuperSignal WestPico Chemiluminescent reagent (Pierce) and the LAS 3000 imaging system (Fujifilm).

Microtubule regrowth

Microtubule regrowth from centrosomes was followed by nocodazole-washout experiments. Cells, cultured on coverslips were treated with nocodazole (Sigma-Aldrich) at a final concentration of 10 μM for 1 h at 37°C to depolymerize microtubules, then washed with PBS precooled to 4°C (three times, 5 min each) and, unless stated differently followed by regrowth for 3 min at 28°C in complete medium after which the cells were fixed and stained for α-tubulin and γ-tubulin as described previously (50). Briefly, cells cultured on coverslips were fixed in 3% formaldehyde, extracted with 0.5% Triton X-100 and post-fixed with cold methanol (F/Tx/M). The samples were then incubated sequentially with mAb to γ-tubulin (GTU-88) and rabbit Ab to α-tubulin followed by simultaneous labeling with secondary Abs being conjugated

with distinct fluorophores (DyLight 549-antimouse and AF488-antirabbit, respectively). The coverslips were mounted in MOWIOL 4-88 (Calbiochem) supplemented with 4,6-diamidino-2-phenylindole (DAPI; Sigma-Aldrich) and examined with a Delta Vision Core System (Applied Precission) equipped with a 60×/1.42 NA oil objective. Finally, the microtubule regrowth was determined by capturing the fluorescent signal in both channels from different areas per sample and the sum of fluorescence intensities, representing γ-tubulin and α-tubulin, respectively, was obtained from nine consecutive frames (0.2 μm steps), with the middle frame chosen with respect to the highest γ-tubulin intensity. Intensity quantification of a region of interest, defined as concentric circles of a radius of 1 μm and centered around the γ-tubulin marked centrosome was then done automatically using an in-house written macro for Fiji ([51], [52]).

Fluorescence microscopy

Wide-field microscopy was performed using an Axiovert 200 M microscope (Carl Zeiss) equipped with a climate chamber, an EC-Plan-Neofluar 63×/1.4 objective lens, and a DG-4 light source (Sutter Instruments). Images were captured with a Cascade 1K camera (Roper). High-resolution confocal imaging was performed using an LSM800 AiryScan instrument (Carl Zeiss).

To simultaneously visualize γ-tubulin and citrine-profilin in B16 cells, permeabilization was performed with 10 μM digitonin (Calbiochem) in 25 mM Hepes buffer, pH 7.4, containing 2 mM EGTA, 115 mM CH_3COOK, 2.5 mM $MgCl_2$, and 150 mM sucrose ([53]) for 30 s, fixed with 3% formaldehyde in microtubule stabilizing buffer ([50]) for 20 min at room temperature and post-fixed with cold methanol at −20°C for 5 min. For γ-tubulin staining mAbs (GTU-88) and secondary Abs conjugated to DyLight 649 were used. Samples were mounted in Fluoromount-G (SouthernBiotech) and imaged using Andor Dragonfly 503 spinning disc confocal system (Oxford Instruments) with 40-μm pinhole size, equipped with Ixon Ultra 888 EMCCD 16 bit camera and 63×/1.4 NA oil objective. Consecutive z-stack images were captured with a step size of 0.1 μm and deconvoluted using Huygens Professional software v. 19.04 (Scientific Volume Imaging) with spinning disc module, SNR 20, and maximum iterations of 50, CMLE mode, and quality threshold set to 0.01. Citrine-tagged cathepsin B (56554; Addgene), which targets lysosomes served as negative control for citrine-profilin localization. The staining of γ-tubulin in cells expressing citrine-tagged cathepsin B revealed no association with centrosomes of the latter.

Imaging of microtubule nucleation

B16 cells expressing EB3-mNeonGreen were cultured in a 35 mm μ-Dish with ibidi polymer coverslip bottom (Ibidi GmbH); 30 min before imaging, the medium was replaced with FluoroBrite DMEM (Thermo Fisher Scientific), supplemented with 25 mM Hepes and 1% FCS. Time-lapse sequences were collected in three optical slices (0.13 μm steps) for 1 min at 1 s interval with the Andor Dragonfly 503 spinning disc confocal system (Oxford Instruments) equipped with a stage top microscopy incubator (Okolab), a 488 nm solid-state 150 mW laser, HCX PL APO 63× oil objective, NA 1.4, and a Zyla sCMOS 16 bit camera. For each experiment, at least 10 cells were imaged using the following acquisition parameters: 40-μm

pinhole size, 15% laser power, 150-ms exposure time, and an 525/50-nm emission filter. The time-lapse sequences were deconvoluted with Huygens Professional software version 19.04 (Scientific Volume Imaging), and maximum intensity projection of z stacks was made for each time point in Fiji. Newly nucleated microtubules were detected by manual counting of EB3 comets emanating from the centrosomes. For time-lapse imaging in phenotypic rescue experiments, B16 cells co-expressing EB1-tdTomato with citrine-profilin 1 or citrine-cathepsin B were cultivated and imaged as described above using a 561 nm solid-state 100 mW laser and an Ixon Ultra 888 EMCCD 16 bit camera. For each experiment, at least 10 cells, expressing both EB1-tdTomato and citrine-tagged protein at a comparable level, were imaged using the following acquisition parameters: 40-μm pinhole size, 15% laser power, 150-ms exposure time, and an 600/50-nm emission filter. Reference still images of citrine-tagged proteins were obtained with a 488 nm solid-state 150 mV laser using the acquisition parameters: 40-μm pinhole size, 15% laser power, 150-ms exposure time, and an 525/50-nm emission filter. Deconvolution was performed as described above.

Statistics

Significance was tested using a two-tailed, unpaired t test or one-way ANOVA followed by a Sidak's post hoc test using Prism 8 software (GraphPad Software). For all analyses, P-values were represented as follows: **$P < 0.01$; ***$P < 0.001$; ****$P < 0.0001$.

Supplementary Information

Acknowledgements

Author Contributions

M Nejedlá: formal analysis, investigation, and writing—review and editing.
A Klebanovych: formal analysis and investigation.
V Sulimenko: investigation.
T Sulimenko: formal analysis and investigation.
E Dráberová: investigation.
P Dráber: conceptualization, resources, formal analysis, supervision, validation, project administration, and writing—review and editing.

Conflict of Interest Statement

References

1. Conduit PT, Wainman A, Raff JW (2015) Centrosome function and assembly in animal cells. *Nat Rev Mol Cell Biol* 16: 611–624. doi:10.1038/nrm4062

2. Farina F, Gaillard J, Guerin C, Coute Y, Sillibourne J, Blanchoin L, Théry M (2016) The centrosome is an actin-organizing centre. *Nat Cell Biol* 18: 65–75. doi:10.1038/ncb3285

3. Meiring JCM, Shneyer BI, Akhmanova A (2019) Generation and regulation of microtubule network asymmetry to drive cell polarity. *Curr Opin Cell Biol* 62: 86–95. doi:10.1016/j.ceb.2019.10.004

4. Sulimenko V, Hájková Z, Klebanovych A, Dráber P (2017) Regulation of microtubule nucleation mediated by γ-tubulin complexes. *Protoplasma* 254: 1187–1199. doi:10.1007/s00709-016-1070-z

5. Au FK, Jia Y, Jiang K, Grigoriev I, Hau BK, Shen Y, Du S, Akhmanova A, Qi RZ (2017) GAS2L1 is a centriole-associated protein required for centrosome dynamics and disjunction. *Dev Cell* 40: 81–94. doi:10.1016/j.devcel.2016.11.019

6. Colin A, Singaravelu P, Thery M, Blanchoin L, Gueroui Z (2018) Actin-network architecture regulates microtubule dynamics. *Curr Biol* 28: 2647–2656. doi:10.1016/j.cub.2018.06.028

7. Hubert T, Vandekerckhove J, Gettemans J (2011) Actin and Arp2/3 localize at the centrosome of interphase cells. *Biochem Biophys Res Commun* 404: 153–158. doi:10.1016/j.bbrc.2010.11.084

8. Inoue D, Obino D, Pineau J, Farina F, Gaillard J, Guerin C, Blanchoin L, Lennon-Duménil AM, Théry M (2019) Actin filaments regulate microtubule growth at the centrosome. *EMBO J* 38: e99630. doi:10.15252/embj.201899630

9. Obino D, Farina F, Malbec O, Saez PJ, Maurin M, Gaillard J, Dingli F, Loew D, Gautreau A, Yuseff MI, et al (2016) Actin nucleation at the centrosome controls lymphocyte polarity. *Nat Commun* 7: 10969. doi:10.1038/ncomms10969

10. van de Willige D, Hummel JJ, Alkemade C, Kahn OI, Au FK, Qi RZ, Dogterom M, Koenderink GH, Hoogenraad CC, Akhmanova A (2019) Cytolinker Gas2L1 regulates axon morphology through microtubule-modulated actin stabilization. *EMBO Rep* 20: e47732. doi:10.15252/embr.201947732

11. Antoniades I, Stylianou P, Skourides PA (2014) Making the connection: Ciliary adhesion complexes anchor basal bodies to the actin cytoskeleton. *Dev Cell* 28: 70–80. doi:10.1016/j.devcel.2013.12.003

12. Dogterom M, Koenderink GH (2019) Actin-microtubule crosstalk in cell biology. *Nat Rev Mol Cell Biol* 20: 38–54. doi:10.1038/s41580-018-0067-1

13. Tang N, Marshall WF (2012) Centrosome positioning in vertebrate development. *J Cell Sci* 125: 4951–4961. doi:10.1242/jcs.038083

14. Gomez TS, Kumar K, Medeiros RB, Shimizu Y, Leibson PJ, Billadeau DD (2007) Formins regulate the actin-related protein 2/3 complex-independent polarization of the centrosome to the immunological synapse. *Immunity* 26: 177–190. doi:10.1016/j.immuni.2007.01.008

15. Plessner M, Knerr J, Grosse R (2019) Centrosomal actin assembly is required for proper mitotic spindle formation and chromosome congression. *iScience* 15: 274–281. doi:10.1016/j.isci.2019.04.022

16. Luo Y, Barrios-Rodiles M, Gupta GD, Zhang YY, Ogunjimi AA, Bashkurov M, Tkach JM, Underhill AQ, Zhang L, Bourmoum M, et al (2019) Atypical function of a centrosomal module in WNT signalling drives contextual cancer cell motility. *Nat Commun* 10: 2356–2374. doi:10.1038/s41467-019-10241-w

17. Zheng Y, Wong ML, Alberts B, Mitchison T (1995) Nucleation of microtubule assembly by a γ-tubulin-containing ring complex. *Nature* 378: 578–583. doi:10.1038/378578a0

18. Oakley CE, Oakley BR (1989) Identification of γ-tubulin, a new member of the tubulin superfamily encoded by mipA gene of Aspergillus nidulans. *Nature* 338: 662–664. doi:10.1038/338662a0

19. Murphy SM, Preble AM, Patel UK, O'Connell KL, Dias DP, Moritz M, Agard D, Stults JT, Stearns T (2001) GCP5 and GCP6: Two new members of the human γ-tubulin complex. *Mol Biol Cell* 12: 3340–3352. doi:10.1091/mbc.12.11.3340

20. Kollman JM, Greenberg CH, Li S, Moritz M, Zelter A, Fong KK, Fernandez JJ, Sali A, Kilmartin J, Davis TN, et al (2015) Ring closure activates yeast γ-TuRC for species-specific microtubule nucleation. *Nat Struct Mol Biol* 22: 132–137. doi:10.1038/nsmb.2953

21. Peng Y, Moritz M, Han X, Giddings TH, Lyon A, Kollman J, Winey M, Yates J 3rd, Agard DA, Drubin DG, et al (2015) Interaction of CK1δ with γ-TuSC ensures proper microtubule assembly and spindle positioning. *Mol Biol Cell* 26: 2505–2518. doi:10.1091/mbc.e14-12-1627

22. Consolati T, Locke J, Roostalu J, Chen ZA, Gannon J, Asthana J, Lim WM, Martino F, Cvetkovic MA, Rappsilber J, et al (2020) Microtubule nucleation properties of single human γTuRCs explained by their Cryo-EM structure. *Dev Cell* 53: 603–617.e8. doi:10.1016/j.devcel.2020.04.019

23. Liu P, Zupa E, Neuner A, Bohler A, Loerke J, Flemming D, Ruppert T, Rudack T, Peter C, Spahn C, et al (2019) Insights into the assembly and activation of the microtubule nucleator γ-TuRC. *Nature* 578: 467–471. doi:10.1038/s41586-019-1896-6

24. Wieczorek M, Urnavicius L, Ti SC, Molloy KR, Chait BT, Kapoor TM (2020) Asymmetric molecular architecture of the human γ-tubulin ring complex. *Cell* 180: 165–175. doi:10.1016/j.cell.2019.12.007

25. Hubert T, Perdu S, Vandekerckhove J, Gettemans J (2011) γ-tubulin localizes at actin-based membrane protrusions and inhibits formation of stress-fibers. *Biochem Biophys Res Commun* 408: 248–252. doi:10.1016/j.bbrc.2011.04.007

26. Carlier MF, Shekhar S (2017) Global treadmilling coordinates actin turnover and controls the size of actin networks. *Nat Rev Mol Cell Biol* 18: 389–401. doi:10.1038/nrm.2016.172

27. Karlsson R, Lindberg U (2007) Profilin, an essential control element for actin polymerization. In *Actin Monomer-Binding Proteins*. Lappalainen P (ed), pp 29–44. Austin, TX/New York, NY: Landes Bioscience/Springer.

28. Mullins RD, Bieling P, Fletcher DA (2018) From solution to surface to filament: Actin flux into branched networks. *Biophys Rev* 10: 1537–1551. doi:10.1007/s12551-018-0469-5

29. Witke W (2004) The role of profilin complexes in cell motility and other cellular processes. *Trends Cell Biol* 14: 461–469. doi:10.1016/j.tcb.2004.07.003

30. Nejedlá M, Sadi S, Sulimenko V, de Almeida FN, Blom H, Dráber P, Aspenstrom P, Karlsson R (2016) Profilin connects actin assembly with microtubule dynamics. *Mol Biol Cell* 27: 2381–2393. doi:10.1091/mbc.e15-11-0799

31. Nejedlá M, Li Z, Masser AE, Biancospino M, Spiess M, Mackowiak SD, Friedländer MR, Karlsson R (2017) A fluorophore fusion-construct of human profilin I with non-compromized poly(L-Proline) binding capacity suitable for imaging. *J Mol Biol* 429: 964–976. doi:10.1016/j.jmb.2017.01.004

32. Connolly JA, Kalnins VI (1978) Visualization of centrioles and basal bodies by fluorescent staining with nonimmune rabbit sera. *J Cell Biol* 79: 526–532. doi:10.1083/jcb.79.2.526

33. Jockusch BM, Murk K, Rothkegel M (2007) The profile of profilins. *Rev Physiol Biochem Pharmacol* 159: 131–149. doi:10.1007/112_2007_704

34. Bjorkegren C, Rozycki M, Schutt CE, Lindberg U, Karlsson R (1993) Mutagenesis of human profilin locates its poly(L-proline)-binding site to a hydrophobic patch of aromatic amino acids. *FEBS Lett* 333: 123–126. doi:10.1016/0014-5793(93)80388-b

35. Colello D, Reverte CG, Ward R, Jones CW, Magidson V, Khodjakov A, LaFlamme SE (2010) Androgen and Src signaling regulate centrosome activity. *J Cell Sci* 123: 2094–2102. doi:10.1242/jcs.057505

36. Sulimenko V, Hájková Z, Černohorská M, Sulimenko T, Sládková V, Dráberová L, Vinopal S, Dráberová E, Dráber P (2015) Microtubule nucleation in mouse bone marrow-derived mast cells is regulated by the concerted action of GIT1/βPIX proteins and calcium. *J Immunol* 194: 4099–4111. doi:10.4049/jimmunol.1402459

37. Akhmanova A, Steinmetz MO (2008) Tracking the ends: A dynamic protein network controls the fate of microtubule tips. *Nat Rev Mol Cell Biol* 9: 309–322. doi:10.1038/nrm2369

38. Henty-Ridilla JL, Juanes MA, Goode BL (2017) Profilin directly promotes microtubule growth through residues mutated in amyotrophic lateral sclerosis. *Curr Biol* 27: 3535–3543. doi:10.1016/j.cub.2017.10.002

39. Pimm ML, Hotaling J, Henty-Ridilla JL (2020) Profilin choreographs actin and microtubules in cells and cancer. *Int Rev Cell Mol Biol* 355: 155–204. doi:10.1016/bs.ircmb.2020.05.005

40. Grantham J, Lassing I, Karlsson R (2012) Controlling the cortical actin motor. *Protoplasma* 249: 1001–1015. doi:10.1007/s00709-012-0403-9

41. Skruber K, Warp PV, Shklyarov R, Thomas JD, Swanson MS, Henty-Ridilla JL, Read TA, Vitriol EA (2020) Arp2/3 and Mena/VASP require profilin 1 for actin network assembly at the leading edge. *Curr Biol* 30: 2651–2664.e5. doi:10.1016/j.cub.2020.04.085

42. Farina F, Ramkumar N, Brown L, Samandar Eweis D, Anstatt J, Waring T, Bithell J, Scita G, Thery M, Blanchoin L, et al (2019) Local actin nucleation tunes centrosomal microtubule nucleation during passage through mitosis. *EMBO J* 38: e99843. doi:10.15252/embj.201899843

43. Dráberová E, D'Agostino L, Caracciolo V, Sládková V, Sulimenko T, Sulimenko V, Sobol M, Maounis NF, Tzelepis E, Mahera E, et al (2015) Overexpression and nucleolar localization of γ-tubulin small complex proteins GCP2 and GCP3 in glioblastoma. *J Neuropathol Exp Neurol* 74: 723–742. doi:10.1097/nen.0000000000000212

44. Dráberová E, Sulimenko V, Vinopal S, Sulimenko T, Sládková V, D'Agostino L, Sobol M, Hozák P, Křen L, Katsetos CD, et al (2017) Differential expression of human γ-tubulin isotypes during neuronal development and oxidative stress points to a γ-tubulin-2 prosurvival function. *FASEB J* 31: 1828–1846. doi:10.1096/fj.201600846rr

45. Nováková M, Dráberová E, Schürmann W, Czihak G, Viklický V, Dráber P (1996) γ-Tubulin redistribution in taxol-treated mitotic cells probed by monoclonal antibodies. *Cell Motil Cytoskeleton* 33: 38–51. doi:10.1002/(sici)1097-0169(1996)33:1<38::aid-cm5>3.0.co;2-e

46. Dráberová E, Sulimenko V, Kukharskyy V, Dráber P (1999) Monoclonal antibody NF-09 specific for neurofilament protein NF-M. *Folia Biol (Praha)* 45: 163–165. https://fb.cuni.cz/volume-45-1999-no-4

47. Blume Y, Yemets A, Sulimenko V, Sulimenko T, Chan J, Lloyd C, Dráber P (2008) Tyrosine phosphorylation of plant tubulin. *Planta* 229: 143–150. doi:10.1007/s00425-008-0816-z

48. Kukharskyy V, Sulimenko V, Macurek L, Sulimenko T, Dráberová E, Dráber P (2004) Complexes of γ-tubulin with nonreceptor protein tyrosine kinases Src and Fyn in differentiating P19 embryonal carcinoma cells. *Exp Cell Res* 298: 218–228. doi:10.1016/j.yexcr.2004.04.016

49. Dráber P, Lagunowich LA, Dráberová E, Viklický V, Damjanov I (1988) Heterogeneity of tubulin epitopes in mouse fetal tissues. *Histochemistry* 89: 485–492. doi:10.1007/BF00492606

50. Dráberová E, Dráber P (1993) A microtubule-interacting protein involved in coalignment of vimentin intermediate filaments with microtubules. *J Cell Sci* 106: 1263–1273. https://jcs.biologists.org/content/106/4/1263

51. Klebanovych A, Sládková V, Sulimenko T, Vosecká V, Rubiková Z, Čapek M, Dráberová E, Dráber P, Sulimenko V (2019) Regulation of microtubule nucleation in mouse bone marrow-derived mast cells by protein tyrosine phosphatase SHP-1. *Cells* 8: 345–368. doi:10.3390/cells8040345

52. Schindelin J, Arganda-Carreras I, Frise E, Kaynig V, Longair M, Pietzsch T, Preibisch S, Rueden C, Saalfeld S, Schmid B, et al (2012) Fiji: An open-source platform for biological-image analysis. *Nat Methods* 9: 676–682. doi:10.1038/nmeth.2019

53. Cui XA, Palazzo AF (2012) Visualization of endoplasmic reticulum localized mRNAs in mammalian cells. *J Vis Exp* 70: e50066. doi:10.3791/50066

Figure S1
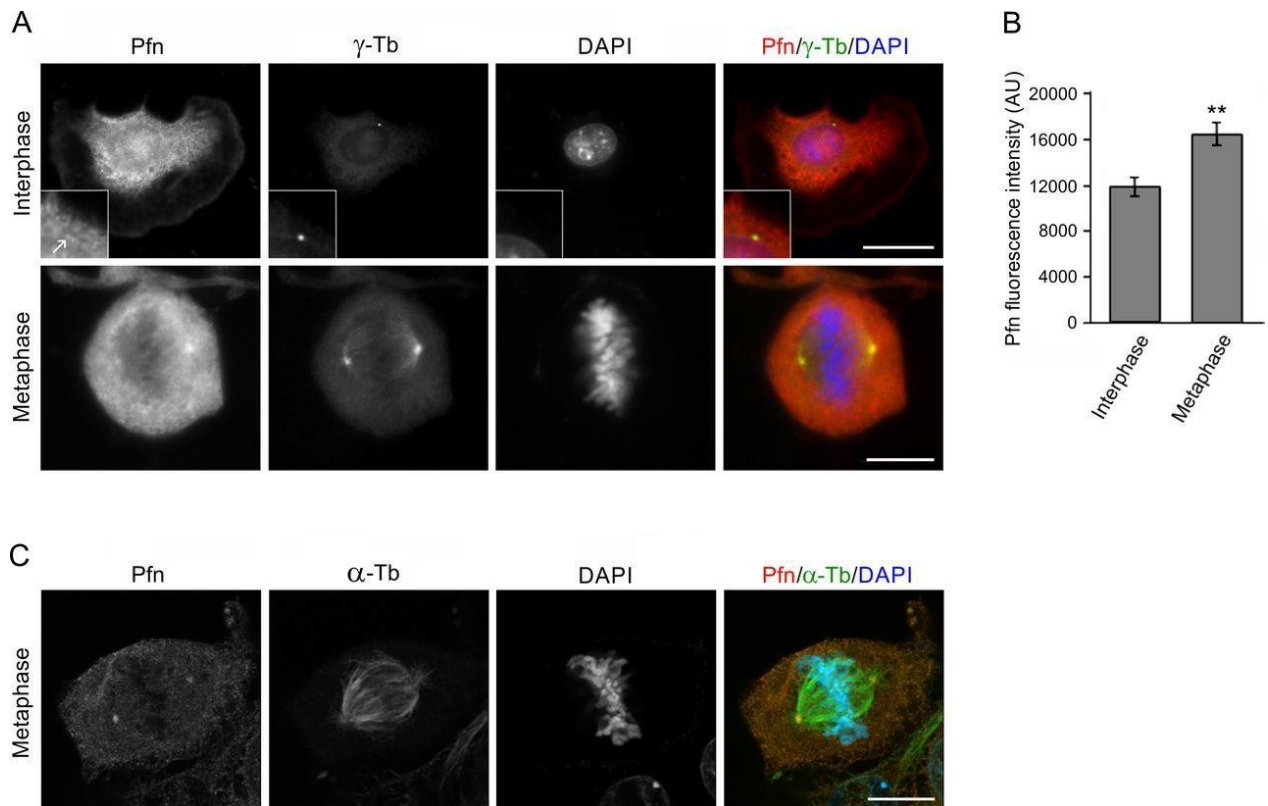
Profilin accumulates in centrosomes during mitosis.

Immunofluorescence staining of profilin and γ-tubulin in B16 cells followed by intensity measurements of centrosomal fluorescence reveals increased labeling of Pfn in mitotic cells. **(A)** Cells captured during interphase (top) and during metaphase (bottom). Wide-field microscopy after simultaneous staining for Pfn, γ-tubulin (γ-Tb) and DNA (DAPI). The centrosomal region is shown at higher magnification at the bottom left corner (inset); the arrow points to the centrosome. **(B)** Bar graph illustrating fluorescence intensity of Pfn labeling in a standardized circular area (1.2 μm^2) around the centrosomes in interphase (n = 31) and metaphase cells (n = 44) as determined by wide-field microscopy. Mean ± SEM, **$P < 0.01$. **(C)** High-resolution confocal microscopy (AiryScan) of a metaphase cell after simultaneous staining for Pfn, α-tubulin (α-Tb), and DNA (DAPI). Scale bars 10 μm.

Figure S2
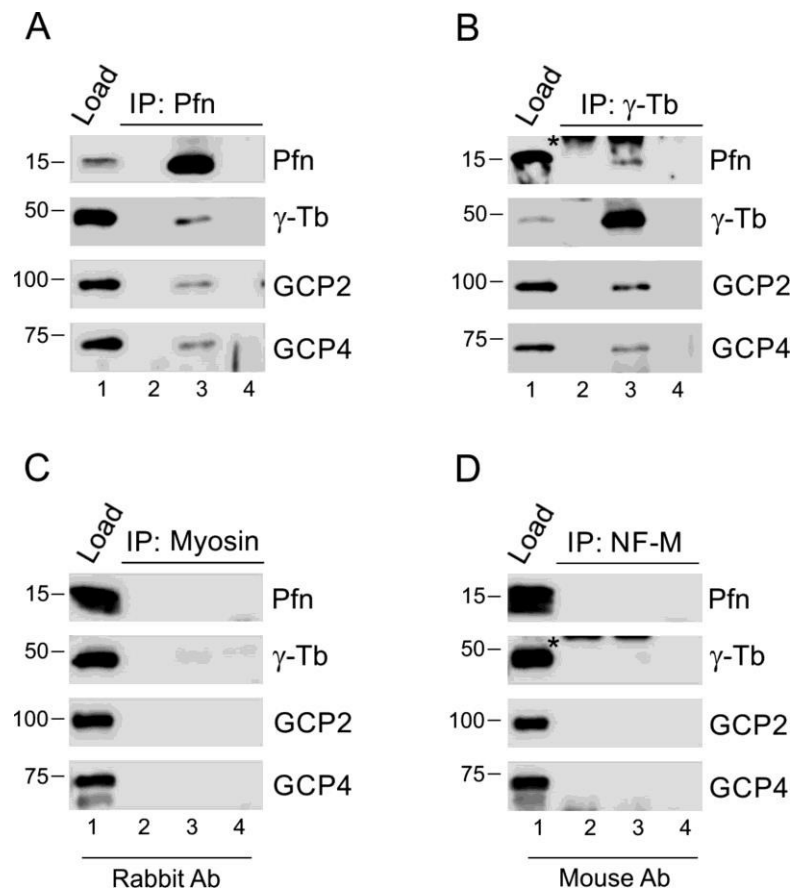
Profilin associates with γ-tubulin complex proteins in Caco-2 cells, and isotype controls of immunoprecipitations are negative.

(A, B) Extracts from Caco-2 cells were precipitated with immobilized Abs to profilin (A) and γ-tubulin (B), respectively, followed by Western blot analysis, using Abs against profilin (Pfn), γ-tubulin (γ-Tb), GCP2 and GCP4. Sample lanes 1–4 represent: total cell extract, gel load (1); no cell extract (2); precipitated proteins (3); carrier without Ab (4). **(C, D)** extracts of B16 cells were incubated with immobilized isotype control Abs, using rabbit Ab to myosin (C) and mouse mAbs (IgG2a) to neurofilament NF-M (D), respectively. **(A, B)** Subsequent Western blotting and analyzes were performed as in (A, B), using the same sample denotations. **(B, D)** Asterisks (*) in panels (B) and (D), lanes 2 and 3 denote cut off bands reflecting precipitating Ab.

Figure S3
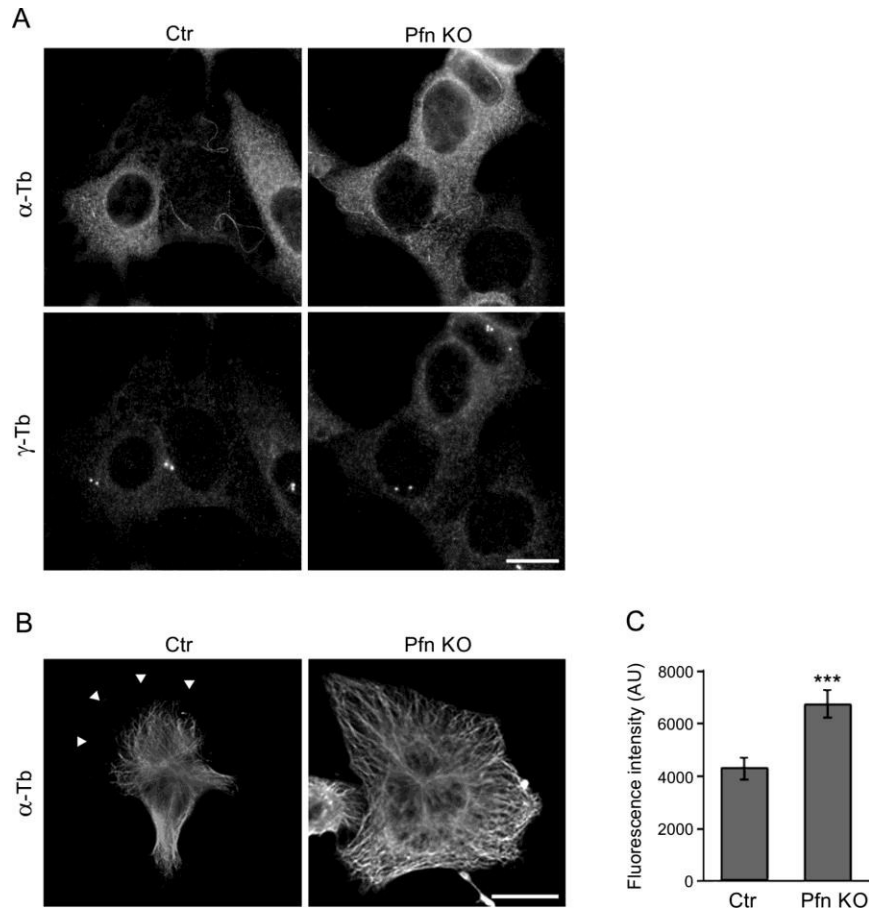
Nocodazole-resistant microtubules and microtubule organization in profilin knock-out cells (KO27).

(A) Nocodazole-resistant microtubules in B16 control (Ctr) and KO27 (Pfn KO) cells simultaneously stained by Abs to α-tubulin (α-Tb) and γ-tubulin (γ-Tb). Fixation F/Tx/M (see the Materials and Methods section). Scale bar, 10 μm. **(B)** Microtubule organization in B16 control (Ctr) and KO27 (Pfn KO) cells stained by Ab to α-tubulin (α-Tb). Arrowheads in left panel (Ctr) denote the tip of the cell edge. Scale bar, 10 μm. **(C)** Bar graph showing increased α-tubulin fluorescence in two randomly picked areas of standardized size (144 μm^2) in the lamellae of control (n = 29) and KO27 (n = 33) cells, respectively. Mean ± SEM, ***$P < 0.001$.

VII.5 **Klebanovych, A.,** Vinopal, S., Dráberová, E., Sládková, V., Sulimenko, T., Sulimenko, V., Vosecká, V., Macůrek, L., Legido, A., Dráber, P. (2021) C53 interacting with UFM1-protein ligase 1 regulates microtubule nucleation in response to ER stress (bioRxiv 10.1101/2020.12.23.424116)

C53 interacting with UFM1-protein ligase 1 regulates microtubule nucleation in response to ER stress

Anastasiya Klebanovych*[1], Stanislav Vinopal*[1, 2], Eduarda Dráberová*, Vladimíra Sládková*, Tetyana Sulimenko*, Vadym Sulimenko*, Věra Vosecká*, Libor Macůrek*[3], Agustin Legido†[4] and Pavel Dráber*[5]

*Laboratory of Biology of Cytoskeleton, Institute of Molecular Genetics of the Czech Academy of Sciences, CZ 142 20 Prague 4, Czech Republic

†Section of Neurology, St. Christopher's Hospital for Children, Department of Pediatrics, Drexel University College of Medicine, Philadelphia, PA 19134, USA

[1]A.K. and S.V. contributed equally to this work.

[2]Current address: Department of Biology, Faculty of Science, Jan Evangelista Purkyně University, CZ 400 96 Ústí nad Labem, Czech Republic

[3]Current address: Laboratory of Cancer Cell Biology, Institute of Molecular Genetics of the Czech Academy of Sciences, CZ 142 20 Prague 4, Czech Republic

[4]Current address: Department of Pediatrics, Cooper University Hospital, Cooper Medical School of Rowan University, Camden, NJ 08103, USA

[5]Address correspondence to Dr. Pavel Dráber, Laboratory of Biology of Cytoskeleton, Institute of Molecular Genetics of the Czech Academy of Sciences, Vídeňská 1083, 142 20 Prague 4, Czech Republic.

Tel.: (420) 241 062 632, Fax: (420) 241 062 758, E-mail:paveldra@img.cas.cz

Abstract

Homeostasis of ER is essential for cellular functions, and its disturbance activates the unfolded protein response resulting in ER remodeling. ER distribution depends on microtubules. CDK5RAP3 (C53) implicated in various signaling pathways interacts with UFM1-protein ligase 1 (UFL1), which mediates the ufmylation of proteins in response to ER stress. Here we find that UFL1 and C53 associate with γ-tubulin ring complex proteins. Knockout of *UFL1* or *C53* induces ER stress, centrosomal γ-tubulin accumulation, and microtubule nucleation. C53, whose protein level is modulated by UFL1, associates with the centrosome and can rescue microtubule nucleation in cells lacking UFL1. Pharmacological induction of ER stress by tunicamycin also leads to increased microtubule nucleation and ER expansion. Furthermore, tunicamycin suppresses the association of C53 with the centrosome. These findings point to a novel mechanism for the relief of ER stress by stimulation of microtubule nucleation. The interaction of ER with newly formed microtubules could promote its expansion to restore ER homeostasis.

Summary: Distribution of ER depends on microtubules, and ER stress triggers effector mechanisms leading to the restoration of ER homeostasis. The current study shows that C53, interacting with UFM1-protein ligase, associates with the centrosome and regulates microtubule nucleation in response to ER stress.

Condensed title: C53 regulates microtubule nucleation

Introduction

The endoplasmic reticulum consists of a continuous network of membranous sheets and tubules spanning the cytoplasm. It plays critical roles in a wide range of processes, including synthesis, folding, modification, and transport of proteins, synthesis and distribution of lipids, and Ca^{2+} storage. A diverse array of cellular stresses can lead to an imbalance between the protein-folding capacity and protein-folding load (Chakrabarti et al., 2011). The perturbation of ER homeostasis (ER stress) is ameliorated by triggering signaling cascades of the unfolded protein response (UPR), which engage effector mechanisms leading to homeostasis restoration. These mechanisms include increasing the capacity of the ER, increasing the degradation of ER luminal proteins or upregulation of chaperones and luminal protein modifications, or folding enzymes (Smith and Wilkinson, 2017). In the course of ER stress, the ER undergoes rapid and extensive remodeling hallmarked by the expansion of its lumen and an increase in tubules (Schuck et al., 2009). In mammalian cells, ER distribution is dependent on microtubules (Waterman-Storer and Salmon, 1998).

Microtubules, composed of α- and β-tubulin heterodimers, are highly dynamic and display dynamic instability characterized by altering phases of growth and shrinkage. During interphase, microtubules are mainly nucleated at the centrosome (microtubule organizing centers; MTOC) and radiate toward the cell periphery.

γ-Tubulin, a conserved member of the tubulin superfamily, is essential for microtubule nucleation in all eukaryotes (Oakley and Oakley, 1989). Together with other proteins named Gamma-tubulin Complex Proteins (GCPs; GCP2-6), it assembles into γ-Tubulin Ring Complex (γTuRC), which in mammalian cells effectively catalyzes microtubule nucleation. GCP2-6 each bind directly to γ-tubulin and assemble into cone-shaped structure of γTuRC (Kollman et al., 2011; Oakley et al., 2015). Recent high-resolution structural studies revealed details of asymmetric structure of γTuRC (Consolati et al., 2020; Liu et al., 2020; Wieczorek et al., 2020).

The γTuRCs are typically concentrated at MTOCs such as centrosomes and basal bodies in animals. They also associate with cellular membranes, including Golgi apparatus (Chabin-Brion et al., 2001), where they participate in non-centrosomal microtubule nucleation (Oakley et al., 2015). The majority of γTuRCs are generally inactive in the cytosol and become active at MTOCs. The mechanisms of γTuRC activation in cells are not fully understood. Current data suggest that γTuRC can be activated by structural rearrangement of γTuRC, phosphorylation or allosterically by binding to γTuRC tethering or modulating proteins accumulated in MTOCs (Liu et al., 2020; Sulimenko et al., 2017).

Ubiquitin-fold modifier (UFM1) is an ubiquitin-like posttranslational modifier that targets proteins through a process called ufmylation (Komatsu et al., 2004; Tatsumi et al., 2010). Conjugation of UFM1 to proteins is mediated by a process analogous to ubiquitination and requires specific activating (E1), conjugating (E2), and ligating (E3) enzymes. Unlike ubiquitination, the modification of proteins by ubiquitin-like modifiers generally serves as a non-proteolysis signal. It regulates various cellular processes by altering the substrate structure, stability, localization, or protein-protein interactions. The ufmylation has been reported to regulate multiple cellular processes, including the ER stress response, ribosome function,

control of gene expression, DNA damage response, and cell differentiation (Gerakis et al., 2019). Whether ufmylation controls microtubule organization is unknown. E3 UFM1-protein ligase 1 (also known as KIAA0776, RCAD, NLBP or Maxer; hereafter denoted as UFL1) (Kwon et al., 2010; Shiwaku et al., 2010; Tatsumi et al., 2010; Wu et al., 2010) is mainly located at the cytosolic side of the ER membrane (Shiwaku et al., 2010), where it is found in complex with DDRGK domain-containing protein 1 (DDRGK1, UFBP1) (Lemaire et al., 2011), the first identified substrate of ufmylation (Tatsumi et al., 2010). UPR directly controls the ufmylation pathway under ER stress at the transcriptional level (Zhang et al., 2012; Zhu et al., 2019).

Putative tumor suppressor CDK5 regulatory subunit-associated protein 3 (also known as CDK5RAP3, LZAP; hereafter denoted as C53) has initially been identified as a binding protein of CDK5 activator (Ching et al., 2000). Subsequent research showed that C53 exerts multiple roles in regulating the cell cycle, DNA damage response, cell survival, cell adherence/invasion, tumorigenesis, and metastasis (Jiang et al., 2005; Jiang et al., 2009; Liu et al., 2011; Wang et al., 2007; Zhao et al., 2011). Moreover, C53 is also involved in UPR (Zhang et al., 2012). Several studies have reported the interactions between C53 and UFL1 (Kwon et al., 2010; Shiwaku et al., 2010; Wu et al., 2010), and it was suggested that C53 could serve as UFL1 substrate adaptor (Yang et al., 2019). On the other hand, UFL1 regulates the stability of both C53 and DDRGK1 (Wu et al., 2010). Reports indicating the involvement of C53 in the modulation of microtubule organization are rare. It has been shown that a peptide from caspase-dependent cleavage of C53 participates in microtubule bundling and rupture of the nuclear envelope in apoptotic cells (Wu et al., 2013). In addition, we have demonstrated that C53 forms complexes with nuclear γ-tubulin and that γ-tubulin antagonizes the inhibitory effect of C53 on G_2/M checkpoint activation by DNA damage (Hořejší et al., 2012).

In the present study, we provide evidence that C53, which associates with UFL1 and γTuRC proteins, has an important role in the modulation of centrosomal microtubule nucleation in cells under ER stress. The interaction of ER membranes with newly formed microtubules could promote ER expansion to the cell periphery and help restore ER homeostasis.

Results

Identification of UFL1 as γ-tubulin interactor

We have previously reported the intrinsic association of γ-tubulin with cellular membranes in mouse P19 embryonal carcinoma cells undergoing neuronal differentiation (Macurek et al., 2008). To identify the potential interacting partners for membrane-bound γ-tubulin, we performed immunoprecipitation experiments with anti-peptide mAb to γ-tubulin and extracts from the microsomal fraction of differentiated P19 cells. The bound proteins were eluted with the peptide used for immunization or with a negative control peptide. In repeated experiments, a 90-kDa protein was specifically eluted with the immunization peptide but not with the control peptide. The protein was subjected to MALDI/MS fingerprint analysis and identified as UFL1 (UniProtKB identifier O94874) (Table S1). UFL1 mainly associates with the endoplasmic reticulum

(ER) membranes (Shiwaku et al., 2010; Tatsumi et al., 2010) and interacts with C53 (Kwon et al., 2010; Wu et al., 2010). We showed that C53 is present in γ-tubulin immunocomplexes from the nuclear fraction of human HeLa S3 cells (Hořejší et al., 2012). Collectively these data indicate that UFL1 and C53 can form complexes containing γ-tubulin.

UFL1 and C53 associate with γTuRC proteins

To ascertain whether membranous UFL1 associates both with C53 and γTuRC proteins in different cell types, we first performed immunoprecipitation experiments with extracts from the crude membranous fraction (P2) from human osteosarcoma U2OS cells. The fraction comprised UFL1, C53, γ-tubulin, GCP2, and calnexin (a marker of ER) but was devoid of α-tubulin, GM130, and histone H1.4 representing, cytosolic, Golgi apparatus and nuclear proteins, respectively (Fig. S1A, lane 5). Using two anti-UFL1 Abs recognizing epitopes in distinct UFL1 aa sequence regions (301-389 [$UFL1_{301-389}$] and 438-793 [$UFL1_{438-793}$]) and Abs to C53, γ-tubulin, and GCP2 for reciprocal precipitations, we revealed association of UFL1 and C53 with γTuRC proteins (Fig. 1A; Fig. S1B). As expected, we also verified the association of C53 with UFL1 (Fig. 1A, b and e).

We separated the extract from the membranous fraction (P2) on the Superose 6B column to learn about the size of studied complexes. UFL1 was mainly distributed in high molecular weight fractions, while C53 was detected both in high molecular and low molecular weight pools. Both γ-tubulin and GCP2 were partly located in high molecular weight fractions, where γTuRCs could be present. On the other hand, the control actin was not detected in the high molecular weight pools (Fig. 1B). We confirmed the interaction of γ-tubulin with UFL1 and C53 in pooled high molecular weight fractions from the column by an immunoprecipitation experiment (Fig. 1C).

When we performed immunoprecipitation experiments with membranous fractions from glioblastoma T98G cells, we likewise detected complexes comprising UFL1, C53, and γ-tubulin (Fig. S1C), indicating that such protein interactions are not limited to U2OS cells. The formation of complexes between UFL1, C53, γ-tubulin, and GCPs was not restricted to the membranous fractions, as we found interactions between these proteins using whole-cell extracts for immunoprecipitation (Fig. S1D). Moreover, separation of whole-cell extracts on the Superose 6B column resulted in partial co-distribution of UFL1, C53, γ-tubulin, and GCP2 in high molecular weight pools (Fig. S1E). Altogether, these results document that the mutually interacting UFL1 and C53 form complexes with γTuRC proteins.

Association of exogenous UFL1 and C53 with γTuRC proteins and centrosome

To independently validate the interaction of UFL1 and C53 with γTuRC proteins, we performed immunoprecipitation experiments from cells expressing EGFP-tagged UFL1 or C53 and control cells expressing EGFP alone. The Ab to GFP co-precipitated γ-tubulin, GCP2, GCP4, GCP6, and C53 from the cells expressing EGFP-UFL1 or C53-EGFP (Fig. 2A). Reciprocal precipitation with Ab to γ-tubulin confirmed the interaction of EGFP-tagged UFL1 or EGFP-tagged C53 with γ-tubulin (Fig. 2B). On the other hand, the Ab to GFP did not co-precipitate UFL1, C53, γ-tubulin, GCP2, or GCP4 from control cells

expressing EGFP alone. Similarly, Ab to γ-tubulin did not co-precipitate EGFP from the cells expressing EGFP alone (Fig. S1G). The isotype controls for the immunoprecipitation experiments with rabbit and mouse Abs are shown in Fig. S1F.

To further verify the interaction of UFL1 and C53 with γTuRC proteins, we performed pull-down assays with GST-tagged C53, UFL1, or γ-tubulin. The experiments revealed that γ-tubulin and GCP2 bound to GST-UFL1 or GST-C53, but not to GST alone (Fig. 2, C and D). Similarly, UFL1 and C53 bound to GST-tagged γ-tubulin but not to GST alone (Fig. 2E). The negative control protein (calcineurin) did not bind to GST-fusion proteins, although the amounts of immobilized GST fusion proteins were comparable, as evidenced by staining with Ab to GST (Fig. 2, C-E). Collectively, these data strongly suggest that exogenous UFL1 and C53 also form complexes with γTuRC proteins.

As γTuRCs are essential for normal microtubule nucleation from centrosomes, we tested whether UFL1 or C53 localize to the centrosome. However, using immunofluorescence microscopy with a limited number of commercially available Abs to UFL1 and C53, we failed to localize these proteins on the centrosome. We, therefore, expressed TagRFP-tagged UFL1, C53, or protein tyrosine phosphatase SHP-1 (negative control) in U2OS cells. While C53-TagRFP localized to interphase centrosomes, cytosol, and nuclei (Fig. 3A, a-c), UFL1-TagRFP was found only in the cytosol (Fig. 3A, d-f), similarly to control SHP-1-TagRFP (Fig. 3A, g-i). C53-TagRFP was also clearly detected on centrosomes in living cells (Fig. 3B, a-c), in contrast to UFL1-TagRFP. These data document that although UFL1 and C53 interact with each other and form complexes with γTuRC proteins, only C53 was detected at the centrosome.

Preparation and characterization of cell lines lacking UFL1 or C53

To evaluate the possible effect of UFL1 and C53 on microtubule nucleation, we prepared U2OS cell lines lacking UFL1. For that, we took advantage of CRISPR/Cas 9 editing. To delete the gene region containing the canonical and alternative start codons, cells were transfected with CRISPR/Cas9 vectors (sgRNA#1, sgRNA#2, SpCas9) together with reporter plasmid pRR-hUFL1-puro for the enrichment of cells not expressing UFL1. A schematic diagram of the human *UFL1* gene with sites targeted by sgRNA#1 and sgRNA#2, enabling efficient deletion of all UFL1 isoforms, is shown in Fig. S2A. We established three independent cell lines (denoted UFL1_KO1, UFL1_KO2, and UFL1_KO3) that have deletions in the targeted region (Fig. S2B) and undetectable UFL1 in immunoblotting (Fig. S2C). When compared to control cells, a radical decrease in immunofluorescence staining was observed in UFL1_KO cells (Fig. S2D) with Ab to UFL1. If not mentioned otherwise, the following results are based on UFL1_KO1 cells (abbreviated UFL1_KO).

We used the same approach to prepare U2OS cells lacking C53. For enrichment of cells not expressing C53, we prepared reporter plasmid pRR-hCDK5RAP3-puro. A schematic diagram of the human *CDK5RAP3* gene with sites targeted by sgRNA#1 and sgRNA#2, enabling efficient deletion of all C53 isoforms, is shown in Fig. S2E. We established three independent cell lines (denoted C53_KO1, C53_KO2, and C53_KO3) that have deletions in the targeted region (Fig. S2F) and undetectable C53 in immunoblotting (Fig. S2G). When compared to control cells, a substantial decrease in immunofluorescence staining was

observed in C53_KO cells (Fig. S2H). If not mentioned otherwise, the following results are based on C53_KO1 cells (abbreviated C53_KO).

To assess the effect of UFL1 or C53 deletion on cell division, we determined cell growth in control and UFL1_KO or C53_KO cells. When compared to control cells, the number of viable cells decreased both in UFL1-KO and C53_KO, but proliferation was hampered more in UFL1_KO cells (Fig. 4A). Quantitative immunoblot analysis showed that the deletion of UFL1 resulted in a substantial reduction of C53 and DDRGK1. On the other hand, the deletion of C53 only resulted in a moderate decrease in UFL1 and DDRGK1. In cells lacking UFL1, the amount of C53 and DDRGK1 dropped to ~10% and ~40% of the wild-type level, respectively. In cells lacking C53, the amount of UFL1 and DDRGK1 decreased to ~75% and ~80% of the wild-type level, respectively (Fig. 4B). The deletion of UFL1 or C53 did not affect the expression of γ-tubulin or GCP2. Changes in cell proliferation were also documented by quantitative immunoblot analysis with Abs to cyclin B1 and mitotic p-Histone H3. Lower amounts of cyclin B1 and p-Histone H3 were detected in UFL1_KO cells when compared to controls. A similar tendency, but less prominent, was observed in the case of C53_KO cells (Fig. 4C).

Experiments on knockout mouse models revealed that the deletion of UFL1 (Li et al., 2018; Zhang et al., 2015) or C53 (Yang et al., 2019) triggered ER stress and activated the unfolded protein response (UPR). One of the characteristic features of stressed cells is the expansion of the ER network (Sriburi et al., 2004). To characterize the prepared cell lines with respect to ER stress, we visualized ER in living cells by cell-permeant ER-Tracker. Substantial changes in ER distribution were observed both in UFL1_KO and C53_KO cells. In control cells, the staining intensity of ER-Tracker cumulated in the perinuclear region. The ER tubules at the cell periphery were sparse (Fig. 4D, a). In UFL1_KO cells, ER-Tracker staining intensity was more evenly distributed throughout the cells, suggesting the expansion of the ER network (Fig. 4D, b). The ER expansion in the C53_KO cell was less prominent than in UFL1_KO cells (Fig. 4D, c).

Collectively these findings point to the vital role of UFL1 and C53 in cell proliferation and ER homeostasis. In good agreement with previous studies (Kwon et al., 2010; Wu et al., 2010), UFL1 effectively regulates the C53 protein level.

UFL1 or C53 deficiency increase centrosomal microtubule nucleation

To unravel the effect of UFL1 and C53 deficiency on microtubule nucleation, we followed microtubule regrowth from U2OS centrosomes, which represent the major nucleation centers in interphase cells. Microtubule regrowth in nocodazole-washout experiments in control, UFL1_KO, and C53_KO cells were performed as previously described (Sulimenko et al., 2015). The extent of microtubule regrowth could be modulated by mechanisms regulating either microtubule nucleation or microtubule dynamics. It was reported previously that microtubule dynamics is regulated in the cell periphery and that a delay in microtubule regrowth is associated with defects in microtubule nucleation (Colello et al., 2010). We measured α-tubulin and γ-tubulin immunofluorescence signals in a 2.0 μm ROI, 2.0 min after nocodazole-washout in UFL1- or C53-deficient cells and controls. When compared with control cells, an increase in microtubule regrowth was observed both in UFL1_KO1 (Fig. 5A) and C53_KO1 (Fig. 5D) cells. Quantification of γ-tubulin

immunofluorescence revealed that the amount of γ-tubulin in centrosomes increased in both UFL1_KO1 (Fig. 5B) and C53_KO1 (Fig. 5E) cells. Typical staining of α-tubulin and γ-tubulin in control, UFL1_KO1, and C53_KO1 cells is shown in Fig. 5C and Fig. 5F. When microtubule regrowth experiments were performed with the other deficient cell lines (UFL1_KO2, UFL1_KO3 or C53_KO2, C53_KO3), similar results were obtained. While the amount of centrosomal γ-tubulin increased in the cells lacking UFL1 or C53, the amount of centrosomal pericentrin was not affected (Fig. S3, A-D).

To independently evaluate the role of UFL1 and C53 in microtubule nucleation, we performed time-lapse imaging in cells expressing mNeonGreen-tagged microtubule end-binding protein 3 (EB3), decorating plus ends of the growing microtubules (Akhmanova and Steinmetz, 2008), and counted the number of EB3 comets leaving the centrosomes per unit time (nucleation rate) (Černohorská et al., 2016; Colello et al., 2010). When compared to control cells, the nucleation rate increased in cells lacking UFL1 (Fig. 5G). A similar effect was observed after deletion of C53 (Fig. 5H). A comparison of a single frame or 10-frame projections from control and UFL1_KO1 or C53_KO1 cells is shown in Fig. S3E and Fig. S3F. These live-imaging data corresponded to the results obtained by measuring the α-tubulin signal during the microtubule regrowth experiment.

To verify the specificity of observed changes in microtubule nucleation, we performed rescue experiments by expressing UFL1-TagRFP or TagRFP alone in UFL1_KO cells. The introduction of UFL1-TagRFP into UFL1-deficient cells restored UFL1 expression and enhanced the expression of C53 (Fig. 6A). While the introduction of UFL1-TagRFP into UFL1_KO cells decreased the microtubule regrowth to that in control cells, the expression of TagRFP failed to do so (Fig. 6B). Correspondingly, the amount of centrosomal γ-tubulin decreased after the introduction of UFL1-TagRFP into UFL1-KO cells, whereas it remained elevated in UFL1_KO cells expressing TagRFP alone (Fig. 6C). A similar set of phenotypic rescue experiments was performed in C53_KO cells. C53-TagRFP efficiently restored the C53 level in deficient cells (Fig. 6D), and microtubule regrowth was restored to that in control cells (Fig. 6E). Also, the amount of γ-tubulin in centrosomes decreased after introducing C53-TagRFP to deficient cells (Fig. 6F).

To test whether C53 can rescue increased microtubule nucleation phenotype in UFL1_KO cells, C53-TagRFP or TagRFP alone were expressed in UFL1_KO cells. C53-TagRFP was efficiently expressed in UFL1_KO cells that are characterized by a low amount of C53 (Fig. 4B and Fig. 6G). In UFL1_KO cells expressing C53-TagRFP, both microtubule regrowth (Fig. 6H) and the amount of centrosomal γ-tubulin (Fig. 6I) decreased to the levels in control cells. These data highlight C53 as a novel regulator of centrosomal microtubule nucleation.

Altogether, these data indicate that both UFL1 and C53 negatively regulate microtubule nucleation from the interphase centrosome by influencing centrosomal γ-tubulin/γTuRCs levels. The modulation of microtubule nucleation by UFL1 likely occurs by reducing the amount of centrosomal C53.

Enhancement of microtubule nucleation in cells under ER stress

As live-cell imaging of ER in control, UFL1_KO, and C53_KO cells indicated generation of ER stress in cells lacking UFL1 and C53 (Fig. 4D), we evaluated changes in the expression and cellular distribution of

chaperone calnexin and protein disulfide-isomerase (PDI), well-established markers of UPR, facilitating protein folding (Chakrabarti et al., 2011). Densitometric analysis of immunoblotting experiments revealed a significantly increased expression of calnexin and PDI in UFL1_KO cells. These UPR markers also increased in C53_KO cells, albeit PDI only moderately (Fig. 7A). Immunofluorescence microscopy verified increased expression of calnexin (Fig. 7B, e and i) and PDI (Fig. S4A, e and i) in cells lacking UFL1 or C53. When compared with control cells, immunostaining for calnexin spread to the cell periphery delineated by ends of microtubules both in UFL1_KO and C53_KO cells, as shown in magnified regions (Fig. 7B, g and k). Similarly, the PDI immunostaining also expanded to the cell periphery in cells lacking UFL1 or C53 (Fig. S4A, g and k). To evaluate whether C53 can rescue calnexin spreading to the cell periphery in UFL1_KO cells, C53-TagRFP or TagRFP alone were expressed in UFL1_KO cells. In UFL1_KO cells expressing C53-TagRFP, the distribution of calnexin in the cell periphery approached that in control cells (Fig. 7C, a-c). Staining for TagRFP delineated cell periphery (Fig. 7C, d-f). Densitometric analysis of immunoblots revealed a partial decrease in calnexin protein level in UFL1_KO cells expressing C53-TagRFP (Fig. S4B), indicating that C53 cannot completely rescue significant ER stress induced in UFL1-KO cells lacking the ufmylation capability.

Microtubules are known to regulate ER homeostasis, with ER dynamics tightly linked to the dynamics of microtubules. This is particularly important during ER stress, as the expansion of the ER is one of the relief mechanisms (Schuck et al., 2009). To evaluate whether the expansion of ER in stressed cells could be potentially promoted by *de novo* microtubule nucleation, we pretreated U2OS cells with tunicamycin, a potent inhibitor of protein glycosylation and ER stress activator (Ding et al., 2007). Immunofluorescence microscopy in tunicamycin-treated cells showed expansion of ER, as documented by staining of live cells with ER-Tracker which was more evenly distributed throughout treated-cells than in controls (Fig. 8A, a and b), and by staining fixed cells with Abs to calnexin (Fig. 8A, c and d) and PDI (Fig. 8A, e and f). Moreover, DNA damage-inducible transcript 3 (DDIT3), representing another UPR marker (Chakrabarti et al., 2011), accumulated in nuclei after tunicamycin treatment (Fig. 8A, g and h). Increased expression of calnexin, PDI, and DDIT3 after tunicamycin treatment was confirmed by immunoblotting (Fig. 8B). Changes in the protein level corresponded to changes in the transcript level (Fig. S4C). Interestingly, we detected increased microtubule regrowth (Fig. 8C) and centrosomal γ-tubulin accumulation (Fig. 8D) in tunicamycin-treated cells. Correspondingly, the nucleation rate also increased in treated cells (Fig. 8E and Fig. 8F). When cells expressing C53-TagRFP were pretreated with tunicamycin, fluorescence microscopy revealed that the overall C53-TagRFP signal decreased, and its association with the centrosome was suppressed (Fig. 9A). Immunoblot analysis showed that while the amount of C53-TagRFP diminished in tunicamycin-treated cells, protein levels of UFL1, endogenous C53 or γ-tubulin were similar in control and drug-treated cells (Fig. 9B). No changes in fluorescence staining intensity were observed in cells expressing TagRFP alone and treated or not with tunicamycin (Fig. 9C). Immunoblot analysis also did not reveal changes in the amount of TagRFP (Fig. 9D), ruling out the possibility that tunicamycin affects expression of tagged proteins. Interestingly, lower amount of C53 associated with P1 fraction, comprising centrosomes and nuclei with connected membranes, in tunicamycin-treated cells. On the other hand, a comparable amount of pericentrin was found

in P1 fractions of control and drug-treated cells (Fig. 9E). Obtained data indicate that tunicamycin induced subcellular redistribution of C53 away from the centrosome.

Collectively taken, these results suggest that also during pharmacologically induced ER stress, centrosomal microtubule nucleation is enhanced.

Discussion

The ER distribution is dependent on microtubules. Although ER expansion is characteristic of cells under ER stress (Smith and Wilkinson, 2017), the molecular mechanisms of microtubule regulation in this process are not fully understood. UFL1 and its adaptor C53 are essential for ER homeostasis (Gerakis et al., 2019), and their deletions generate ER stress (Yang et al., 2019). To evaluate the role of UFL1 and C53 in microtubule organization, we made use of well-adherent U2OS cells suitable for analysis of microtubule nucleation from interphase centrosomes. We report on UFL1 and C53 association with γTuRC proteins and their involvement in the regulation of centrosomal microtubule nucleation. Increased microtubule nucleation in cells under ER stress could facilitate ER expansion to the cell periphery.

Interaction of UFL1 and C53 with γTuRC proteins
Several lines of evidence support the conclusion that UFL1 and C53 (UFL1/C53) associate with γTuRC proteins. First, UFL1 was identified by MALDI/MS fingerprinting analysis after immunoprecipitation with anti-peptide mAb to γ-tubulin and elution of bound proteins with the immunizing peptide. Second, reciprocal immunoprecipitations confirmed the formation of complexes containing UFL1, C53, γ-tubulin, and GCPs. Third, separation of extracts by gel filtration revealed co-distribution of UFL1, C53, γ-tubulin, and GCP2 in high molecular weight fractions, in which both UFL1 and C53 co-precipitated with γ-tubulin. Fourth, γ-tubulin and GCPs associated with EGFP-tagged UFL1 or C53. Finally, γ-tubulin and GCP2 bound to GST-tagged UFL1 or C53, and both UFL1 and C53 interacted with GST-γ-tubulin. Interaction of UFL1/C53 with γ-tubulin was observed in cells of different tissue origin. Association was found in human osteogenic sarcoma (U2OS), glioblastoma (T98G), and cervix adenocarcinoma (HeLa S3) cells. These findings suggest that multiprotein complexes containing UFL1/C53 and γTuRC proteins occur in various cell types.

UFL1 directly interacts with C53 (Kwon et al., 2010; Wu et al., 2010), which can serve as a substrate adaptor for UFL1 (Yang et al., 2019). Both UFL1 and C53 are largely ER-associated proteins (Shiwaku et al., 2010; Tatsumi et al., 2010; Wu et al., 2010). Reciprocal precipitation of these proteins from membranous fractions was therefore expected. On the other hand, the association of UFL1/C53 with membrane-bound γTuRC proteins was surprising. To our knowledge, such interaction has not been reported. We have previously shown that γ-tubulin associated with detergent-resistant membranes in mouse embryonic carcinoma P19 cells induced to neuronal differentiation (Macurek et al., 2008) and in the human brain (Dráberová et al., 2017). In this context, it should be noted that γ-tubulin is associated with vesicular structures and Golgi-derived vesicles (Chabin-Brion et al., 2001), and γ-tubulin is essential for microtubule

nucleation from the Golgi membranes (Wu et al., 2016). γ-Tubulin has also been found on recycling endosomes (Hehnly and Doxsey, 2014) and mitochondrial membranes (Dráberová et al., 2017). It was reported that UFL1 regulates the mitochondrial mass (Zhang et al., 2015). Since ER and mitochondria are known to cross-talk at membrane contact sites (Lombardi and Elrod, 2017), deciphering the role of UFL1/C53 in the regulation of microtubule nucleation from membrane-bound γ-tubulin complexes warrants further investigation.

Microtubule nucleation in cells lacking UFL1 or C53

Although UFL1/C53 interacted with γTuRC proteins, tagged fluorescent proteins revealed a centrosomal association in fixed and living cells only in the case of C53. Centrosomal localization of C53 was previously reported with antibodies (Jiang et al., 2009). We failed to localize C53 to centrosomes using a panel of commercial antibodies under various fixation conditions. The differences in immunofluorescence localization of C53 could reflect the exposure of epitopes for the used Abs. Reports on centrosomal localization of UFL1 are missing.

We prepared, using CRISPR/Cas 9 gene editing, cell lines lacking either UFL1 or C53. Cell growth inhibition, a decrease in mitotic p-Histone H3, and cyclin B1 suppression were characteristic features of UFL1_KO cells. A similar tendency, but less prominent, was also observed in the case of C53_KO cells. Decreased proliferation was described after the depletion of UFL1 by siRNA in glioma C6 cells (Shiwaku et al., 2010) and by shRNA in U2OS (Zhang et al., 2012). A decrease in proliferation and mitosis was reported in C53-deficient zebrafish embryos (Liu et al., 2011), and suppression of cyclin B1 was shown in fetal livers from C53 knockout mice (Yang et al., 2019). Our data confirm that both UFL1 and C53 participate in the regulation of the cell cycle. The absence of UFL1 resulted in a substantial reduction of C53 and DDRGK1. On the other hand, only a moderate decrease in the amount of UFL1 and DDRGK1 was observed in cells lacking C53 (Fig. 4B). It was reported that UFL1 and C53 mutually affect the stability of each other by inhibiting the ubiquitination of the other system (Kwon et al., 2010). The depletion of UFL1 rendered both C53 and DDRGK1 more susceptible to ubiquitin/proteasome system-mediated protein degradation (Wu et al., 2010). UFL1 thus plays a vital role in the regulation of the C53 protein level.

Our data demonstrate that UFL1 and C53 represent negative regulators of microtubule nucleation from interphase centrosomes. The deletion of both UFL1 and C53 increased centrosomal microtubule nucleation. Nevertheless, loss of UFL1 also leads to a strong reduction of the C53 level. The rescue of microtubule nucleation phenotype in UFL1_KO cells by C53 (Fig. 6, G-I), therefore, strongly suggests that C53 is a novel regulator of centrosomal microtubule nucleation. The regulatory role of UFL1 in microtubule nucleation could thus be indirect through modulation of the C53 amount or subcellular localization. As complexes of C53 and UFM1 have been reported (Lemaire et al., 2011; Yoo et al., 2014), it was proposed that C53 may represent an ufmylation target. However, our results from rescue experiments indicate that putative C53 ufmylation is not required for the modulation of centrosomal microtubule nucleation.

Microtubule nucleation at the centrosome occurs from γTuRCs located in the pericentriolar material (Teixidó-Travesa et al., 2012). We, therefore, examined whether UFL1 and C53 regulate microtubule

nucleation by affecting the centrosomal γ-tubulin levels. Our data suggest that in wild-type cells, both proteins suppress γ-tubulin accumulation at the centrosome. On the other hand, no changes in the amount of pericentrin were detected, showing that the general pericentriolar matrix integrity is not affected by C53 or UFL1 depletion. Altogether, these data suggest that the regulatory roles of UFL1 and C53 are conveyed by γ-tubulin/γTuRC accumulation on centrosomes. Such a regulatory mechanism of microtubule nucleation is not unique only for UFL1/C53. It has been reported that androgen and Src signaling, which leads to the activation of the ERK, regulate microtubule nucleation by promoting the accumulation of γ-tubulin at the centrosome (Colello et al., 2010). Modulation of γ-tubulin accumulation in centrosomes was also shown for GIT1/βPIX signaling proteins and PAK1 kinase (Černohorská et al., 2016), and for tyrosine phosphatase SHP-1 (Klebanovych et al., 2019).

Regulatory mechanisms by which UFL1/C53 can control microtubule nucleation

C53 binds to multiple targets but has no enzymatic domain or other well-characterized functional motifs, suggesting that it may exert its activity through interaction with other proteins. Recently, C53 was identified as a highly conserved regulator of ER-stress-induced ER-phagy (Stephani et al., 2020). Interestingly, accumulating evidence suggests that C53 is also implicated in the regulation of protein phosphorylation. It was reported that C53 directly bound to protein serine/threonine-protein phosphatase 1D (PP2Cδ) and promoted its phosphatase activity toward several C53 targets. (Wamsley et al., 2017). Phosphorylation sites have been identified in building components of γTuRC. In contrast to αβ-tubulin dimers (Linhartová et al., 1992), posttranslational modification of γ-tubulin is less prominent (Vinopal et al., 2012). However, several reports have shown γ-tubulin phosphorylation (Keck et al., 2011; Kukharskyy et al., 2004; Vogel et al., 2001). Similarly, proteomic studies revealed multiple phosphorylation sites on GCPs (Teixidó-Travesa et al., 2012). Many phosphorylation sites have also been identified in various γ-TuRC tethering proteins, including NEDD1/Grip71, pericentrin, CDK5RAP2, Cnn, Mto2, and Spc110 as reviewed (Tovey and Conduit, 2018). Several of these sites have been characterized and have been shown to stimulate γTuRC assembly, recruitment, or activation (Tovey and Conduit, 2018). On the other hand, phosphorylation can also negatively regulate γTuRC recruitment and activity, as hyperphosphorylation of Mto2 in fission yeast leads to the inactivation of γTuRCs at non-spindle pole body sites (Borek et al., 2015). The activities of kinases and phosphatases have to be balanced to finely tune microtubule nucleation events during the cell cycle and in response to stress conditions. It was reported that serine/threonine-protein phosphatase 4 (PP4C) in complex with its regulatory subunits R2 and R3A associates with the centrosome, interacts with γ-tubulin and GCP2, and dephosphorylates phosphorylated γ-tubulin (Voss et al., 2013). We have recently demonstrated that tyrosine-protein phosphatase SHP-1 forms complexes with γTuRC proteins and suppresses microtubule nucleation. This indicates that different protein phosphatases might be involved in distinct signaling pathways with respect to the regulation of microtubule nucleation (Klebanovych et al., 2019). The activation of phosphatase(s) by C53 might maintain a low level of phosphorylated γTuRCs or TuRC-tethering proteins, resulting in the attenuation of microtubule nucleation.

Although the regulation of microtubule nucleation in interphase UFL1_KO cells could be explained by a low amount of C53, one cannot rule out that in mitotic cells, UFL1 affects microtubule nucleation independently of C53. It was reported that the UFM1 cascade is essential for the organization of the mitotic apparatus in *Drosophila* and alters the level of phosphorylation on tyrosine-15 of Cdk1 (pY15-Cdk1), which serves as an inhibitor of G2/M transition. In cells lacking UFL1, the level of pY15-Cdk1 was significantly reduced, indicating increased activity of Cdk1 (Yu et al., 2020). Sequential phosphorylation of NEDD1 by Cdk1 and Plk1 is required for targeting γTuRCs to centrosomes during mitosis (Zhang et al., 2009).

Enhanced microtubule nucleation in cells under ER stress

One of the characteristic features of U2OS cells without UFL1 is the generation of ER stress, which was previously reported in mouse UFL1 knockout models for bone marrow cells (Zhang et al., 2015) and cardiomyocytes (Li et al., 2018). Similarly, U2OS cells lacking C53 are under ER stress, which was also recently reported in the mouse C53 knockout model for hepatocytes (Yang et al., 2019). When compared to control cells, where ER was unevenly distributed in the cytosol and concentrated around the nucleus, the UFL1_KO or C53_KO cells had an ER network more evenly distributed to the periphery. This was clearly evident by visualizing ER with ER-Tracker or by immunostaining for PDI or calnexin, which protein level increased in cells lacking UFL1 or C53. Expansion of ER to the cell periphery was described using staining with Ab to PDI, after partial depletion of UFL1 and C53 by RNAi (Zhang et al., 2012). Expansion of ER to the cell periphery was also clearly observable in cells pretreated with tunicamycin, a pharmacological inducer of ER stress (Ding et al., 2007).

In mammalian cells, the ER network rearrangements strongly depend on the interactions with dynamic microtubules (Terasaki et al., 1986). This is very important during ER stress, as the expansion of ER alleviates ER stress (Schuck et al., 2009; Sriburi et al., 2004). There are four distinct mechanisms of how ER can be rearranged with the help of microtubules. ER tubules can be pulled out of the existing ER membranes by associating with motor proteins and then extending along microtubules (sliding mechanism), or by attaching to the tips of growing microtubules (Waterman-Storer and Salmon, 1998). New ER tubules can also be generated by hitchhiking on organelles that are transported along microtubules by molecular motors. Finally, recent work has shown that ER tubules can be pulled by shrinking microtubule ends (Guo et al., 2018). The increased microtubule nucleation in the cells under ER stress shown in this work extends the microtubule network, which could help to expand ER membranes to the cell periphery.

The regulatory mechanism of microtubule nucleation in tunicamycin-treated cells is unknown. However, C53 likely plays a role in this process since exogenous C53 decreased in the whole cell, including the centrosome in tunicamycin-treated cells. Moreover, endogenous C53 relocated from the subcellular fraction containing centrosomes after tunicamycin treatment. Thus the relocation of C53 from the centrosome could unblock microtubule nucleation in cells under ER stress. UFL1-catalyzed ufmylation is vital for relieving ER stress via ER-phagy (Liang e al., 2020). An increase in centrosomal microtubule nucleation might facilitate increased autophagic flux, ER expansion, and relief of ER stress.

In conclusion, in this study, we show that UFL1 and C53 interacting with γTuRC proteins play an important role in microtubule nucleation. C53, whose protein level is modulated by UFL1, associates with centrosome and represents a negative regulator of microtubule nucleation from the centrosomes. We demonstrate that the ER stress generated either by UFL1/C53 deletion or by pharmacological stressor stimulates centrosomal microtubule nucleation. The interaction of ER with newly formed microtubules could promote its enlargement to restore ER homeostasis. This suggests a novel mechanism for facilitating the ER network expansion under stress conditions.

Material and methods

Reagents

Nocodazole, puromycin, geneticin (G418), dimethyl pimelimidate dihydrochloride and all-*trans*-retinoic acid were from Sigma-Aldrich (St. Louis, MO, USA). Lipofectamine 3000 was purchased from Invitrogen (Carlsbad, CA, USA). Protein A Sepharose CL-4B and Glutathione Sepharose 4 Fast Flow were from GE Healthcare Life Sciences (Chicago, IL, USA). Protease-inhibitor mixture tablets (Complete EDTA-free) were from Roche Molecular Biochemicals (Mannheim, Germany). Restriction enzymes were from New England Biolabs (Ipswich, MA, USA). Oligonucleotides were synthesized by Sigma-Aldrich. Oligopeptides EYHAATRPDYISWGTQ (human γ-tubulin amino acid [aa] sequence 434-449) and EEFATEGTDRKDVFFY (human γ-tubulin aa sequence 38-53) (Zheng et al., 1991) were synthesized by Jerini Peptide Technologies (Berlin, Germany). ER-Tracker Green (BODIPY FL Glibenclamide) was from Molecular Probes (Eugene, OR, USA), and 1mM stock was prepared in DMSO. Tunicamycin was from Sigma-Aldrich, and 1mg/ml stock was prepared in DMSO.

Antibodie*s*

Catalog numbers for primary commercial Abs are shown in parentheses. Mouse mAbs TU-30 (IgG1) and TU-31 (IgG2b) to γ-tubulin aa sequence 434-449 were described previously (Nováková et al., 1996). Mouse mAbs GTU-88 to γ-tubulin aa sequence 38-53 (IgG1; T6557) and TUB2.1 to β-tubulin (IgG1, T4026), as well as rabbit Abs to actin (A2066), C53 (HPA022141), calnexin (C4731), DDRGK1 (HPA013373), GAPDH (G9545), GFP (G1544), histone H1.4 (H7665), PDI (P7496) and UFL1 (HPA030560; aa sequence 301-389) were from Sigma-Aldrich. Mouse mAbs to GCP4 (IgG1, sc-271876) and GCP6 (IgG1, sc-374063), as well as rabbit Abs to SHP-1 (sc-287) and p-Histone H3 (Ser 10) (sc-8656) were from Santa Cruz Biotechnology (Dallas, TX, USA). Rabbit Abs to calcineurin (2614) and cyclin B1 (4138) were from Cell Signaling Technology (Danvers, MA, USA). Mouse mAbs to C53 (IgG1; ab-57817) and DDIT3 (IgG2b, ab11419), as well as rabbit Ab to pericentrin (ab4448) were from Abcam (Cambridge, UK). Mouse mAb to GM130 (IgG1; 610822) was from BD Transduction Laboratories (San Jose, CA, USA), rabbit Ab to GFP (11-476-C100) was from Exbio (Prague, Czech Republic), and rabbit Ab to pericentrin (ABT59) was from EMD-Millipore (La Jolla, CA, USA). Rabbit Ab to α-tubulin (600-401-880) was from Rockland

Immunochemicals (Limerick, PA, USA). Rabbit Ab to tRFP was from Evrogen (Moscow, Russia). Mouse mAbs GCP2-01 (IgG2b) and GCP2-02 (IgG1) to GCP2 were described previously (Dráberová et al., 2015), as well as mAb to α-tubulin TU-01 (Viklický et al., 1982). Rabbit Ab to non-muscle myosin heavy chain (BT-561; Biomedical Technologies., Stoughton, MA, USA) and mAb NF-09 (IgG2a) to neurofilament NF-M protein (Dráberová et al., 1999) served as negative controls in the immunoprecipitation experiments. Rabbit Ab to GST was from Dr. Pe. Dráber (Institute of Molecular Genetics, CAS, Prague, Czech Republic).

Anti-mouse and anti-rabbit Abs conjugated with horseradish peroxidase (HRP) were from Promega Biotec (Madison, WI, USA). TrueBlot anti-rabbit IgG HRP was purchased from Rockland Immunochemicals. Anti-mouse Abs conjugated with DyLight649, DyLight549, or AlexaFluor488 and anti-rabbit Abs conjugated with Cy3 or AlexaFluor488 were from Jackson Immunoresearch Laboratories (West Grove, PA, USA).

Rabbit Ab to human UFL1 sequence 438-793 was prepared by immunizing three rabbits with purified GST-tagged human UFL1 fragment (GST-hUFL1_438-793). The procedure of immunization has been described previously (Dráber et al., 1991). Titers of sera were determined in ELISA using immobilized GST-hUFL1_438-793 or GST alone. Serum with the highest titer to GST-hUFL1_438-793 was partially purified and concentrated by ammonium sulfate precipitation. The precipitate was dissolved and dialyzed against PBS. Antigen or GST alone were covalently linked to Glutathione Sepharose 4 Fast Flow by dimethyl pimelimidate dihydrochloride as described (Bar-Peled and Raikhel, 1996). Prepared carriers were thereafter used for affinity isolation of Ab to UFL1. Shortly, a partially purified Ab was first preabsorbed with immobilized GST to remove anti-GST Abs. Then, Ab was bound onto the carrier with GST-hUFL_438-793. The solution of 0.1 M glycine-HCl, pH 2.5 was used for elution, and 0.2 ml fractions were immediately neutralized by adding 20 µl of 1M Tris-Cl, pH 8.0. Affinity-purified Ab stained GST-UFL1, but not GST alone, on the immunoblot, and detected UFL1 in whole-cell lysates.

Cell cultures

Human osteogenic sarcoma cell line U-2 OS (U2OS) (Catalog No. ATCC, HTB-96), human glioblastoma cell line T98G (Catalog No. ATCC, CRL-1690), and human cervix adenocarcinoma HeLa S3 (Catalog. No. ATCC, CCL-2.2) were obtained from the American Type Culture Collection (Manassa, VA, USA). Cells were grown at 37°C in 5% CO_2 in DMEM supplemented with 10% FCS and antibiotics. P19.X1 cells, a subclone of mouse embryonal carcinoma cells P19, were cultured and subsequently differentiated by incubating cells with 1 µM all-*trans*-retinoic acid for nine days as described (Kukharskyy et al., 2004).

For ER live-cell imaging, cells were incubated with 1 µM ER-Tracker Green in Hank's Balanced Salt Solution with calcium and magnesium (HBSS/Ca/Mg) for 30 min at 37°C. The staining solution was replaced with a probe-free medium and viewed by fluorescence microscopy. In some cases, cells were treated with 1 µg/ml tunicamycin or carrier (DMSO) for 24 h.

DNA constructs

To prepare N-terminally EGFP-tagged human UFL1 (*UFL1*; Ref ID: NM_015323.4), the coding sequence was amplified by PCR from pF1KA0776 plasmid (Kasuza DNA Research Institute, Japan), containing the full-length cDNA of human UFL1. The following forward and reverse primers containing sites recognized by *Kpn*I/*Bam*HI restriction endonucleases (underlined) were used: forward 5`-AC<u>GGTACC</u>ATGGCGGACGCCT -3` and reverse 5`- GGT<u>GGATCC</u>TTACTCTTCCGTCACAGATGA -3`. The PCR product was ligated to pEGFP-C1 vector (Clontech Laboratories, Mountain View, CA, USA), resulting in plasmid pEGFP-hUFL1. To prepare C-terminally TagRFP-tagged human UFL1, the coding sequence without stop codon was amplified by PCR from pF1KA0776 plasmid. The following primers containing sites recognized by *Nhe*I/*Sal*I were used: forward 5`-ATT<u>GCTAGC</u>AGAACCATGGCGGACGCCT -3` and reverse 5`-CGC<u>GTCGAC</u>CTCTTCCGTCACAGATGATT -3`. The PCR product was ligated to pCI-TagRFP vector (Vinopal et al., 2012), resulting in plasmid phUFL1-TagRFP. To prepare N-terminally GST-tagged full-length UFL1 (aa 1-794), the coding sequence was amplified from pF1KA0776 plasmid by PCR. The following primers containing sites recognized by *Bam*HI/*Sal*I were used: forward 5`-ATA<u>GGATCC</u>ATGGCGGACGCCTGG -3`and reverse 5`-CGA<u>GTCGAC</u>TTACTCTTCCGTCACAGATGATT -3`. The PCR product was ligated into pGEX-6P-1 (Amersham Biosciences, Uppsala, Sweden) using *Bam*HI/*Sal*I restriction sites, resulting in plasmid pGST-hUFL1_1-794. To generate Ab to human UFL1, the GST-tagged C-terminal fragment (aa 438-793) of UFL1 was prepared. The coding sequence was amplified from plasmid pF1KA0776 by PCR using the following primers containing sites recognized by *Bam*HI/*Sal*I: forward 5`- ATA<u>GGATCC</u>GGCAATGCCAGAGAG -3`; reverse 5`- TAT<u>GTCGAC</u>TCACTCTTCCGTCACAG-3. The PCR product was ligated into pGEX-6P-1 using *Bam*HI/*Sal*I restriction sites, resulting in plasmid pGST-hUFL1_438-793.

To prepare C-terminally EGFP-tagged human CDK5RAP3 (*CDK5RAP3*; Ref ID: NM_176096.3), the coding sequence without stop codon was amplified by PCR from the Myc-DDK-tagged CDK5RAP3 (tv3) plasmid (Origene Technologies, Rockville, MD, USA; Catalog No. RC209901). The following primers containing sites recognized by *Nhe*I/*Sal*I were used: forward 5`- T<u>GCTAGC</u>GGAGGAAAGATGGAGGAC -3` and reverse 5`- T<u>GTCGAC</u>CAGAGAGGTTCCCATCAG -3`. The PCR product was ligated into pCR2.1 vector (Invitrogen) using *Nhe*I/*Sal*I sites, resulting in plasmid pCR-hCDK5RAP3. The complete sequence of CDK5RAP3 without the stop codon was excised from pCR-hCDK5RAP3 by *Nhe*I/*Sal*I and ligated into pEGFP-N3 (Clontech), resulting in plasmid phCDK5RAP3-EGFP. To prepare C-terminally TagRFP-tagged human CDK5RAP3, the coding sequence without stop codon was excised from pCR-hCDK5RAP3 by *Nhe*I/*Sal*I and inserted into pCI-TagRFP (Vinopal et al., 2012), resulting in plasmid phCDK5RAP3-TagRFP. Plasmid pGST-hCDK5RAP3 encoding N-terminally GST-tagged full-length human CDK5RAP3 was described previously (Hořejší et al., 2012).

To prepare mNeonGreen-tagged lentiviral vector with puromycin resistance, the coding sequence of mNeonGreen was digested out from the mNeonGreen-EB3-7 plasmid (Allele Biotechnology, San Diego, CA, USA) by *Bam*HI/*Not*I. It was thereafter inserted into pCDH-CMV-MCS-EF1-puro vector (System Biosciences, Palo Alto, CA, USA), resulting in vector mNeonGreen-puro. To prepare C-terminally

mNeonGreen-tagged human γ-tubulin 1, the coding sequence was excised from pH3-16 plasmid (Zheng et al., 1991) by *Nhe*I/*Eco*RI and ligated into mNeonGreen-puro, resulting in vector phTUBG1-mNeonGreen-puro. Plasmid pGST-hTUBG1 encoding N-terminally GST-tagged full-length human γ-tubulin-1 was described previously (Macurek et al., 2008).

To prepare control C-terminally TagRFP-tagged mouse SHP-1, the coding sequence was excised from pmSHP-1-EGFP plasmid (Klebanovych, 2019) by *Eco*RI/*Sal*I and ligated into pCI-Tag-RFP (Vinopal et al., 2012), resulting in plasmid pmSHP-1-TagRFP.

CRISPR/Cas9 gene editing (Sander and Joung, 2014) was used to disrupt the expression of human UFL1 (Ensembl: ENSG00000014123) or all human CDK5RAP3 variants (Ensembl: ENSG00000108465). Plasmids SpCas9 and pU6-sgRNAnew-III (donated by Dr. R. Malík, Institute of Molecular Genetics, CAS, Prague, Czech Republic) were used for optimal production of Cas9 and single-guide RNA (sgRNA), respectively. The CRISPR tool (https://zlab.bio/guide-design-resources) was used to design the DNA oligonucleotides (for production of sgRNA) that were cloned into *Bsm*BI sites of pU6-sgRNAnew-III. To enrich for cells with disrupted expression of UFL1 or CDK5RAP3, we used the pRR-puro plasmid with a multiple cloning site that encodes a non-functional puromycin resistance cassette (Flemr and Buhler, 2015). Annealed sense and anti-sense oligonucleotides containing the sequences from the region of interest and overhangs with *Aat*II/*Sac*I restriction sites were ligated into pRR-puro digested with *Aat*II/*Sac*I, resulting in reporter plasmids pRR-hUFL1-puro or pRR-hCDK5RAP3-puro. Co-transfection of the reporter plasmid with the plasmids encoding sgRNAs and Cas9 led to CRISPR-induced double-strand break (DSB) in the reporter plasmid. When the DSB was repaired by homologous recombination, the puromycin resistance was restored.

Generation of UFL-1 and CDK5RAP3 deficient cell lines
In order to delete part of the 5' region of the UFL1 gene, U2OS cells were transfected with CRISPR/Cas9 vectors (sgRNA#1, sgRNA#2, SpCas9) together with reporter plasmid pRR-hUFL1-puro by transfection using Lipofectamine 3000 according to the manufacturer's instructions. The final transfection mixture in a 24-well plate contained 200 ng of sgRNA#1, 200 ng of sgRNA#2, 200 ng of reporter plasmid, and 400 ng of SpCas9 in 1 ml of Dulbecco's modified Eagle's medium (DMEM) containing 10% FCS, penicillin (100 units/ml), and streptomycin (0.1 mg/ml). The medium was changed after 48 h, and puromycin was added to the final concentration of 2 μg/ml. The stable selection was achieved by culturing cells for 1 wk in the presence of puromycin. The single-cell dilution protocol (Green and Sambrook, 2012) was used to obtain cell clones that were thereafter analyzed by PCR and immunoblotting. Single-cell clones were expanded, genomic DNA was extracted with the QIAamp DNA Mini Kit (QIAGEN, Gilden, Germany), and deletion in the UFL1 gene was determined by PCR amplification with primers flanking the deleted region: forward 5'-AGGCGCCAATCTTAGACACAG -3'; reverse 5′- CAAAAGCTGCCCTTTTATCTGT -3'. Amplified fragments were visualized in 2% agarose gels stained by GelRed Nucleic Acid Gel Stain (Biotium, Fremont, CA USA). While amplification of short fragments (~ 570 bp) was detected in UFL1 deficient clones, no amplification was found in control U2OS due to the large size of the deleted region (~ 7 kb). The PCR fragments were subcloned into pCR2.1 vector (Invitrogen), and individual colonies were sequenced.

A similar approach was applied to the preparation of cells deficient in CDK5RAP3. In order to delete part of the 5' region of the GDK5RAP3 gene containing the canonical and alternative start codons, U2OS cells were transfected with CRISPR/Cas9 vectors (sgRNA#1, sgRNA#2, SpCas9) together with reporter plasmid pRR-hCDK5RAP3-puro. Deletion in the CDK5RAP3 gene was determined by PCR amplification with primers flanking the deleted region: forward 5'- CATGCATCCATCATCCCAG -3'; reverse 5′- TGACATGTGACGTGTGAAACTCT -3'. Amplified fragments were visualized in agarose gels. While amplification of short fragments (~ 700 bp) was detected in CDK5RAP3 deficient clones, no amplification was found in control U2OS due to the large size of the deleted region (~ 6 kb). The PCR fragments were subcloned into pCR2.1 vector (Invitrogen), and individual colonies were sequenced.

Generation of cell lines expressing tagged proteins

To prepare U2OS cells expressing EGFP-, TagRFP- or mNeonGreen-tagged proteins, cells were transfected with 2.5 µg DNA per 3-cm tissue culture dish using Lipofectamine 3000 according to the manufacturer's instructions. After 12 h, the transfection mixture was replaced with a complete fresh medium, and cells were incubated for 48 h. Cells were thereafter incubated for one wk in complete fresh medium containing G418 at concentration 1.2 mg/ml. In the case of phTUBG1-mNeonGreen-puro transfection, cells were incubated in the presence of puromycin at a concentration of 2 µg/ml. For phenotypic rescue experiments, cells expressing TagRFP-tagged proteins were flow-sorted using a BD Influx cell sorter (BD Bioscience, San Jose, CA, USA). TagRFP emission was triggered by 561 nm laser; fluorescence was detected with a 585/29 band-pass filter.

Real-time qRT-PCR

Total RNA from control or tunicamycin-treated cells was isolated with the RNeasy Mini Kit (QIAGEN, Gilden, Germany) and converted to cDNA using the High-Capacity cDNA Reverse Transcription Kit (Applied Biosystems, Waltham, MA, USA) according to the manufacturer's protocol. The quantitative PCRs were performed with primers specific for human calnexin (*CANX*; forward 5'- GAACATTCTTCCCTTTGACC-3' and reverse 5'- TCTTAGAGTTCTCATCTGGAC-3'; primers anneal to all transcript variants), DNA damage-inducible transcript 3 (*DDIT3*; forward 5'- AACATCACTGGTGTGGAGGC-3' and reverse 5'- TGCACAGTTCAGCGGGTA-3'; primers anneal to all transcript variants except NM_001195057.1), and prolyl 4-hydroxylase subunit beta (protein disulfide-isomerase; *P4HB*; forward 5'- CTTAAGGAGCTTATTGAGGAG-3' and reverse 5'- CATTGCAATTGGAGATGTTG-3'). Peptidylprolyl isomerase A (cyclophilin A; *PPIA*; forward 5'- GAGCACTGGGGAGAAAGGAT-3' and reverse 5'- CTTGCCATCCAGCCACTCAG-3'; primers anneal to all transcript variants) served as an internal control. All primers were tested in silico by the Basic Local Alignment Search Tool from the National Center for Biotechnology Information (BLAST NCBI; NIH, Bethesda, MD, USA) to amplify the specific targets. Quantitative PCRs were performed in a LightCycler 480System (Roche, Mannheim, Germany) as described (Dráberová et al., 2017). Each sample was run in triplicate. The identity of the PCR products was verified by sequencing.

Preparation of cell extracts

Whole-cell lysates for SDS-PAGE were prepared by washing the cells in cold HEPES buffer (50 mM HEPES pH 7.6, 75 mM NaCl, 1 mM $MgCl_2$, and 1 mM EGTA), solubilizing them in hot SDS-sample buffer, and boiling for 5 min. When preparing whole-cell extracts for immunoprecipitation and GST pull-down assays, cells grown on a 9-cm Petri dish (cell confluence 80%) were rinsed in HEPES buffer and extracted (0.7 ml/Petri dish) for 10 min at 4°C with HEPES buffer supplemented with protease and phosphatase (1 mM Na_3VO_4 and 1 mM NaF) inhibitors and 1% NP-40 (extraction buffer). The suspension was then spun down (12,000 x g, 15 min, 4°C), and the supernatant was collected. When preparing whole-cell extracts for gel filtration chromatography, cells grown on six 9-cm Petri dishes were scraped into cold HEPES buffer, and pelleted cells were extracted in 1 ml of extraction buffer.

To prepare the crude membranous fraction, cells from five 9-cm Petri dishes were released by trypsin, washed in HEPES, and mechanically disrupted in 3.5 ml of cold HEPES buffer supplemented with inhibitors using a Dounce homogenizer (disruption efficiency was verified under a microscope). The homogenate was centrifuged at 300 x g for 5 min (supernatant S1, pellet P1). Post-nuclear supernatant was centrifuged at 1,400 x g for 10 min (supernatant S2, pellet P2). Pelleted material (P2; crude membranous fraction) was solubilized for 5 min at 4°C with 1.4 ml of extraction buffer, and the suspension was spun down (12,000 x g, 15 min, 4°C). The supernatant was collected for immunoprecipitation experiments. For gel filtration chromatography, membranes prepared from twelve 9-cm Petri dishes were solubilized in 1 ml of extraction buffer.

Gel filtration chromatography

Gel filtration was performed using fast protein liquid chromatography (AKTA-FPLC system) on a Superose 6 10/300 GL column (GE Healthcare Life Sciences) as described previously (Hořejší et al., 2012). The column equilibration and chromatography were performed in HEPES buffer, and 0.5-ml aliquots were collected. Samples for SDS-PAGE were prepared by mixing with 5x concentrated SDS-sample buffer.

Immunoprecipitation, GST pull-down assay, gel electrophoresis, and immunoblotting

Immunoprecipitation was performed as previously described (Blume et al., 2008). Extracts were incubated with beads of protein A saturated with mouse mAbs to (i) γ-tubulin (TU-31; IgG2b), (ii) GCP2 (GCP2-01; IgG2b), (iii) NF-M (NF-09; IgG2a, negative control), or with rabbit Abs to (iv) UFL1$_{301-389}$, (v) UFL1$_{438-793}$, (vi) C53 (Sigma-Aldrich), (vii) (GFP), (viii) non-muscle myosin (negative control) or with (ix) immobilized protein A alone. Antibodies C53, GFP, UFL1$_{301-389}$, and UFL1$_{438-793}$, were used at Ig concentrations 0.5-2.5 µg/ml. Ab to myosin was used at a dilution of 1:100. The mAbs TU-31, GCP2-01, and NF-09, in the form of hybridoma supernatants, were diluted 1:2.

To identify proteins interacting with membrane-bound γ-tubulin, 1% NP-40 extract from the microsomal fraction (P$_{100}$) of differentiated P19 cells (Macurek et al., 2008) was incubated with anti-peptide mAb TU-31 immobilized on protein A carrier. After extensive washing, the bound proteins were eluted with immunizing

peptide EYHAATRPDYISWGTQ (human γ-tubulin, aa sequence 434-449) (Nováková et al., 1996) as described (Hořejší et al., 2012). Peptide EEFATEGTDRKDVFFY (human γ-tubulin, aa sequence 38-53) served as a negative control.

Preparation and purification of GST-tagged fusion proteins were described previously (Frangioni and Neel, 1993), as were pull-down assays with whole-cell extracts (Kukharskyy et al., 2004).

Gel electrophoresis and immunoblotting were performed using standard protocols (Caracciolo et al., 2010). For immunoblotting, mouse mAbs to γ-tubulin (GTU-88), GCP4, GCP6, DDIT3 and GM130 were diluted 1:10,000, 1:1,000, 1:500, 1:500 and 1:250, respectively. Mouse mAbs to α-tubulin (TU-01) and GCP2 (GCP2-02), in the form of spent culture supernatant, were diluted 1:10 and 1:5, respectively. Rabbit Abs to actin, GFP (Sigma-Aldrich), UFL1 (Sigma-Aldrich), C53 (Sigma-Aldrich), tRFP, cyclin B1, calcineurin, and p-Histone H3 were diluted 1:10,000, 1:5,000, 1:3,000, 1:3,000, 1:2,000, 1:1,000, 1:1,000, and 1:700, respectively. Rabbit Abs to PDI, histone H1.4, pericentrin (EMD-Millipore) and DDRGK1 were diluted 1:50,000, 1:1,000, 1:1,000 and 1:500, respectively. Rabbit Abs to calnexin, GAPDH, GST, and SHP-1 were diluted 1:100,000. Secondary anti-mouse and anti-rabbit Abs conjugated with HRP were diluted 1:10,000. TrueBlot anti-rabbit IgG HRP was diluted 1:100,000. The HRP signal was detected with SuperSignal WestPico or Supersignal West Femto Chemiluminescent reagents from Pierce (Rockford, IL, USA) and the LAS 3000 imaging system (Fujifilm, Düsseldorf, Germany). The AIDA image analyzer v5 software (Raytest, Straubenhardt, Germany) was used to quantify signals from the immunoblots.

Mass spectrometry

Concentrated samples after peptide elution were dissolved in 2x Laemmli sample buffer and separated in 8% SDS-PAGE. Gels were stained with Coomassie Brilliant Blue G-250. The bands of interest were excised from the gel, destained, and digested by trypsin. The extracted peptides were analyzed by a MALDI-TOF mass spectrometer (Ultraflex III; Bruker Daltonics, Bremen, Germany) in a mass range of 700-4000 Da and calibrated internally using the monoisotopic $[M+H]^+$ ions of trypsin auto-proteolytic fragments (842.51 and 2211.10 Da). Data were processed using FlexAnalysis 3.3 software (Bruker Daltonics, Bremen Germany) and searched by the in-house Mascot search engine against the SwissProt database subset of all *Mus musculus* proteins.

Evaluation of cell growth

Cell proliferation was assessed by manual cell counting of control U2OS, UFL1_KO or C53_KO cells. A total of 2×10^5 cells diluted in culture medium were plated on a 6-cm-diameter Petri dish. Cells were counted at various time intervals from 1 to 4 days. Samples were counted in doublets in a total of three independent experiments.

Microtubule regrowth experiments

Microtubule regrowth from centrosomes was followed in a nocodazole washout experiment. Cells growing on coverslips were treated with nocodazole at a final concentration of 10 μM for 90 min at 37 °C to

depolymerize microtubules. Cells were then washed with phosphate-buffered saline (PBS) precooled to 4 °C (3 times 5 min each) to remove the drug, transferred to complete medium tempered to 28 °C, and microtubule regrowth was allowed for 1-3 min at 28 °C. Cells were after that fixed in formaldehyde and extracted in Triton X-100 (F/Tx) and postfixed in cold methanol (F/Tx/M).

Immunofluorescence microscopy

Cells were fixed and immunostained as described (Dráberová and Dráber, 1993). Samples were fixed in F/Tx, and for double-label experiments with anti-γ-tubulin Ab, they were postfixed in methanol (F/Tx/M). To visualize TagRFP-tagged proteins, cells were permeabilized with 10 μM digitonin in CHO buffer (25 mM HEPES, 2 mM EGTA, 115 mM CH_3COOK, 2.5 mM $MgCl_2$, 150 mM sucrose, pH 7.4) for 30 sec, then fixed with 3% formaldehyde in microtubule-stabilizing buffer (MSB) (Dráberová and Dráber, 1993) for 20 min at room temperature and postfixed in methanol at -20°C for 5 min (D/F/M). Alternatively, TagRFP-tagged proteins were visualized in samples extracted in 0.5% Triton X-100 for 1 min at room temperature, then fixed with 3% formaldehyde in MSB for 20 min at room temperature, and postfixed in methanol (Tx/F/M). Mouse mAbs to β-tubulin (TUB2.1), C53 (Abcam), and DDIT3 were diluted 1:500, 1:200, and 1:50, respectively. Rabbit Abs to calnexin, PDI, pericentrin, and $UFL1_{438-793}$ were diluted 1:1,000, 1:1,000, 1:250, and 1:50, respectively. Mouse mAb to γ-tubulin (TU-30), in the form of spent culture supernatant, and rabbit Ab to α-tubulin were diluted 1:10 and 1:100, respectively. Secondary AlexaFluor488-, DyLight549- and DyLight649-conjugated anti-mouse Abs were diluted 1:200, 1:1,000 and 1:1,000, respectively. The AlexaFluor488- and Cy3-conjugated anti-rabbit Abs were diluted 1:200 and 1:1,000, respectively. Samples were mounted in MOWIOL 4-88 (Calbiochem, San Diego, CA, USA) and examined with an Olympus AX-70 Provis microscope (Olympus, Hamburg Germany) equipped with a 60×/1.0 NA water objective or with a Delta Vision Core system (AppliedPrecision, Issaquah, WA, USA) equipped with a 60×/1.42 NA oil objective.

To quantify the microtubule regrowth, different areas per sample were taken in both fluorescence channels. The sum of γ-tubulin or α-tubulin immunofluorescence intensities was obtained from nine consecutive frames (0.2 μm steps), with the middle frame chosen with respect to the highest γ-tubulin intensity. Quantification of the microtubule regrowth assay was analyzed automatically in 2-μm regions of interest (ROIs) centered at the centrosomes, marked by γ-tubulin staining, using an in-house written macro for Fiji processing program (Klebanovych et al., 2019; Schindelin et al., 2012).

Microtubule nucleation visualized by time-lapse imaging

For time-lapse imaging, U2OS cells expressing EB3-mNeonGreen were grown on a 35 mm μ-Dish with ibidi polymer coverslip bottom (Ibidi GmbH, Gräfelfing, Germany). Prior to imaging, the medium was replaced for FluoroBrite™ DMEM (ThermoFisher Scientific, Waltham, MA, USA), supplemented with 25 mM HEPES and 1% FCS, 30 min before imaging. Time-lapse sequences were collected in seven optical slices (0.1 μm steps) for 1 min at 1 s interval with the Andor Dragonfly 503 spinning disc confocal system (Oxford Instruments, Abingdon, UK) equipped with a stage top microscopy incubator (Okolab, Ottaviano,

Italy), 488 nm solid-state 150 mW laser, HCX PL APO 63x oil objective, NA 1.4, and Zyla sCMOS 16 bit camera. For each experiment, at least 10 cells were imaged (acquisition parameters: 40 µm pinhole size, 15% laser power, 50 ms exposure time, 525/50 nm emission filter). The time-lapse sequences were deconvoluted with Huygens Professional software v. 19.04 (Scientific Volume Imaging, Hilversum, the Netherlands), and maximum intensity projection of z stack was made for each time point in Fiji. Newly nucleated microtubules were detected by manual counting of EB3 comets emanating from the centrosomes.

Statistical analysis

A minimum of three independent experiments was analyzed for each quantification. The counts of individual data points were indicated in the figure legends. All data were presented as mean ± SD. Significance was tested using a two-tailed, unpaired Student's *t* test or one-way ANOVA followed by a Sidak's post hoc test using Prism 8 software (GraphPad Software, San Diego, USA). The used test are indicated in the figure legends. For all analyses, *p* values were represented as follows: *, $p < 0.05$; **, $p < 0.01$; ***, $p < 0.001$; ****, $p < 0.0001$

On line supplemental material

Table S1 shows mass spectrometry identification of UFL1. Fig S1 shows results from the additional experiments supplementing Fig. 1, and controls for immunoprecipitation experiments. Fig. S2 documents preparation and properties of *UFL1 and CDK5RAP3* knockout cell lines. Fig. S3 shows that deletion of UFL1 and C53 stimulates accumulation of γ-tubulin but not pericentrin at the centrosome, and promotes microtubule nucleation. Fig. S4 presents the distribution of PDI in knockout cell lines, expression of calnexin in phenotypic rescue experiment and upregulation of ER stress-associated proteins after tunicamycin treatment.

Acknowledgments

The authors declare no competing financial interests.

Abbreviations

C53; CDK5RAP3

DDIT3; DNA damage-inducible transcript 3 protein

DDRGK1; DDRGK domain-containing protein 1

GCP; γ-tubulin complex protein

MTOC; microtubule-organizing center

PDI; protein disulfide-isomerase

γTuRC; γ-Tubulin ring complex

UFL1; E3 UFM1-protein ligase 1

UFM; ubiquitin-fold modifier 1

UPR; unfolded protein response

References

Akhmanova, A., and M.O. Steinmetz. 2008. Tracking the ends: a dynamic protein network controls the fate of microtubule tips. *Nat. Rev. Mol. Cell Biol*. 9:309-322.

Bar-Peled, M., and N.V. Raikhel. 1996. A method for isolation and purification of specific antibodies to a protein fused to the GST. *Anal. Biochem*. 241:140-142.

Blume, Y., A. Yemets, V. Sulimenko, T. Sulimenko, J. Chan, C. Lloyd, and P. Dráber. 2008. Tyrosine phosphorylation of plant tubulin. *Planta*. 229:143-150.

Borek, W.E., L.M. Groocock, I. Samejima, J. Zou, F. de Lima Alves, J. Rappsilber, and K.E. Sawin. 2015. Mto2 multisite phosphorylation inactivates non-spindle microtubule nucleation complexes during mitosis. *Nat. Commun*. 6:7929.

Caracciolo, V., L. D'Agostino, E. Dráberová, V. Sládková, C. Crozier-Fitzgerald, D.P. Agamanolis, J.P. de Chadarevian, A. Legido, A. Giordano, P. Dráber, and C.D. Katsetos. 2010. Differential expression and cellular distribution of γ-tubulin and βIII-tubulin in medulloblastomas and human medulloblastoma cell lines. *J. Cell Physiol*. 223:519-529.

Černohorská, M., V. Sulimenko, Z. Hájková, T. Sulimenko, V. Sládková, S. Vinopal, E. Dráberová, and P. Dráber. 2016. GIT1/βPIX signaling proteins and PAK1 kinase regulate microtubule nucleation. *BBA Mol. Cell. Res.* 1863:1282-1297.

Chabin-Brion, K., J. Marceiller, F. Perez, C. Settegrana, A. Drechou, G. Durand, and C. Pous. 2001. The Golgi complex is a microtubule-organizing organelle. *Mol. Biol. Cell*. 12:2047-2060.

Chakrabarti, A., A.W. Chen, and J.D. Varner. 2011. A review of the mammalian unfolded protein response. *Biotechnol. Bioeng*. 108:2777-2793.

Ching, Y.P., Z. Qi, and J.H. Wang. 2000. Cloning of three novel neuronal Cdk5 activator binding proteins. *Gene*. 242:285-294.

Colello, D., C.G. Reverte, R. Ward, C.W. Jones, V. Magidson, A. Khodjakov, and S.E. LaFlamme. 2010. Androgen and Src signaling regulate centrosome activity. *J. Cell Sci.* 123:2094-2102.

Consolati, T., J. Locke, J. Roostalu, Z.A. Chen, J. Gannon, J. Asthana, W.M. Lim, F. Martino, M.A. Cvetkovic, J. Rappsilber, A. Costa, and T. Surrey. 2020. Microtubule nucleation properties of single human γTuRCs explained by their Cryo-EM structure. *Dev. Cell*. 53:603-617 e608.

Ding, W.X., H.M. Ni, W. Gao, Y.F. Hou, M.A. Melan, X. Chen, D.B. Stolz, Z.M. Shao, and X.M. Yin. 2007. Differential effects of endoplasmic reticulum stress-induced autophagy on cell survival. *J Biol. Chem*. 282:4702-4710.

Dráber, P., E. Dráberová, and V. Viklický. 1991. Immunostaining of human spermatozoa with tubulin domain-specific monoclonal antibodies. *Histochemistry*. 195:519-524.

Dráberová, E., L. D'Agostino, V. Caracciolo, V. Sládková, T. Sulimenko, V. Sulimenko, M. Sobol, N.F. Maounis, E. Tzelepis, E. Mahera, L. Kren, A. Legido, A. Giordano, S. Mörk, P. Hozák, P. Dráber, and C.D. Katsetos. 2015. Overexpression and nucleolar localization of γ-tubulin small complex proteins GCP2 and GCP3 in glioblastoma. *J. Neuropathol. Exp. Neurol.* 74:723-742.

Dráberová, E., and P. Dráber. 1993. A microtubule-interacting protein involved in coalignment of vimentin intermediate filaments with microtubules. *J. Cell Sci.* 106:1263-1273.

Dráberová, E., V. Sulimenko, V. Kukharskyy, and P. Dráber. 1999. Monoclonal antibody NF-09 specific for neurofilament protein NF-M. *Folia Biol. (Praha)*. 45:163-165.

Dráberová, E., V. Sulimenko, S. Vinopal, T. Sulimenko, V. Sládková, L. D'Agostino, M. Sobol, P. Hozák, L. Křen, C.D. Katsetos, and P. Dráber. 2017. Differential expression of human γ-tubulin isotypes during neuronal development and oxidative stress points to a γ-tubulin-2 prosurvival function. *FASEB J.* 31:1828-1846.

Flemr, M., and M. Buhler. 2015. Single-step generation of conditional knockout mouse embryonic stem cells. *Cell Rep.* 12:709-716.

Frangioni, J.V., and B.G. Neel. 1993. Solubilization and purification of enzymatically active glutathione-S-transferase (Pgex) fusion proteins. *Anal. Biochem*. 210:179-187.

Gerakis, Y., M. Quintero, H. Li, and C. Hetz. 2019. The UFMylation System in proteostasis and beyond. *Trends Cell Biol*. 29:974-986.

Green, M.R., and J. Sambrook. 2012. Molecular Cloning; A Laboratory Manual., 4th ed.; Cold Spring Harbor Laboratory Press, Cold Spring Harbor, NY, USA. 1378-1380 pp.

Guo, Y., D. Li, S. Zhang, Y. Yang, J.J. Liu, X. Wang, C. Liu, D.E. Milkie, R.P. Moore, U.S. Tulu, D.P. Kiehart, J. Hu, J. Lippincott-Schwartz, E. Betzig, and D. Li. 2018. Visualizing intracellular organelle and cytoskeletal interactions at nanoscale resolution on millisecond timescales. *Cell*. 175:1430-1442 e1417.

Hehnly, H., and S. Doxsey. 2014. Rab11 endosomes contribute to mitotic spindle organization and orientation. *Dev. Cell*. 28:497-507.

Hořejší, B., S. Vinopal, V. Sládková, E. Dráberová, V. Sulimenko, T. Sulimenko, V. Vosecká, A. Philimonenko, P. Hozák, C.D. Katsetos, and P. Dráber. 2012. Nuclear γ-tubulin associates with nucleoli and interacts with tumor suppressor protein C53. *J. Cell Physiol.* 227:367-382.

Jiang, H., S. Luo, and H. Li. 2005. Cdk5 activator-binding protein C53 regulates apoptosis induced by genotoxic stress via modulating the G2/M DNA damage checkpoint. *J. Biol. Chem*. 280:20651-20659.

Jiang, H., J. Wu, C. He, W. Yang, and H. Li. 2009. A tumor suppressor C53 protein antagonizes checkpoint kinases to promote cyclin-dependent kinase 1 activation. *Cell Res*. 19:458-468.

Keck, J.M., M.H. Jones, C.C. Wong, J. Binkley, D. Chen, S.L. Jaspersen, E.P. Holinger, T. Xu, M. Niepel, M.P. Rout, J. Vogel, A. Sidow, J.R. Yates, III, and M. Winey. 2011. A cell cycle phosphoproteome of the yeast centrosome. *Science*. 332:1557-1561.

Klebanovych, A., V. Sládková, T. Sulimenko, V. Vosecká, Z. Rubíková, M. Čapek, E. Dráberová, P. Dráber, and V. Sulimenko. 2019. Regulation of microtubule nucleation in mouse bone marrow-derived mast cells by protein tyrosine kinase SHP-1. *Cells*. 8:e345.

Kollman, J.M., A. Merdes, L. Mourey, and D.A. Agard. 2011. Microtubule nucleation by γ-tubulin complexes. *Nat. Rev. Mol. Cell Biol.* 12:709-721.

Komatsu, M., T. Chiba, K. Tatsumi, S. Iemura, I. Tanida, N. Okazaki, T. Ueno, E. Kominami, T. Natsume, and K. Tanaka. 2004. A novel protein-conjugating system for Ufm1, a ubiquitin-fold modifier. *EMBO J.* 23:1977-1986.

Kukharskyy, V., V. Sulimenko, L. Macurek, T. Sulimenko, E. Dráberová, and P. Dráber. 2004. Complexes of γ-tubulin with non-receptor protein tyrosine kinases Src and Fyn in differentiating P19 embryonal carcinoma cells. *Exp. Cell Res.* 298:218-228.

Kwon, J., H.J. Cho, S.H. Han, J.G. No, J.Y. Kwon, and H. Kim. 2010. A novel LZAP-Binding Protein, NLBP, inhibits cell invasion. *J. Biol. Chem*. 285:12232-12240.

Lemaire, K., R.F. Moura, M. Granvik, M. Igoillo-Esteve, H.E. Hohmeier, N. Hendrickx, C.B. Newgard, E. Waelkens, M. Cnop, and F. Schuit. 2011. Ubiquitin fold modifier 1 (UFM1) and its target UFBP1 protect pancreatic beta cells from ER stress-induced apoptosis. *PLoS One*. 6:e18517.

Li, J., G. Yue, W. Ma, A. Zhang, J. Zou, Y. Cai, X. Tang, J. Wang, J. Liu, H. Li, and H. Su. 2018. Ufm1-specific ligase Ufl1 regulates endoplasmic reticulum homeostasis and protects against heart failure. *Circ. Heart Fail*. 11:e004917.

Liang, J.R., E. Lingeman, T. Luong, S. Ahmed, M. Muhar, T. Nguyen, J.A. Olzmann, and J.E. Corn. 2020. A Genome-wide ER-phagy screen highlights key roles of mitochondrial metabolism and ER-resident UFMylation. *Cell*. 180:1160-1177.

Linhartová, I., P. Dráber, E. Dráberová, and V. Viklický. 1992. Immunological discrimination of β-tubulin isoforms in developing mouse brain. Posttranslational modification of non-class III β-tubulins. *Biochem. J.* 288:919-924.

Liu, D., W.D. Wang, D.B. Melville, Y.I. Cha, Z. Yin, N. Issaeva, E.W. Knapik, and W.G. Yarbrough. 2011. Tumor suppressor Lzap regulates cell cycle progression, doming, and zebrafish epiboly. *Dev. Dyn*. 240:1613-1625.

Liu, P., E. Zupa, A. Neuner, A. Bohler, J. Loerke, D. Flemming, T. Ruppert, T. Rudack, C. Peter, C. Spahn, O.J. Gruss, S. Pfeffer, and E. Schiebel. 2020. Insights into the assembly and activation of the microtubule nucleator γ-TuRC. *Nature*. 578:467-471.

Lombardi, A.A., and J.W. Elrod. 2017. Mediating ER-mitochondrial cross-talk. *Science*. 358:591-592.

Macurek, L., E. Dráberová, V. Richterová, V. Sulimenko, T. Sulimenko, L. Dráberová, V. Marková, and P. Dráber. 2008. Regulation of microtubule nucleation from membranes by complexes of membrane-bound γ-tubulin with Fyn kinase and phosphoinositide 3-kinase. *Biochem. J.* 416:421-430.

Nováková, M., E. Dráberová, W. Schürmann, G. Czihak, V. Viklický, and P. Dráber. 1996. γ-Tubulin redistribution in taxol-treated mitotic cells probed by monoclonal antibodies. *Cell Motil. Cytoskel.* 33:38-51.

Oakley, B.R., V. Paolillo, and Y. Zheng. 2015. γ-Tubulin complexes in microtubule nucleation and beyond. *Mol. Biol. Cell*. 26:2957-2962.

Oakley, C.E., and B.R. Oakley. 1989. Identification of γ-tubulin, a new member of the tubulin superfamily encoded by mipA gene of *Aspergillus nidulans*. *Nature*. 338:662-664.

Sander, J.D., and J.K. Joung. 2014. CRISPR-Cas systems for editing, regulating and targeting genomes. *Nature Biotechnol.* 32:347-355.

Schindelin, J., I. Arganda-Carreras, E. Frise, V. Kaynig, M. Longair, T. Pietzsch, S. Preibisch, C. Rueden, S. Saalfeld, B. Schmid, J.Y. Tinevez, D.J. White, V. Hartenstein, K. Eliceiri, P. Tomancak, and A. Cardona. 2012. Fiji: an open-source platform for biological-image analysis. *Nature Methods*. 9:676-682.

Schuck, S., W.A. Prinz, K.S. Thorn, C. Voss, and P. Walter. 2009. Membrane expansion alleviates endoplasmic reticulum stress independently of the unfolded protein response. *J Cell Biol*. 187:525-536.

Shiwaku, H., N. Yoshimura, T. Tamura, M. Sone, S. Ogishima, K. Watase, K. Tagawa, and H. Okazawa. 2010. Suppression of the novel ER protein Maxer by mutant ataxin-1 in Bergman glia contributes to non-cell-autonomous toxicity. *EMBO J*. 29:2446-2460.

Smith, M., and S. Wilkinson. 2017. ER homeostasis and autophagy. *Essays Biochem*. 61:625-635.

Sriburi, R., S. Jackowski, K. Mori, and J.W. Brewer. 2004. XBP1: a link between the unfolded protein response, lipid biosynthesis, and biogenesis of the endoplasmic reticulum. *J Cell Biol*. 167:35-41.

Stephani, M., L. Picchianti, A. Gajic, R. Beveridge, E. Skarwan, V. Sanchez de Medina Hernandez, A. Mohseni, M. Clavel, Y. Zeng, C. Naumann, M. Matuszkiewicz, E. Turco, C. Loefke, B. Li, G. Durnberger, M. Schutzbier, H.T. Chen, A. Abdrakhmanov, A. Savova, K.S. Chia, A. Djamei, I. Schaffner, S. Abel, L. Jiang, K. Mechtler, F. Ikeda, S. Martens, T. Clausen, and Y. Dagdas. 2020. A cross-kingdom conserved ER-phagy receptor maintains endoplasmic reticulum homeostasis during stress. *Elife*. 9:e58396.

Sulimenko, V., Z. Hájková, M. Černohorská, T. Sulimenko, V. Sládková, L. Dráberová, S. Vinopal, E. Dráberová, and P. Dráber. 2015. Microtubule nucleation in mouse bone marrow-derived mast cells is regulated by the concerted action of GIT1/βPIX proteins and calcium. *J. Immunol.* 194:4099-4111.

Sulimenko, V., Z. Hájková, A. Klebanovych, and P. Dráber. 2017. Regulation of microtubule nucleation mediated by γ-tubulin complexes. *Protoplasma*. 254:1187-1199.

Tatsumi, K., Y.S. Sou, N. Tada, E. Nakamura, S. Iemura, T. Natsume, S.H. Kang, C.H. Chung, M. Kasahara, E. Kominami, M. Yamamoto, K. Tanaka, and M. Komatsu. 2010. A novel type of E3 ligase for the Ufm1 conjugation system. *J. Biol. Chem*. 285:5417-5427.

Teixidó-Travesa, N., J. Roig, and J. Lüders. 2012. The where, when and how of microtubule nucleation - one ring to rule them all. *J. Cell Sci.* 125:4445-4456.

Terasaki, M., L.B. Chen, and K. Fujiwara. 1986. Microtubules and the endoplasmic reticulum are highly interdependent structures. *J. Cell Biol*. 103:1557-1568.

Tovey, C.A., and P.T. Conduit. 2018. Microtubule nucleation by γ-tubulin complexes and beyond. *Essays Biochem*. 62:765-780.

Viklický, V., P. Dráber, J. Hašek, and J. Bártek. 1982. Production and characterization of a monoclonal antitubulin antibody. *Cell Biol. Int. Rep.* 6:725-731.

Vinopal, S., M. Černohorská, V. Sulimenko, T. Sulimenko, V. Vosecká, M. Flemr, E. Dráberová, and P. Dráber. 2012. γ-Tubulin 2 nucleates microtubules and is downregulated in mouse early embryogenesis. *PLoS ONE*. 7:e29919.

Vogel, J., B. Drapkin, J. Oomen, D. Beach, K. Bloom, and M. Snyder. 2001. Phosphorylation of γ-tubulin regulates microtubule organization in budding yeast. *Dev. Cell*. 1:621-631.

Voss, M., K. Campbell, N. Saranzewa, D.G. Campbell, C.J. Hastie, M.W. Peggie, C. Martin-Granados, A.R. Prescott, and P.T. Cohen. 2013. Protein phosphatase 4 is phosphorylated and inactivated by Cdk in response to spindle toxins and interacts with γ-tubulin. *Cell Cycle*. 12:2876-2887.

Wamsley, J.J., N. Issaeva, H. An, X. Lu, L.A. Donehower, and W.G. Yarbrough. 2017. LZAP is a novel Wip1 binding partner and positive regulator of its phosphatase activity in vitro. *Cell Cycle*. 16:213-223.

Wang, J., H. An, M.W. Mayo, A.S. Baldwin, and W.G. Yarbrough. 2007. LZAP, a putative tumor suppressor, selectively inhibits NF-κB. *Cancer Cell*. 12:239-251.

Waterman-Storer, C.M., and E.D. Salmon. 1998. Endoplasmic reticulum membrane tubules are distributed by microtubules in living cells using three distinct mechanisms. *Curr. Biol*. 8:798-806.

Wieczorek, M., L. Urnavicius, S.C. Ti, K.R. Molloy, B.T. Chait, and T.M. Kapoor. 2020. Asymmetric molecular architecture of the human γ-tubulin ring complex. *Cell*. 180:165-175 e116.

Wu, J., C. de Heus, Q. Liu, B.P. Bouchet, I. Noordstra, K. Jiang, S. Hua, M. Martin, C. Yang, I. Grigoriev, E.A. Katrukha, A.F.M. Altelaar, C.C. Hoogenraad, R.Z. Qi, J. Klumperman, and A. Akhmanova. 2016. Molecular pathway of microtubule organization at the Golgi apparatus. *Dev. Cell*. 39:44-60.

Wu, J., H. Jiang, S. Luo, M. Zhang, Y. Zhang, F. Sun, S. Huang, and H. Li. 2013. Caspase-mediated cleavage of C53/LZAP protein causes abnormal microtubule bundling and rupture of the nuclear envelope. *Cell Res*. 23:691-704.

Wu, J., G. Lei, M. Mei, Y. Tang, and H. Li. 2010. A novel C53/LZAP-interacting protein regulates stability of C53/LZAP and DDRGK domain-containing Protein 1 (DDRGK1) and modulates NF-κB signaling. *J. Biol. Chem*. 285:15126-15136.

Yang, R., H. Wang, B. Kang, B. Chen, Y. Shi, S. Yang, L. Sun, Y. Liu, W. Xiao, T. Zhang, J. Yang, Y. Zhang, M. Zhu, P. Xu, Y. Chang, Y. Jia, and Y. Huang. 2019. CDK5RAP3, a UFL1 substrate adaptor, is crucial for liver development. *Development*. 146.

Yoo, H.M., S.H. Kang, J.Y. Kim, J.E. Lee, M.W. Seong, S.W. Lee, S.H. Ka, Y.S. Sou, M. Komatsu, K. Tanaka, S.T. Lee, D.Y. Noh, S.H. Baek, Y.J. Jeon, and C.H. Chung. 2014. Modification of ASC1 by UFM1 is crucial for ERα transactivation and breast cancer development. *Mol. Cell*. 56:261-274.

Yu, L., G. Li, J. Deng, X. Jiang, J. Xue, Y. Zhu, W. Huang, B. Tang, and R. Duan. 2020. The UFM1 cascade times mitosis entry associated with microcephaly. *FASEB J*. 34:1319-1330.

Zhang, M., X. Zhu, Y. Zhang, Y. Cai, J. Chen, S. Sivaprakasam, A. Gurav, W. Pi, L. Makala, J. Wu, B. Pace, D. Tuan-Lo, V. Ganapathy, N. Singh, and H. Li. 2015. RCAD/Ufl1, a Ufm1 E3 ligase, is essential for hematopoietic stem cell function and murine hematopoiesis. *Cell Death. Differ*. 22:1922-1934.

Zhang, X., Q. Chen, J. Feng, J. Hou, F. Yang, J. Liu, Q. Jiang, and C. Zhang. 2009. Sequential phosphorylation of Nedd1 by Cdk1 and Plk1 is required for targeting of the γTuRC to the centrosome. *J. Cell Sci*. 122:2240-2251.

Zhang, Y., M. Zhang, J. Wu, G. Lei, and H. Li. 2012. Transcriptional regulation of the Ufm1 conjugation system in response to disturbance of the endoplasmic reticulum homeostasis and inhibition of vesicle trafficking. *PLoS One*. 7:e48587.

Zhao, J.J., K. Pan, J.J. Li, Y.B. Chen, J.G. Chen, L. Lv, D.D. Wang, Q.Z. Pan, M.S. Chen, and J.C. Xia. 2011. Identification of LZAP as a new candidate tumor suppressor in hepatocellular carcinoma. *PLoS One*. 6:e26608.

Zheng, Y., M.K. Jung, and B.R. Oakley. 1991. γ-Tubulin is present in Drosophila melanogaster and Homo sapiens and is associated with centrosome. *Cell*. 65:817-823.

Zhu, H., B. Bhatt, S. Sivaprakasam, Y. Cai, S. Liu, S.K. Kodeboyina, N. Patel, N.M. Savage, A. Sharma, R.J. Kaufman, H. Li, and N. Singh. 2019. Ufbp1 promotes plasma cell development and ER expansion by modulating distinct branches of UPR. *Nat. Commun*. 10:1084.
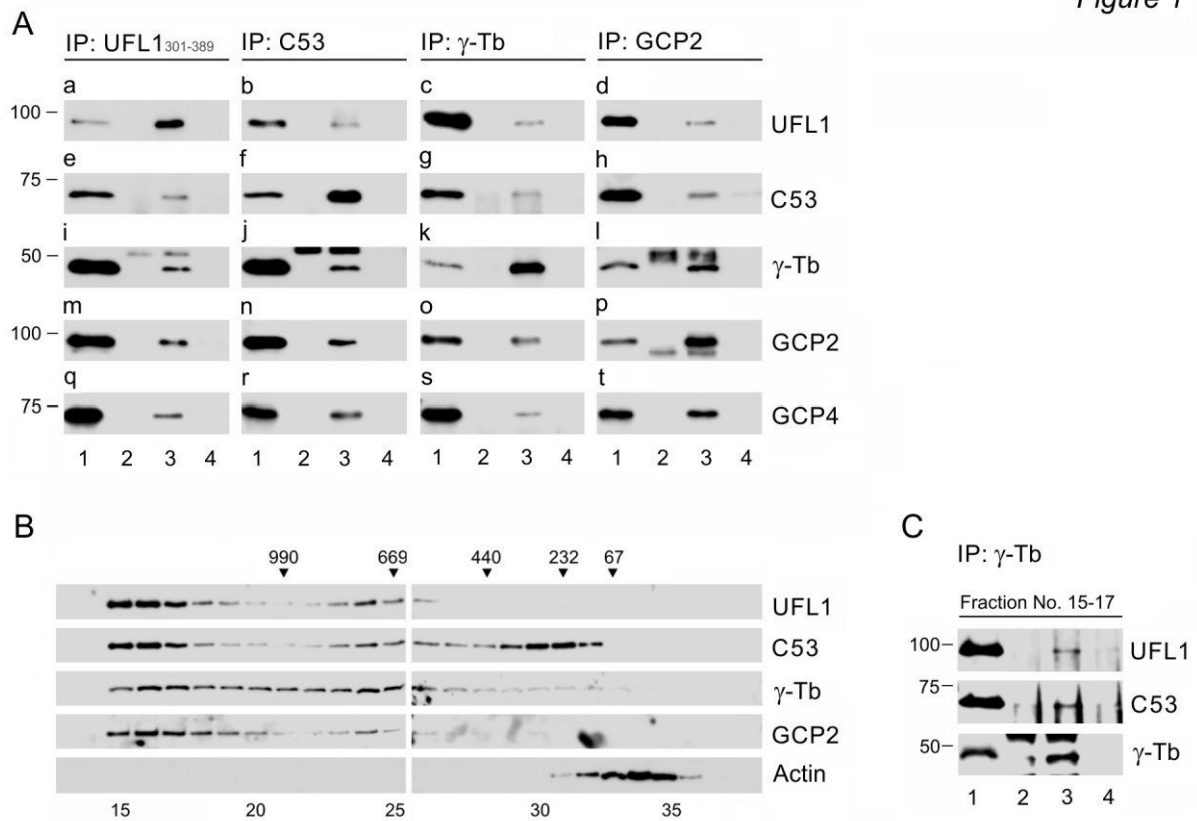
Figure legends

Figure 1. **UFL1 and C53 interact with γTuRC proteins.**

(A) Immunoprecipitation experiments. Extracts from the membranous fraction (P2) of U2OS cells were precipitated with immobilized Abs specific to UFL1$_{301\text{-}389}$ (**a, e, i, m, q**), C53 (**b, f, j, n, r**), γ-tubulin (**c, g, k, o, s**), or GCP2 (**d, h, l, p, t**). The blots were probed with Abs to UFL1, C53, γ-tubulin (γ-Tb), GCP2, or GCP4. Load (*lane 1*), immobilized Abs not incubated with cell extracts (*lane 2*), precipitated proteins (*lane 3*), and carriers without Abs and incubated with cell extracts (*lane 4*). (**B**) The size distribution of proteins extracted from the membranous fraction of U2OS cells fractionated on the Superose 6 column. The blots of the collected fractions were probed with Abs to UFL1, C53, γ-tubulin (γ-Tb), GCP2, and actin. The calibration standards (in kDa) are indicated on the top. The numbers at the bottom denote individual fractions. (**C**) Pooled fractions (Nos. 15-17) from fractionation (panel **B**) were precipitated with Ab to γ-tubulin. The blots were probed with Abs to UFL1, C53, and γ-tubulin (γ-Tb). Load (*lane 1*), immobilized Ab not incubated with cell extracts (*lane 2*), precipitated proteins (*lane 3*), and the carrier without Ab and incubated with cell extracts (*lane 4*).
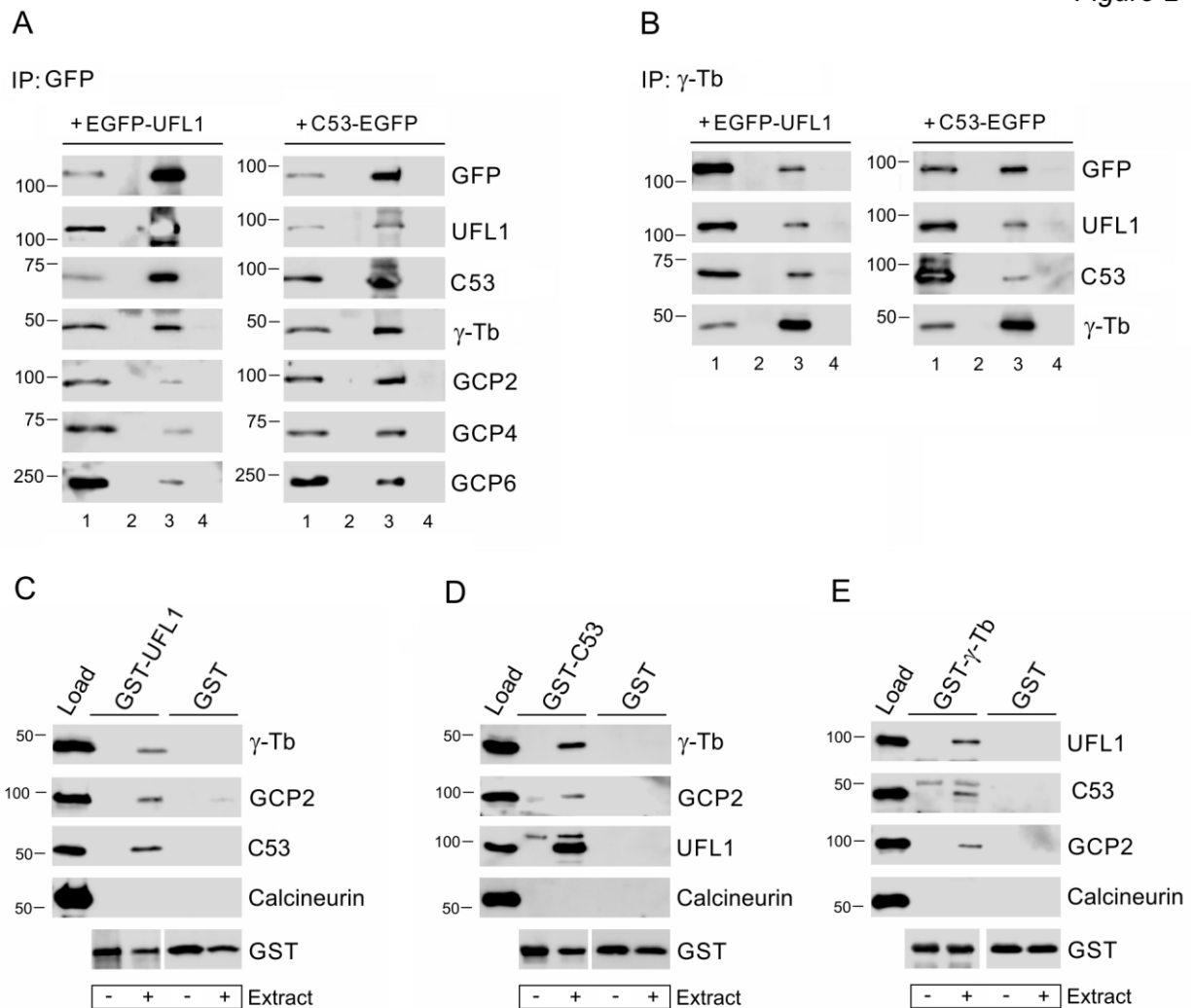
Figure 2. **Exogenous UFL1 and C53 interact with γTuRC proteins.**

(**A-B**) Immunoprecipitation experiments with the whole-cell extract from U2OS cells expressing EGFP-tagged UFL1 (EGFP-UFL1) or C53 (C53-EGFP). (**A**) Precipitation with immobilized Ab to GFP. (**B**) Precipitation with immobilized Ab to γ-tubulin. The blots were probed with Abs to GFP, UFL1, C53, γ-tubulin (γ-Tb), GCP2, GCP4, or GCP6. Load (*lane 1*), immobilized Abs not incubated with cell extracts (*lane 2*), precipitated proteins (*lane 3*), and carriers without Abs and incubated with cell extracts (*lane 4*). (**C-E**) Pull-down assay with GST-tagged UFL1 (**C**), C53 (**D**), and γ-tubulin (**E**). Immobilized GST-fusion proteins (GST-UFL1, GST-C53, GST-γ-tubulin) or immobilized GST alone were incubated with whole-cell extracts from U2OS cells (Load). Blots of bound proteins were probed with Abs to γ-tubulin (γ-Tb), GCP2, UFL1 and C53, calcineurin (negative control), and GST.
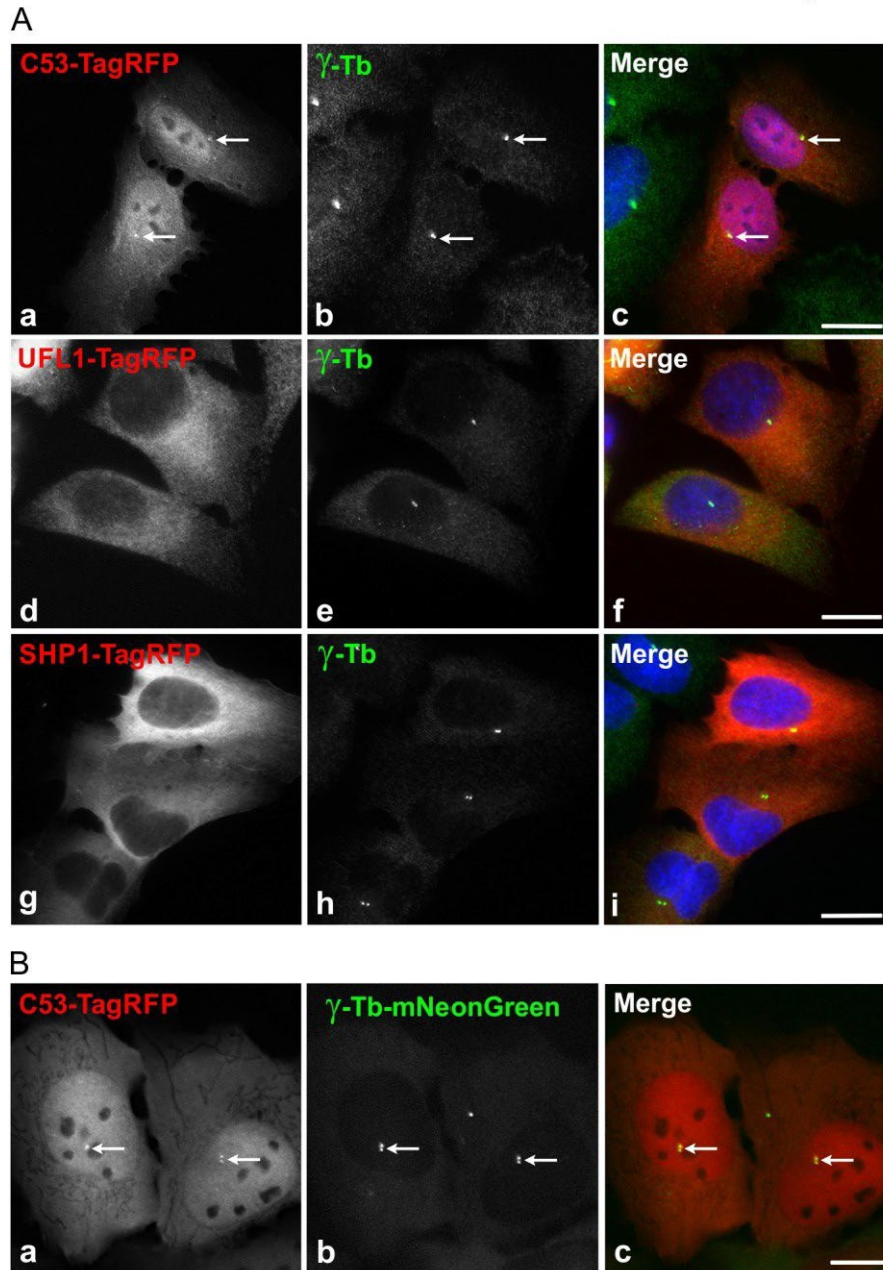
Figure 3

Figure 3. **Subcellular localization of exogenous UFL1 and C53 in interphase cells.**
(**A**) U2OS cells expressing TagRFP-tagged proteins were fixed and stained with Ab to γ-tubulin. (**a-c**)
Localization of C53-TagRFP (**a**) and γ-tubulin (**b**). Superposition of images (**c**, C53-TagRFP, red; γ-tubulin,
green; DAPI, blue). (**d-f**) Localization of UFL1-TagRFP (**d**) and γ-tubulin (**e**). Superposition of images (**f**,
UFL1-TagRFP, red; γ-tubulin, green; DAPI, blue). (**g-i**) Localization of negative control SHP-1-TagRFP (**g**)
and γ-tubulin (**h**). Superposition of images (**i**, SHP-1-TagRFP, red; γ-tubulin, green; DAPI, blue). Arrows
indicate the same positions. Fixation D/F/M. Scale bar, 20 μm. (**B**) Live cell imaging of cells expressing
C53-TagRFP and γ-tubulin-mNeonGreen. (**a-c**) Localization of C53-TagRFP (**a**) and γ-tubulin-mNeonGreen
(**b**). Superposition of images (**c**, C53-TagRFP, red; γ-tubulin-mNeonGreen, green; DAPI, blue). Arrows
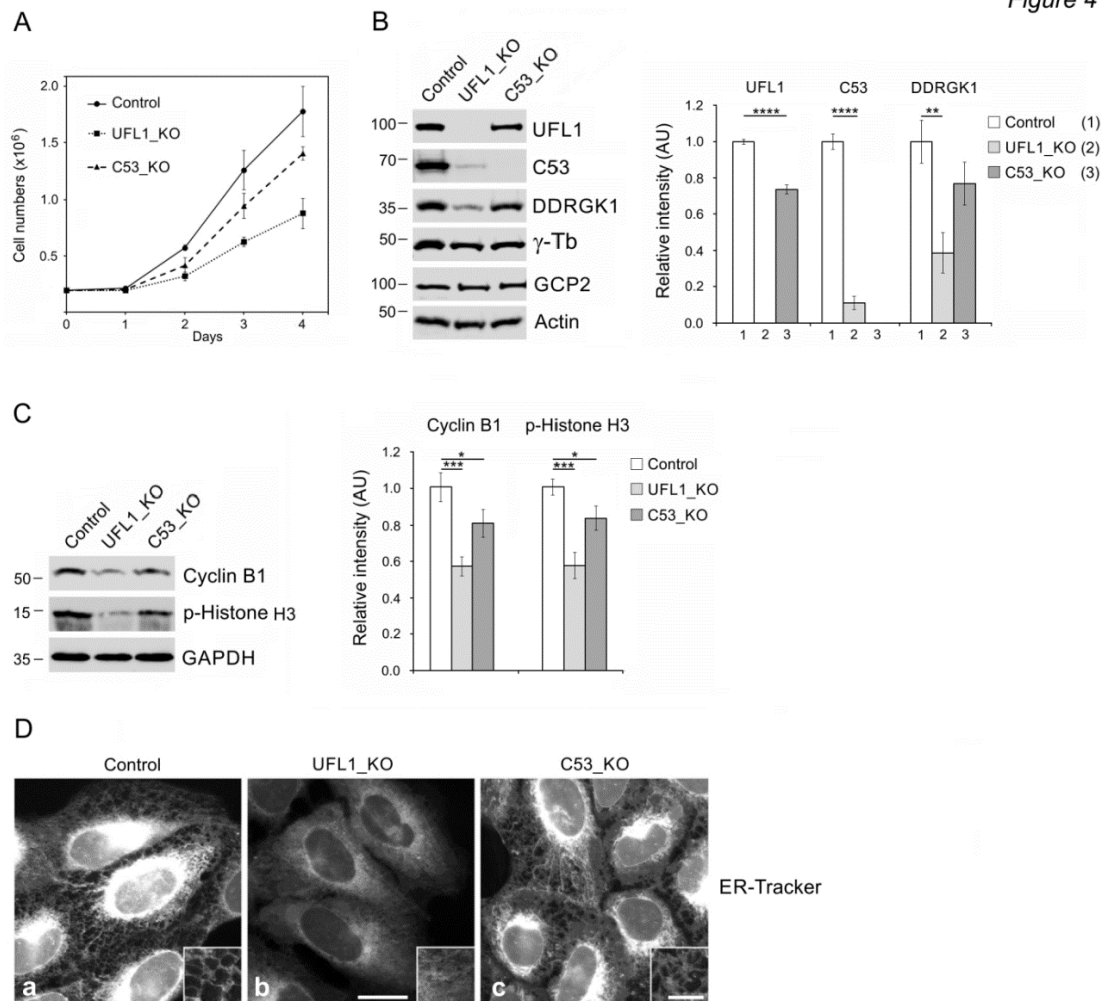indicate the same positions. Scale bar, 10 μm.

Figure 4

Figure 4. **Characterization of cells lacking UFL1 or C53.**

(**A**) Growth curves in control, UFL1-deficient (UFL1_KO), or C53-deficient (C53_KO) U2OS cells. A total of 2×10^5 cells was plated for each cell line. The values indicate mean ± SD (n=3). (**B**) Changes in the expression of UFL1, C53, and DDRGK1. The blots from whole-cell lysates were probed with Abs to UFL1, C53, DDRGK1, γ-tubulin (γ-Tb), GCP2, and actin (loading control). Densitometric quantification of immunoblots is shown on the right. Relative intensities of corresponding proteins normalized to control cells and the amount of actin in individual samples. Values indicate mean ± SD (n=3). (**C**) Changes in the expression of cyclin B1 and p-histone H3. The blots from whole-cell lysates were probed with Abs to Cyclin B1, p-Histone H3, and GAPDH (loading control). Densitometric quantification of immunoblots is shown on the right. Relative intensities of corresponding proteins normalized to control cells and the amount of GAPDH in individual samples. Values indicate mean ± SD (n=3). One-way ANOVA with Sidak's multiple comparisons test was performed to determine statistical significance. *, $p < 0.05$, **, $p < 0.01$, ***, $p < 0.001$, ****, $p < 0.0001$. (**D**). Distribution of ER in control (**a**), UFL1_KO (**b**), and C53_KO (**c**) cells visualized by ER-Tracker in living cells. A higher magnification view of the cell periphery is shown in the image inset (**a-c**). The images (**a, b, c**) were collected and processed in the same manner. Scale bars, 20 μm (**b**) and 5 μm (inset in **c**).
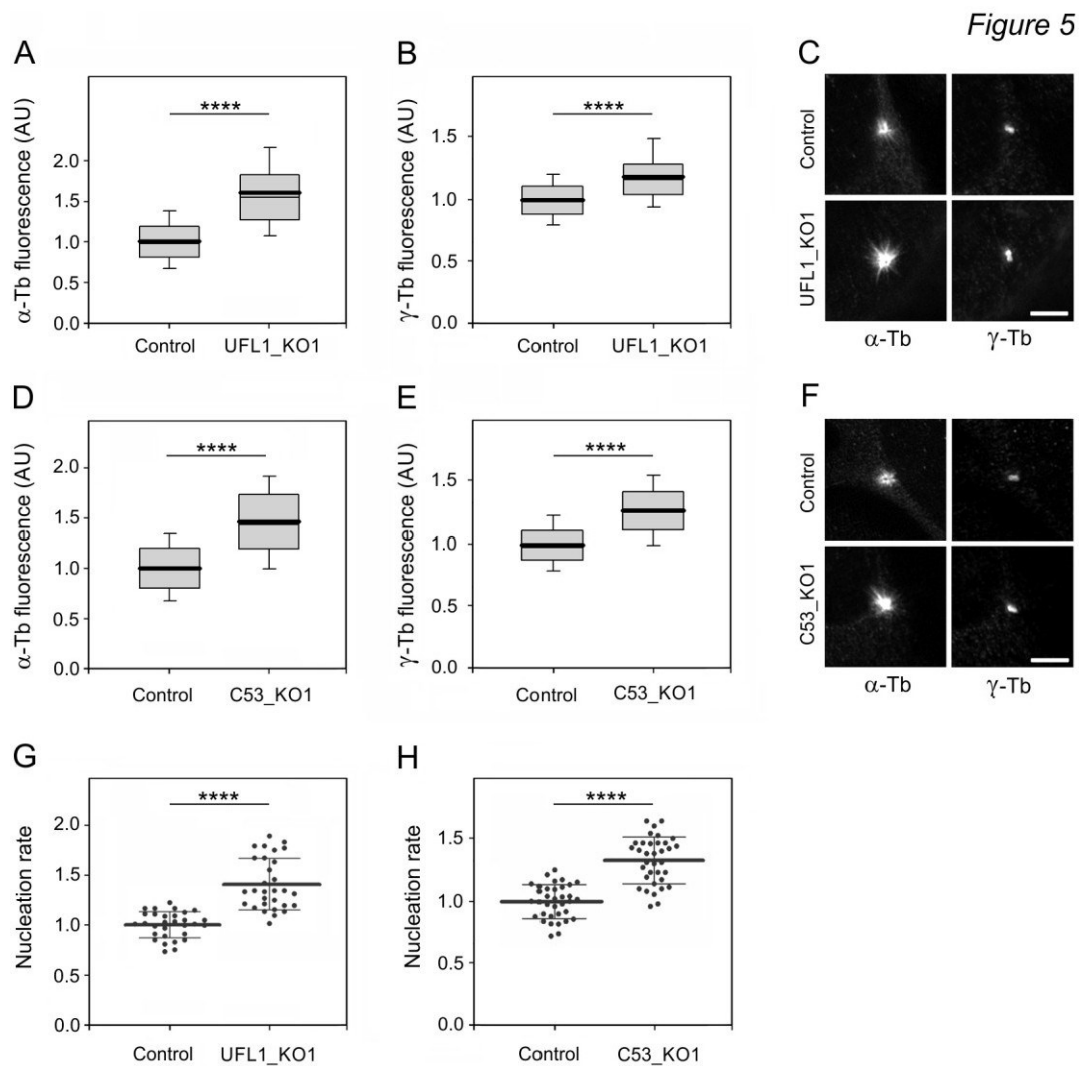
Figure 5. **Deletion of UFL1 or C53 increases centrosomal microtubule nucleation.**
Centrosomal microtubule nucleation was evaluated by quantification of microtubule regrowth in fixed cells
(**A-F**) and by measuring the microtubule nucleation rate in living cells (**G-H**). (**A-B, D-E**) The distribution of
α-tubulin or γ-tubulin fluorescence intensities (arbitrary units [AU]) in 2-μm ROI at 2.0 min of microtubule
regrowth are shown as box plots (three independent experiments, > 58 cells counted for each experimental
condition). (**A-B**) Box plot of α-tubulin (**A**) and γ-tubulin (**B**) fluorescence intensities in UFL1_KO1 cells
(n=239) relative to control cells (n=237). (**D-E**) Box plot of α-tubulin (**D**) and γ-tubulin (**E**) fluorescence
intensities in C53_KO1 cells (n=257) relative to control cells (n=274). The bold and thin lines within the box
represent mean and median (the 50th percentile), respectively. The bottom and top of the box represent the
25th and 75th percentiles. Whiskers below and above the box indicate the 10th and 90th percentiles. (**C, F**)
Labeling of α-tubulin and γ-tubulin in the microtubule regrowth experiment in the control and UFL1_KO
cells (**C**) or the control and C53_KO1 cells (**F**). Cells were fixed (F/Tx/M) at 2.0 min of microtubule
regrowth. The pairs of images (α-Tb), (γ-Tb) were collected and processed in the same manner. Scale bars, 5
μm. (**G**) Microtubule nucleation rate (EB3 comets/min) in UFL1_KO1 cells relative to controls. Three
independent experiments (at least 10 cells counted in each experiment). Control (n=30), UFL1_KO1 (n=30).
The bold and thin lines within dot plot represent mean ± SD. (**H**) Microtubule nucleation rate (EB3

comets/min) in C53_KO1 cells relative to controls. Three independent experiments (at least 10 cells counted in each experiment). Control (n=35), C53_KO1 (n=35). The bold and thin lines within dot plot represent mean ± SD. Two-tailed, unpaired Student's *t* test was performed to determine statistical significance. ****, p < 0.0001.
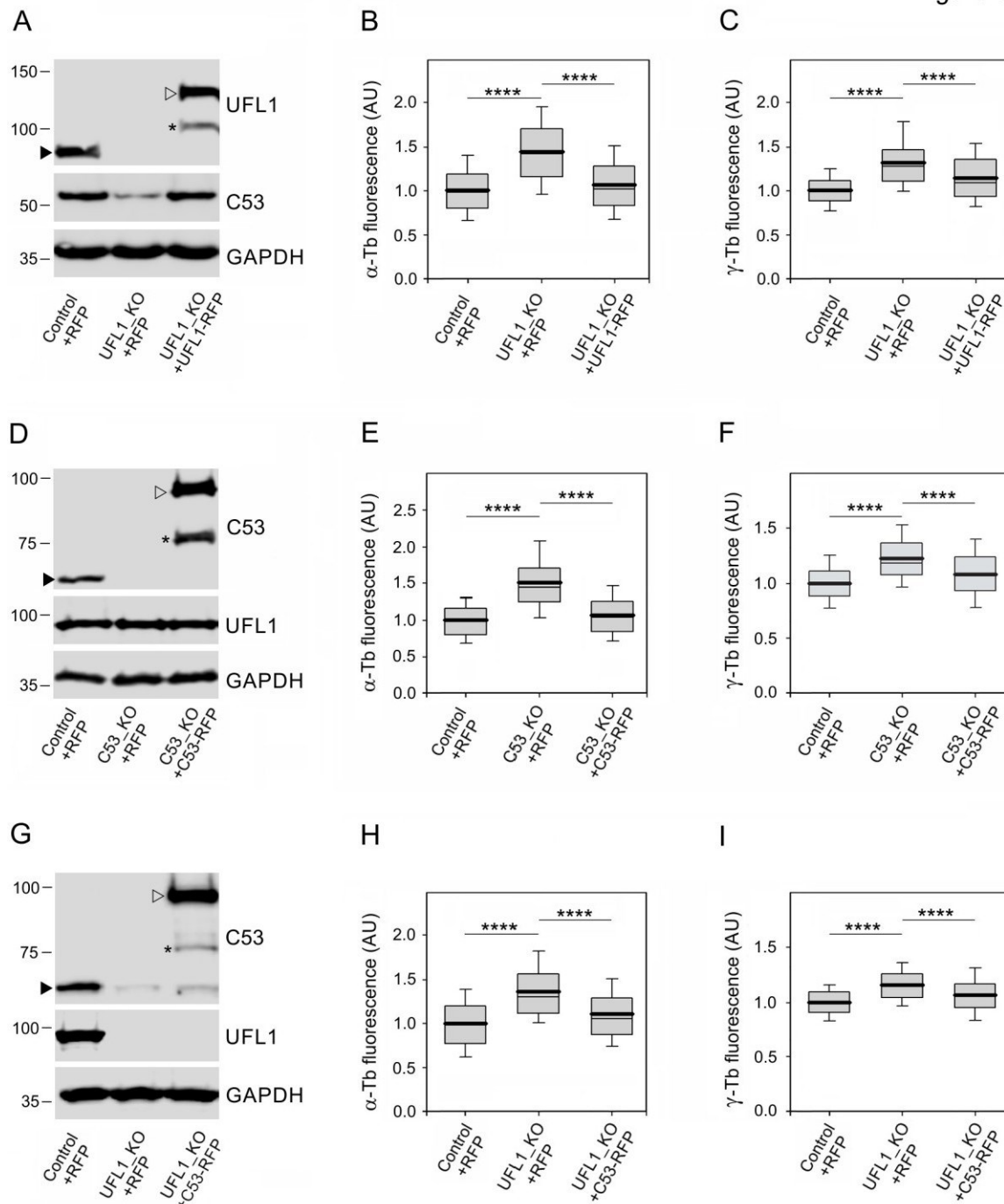
Figure 6. **C53 is sufficient to attenuate centrosomal microtubule nucleation in *UFL1* knockout cells.**
(A) Immunoblot analysis of UFL1 and C53 in whole-cell lysates from control cells expressing TagRFP
(Control+RFP), UFL1_KO cells expressing TagRFP (UFL1_KO+RFP), and UFL1_KO cells rescued by
UFL1-TagRFP (UFL1_KO+UFL1-RFP). Blots were probed with Abs to UFL1, C53, and GAPDH (loading
control). Black and empty arrowheads and asterisk denote, respectively, endogenous UFL1, UFL1-TagRFP,
and its fragment. (**B-C**) The distributions of α-tubulin or γ-tubulin fluorescence intensities (arbitrary units
[AU]) in 2-μm ROI at 2.0 min of microtubule regrowth are shown as box plots (four independent
experiments, > 30 cells counted for each experimental condition). Box plot of α-tubulin (**B**) and γ-tubulin (**C**)
fluorescence intensities in UFL1_KO+RFP (n=181) and UFL1_KO+UFL1-RFP cells (n=298) relative to

control cells (Control+RFP, n=267). (**D**) Immunoblot analysis of C53 and UFL1 in whole-cell lysates from control cells expressing TagRFP (Control+RFP), C53_KO cells expressing TagRFP (C53_KO+RFP), and C53_KO cells rescued by C53-TagRFP (C53_KO+C53-RFP). Blots were probed with Abs to C53, UFL1, and GAPDH (loading control). Black and empty arrowheads and asterisk denote, respectively, endogenous C53, C53-TagRFP, and its fragment. (**E-F**) The distributions of α-tubulin or γ-tubulin fluorescence intensities (arbitrary units [AU]) in 2-μm ROI at 2.0 min of microtubule regrowth are shown as box plots (three independent experiments, > 30 cells counted for each experimental condition). Box plot of α-tubulin (**E**) and γ-tubulin (**F**) fluorescence intensities in C53_KO+RFP (n=191) and C53_KO+C53-RFP cells (n=248) relative to control cells (Control+RFP, n=179). (**G**) Immunoblot analysis of C53 and UFL1 in whole-cell lysates from control cells expressing TagRFP (Control+RFP), UFL1_KO cells expressing TagRFP (UFL1_KO+RFP), and UFL1_KO cells rescued by C53-TagRFP (UFL1_KO+C53-RFP). Blots were probed with Abs to C53, UFL1, and GAPDH (loading control). Black and empty arrowheads and asterisk denote, respectively, endogenous C53, C53-TagRFP, and its fragment. (**H-I**) The distributions of α-tubulin or γ-tubulin fluorescence intensities (arbitrary units [AU]) in 2-μm ROI at 2.0 min of microtubule regrowth are shown as box plots (three independent experiments, > 37 cells counted for each experimental condition). Box plot of α-tubulin (**H**) and γ-tubulin (**I**) fluorescence intensities in UFL1_KO+RFP (n=133) and UFL1_KO+C53-RFP (n=152) relative to control cells (Control+RFP, n=174). (**B, C, E, F, H, I**) Bold and thin lines within the box represent mean and median (the 50th percentile), respectively. The bottom and top of the box represent the 25th and 75th percentiles. Whiskers below and above the box indicate the 10th and 90th percentiles. One-way ANOVA with Sidak's multiple comparisons test was performed to determine statistical significance. ****, $p < 0.0001$.
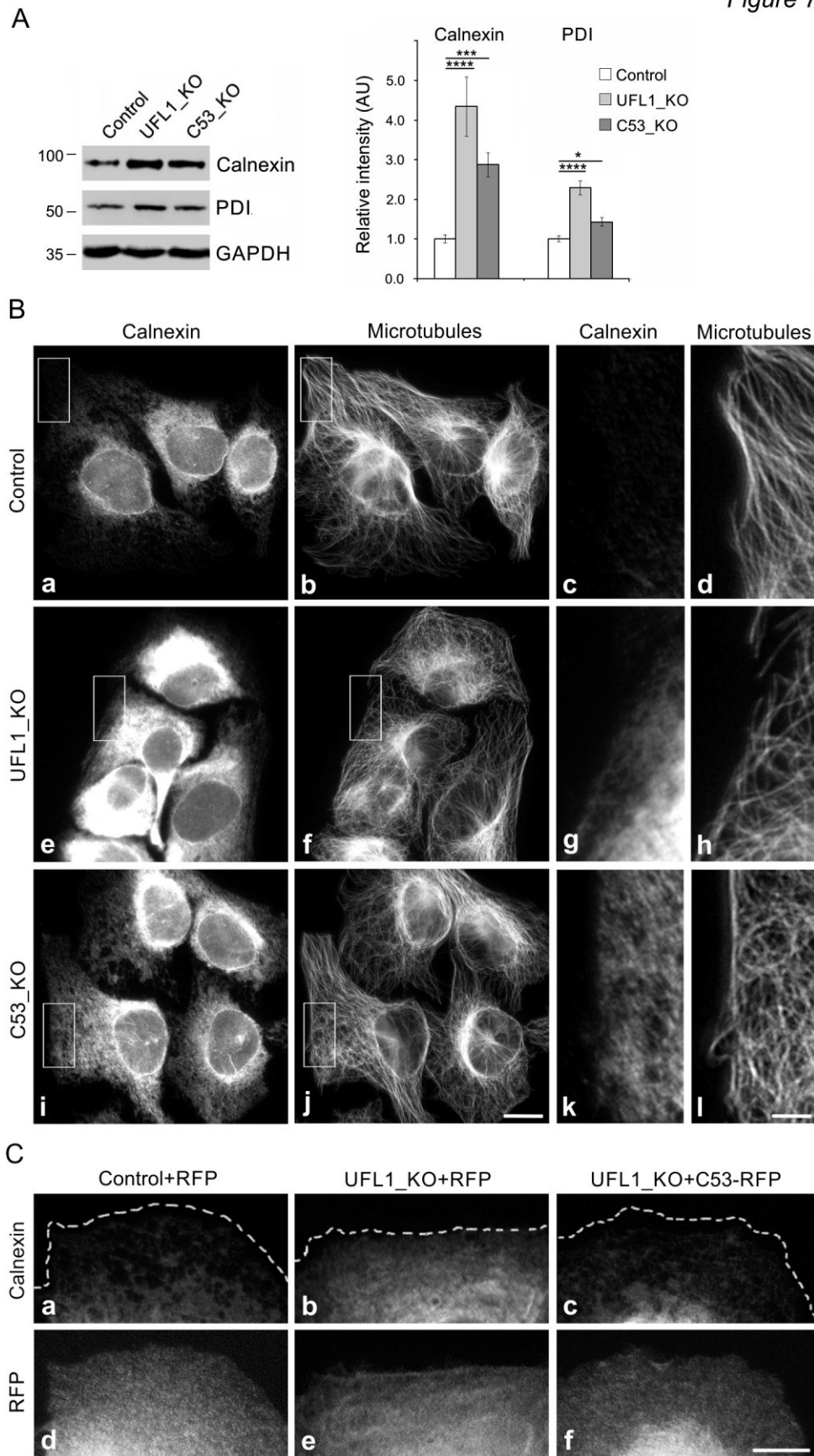
Figure 7

Figure 7. **Deletion of UFL1 or C53 induces UPR and leads to relocation of calnexin to the cell periphery.**

(**A**) Immunoblot analysis of calnexin and PDI in U2OS cells lacking UFL1 or C53. The blots from whole-cell lysates were probed with Abs to calnexin, PDI, and GAPDH (loading control). Densitometric quantification of immunoblots is shown on the right. Relative intensities of corresponding proteins normalized to control cells and the amount of GAPDH in individual samples. Values indicate mean ± SD (n=4 for calnexin; n=3 for PDI). One-way ANOVA with Sidak's multiple comparisons test was performed to determine statistical significance, *, $p < 0.05$, ***, $p < 0.001$, ****, $p < 0.0001$. (**B**) Immunofluorescence microscopy. (**a-d**) Control U2OS cells, (**e-h**) UFL1-deficient cells (UFL1_KO) and (**i-l**) C53-deficient cells (C53_KO). Cells were fixed and double-labeled for calnexin (**a, e, i**) and β-tubulin (**b, f, j**; Microtubules). Higher magnification views of the regions delimited by rectangles are shown on the right of images from control (**c-d**), UFL1_KO (**g-h**), and C53_KO (**k-l**) cells. The images (**a, e, i**) and (**c, g,** k) were collected and processed in the same manner. Fixation F/Tx. Scale bars, 20 μm (**j**), and 5 μm (**l**). (**C**) Calnexin localization in a phenotypic rescue experiment. (**a, d**) Control cells expressing TagRFP (Control+RFP), (**b, e**) UFL1_KO cells expressing TagRFP (UFL1_KO+RFP), and (**c, f**) UFL1_KO cells rescued by C53-TagRFP (UFL1_KO+C53-RFP). Cells were fixed and stained for calnexin (**a-c**). The images (**a, b, c**) were collected and processed in the same manner. Fixation F/Tx. Scale bar, 10 μm.
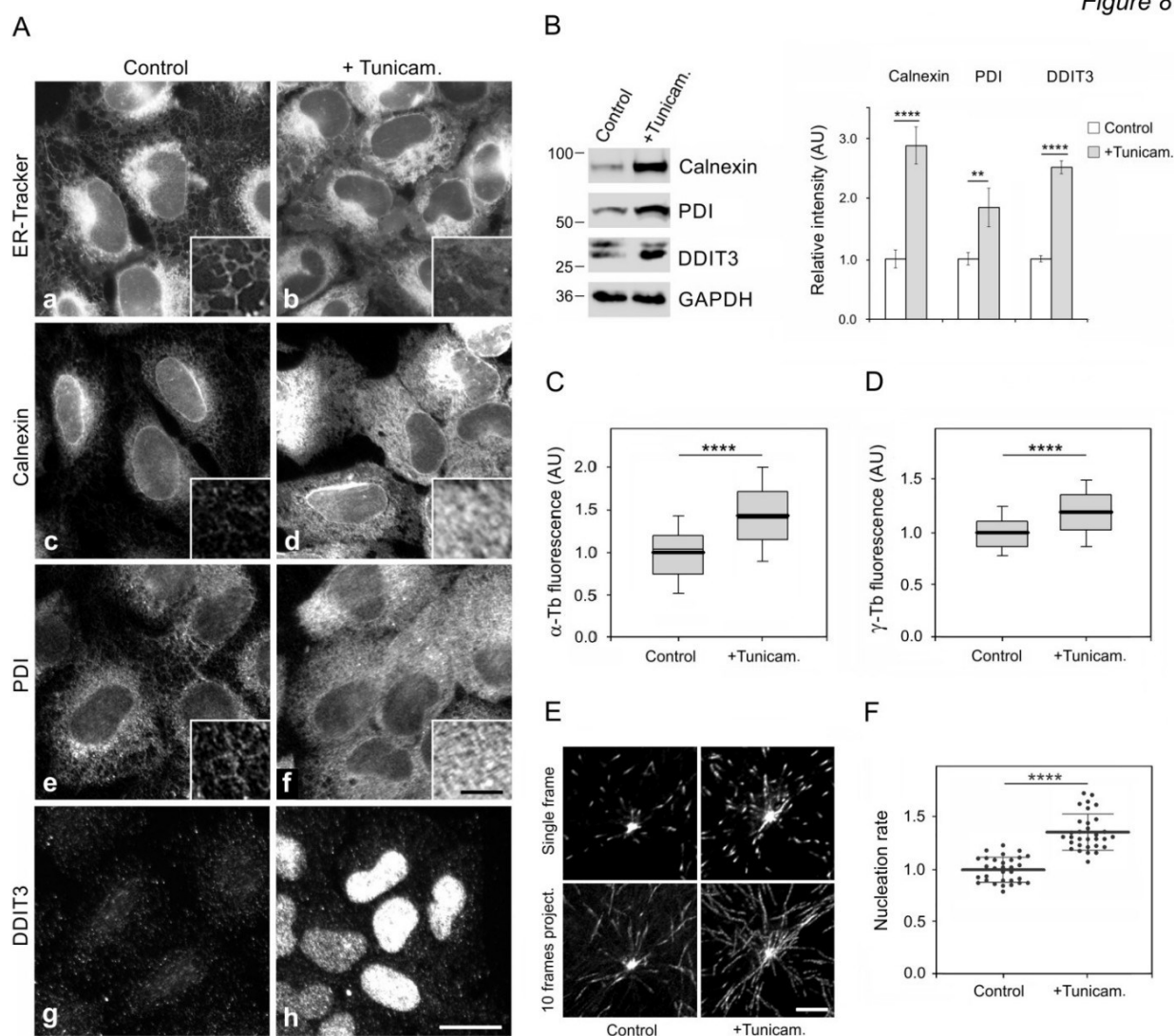
Figure 8. **Generation of ER stress by tunicamycin induces UPR and increases centrosomal microtubule nucleation.**

U2OS cells were treated with 1 µg/ml tunicamycin (+Tunicam.) or DMSO carrier (Control) for 24 h. (**A**). Effect of tunicamycin on expression and subcellular distribution of calnexin or PDI, and ER stress-induced transcription factor DDIT3. (**a-b**) Visualization of ER in living cells by ER-Tracker. (**c-h**) Fixed cells stained for calnexin (**c-d**), PDI (**e-f**), and DDIT3 (**g-h**). A higher magnification view of the cell periphery is shown in the image insets (**a-f**). Pairs of images (**a-b**), (**c-d**), (**e-f**), and (**g-h**) were collected and processed in the same manner. Fixation F/Tx. Scale bars, 20 µm (**h**) and 5 µm (inset in **f**). (**B**) Immunoblot analysis of untreated and tunicamycin-treated cells. The blots from whole-cell lysates were probed with Abs to calnexin, PDI, DDIT3, and GAPDH (loading control). Densitometric quantification of immunoblots is shown on the right. Relative intensities of corresponding proteins normalized to control cells and the amount of GAPDH in individual samples. Values indicate mean ± SD (n=5 for calnexin; n=4 for PDI; n=3 for DDIT3). (**C-D**) The distributions of α-tubulin or γ-tubulin fluorescence intensities (arbitrary units [AU]) in 2-µm ROIs at 3.0 min of microtubule regrowth in control and tunicamycin-treated cells are shown as box plots (four independent experiments, > 46 cells counted for each experimental condition). Box plot of α-tubulin (**C**) and γ-tubulin (**D**) fluorescence intensities in tunicamycin-treated cells (n=252) relative to control cells (n=206). The bold

38

and thin lines within the box represent mean and median (the 50th percentile), respectively. The bottom and top of the box represent the 25th and 75th percentiles. Whiskers below and above the box indicate the 10th and 90th percentiles. (**E**) Time-lapse imaging of control and tunicamycin-treated cells expressing EB3-mNeonGreen. Still images of EB3 (Single frame) and tracks of EB3 comets over 10 s (10 frames project.). Scale bar, 5 µm. (**F**) Microtubule nucleation rate (EB3 comets/min) in tunicamycin-treated cells relative to control cells. Three independent experiments (at least 10 cells counted in each experiment). Control (n=31), tunicamycin-treated cells (n=31). The bold and thin lines within the dot plot represent mean ± SD. Two-tailed, unpaired Student's *t* test was performed to determine statistical significance **, $p < 0.01$; **** $p < 0.0001$.
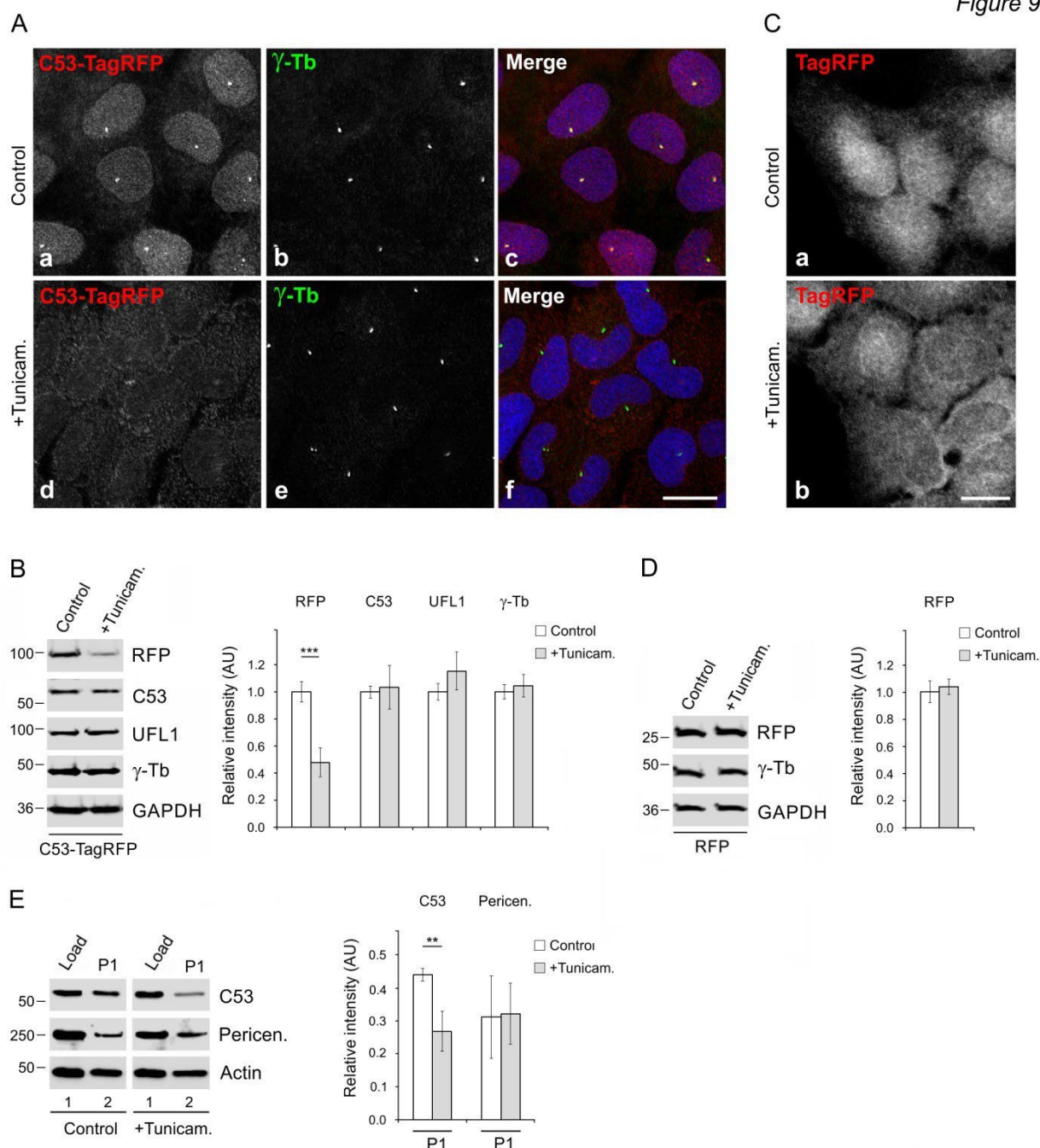
Figure 9

Figure 9. **Tunicamycin affects the distribution and protein level of C53-TagRFP.**

U2OS cells were treated with 1 µg/ml tunicamycin (+Tunicam.) or DMSO carrier (Control) for 24 h. (**A-B**) Cells expressing C53-TagRFP. (**A**) Immunofluorescence microscopy of cells fixed and stained with Ab to γ-tubulin. (**a-c**) Control cells. C53-TagRFP (**a**), γ-tubulin (**b**), superposition of images (**c**, C53-TagRFP, red; γ-tubulin, green; DAPI, blue). (**d-f**) Tunicamycin-treated cells. C53-TagRFP (**d**), γ-tubulin (**e**), superposition of images (**f**, C53-TagRFP, red; γ-tubulin, green; DAPI, blue). Images (**a, d**) and (**b, e**) were collected and processed in the exactly same manner. Fixation Tx/F/M. Scale bar, 20 µm. (**B**) Immunoblot analysis of whole-cell lysates with Abs to RFP, C53, UFL1, γ-tubulin (γ-Tb), and GAPDH (loading control). Densitometric quantification of immunoblots is shown on the right. Relative intensities of corresponding proteins normalized to control cells and the amount of GAPDH in individual samples. Values indicate mean ± SD (n=4). (**C-D**) Cells expressing TagRFP. (**C**) Immunofluorescence microscopy of fixed control cells (**a**)

and tunicamycin-treated cells (**b**). Images (**a, b**) were collected and processed in exactly the same manner. Fixation F/Tx. Scale bar, 20 µm. (**D**) Immunoblot analysis of whole-cell lysates with Abs to RFP, γ-tubulin (γ-Tb), and GAPDH (loading control). Densitometric quantification of immunoblots is shown on the right. Relative intensities of corresponding proteins normalized to control cells and the amount of GAPDH in individual samples. Values indicate mean ± SD (n=3). (**E**) Distribution of proteins in fractions after differential centrifugation of the cell homogenate. Cell fractions were prepared as described in the Materials and Methods section. Cell homogenate (*lane 1*), pellet P1 (*lane 2*). Immunoblot analysis with Abs to C53, pericentrin, and actin (loading control). Densitometric quantification of immunoblots is shown on the right. Intensities of corresponding proteins in P1 normalized to loads (relative intensity 1.0). Values indicate mean ± SD (n=4). Two-tailed, unpaired Student's *t* test was performed to determine statistical significance. ** $p < 0.01$; ***, $p < 0.001$.

Supplemental material

Table S1 **Mass spectrometry identification of E3 UFM1-protein ligase 1 (UFL1).**

Measured mass [M+H]	Computed mass [M+H]	Error (ppm)	Peptide sequence	Peptide position
1292.619	1292.605	11	MoxADAWEEIRR	1 – 10
820.454	820.431	28	LAADFQR	11 – 17
1037.488	1037.501	13	AQFAESTQR	18 – 26
2369.293	2369.271	9	QLEVVHTLDGKEYITPAQISK	44 – 64
2305.286	2305.251	15	VNIVDLQQVINVDLTHIESR	77 – 96
1808.942	1808.918	13	AYDLPGDFLTQALTQR	145 – 160
1279.699	1279.675	19	IINGHLDLDNR	164 – 174
1209.630	1209.663	27	GVIFTEAFVAR	175 – 185
2317.226	2317.171	24	YGFQEQLLYSVLEDLVSTGR	210 – 229
1166.597	1166.620	20	AVFVPDIYSR	242 – 251
1373.633	1373.648	11	TQSTWVDSFFR	252 – 262
1412.713	1412.681	23	QNGYLEFDALSR	263 – 274
1445.695	1445.673	15	FITDCcamTGLFSER	368 – 379
1521.752	1521.791	26	NNPVHLITEEDLK	390 – 402
2049.112	2049.061	25	TIKDLQEEVSNLYNNIR	535 – 551
1706.800	1706.834	20	DLQEEVSNLYNNIR	538 – 551
941.514	941.532	19	QILFQHR	662 – 668

Mox: oxidized methionine; Ccam: carbamidomethylated cysteine

```
  1 MADAWEEIRR LAADFQRAQF AESTQRLSER NCIEIVNKLI SQKQLEVVHT LDGKEYITPA
 61 QISKEMRDEL HVRGGRVNIV DLQQVINVDL THIESRVSDI IKSEKHVQMV LGQLIDENYL
121 DQLSEEVNDK LQESGQVTVS ELCKAYDLPG DFLTQALTQR LGRIINGHLD LDNRGVIFTE
181 AFVARHKARI RGLFSAITRP TPVNSLVSKY GFQEQLLYSV LEDLVSTGRL RGTVVGGRQD
241 KAVFVPDIYS RTQSTWVDSF FRQNGYLEFD ALSRLGIPDA VNYIKKRYKN TQLLFLKATC
301 VGQGLVDQVE ASVEEAISSG TWVDISPLLP SSLSVEDAAM LLQQVMRPFG KLASAIVFSD
361 TVVVSEKFIT DCTGLFSERM HQKAEKEMKN NPVHLITEED LKQISILESV NTSKKDKKDE
421 RRKKATEGSG SVRGGGGGNA REYKIKKTKK KGRKDEDSDD ESQSSHGGKK KPDITFMFQD
481 EIEDCLRKHI QDAPEEFISE LAEYLIKPLN KMYLEVVRSV FMSSTSASGT GRKRTIKDLQ
541 EEVSNLYNNI RLFEKGMKYF ADDTQTALTK HLLKTVCTDI TNLMFNFLAS DFLMAVEEPA
601 AITSDIRKKI LSKLTEETKV ALTKLHNSLN EKSIEDFLSC LDSATEACDI MVKKGDKKRE
661 RQILFQHRQA LCEQLKVTED PALILHLTAV LLFQLSTHSM LHAPGRCVPQ IIAFLHSKIP
721 EDQHTLLVKY QGLVVKQLVS QNKKTGQGED PSSDELDKEQ HDVTNATRKE LQELSLSIKD
781 LVLKSRKSSV TEE
```

Amino acids of the identified peptides in the mouse E3 UFM1-protein ligase 1 (Uniprot identifier Q8CCJ3) are indicated in bold and underlined (bottom part of the table). The matched peptides cover 26% of the protein sequence.
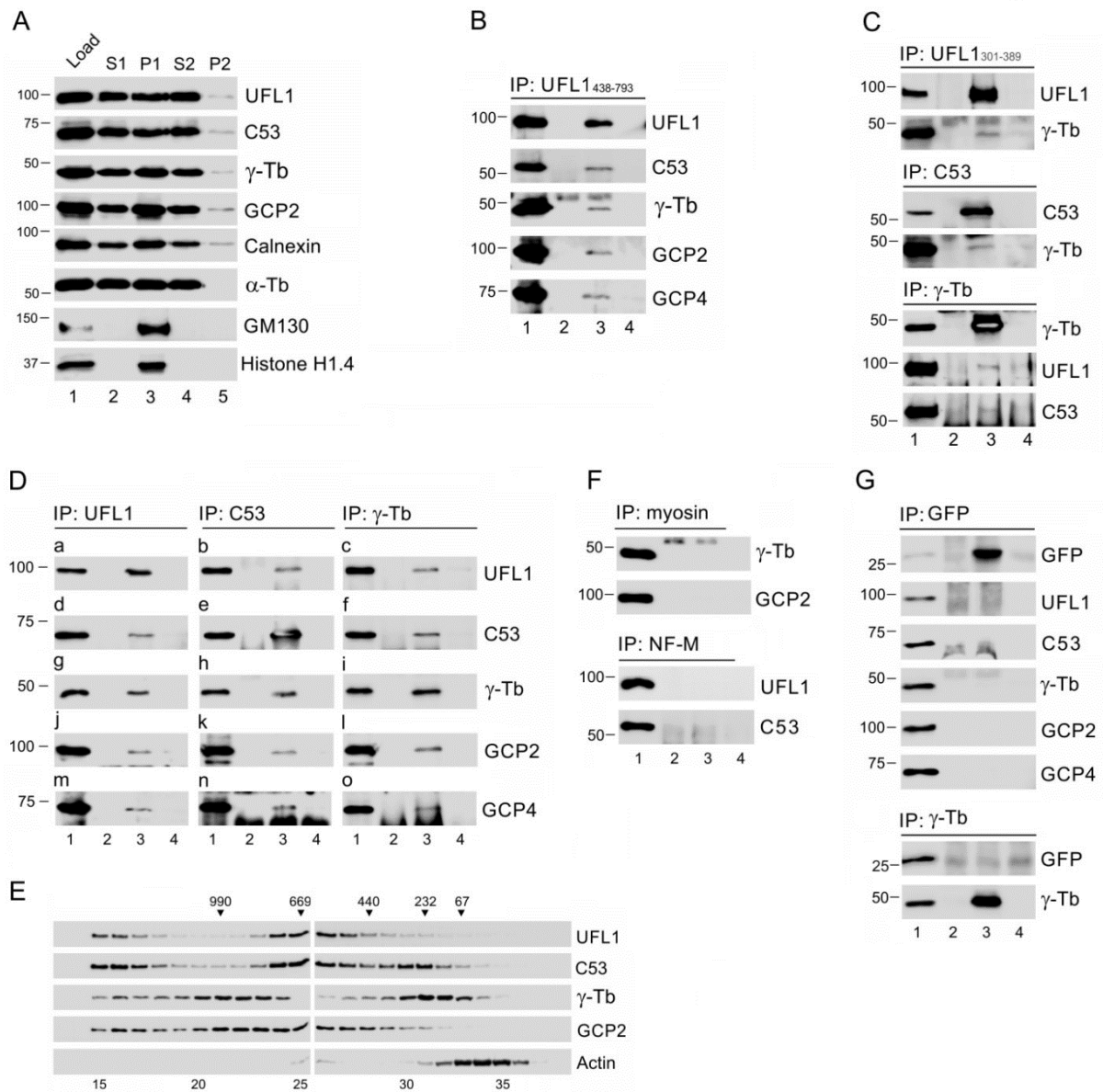
Figure S1. **UFL1 and C53 associate with γTuRC proteins. Controls for immunoprecipitation experiments.**

(**A-C**) Membrane-bound UFL1 and C53 interact with γTuRC proteins. (**A**) Relative distribution of proteins in fractions after differential centrifugation of the U2OS cell homogenate. Cell fractions were prepared as described in the Materials and Methods section. Cell homogenate (*lane 1*), supernatant S1 (*lane 2*), pellet P1 (*lane 3*), supernatant S2 (*lane 4*), pellet P2 (*lane 5*). To compare the relative distribution of proteins, pelleted material was resuspended in a volume equal to that of the corresponding supernatant. Blots were probed with Abs to UFL1, C53, γ-tubulin (γ-Tb), GCP2, calnexin, α-tubulin (α-Tb), GM130 and Histone H1.4. (**B-C**) Immunoprecipitation experiments. Extracts from the membranous fraction (P2) of U2OS (**B**) or T98G (**C**) cells were precipitated with immobilized Abs specific to UFL1$_{438-793}$ (**B**) or UFL1$_{301-389}$, C53 and γ-tubulin (**C**). The blots were probed with Abs to UFL1, C53, γ-tubulin (γ-Tb), GCP2, and GCP4. Load (*lane 1*),

immobilized Abs not incubated with cell extracts (*lane 2*), precipitated proteins (*lane 3*), and carriers without Abs and incubated with cell extracts (*lane 4*). (**D-E**). UFL1 and C53 in the whole-cell extract interacts with γTuRC proteins. (**D**) Immunoprecipitation experiments. Precipitation of U2OS whole-cell extracts with immobilized Abs specific to UFL1 (**a, d, g, j, m**), C53 (**b, e, h, k, n**), or γ-tubulin (**c, f, i, l, o**). The blots were probed with Abs to UFL1, C53, γ-tubulin (γ-Tb), GCP2, or GCP4. Load (*lane 1*), immobilized Abs not incubated with cell extracts (*lane 2*), precipitated proteins (*lane 3*), and carriers without Abs and incubated with cell extracts (*lane 4*). (**E**) The size distribution of proteins in U2OS whole-cell extracts fractionated on the Superose 6 column. The blots of the collected fractions were probed with Abs to UFL1, C53, γ-tubulin (γ-Tb), GCP2, and actin. The calibration standards (in kDa) are indicated on the top. The numbers at the bottom denote individual fractions. (**F-G**) Negative controls for immunoprecipitation experiments. (**F**) Isotype controls. Whole-cell extracts from the U2OS membranes were precipitated with immobilized rabbit Ab to myosin or mouse mAb to NF-M (IgG2a). Blots were probed with Abs to γ-tubulin (γ-Tb), GCP2, UFL1, or C53. Load (*lane 1*), immobilized Abs not incubated with cell extracts (*lane 2*), precipitated proteins (*lane 3*), and carriers without Abs and incubated with cell extracts (*lane 4*). (**G**) Whole-cell extracts from the U2OS cells expressing EGFP alone precipitated with immobilized Abs to GFP and γ-tubulin. The blots were probed with Abs to GFP, UFL1, C53, γ-tubulin (γ-Tb), GCP2, or GCP4. Load (*lane 1*), immobilized Abs not incubated with cell extracts (*lane 2*), precipitated proteins (*lane 3*), and carriers without Abs and incubated with cell extracts (*lane 4*).
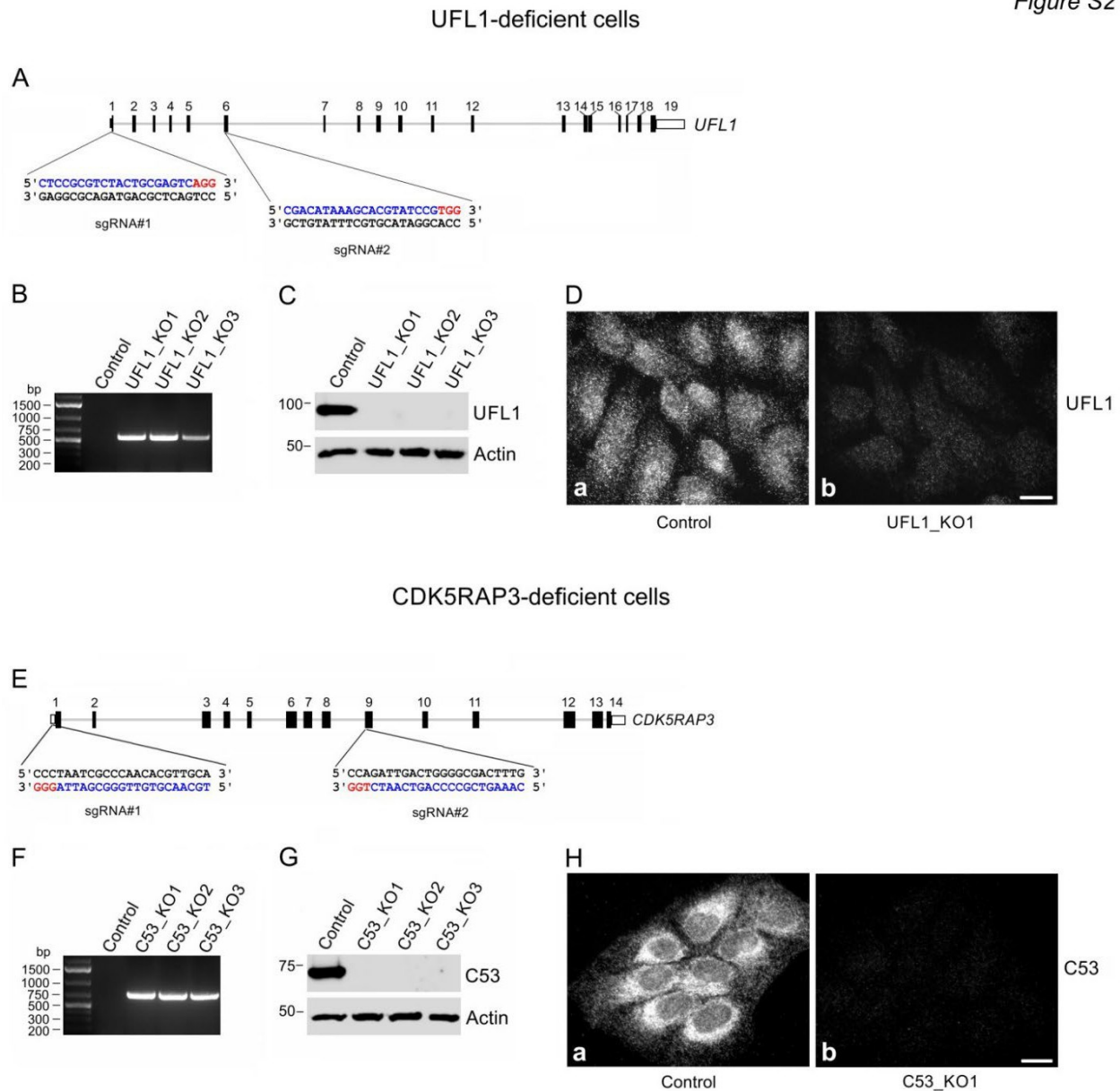
UFL1-deficient cells

CDK5RAP3-deficient cells

Figure S2. **Generation of *UFL1* and *CDK5RAP3* knockout cell lines.**

(**A-D**) UFL1-deficient cells. (**A**) Schematic diagram of the longest transcript of *UFL1* gene (34.9 kb), containing 19 exons, with sites targeted by guide RNA (sgRNA) sequences. Targeted sites (blue) and protospacer adjacent motifs (PAM; red) are depicted. (**B**) PCR amplification of genomic DNA from control U2OS cells (Control) and UFL1-deficient U2OS cell lines (UFL1_KO1, UFL1_KO2, UFL2_KO3) with primers flanking the deleted region. Due to the large size of the deleted region (~6.8kb), no amplification

was found in control cells. Amplification of short fragments (~560bp) was detected in UFL1-deficient clones. (**C**) UFL1 protein levels in U2OS and UFL1-deficient U2OS cell lines analyzed by immunoblotting of whole-cell lysates. Actin served as the loading control. (**D**) UFL1 protein levels in control (a) and UFL1_KO1 (**b**) cells analyzed by immunofluorescence microscopy with Ab to UFL1$_{438-793}$. Fixation F/Tx. The pairs of images were collected and processed in the same manner. Scale bar, 20 μm. (**E-H**) CDK5RAP3-deficient cells. (**E**) Schematic diagram of the longest transcript of *CDK5RAP3* gene (15.2 kb), containing 14 exons, with sites targeted by guide RNA (sgRNA) sequences. Targeted sites (blue) and protospacer adjacent motifs (PAM; red) are depicted. (**F**) PCR amplification of genomic DNA from control U2OS cells (Control) and CDK5RAP3 (C53)-deficient U2OS cell lines (C53_KO1, C53_KO2, C53_KO3) with primers flanking the deleted region. Due to the large size of the deleted region (~6.1 kb), no amplification was found in control cells. Amplification of short fragments (~720bp) was detected in C53-deficient clones. (**G**) C53 protein levels in U2OS and C53-deficient U2OS cell lines analyzed by immunoblotting of whole-cell lysates. Actin served as the loading control. (**H**) C53 protein levels in control (a) and C53_KO1 (**b**) cells analyzed by immunofluorescence microscopy with Ab to C53. Fixation F/Tx. The pairs of images were collected and processed in the same manner. Scale bar, 20 μm.
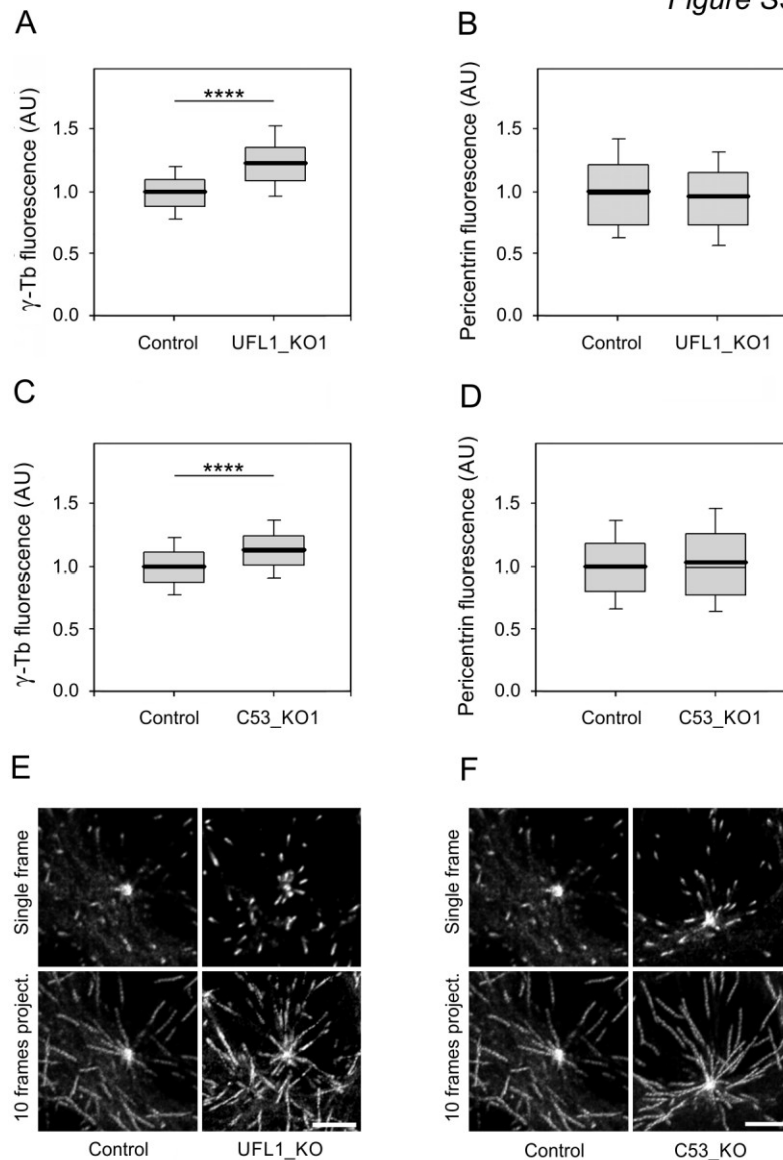
Figure S3. **Deletion of UFL1 or C53 stimulates accumulation of γ-tubulin but not pericentrin at the centrosome, and promotes microtubule nucleation.**

(**A-D**) The distributions of γ-tubulin or pericentrin fluorescence intensities (arbitrary units [AU]) in 2-μm ROI at 2.0 min of microtubule regrowth in control, UFL1-deficient (UFL1_KO1) or C53-deficient (C53_KO1) cells are shown as box plots (three experiments for UFL1-KO1 and four experiments for C53_KO1, > 49 cells counted for each experimental condition). (**A-B**) Box plot of γ-tubulin (**A**) and pericentrin (**B**) fluorescence intensities in UFL1_KO1 cells (n=234) relative to control cells (Control, n=247). (**C-D**) Box plot of γ-tubulin (**C**) and pericentrin (**D**) fluorescence intensities in C53_KO1 cells (n=358) relative to control cells (Control, n=322). The bold and thin lines within the box represent mean and median (the 50th percentile), respectively. The bottom and top of the box represent the 25th and 75th percentiles. Whiskers below and above the box indicate the 10th and 90th percentiles. Two-tailed, unpaired Student's *t* test was performed to determine statistical significance. ****, p < 0.0001. (**E-F**) Time-lapse imaging of control and UFL1_KO1 (**E**) or C53_KO1 (**F**) cells expressing EB3-mNeonGreen. Still images of EB3 (Single frame) and tracks of EB3 comets over 10 s (10 frames project.). Scale bars, 5 μm.
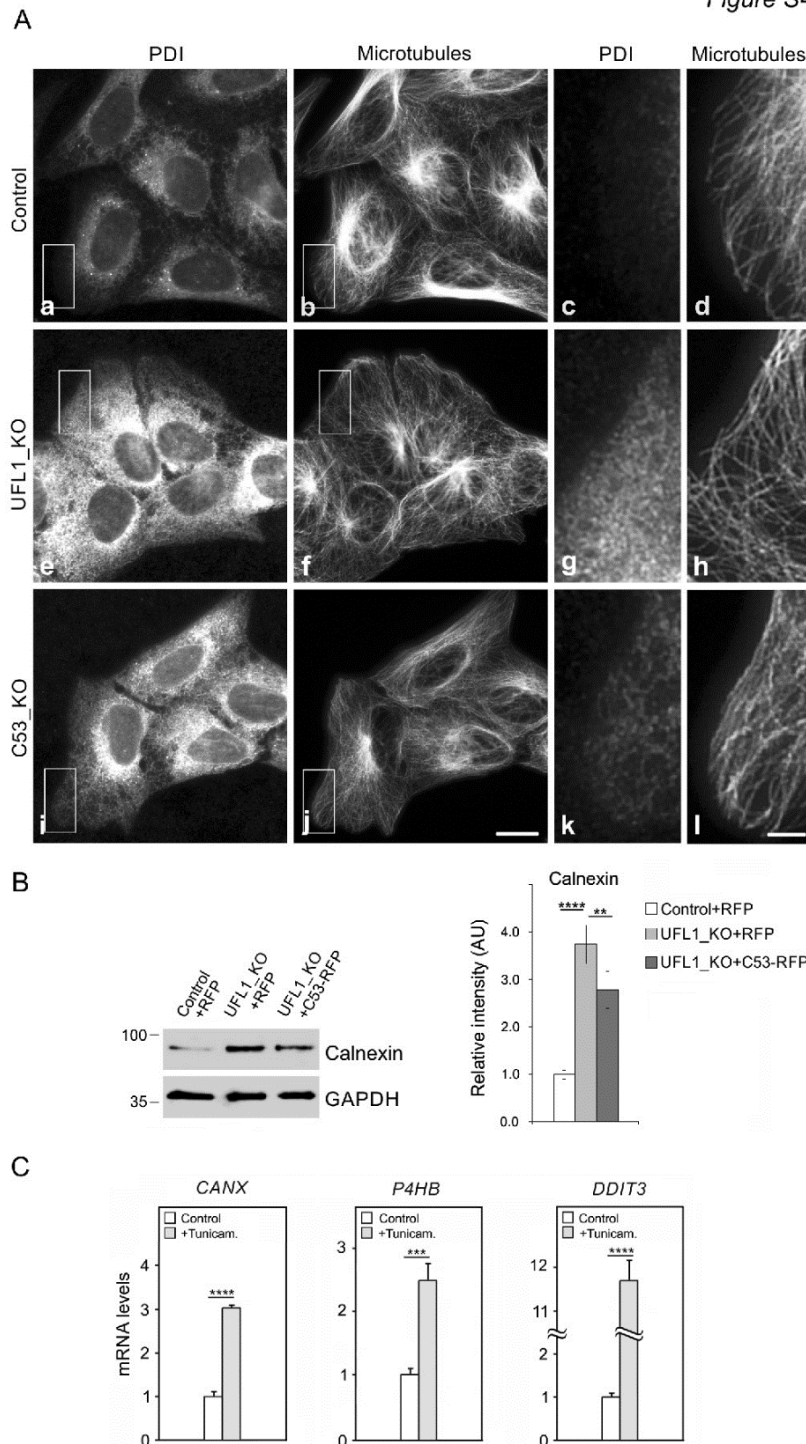
Figure S4. **Deletion of UFL1 or C53 induces subcellular redistribution of PDI, and C53 attenuates calnexin expression in cells lacking UFL1. Tunicamycin causes transcriptional upregulation of ER stress-associated proteins.** (**A**) Immunofluorescence microscopy. (**a-d**) Control, (**e-h**) UFL1-deficient (UFL1_KO) and (**i-l**) C53-deficient (C53_KO) U2OS cells. Cells were fixed and double-labeled for PDI (**a, e, i**) and β-tubulin (**b, f, j**; Microtubules). Higher magnification views of the regions delimited by rectangles are shown on the right of images from control (**c-d**), UFL1_KO (**g-h**), and C53_KO cells (**k-l**). Images (**a, e, i**) and (**c, g, k**) were collected and processed in exactly the same manner. Fixation F/Tx. Scale bars, 20 μm (**j**)

and 5 μm (**l**). (**B**) Immunoblot analysis of a phenotypic rescue experiment. Whole-cell lysates from control cells expressing TagRFP (Control+RFP), UFL1_KO cells expressing TagRFP (UFL1_KO+RFP), and UFL1_KO cells rescued by C53-TagRFP (UFL1_KO+C53-RFP). Blots were probed with Abs to calnexin and GAPDH (loading control). Densitometric quantification of immunoblots is shown on the right. Relativeintensities of corresponding proteins normalized to control cells and the amount of GAPDH in individual samples. Values indicate mean ± SD (n=4). One-way ANOVA with Sidak's multiple comparisons test was performed to determine statistical significance. (**C**) Transcription of calnexin (*CANX*), PDI (*P4HB*), and DDIT3 (*DDIT3*) genes in cells treated with tunicamycin relative to the levels in untreated control cells. Datarepresent the mean ± SD (n=3). Two-tailed, unpaired Student's *t* test was performed to determine statistical significance.

**, $p < 0.01$; ***, $p < 0.001$; ****, $p < 0.0001$.

VIII   SUPPLEMENTS

VIII.1 Havelka, D., Chafai, D.E., Krivosudský, O., **Klebanovych, A.,** Vostárek, F., Kubínová, L., Dráber, P., Cifra, M. (2020) Nanosecond pulsed electric field lab-on-chip integrated in super-resolution microscope for cytoskeleton imaging. Adv. Mater. Technol. *5:* e1900669.

Nanosecond Pulsed Electric Field Lab-on-Chip Integrated in Super-Resolution Microscope for Cytoskeleton Imaging

Daniel Havelka, Djamel Eddine Chafai, Ondrej Krivosudský, Anastasiya Klebanovych, František Vostárek, Lucie Kubínová, Pavel Dráber, and Michal Cifra*

Nanosecond pulsed electric field offers novel opportunities in bionanotechnology and biomedicine enabling ultrafast physical control of membrane, and protein-based processes for the development of novel bionanomaterials and biomedical theranostic methods. However, the mechanisms of nanosecond pulsed electric field action at the nano- and molecular scale are not fully understood due to lack of appropriate research tools. In order to overcome this challenge, a technological platform for the exploration of these mechanisms in live biological samples is provided here. This paper describes step by step the proposed chip platform, including the design, fabrication, installation, and testing of the chip. The developed chip is capable of delivering hundreds of volts of nanosecond electric pulses compared to conventional chips using few volts. Moreover, the chip is fully integrated into a super-resolution microscope. Later on, the chip function is demonstrated by affecting microtubule architecture in living cells. Therefore, the chip-based technological advancement enables the assessment of pulsed electric field effects on bionanostructures and observing their effects in real-time. The results contribute to the chip-based high-frequency bioelectronics technology for modulating the function of biological matter at the nanoscale level.

1. Introduction

Pulsed electric field (PEF) technology is becoming increasingly used in many areas of research and industry. For instance, electroporation and electropermeabilization of membranes by µs–ms time-scale PEF enables gene transfection in molecular biology,[1] drug[2–4] and gene[5–8] delivery, nonthermal tissue ablation[9] in clinical research and clinics, and effective nutrient extraction[10–12] and preservation[13,14] in food industry and biotechnology.[15–17]

A new branch of PEF exploring pulses of a duration between 1 ns to a few hundred nanoseconds (nsPEF)[18–21] is under investigation. nsPEF offers several distinct features, especially at the nanoscale, which make it a unique tool for modulating structure and function of biological matter. At first, compared to µs–ms PEF, nsPEF can be applied at a very high field strength (MV m^{-1}), yet it does not cause heating as long as the pulse firing rate is kept low.[22] This is because the pulse duration is very short and consequently the total energy in the pulse is low. Having electric field strong enough, nsPEF acting on biomolecule charges and dipoles can overcome thermal motion of a biomolecule and effectively manipulate its structure and function.[23] At second, ns duration of pulses potentially enables control of biomolecular materials at the similar time scales as long as the system responds within ns time scale. At third, due to a sharp rise time (<few nanoseconds) and short duration of the nsPEF, the energy carried by nsPEF is distributed to much broader spectrum than in µs–ms PEF. High energy content of nsPEF at radio-frequencies[24] principally enables nsPEF propagation in free space and also in biological tissues. Therefore, nsPEF has a potential for wireless noncontact modulation of biological tissues and materials function. Since the size of the laboratory objects and wiring is comparable to the wavelengths contained in nsPEF signals (meters down to centimeters), nsPEF systems require careful electromagnetic design in order to properly deliver nsPEF from generator to the target sample or tissue.

In a complex biological material, PEF is known to act primarily at the level of membranes, which being insulators, cause a significant "enhancement" of the electric field inside them compared to externally applied electric field.[25] This amplification occurs because membrane is an electrical insulator and causes a significant voltage drop across it when external electric potential is applied. Consequently, most research efforts on PEF mechanisms of action have been focused on membranes,[26] where membrane electroporation and permeabilization is typically visualized by fluorescence of the substances penetrating the membranes after PEF treatment.[27] In contrast, several

Dr. D. Havelka, Dr. D. E. Chafai, Dr. O. Krivosudský, Dr. M. Cifra
Institute of Photonics and Electronics of the Czech Academy of Sciences
Prague 18251, Czechia
E-mail: cifra@ufe.cz

A. Klebanovych, Prof. P. Dráber
Institute of Molecular Genetics of the Czech Academy of Sciences
Prague 14220, Czechia

Dr. F. Vostárek, Dr. L. Kubínová
Institute of Physiology of the Czech Academy of Sciences
Prague 14220, Czechia

The ORCID identification number(s) for the author(s) of this article can be found under https://doi.org/10.1002/admt.201900669.

ADVANCED
SCIENCE NEWS
www.advancedsciencenews.com

ADVANCED
MATERIALS
TECHNOLOGIES
www.advmattechnol.de

recent works indicated that also proteins could be a target of nsPEF,[28–32] including proteins which form microtubules.[23]

Microtubules, formed by $\alpha\beta$-tubulin heterodimers, are hollow cylinders with outer diameter about 25 nm. They are involved in such important cellular functions as keeping cell shape and position of organelles, ordered intracellular transport, cell movement, mitosis and meiosis.[33] Microtubule wall is usually assembled from 13 protofilaments in which tubulin dimers are ordered in a head-to-tail fashion. Due to this arrangement, microtubule is polar structure with one end ringed by α-tubulin (minus end) and opposite end ringed by β-tubulin (plus end). While microtubule minus ends associate in cells with microtubule organizing centers (MTOCs), plus ends dynamically switch between stages of growth and shrinkage.[33] Microtubule plus-end tracking proteins (+TIPs) such as end-binding protein 3 (EB3) are linked to plus ends of growing microtubules.[34] Recently, we have predicted using molecular dynamics simulations, that tubulin might be highly sensitive target to nanosecond scale intense electric field.[23]

To visualize the effects of nsPEF on microtubules and other nanoscopic protein structures with sufficient spatial resolution, modern super-resolution microscopy techniques are needed. Acquiring microscopic images while exposing biological samples to nsPEF typically requires planar chip structures that can be placed close to microscope objective. Ideally, they should operate at voltage not too high to prevent electromagnetic interference and damage to microscope electronics. When macroscopic electrodes have been used recently to observe effects of nsPEF on microtubule cytoskeleton using super-resolution microscopy, rather high voltage of >6 kV was required to obtain sufficient field strength (4.4 MV m^{-1}) due to a substantial interelectrode distance.[35] Such high voltage represents potential harm both for the operator and for nearby electronic devices including the microscope. Potentially, miniaturization of nsPEF systems to chips overcomes the issue of high operation voltage and offers also further advantages.

There are several microscope-compatible chip and planar solutions for delivering PEF to biological samples available in the literature.[36–39] However, each of those solutions has at least one of the following limitations preventing them from being super-resolution microscopy-compatible for nsPEF delivery. Some chip structures support PEF containing only a lower band of frequencies (i.e. longer pulses: µs–ms). Other limitation is incapability of low (<200 µm) working distances from the exposed biosamples to microscope objective.[36,37,39] Such short working distance is often necessary for super-resolution imaging.[40] Other solutions have electrode gaps too wide (>150 µm), hence would require very high voltage to achieve sufficient field strength.[38,41]

To alleviate these limitations, we designed, fabricated, and demonstrated, for the first time, the chip for nsPEF delivery to biosamples compatible with super-resolution microscopy. We also developed a platform to integrate the chip to structured illumination super-resolution microscope. We demonstrate the applicability of the chip-platform assembly in evaluation of the nsPEF effects on microtubule dynamics in cells using structured illumination microscopy (SIM), one of the frequently used super-resolution microscopic techniques.

2. Chip-Platform Design and Simulation

We started with the computer design of the whole system to ensure optimal parameters before proceeding to fabrication. The initial requirements for the design were given by a geometrical compatibility of the chip platform with the stage of the DeltaVision OMX microscope, for which the chip platform was designed. Furthermore, since this super-resolution microscope is housed within a light-tight, temperature controlled chamber to increase stability and sensitivity of imaging, access of the chip from a single side only was required. We intended to design the holder which can be fixed to the microscope stage while enabling easy manipulation of the chip. To that end, we created a computer model of a duralumin holder with a spring loaded fixation arm and single push release mechanism of the chip (**Figure 1**A,B). The electromagnetic design with given geometrical constraints posed several engineering challenges.

At first, easy chip removability, yet robust and reproducible electromagnetic connection, had to be ensured for any practical application. To solve this, we decided to split the electric pathway into two parts: i) fixed feeding part with robust end launch connectors to connect the coaxial cables on one side and the Invisipins (conductive rubber pins) to connect feeding part to the chip on opposite side and ii) the removable and potentially disposable chip.

Second, the short working distance (<200 µm) from the nsPEF exposure area on the chip to the microscope objective was required for a high resolution imaging. To comply with this requirement, we decided that the metal pattern will be fabricated on the electromagnetically (low dielectric loss) compatible and optically transparent 1 mm thick quartz glass substrate, yet the objective side of the chip will be complemented by the cover slip with a biological specimen (Figure 1B). Thus, a microfluidic channel was formed by the quartz substrate and the cover slip as the top and the bottom of the channel, with ≈10 µm thick metal pattern creating side walls of the channel.

Third, since we decided to design a two port chip device in order to be able to monitor both reflection and transmission of a signal through the device, both ports needed to be on the same geometrical side of the chip due to geometrical constraints of the microscope setup. To solve this, based on our experience,[42] we decided to base the electromagnetic design of a chip on a coplanar waveguide. We designed a bent 50 Ω coplanar waveguide (Figure 1A,C), which enabled transmission of the nsPEF while exposing the specimen to the electric field.

Fourth, a high electric field strength (>4 MV m^{-1}[35]) with as low voltage applied as possible, was required as explained in the Introduction. We were able to design and optimize a 1 mm long tapered section of the waveguide, where the gap between the central and ground conductor (forming width of the microfluidic channel) had only 33.8 µm (see inset in Figure 1C), enabling accommodation of cells of a smaller diameter, yet achieving ≈3 MV m^{-1} in the gap per 100 V applied between the electrodes. The whole chip platform was carefully designed so that up to 400 V pulse scan could be applied, thus potentially reaching up to 12 MV m^{-1} in the channel. We also performed a full-wave time-domain simulation to ascertain the electric field strength and to visualize spatial distribution of the electric field in the microfluidic channel when nsPEF is applied (Figure 1D).

**ADVANCED
SCIENCE NEWS**
www.advancedsciencenews.com

**ADVANCED
MATERIALS
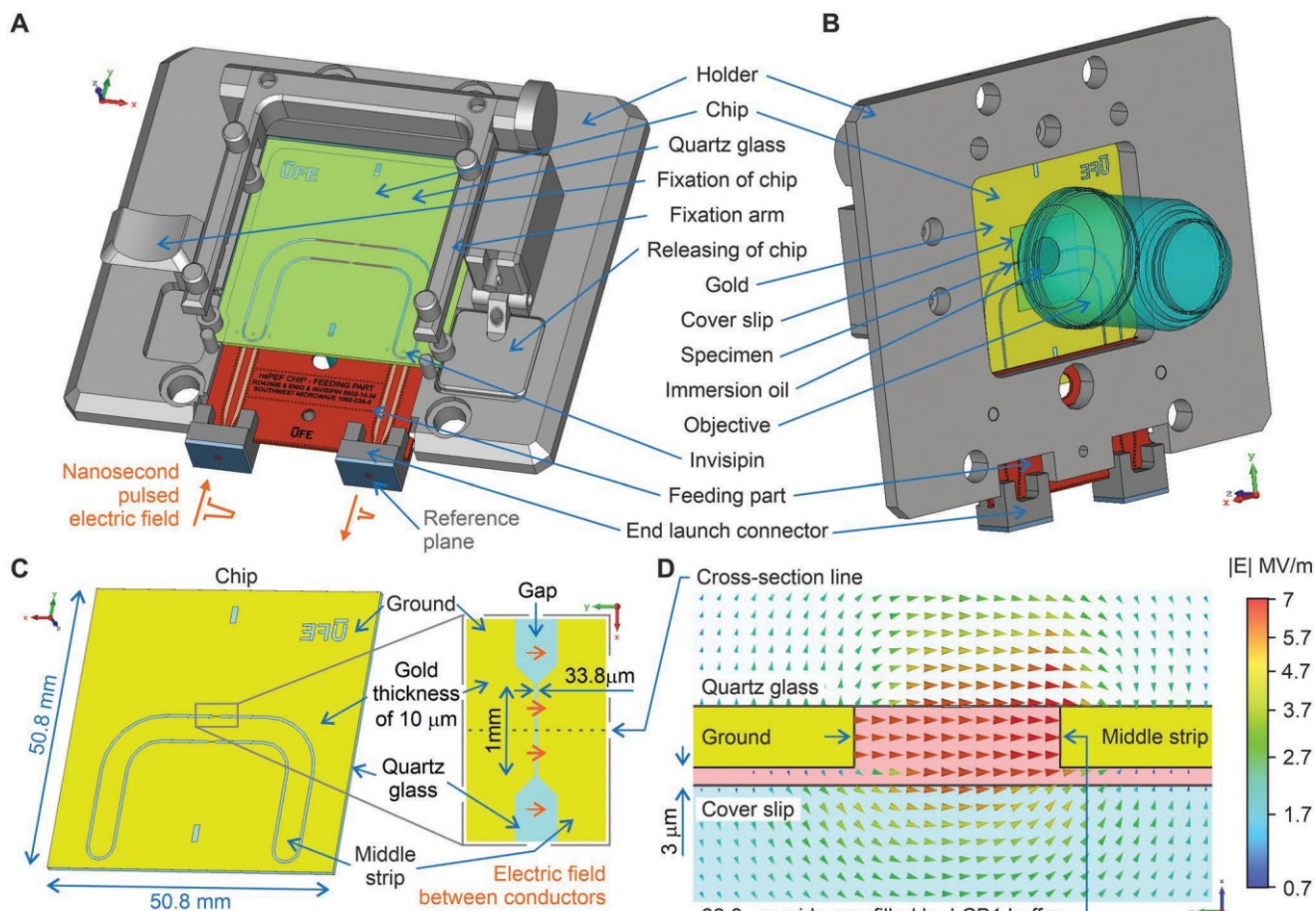TECHNOLOGIES**
www.advmattechnol.de

Figure 1. Computer model of the platform compatible with a DeltaVision OMX super-resolution microscope stage for fixing a chip for delivery of a nanosecond intense electric field into a cell. A) Front view on the chip assembly contains the holder with the fixed chip and the electrical feeding part for the chip. B) The chip assembly with the specimen, the cover glass, and the objective with the immersion oil. C) Coplanar waveguide-based chip on a quartz glass substrate with two gaps, 33.8 μm wide, in the middle of the transmission line. D) Computer simulation time snap of the electric field at the cross-section of the 33.8 μm wide gap with LCB1 buffer between the quartz glass substrate and the coverslip excited by pulse from Figure 2C.

3. Electromagnetic Design and Characterization of the Chip Assembly

As described in the Introduction, nsPEF platforms require careful electromagnetic design. At first, the computational modeling of a chip assembly, composed of the holder, the feeding part, and the chip, with the addition of 5 μL of low conductivity buffer (coded as LCB1) (Figure 1A) was performed in the frequency domain and the transmission and reflection (S-parameters) were analyzed. The same setup was measured by a vector network analyzer and a very good match of the simulated and measured data confirms (**Figure 2**A) that the computational model accurately close to the reality. Reference planes for the analyzed S-parameters are at the end launch connectors on the 2.92 mm connector side (Figure 1A). We see that a very low reflection (<20 dB) is achieved up to 100 MHz, while reasonable reflection (<10 dB) is achieved even up to 1 GHz (Figure 2A). Transmission through the chip is also very good up to 1 GHz, which means that the transmission could be potentially used to monitor the nsPEF, if needed.

Furthermore, we computationally investigated the influence of the presence of the microscope objective and the metal holder on the electromagnetic performance of the chip assembly. This comparison is important in order to assess the sensitivity of the chip to the presence of nearby metal object which might influence the field distribution and affect the nsPEF delivery to the cell sample on the chip. The results are presented in Figure 2B. We see that the influence of the objective and holder is rather small—the reflection is <20 dB up to 100 MHz in all cases. Transmission is similar for all three cases considered even up to 400 MHz.

Figure 2C shows a typical pulse shape as recorded using an oscilloscope in the experiments in the final setup in the microscope and with the LCB1 buffer. We see that the pulse generator operates with a negative polarity. Only small reflections are visible after the pulse, which corresponds to small reflection coefficient presented in Figure 2A,B. Furthermore, the amplitude of reflections is substantially smaller than the variation of the pulse amplitude. Additional confirmation about the chip system capability to deliver the pulse without deformation
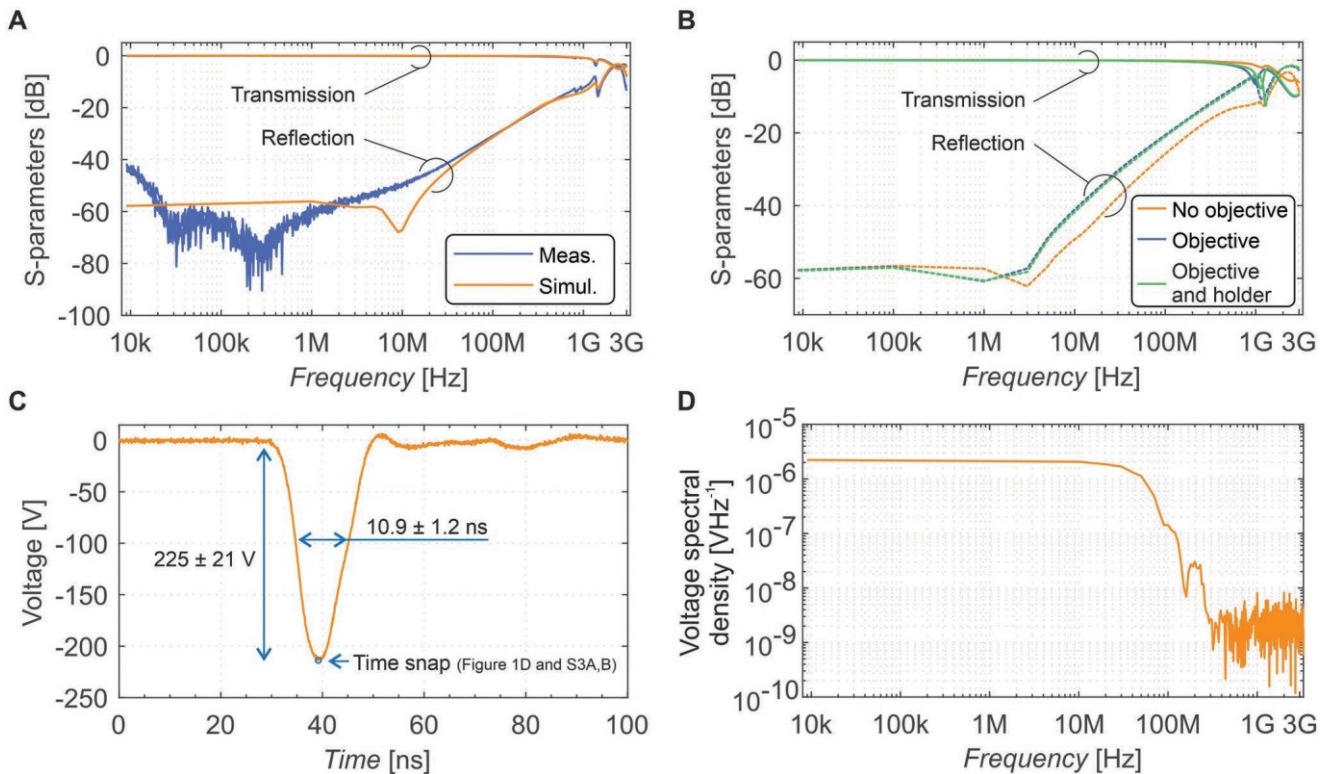
ADVANCED
SCIENCE NEWS
www.advancedsciencenews.com

ADVANCED
MATERIALS
TECHNOLOGIES
www.advmattechnol.de

Figure 2. Electromagnetic characterization of the chip assembly. A) Comparison of S-parameters measurement and simulation of the chip assembly (the holder, the feeding part, and the chip) with 5 μL of LCB1 buffer and a cover glass. B) Comparison of simulated S-parameters of i) chip and feeding part (orange color), ii) chip, feeding part, and objective with immersion oil (blue color), and iii) chip, feeding part, objective with immersion oil, and holder (green color). Models (i)–(iii) contain 5 μL of LCB1 buffer and a cover glass. C) Typical pulse shape used during experiments, mean value of the pulse width and pulse amplitude together with corresponding standard deviations are from $N = 4000$ pulses. D) Voltage spectral density of the pulse in (C).

comes from the analysis of the spectral content of the pulse. Figure 2D displays spectrum of the pulse from Figure 2C. We see that most of the frequency content of the pulse is within 100 MHz bandwidth - the frequency band where the chip assembly has very small reflections (<20 dB, Figure 2A).

4. Experimental nsPEF Setup Based on the Fabricated Chip Platform

After the electromagnetic characterization and testing of the chip assembly approved a very good performance, the whole experimental nsPEF setup was assembled. **Figure 3**A details the fabricated chip with an inset showing the 33.8 μm gap for the cell exposure. The electrical feeding part was fabricated using standard printed circuit board technology (Figure 3B). On the outer side, the feeding part contains end launch connectors to transfer the signals from coaxial cable. On the chip side, the feeding part contains conductive polymer pins, which enable reliable electromagnetic connection of the coplanar waveguide transmission line from the feeding part to the chip. In order to repeatedly and conveniently fix the chip and its electromagnetic connections at the super-resolution microscope stage, we designed and fabricated the holder (Figure 3C). The holder fits the microscope stage (Figure 3D) and provides also appropriate optical alignment of the chip and the objective within

<200 μm working distance, while enabling the free movement of the objective relative to the chip (Figure 3E,F). The scheme of the whole experimental nsPEF setup is depicted in Figure 3G. The nsPEF signal produced using the pulse generator is launched via coaxial cable. The pick-off tee is inserted to the transmission path to couple ≈−39.5 dB of the pulse voltage to the oscilloscope to monitor the pulse shape. The pulse further propagates to the chip platform on the microscope. The length of the cables was deliberately chosen to be 4 m long in order to clearly distinguish reflected pulse, if any, without pulse-overlap. The pulse propagates through the chip creating electric field in the exposure gap (microfluidic channel). The pulse leaves the chip and it is absorbed by 50 Ω load to prevent any reflection of the pulse back to the chip.

5. On-Chip Super-Resolution Imaging of the Microtubule Cytoskeleton

To demonstrate the function of the chip, we applied fluorescence microscopy both in standard widefield (**Figure 4**) and SIM (**Figure 5**) regime. As expected, SIM regime provided better resolution than widefield one.

Interestingly, time-lapse imaging 5 min after application of nsPEF revealed substantial changes on plus ends of microtubules, detectable both in widefield and SIM regime.
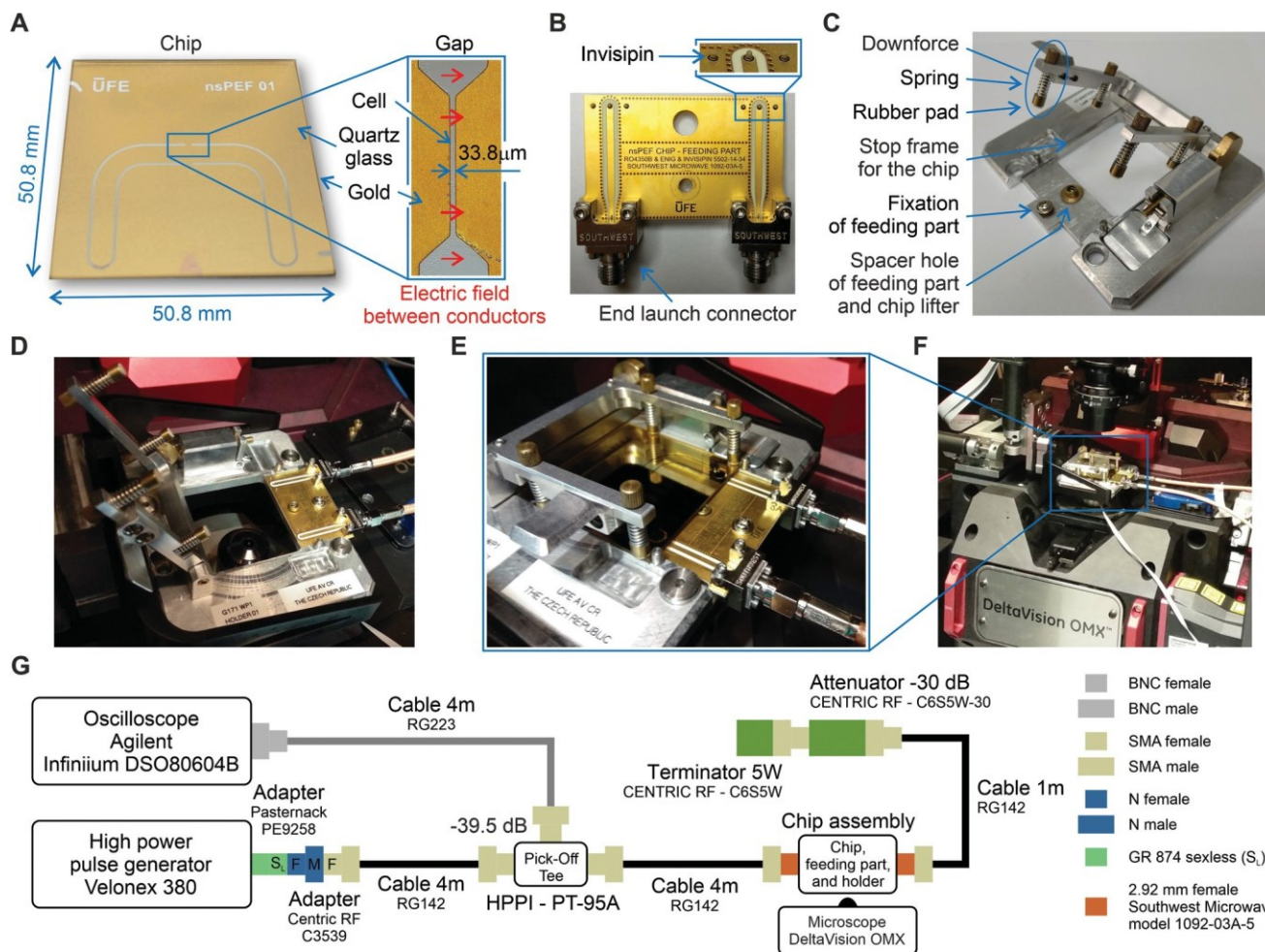
ADVANCED
SCIENCE NEWS

www.advancedsciencenews.com

ADVANCED
MATERIALS
TECHNOLOGIES

www.advmattechnol.de

Figure 3. Experimental nsPEF setup based on the fabricated chip platform. A) Fabricated chip with a close-up on the 33.8 µm wide gap. B) Feeding part for the chip with a close-up on the electrical connection between the chip and the feeding part. C) Holder of the feeding part and the chip. D) The open chip holder and feeding part for the chip. E) The closed holder with the chip inserted. F) The whole setup is fully compatible with the SIM microscope stage DeltaVision OMX which is the super-resolution microscopy technique enabling the enhanced imaging of nanoscopic cell features such as microtubules morphology and dynamics. G) Electrical scheme of the experimental nsPEF setup.

Substantially lower intensity of EB3-mNeonGreen signal was detected in nsPEF-treated cells and the size of the stabilizing cap was decreased. Two experiments, each with five evaluated cells, were performed to confirm the results. It was originally proposed that microtubule stability increases with growth speed as a consequence of longer protective caps.[43,44] More recently it was experimentally demonstrated that faster growing microtubules have longer EB caps and are more stable.[45] Thus our data indicate that nsPEF affect microtubule growth. These findings provide a basis for further detailed studies on the effects of nsPEF on parameters of microtubule dynamics in RBL-2H3 cells. To that end, one can use analysis of time-lapse movies with plusTipTracker software[46] as we demonstrated previously on drug-treated human osteosarcoma cells.[47,48] Interestingly, nsPEF affected staining intensity and size of the stabilizing caps both in cell regions laying between edges of electrodes and outside of these regions. This finding suggests that the nsPEF effects are propagated into the whole cytosol, if the effect was triggered by the field between the

electrodes. Important open question is the effect of nsPEF on microtubule nucleation that can be followed by counting of EB3 comets newly emanating from centrosomes.[49] As density of microtubules in centrosomal region is high, application of the SIM could improve evaluation of time-lapse movies. Nucleation from centrosomes is dependent on the amount of centrosomal gamma-tubulin, and it was repeatedly documented that some cancer cell types have substantially enhanced gamma-tubulin level.[50–52] Potential modulation of micro-tubule nucleation by nsPEF in cancer cells could thus open new therapeutic strategies.

In case of current experiments, we experimentally changed the parameters to observe the obvious cellular effects in order to demonstrate the function of the chip without aiming for detailed parametric analysis of biological effects. When the number of pulses was lower than 4000 pulses, no visible effect was observed on used cells. For future work, various parameters can be explored and utilized in the nsPEF technology. One can vary not only electric field strength, pulse duration,
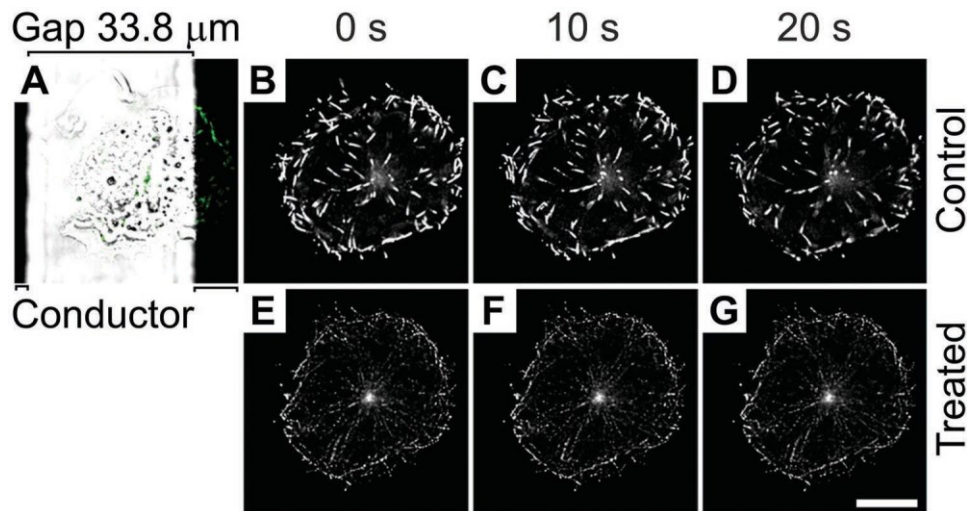
**ADVANCED
SCIENCE NEWS**
www.advancedsciencenews.com

**ADVANCED
MATERIALS
TECHNOLOGIES**
www.advmattechnol.de

Figure 4. Cell expressing EB3-mNeonGreen examined on DeltaVision OMX microscope in the widefield regime. Cell was first imaged for 60 s before nsPEF treatment (control), and time-lapse imaging continued 5 min after nsPEF delivery (treated). A) Cell position between electrodes. Merged image from fluorescence and bright-field channels. Black lines under image depict position of conductor. B–D) Cell before treatment. E–G) Cell after nsPEF treatment (4000 pulses as in Figure 2C with 100 Hz firing rate). 0, 10, and 20 s denote still images from the time-lapse. Images in control and treated cell were collected and processed in exactly the same manner. Bar for (A)–(G): 10 μm. Staining intensities and sizes of the stabilizing microtubule caps were substantially attenuated in the treated cells.

pulse polarity but also the firing frequency and number of pulses. Moreover, one can even generate complex sequences of pulses with various parameters. Our primary focus in this work is on the development, testing, and detailed description of the chip technology, but we briefly discuss potential effects

of various nsPEF parameters on cells and microtubules. At first, one needs to expect that the nsPEF cellular effects will be likely strongly cell type[53] and medium[54] dependent. Carr et al.[35] demonstrated that microtubules in cells are perturbed in a manner independent of calcium signaling. They found
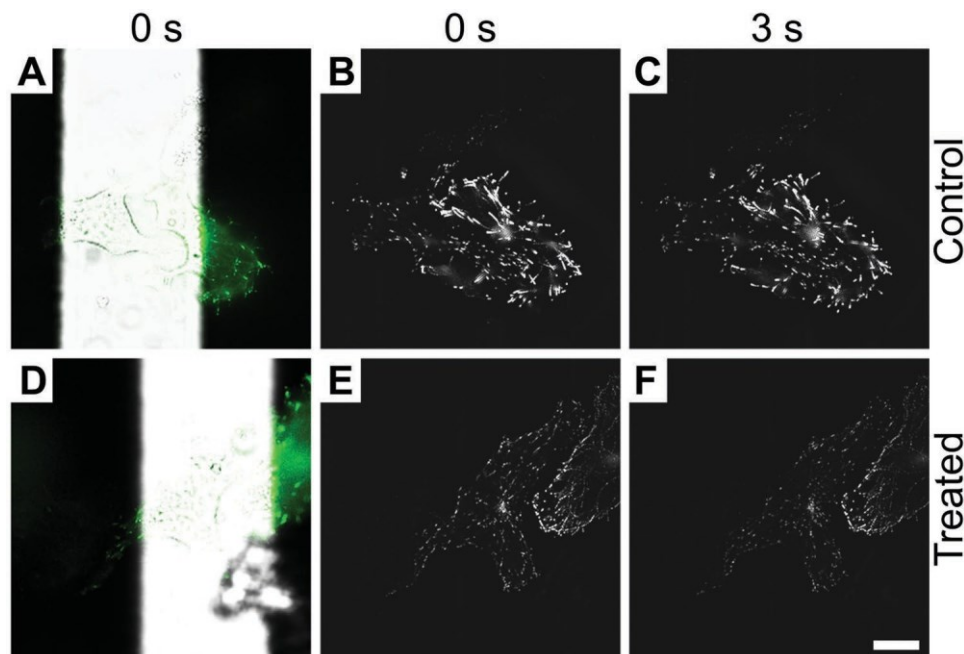

Figure 5. Cells expressing EB3-mNeonGreen examined on DeltaVision OMX microscope in the SIM regime. A–C) Untreated (control) cells. D–F) nsPEF-treated cells (treated; 4000 pulses as in Figure 2C with 100 Hz firing rate). Time-lapse imaging started 5 min after nsPEF delivery. A,D) Position of cells between electrodes. Merged image from fluorescence and bright-field channels. 0 and 3 s denote still images from the time-lapse. Images in control and treated cell were collected and processed in exactly the same manner. Bar for (A)–(F): 10 μm. Staining intensities and sizes of the stabilizing microtubule caps were substantially attenuated in treated cells.

that 100 pulses, 10 ns long, fired at 10 Hz frequency did have observable effect on the tubulin-red fluorescent protein (RFP) and EB3-green fluorescent protein (GFP) fluorescence in U87 cells. In her doctoral thesis,[55] Carr also showed in Figure 50, that increasing pulse number from 100 to 500 and 1000 showed a different qualitative response. While for 100 pulses, only EB3 comet lengthening was observed, for 500 and 1,000 the effects on microtubule nucleation were observed, but they were calcium dependent. In our recent work on nsPEF treatment of tubulin in vitro, we showed that the higher the pulse number, the lower the polymerization of tubulin into microtubules.[56]

For assessing the biophysical mechanisms of nsPEF action on cells, the accurate electric field microdosimetry is crucial. One can imagine further fine-tuning of the biological experiment or selecting smaller cells so that the cell is located only in the gap between the electrodes. However, the mere presence of the cell will locally perturb the field much more substantially (orders of magnitude),[57,58] than the field inhomogeneity due to imperfect electrode geometry or the cell placement. In the further biophysical and biological studies, whenever the exact geometry of the electrodes is available, as in the current work, as well as internal 3D cell structure (can be obtained by confocal microscope), much more accurate field distribution can be obtained.

6. Conclusion

We have developed nsPEF chip technology which has several technological advantages/features, when compared to macroscopic electrodes systems and current chip systems. The microfabrication employed for our chip enables well defined electrode geometry hence accurate field distribution as well as rather low applied voltage yet high field strength in the area of the biological specimen. Our chip system allows for very short working distance to objective enabling high numerical aperture imaging which is necessary for super-resolution and other advanced microscopy techniques. In short, it is for the first time the chip is developed for nsPEF employing super-resolution microscopy monitoring. The chip capability was demonstrated by using it for affecting the structure of cellular skeleton. We believe that this technology will open new avenues for exploration of the nsPEF for modulating the function of active biomaterials at the nanoscale level.

7. Experimental Section

Simulation Details: The chip assembly (the holder, the feeding part, and the chip) with 5 μL of LCB1 buffer covered by a cover glass was used for the simulation of S-parameters with frequency solver of CST MWS (Computer Simulation Technology Microwave Studio, Dassault Systèmes, France) in the frequency range from 9 kHz to 3 GHz and compared with measured data in Figure 2A. The feeding part was based on the conductor backed coplanar waveguide with the RO4350B substrate and chemical gold as a conductor. Connections between coaxial cables and conductor backed coplanar waveguide were realized by end launch connector (1092-03A-5, Southwest Microwave, USA) and the reference planes were on the end launch connectors (Figure 1A). Connection between feeding part and the chip was realized by conductive rubber Invisipin (5502-14-0034, $\sigma = 20\,000$ S m^{-1}, R&D Interconnect Solutions).

The influence of objective was also studied with immersion oil and objective with immersion oil and holder on the S-parameters with the help of frequency solver of CST MWS (Figure 2B). The electric field strength in the cross-section of the 33.8 μm wide gap excited by the pulse from Figure 2C was simulated in transient solver of CST MW and the time snap of electric field in the maximum of the pulse is highlighted by circle in Figure 1D. The presence or absence of the interstitial layer of the LCB1 buffer between the cover glass was also studied with cells and the electrodes. Figure S3A,B in the Supporting Information shows the electric field distribution without and with the interstitial layer, respectively, obtained from the simulation. Figure S3C shows the simulated transmission and reflection through the whole chip assembly. It can be seen that the influence of the interstitial layer on both the field distribution and S-parameters was minor.

Electromagnetic Measurement and Characterization of the Chip Assembly: The fabricated chip assembly with 5 μL of LCB1 buffer and coverslip on it was measured three times (three different application of LCB1 buffer) by a vector network analyzer (ZNB8, Rohde & Schwarz, Germany) in the frequency band from 9 kHz to 3 GHz and the averaged S-parameters are in Figure 2A. The connection between the end launch connector and vector network analyzer was done by VNA Ruggedized Test Cable N Male to N Male 18 GHz (PE3VNA1803, Pasternack, USA) to adapter (C7804, CentricRF, USA) N(f)-3.5(m) to end launch connector. The calibration technique UOSM with the calibration kit (R&S ZV-Z135(f), Rohde & Schwarz, Germany) was used to calibrate the vector network analyzer and move the reference planes to the end launch connectors (Figure 1A).

nsPEF Exposure System: The scheme in Figure 3G summarises the whole setup of nsPEF exposure system. The exposure system included the pulse generator (high power pulse generator VELONEX 380, Delta Electronics, Inc., USA) triggered by function generator (BK Precision 4053B-10 MHz, USA), and the recording was done using an oscilloscope (Agilent Infiniium DSO80604B, 6 GHz 40 GSa, Keysight Technologies, USA). The scheme (Figure 3G) shows different connectors, cables, and adapters used for the pulse application and recording in details. For all biological experiments shown in this article (Figures 4 and 5), 4 000 pulses were used with firing rate of 100 Hz. The shape of the pulse is shown in Figure 2C where the pulse amplitude and pulse width were fixed, 225 V and 11 ns, respectively. Prior to the selection of these parameters, a parametric study was done on different cell lines (results not shown).

Chip Fabrication: For chip fabrication, standard laser lithography manufacturing process was used. As the substrate of proposed nsPEF chip, a quartz glass (Technical Glass Products, Inc., USA) was used with dimensions of 50.8 × 50.8 × 1 mm^3. The slide was thoroughly cleaned as follows. First, the slide was blown aggressively with N$_2$, then the slide was put in piranha solution with 3:1 (H$_2$SO$_4$:H$_2$O$_2$) concentration for 10 min, and then rinsed by a mixture of acetone and ethanol (1:1 ratio). Second, the slide was sonicated for 30 min (37 kHz, 100% power, temperature control set to off, Elma-Elmasonic P, Germany) in mixture of acetone:ethanol:Q-water in the ratio of 1:1:1 and then rinsed with a sufficient amount of Q-water (Direct-Q3 UV with Pump ZRQSVP030, $\sigma = 0.05$ μS cm^{-1} @ 22 °C, Millipore), acetone, and isopropyl alcohol, and dried with N$_2$. Finally, just before the spin-coating process, the slide was additionally cleaned by using ozone cleaner (UVO-Cleaner Model 30, Jelight Company, Inc., USA) for 10 min, then rinsed with Q-water, acetone, and isopropyl alcohol, and dried with N$_2$. Then plasma cleaner (Nano, Diener electronic, Germany) was used for 4 min and dehydration bake at 200 °C for 30 min, to achieve good adhesion of the photoresist. The negative photoresist (SU-8 3050 Permanent Epoxy negative Photoresist, Microchem Corp., Japan) was then spin-coated on the slide for 60 s with 3000 rpm and then was let to stabilize for 10 min to release the photoresist tension and edge bead. Due to the height of the photoresist, soft-bake treatment was unusually long to prevent thermal shocks and to prevent crack formation (10 min at 40 °C and 5 min at 65 °C, and was then allowed to cool to room temperature in ≈2 h). The pattern was transferred by maskless direct optical lithograph (MicroWriter ML 2, Quantum 76 Design Inc., USA) with exposure dose 286 mJ cm^{-2} at 375 nm. After exposure, the postbake procedure was 65 °C for 30 min followed by

1.5 h cooling to room temperature. Pattern was developed by bathing in mr-DEV 600 (micro resist technology GmbH, Germany) for 6 min and then gently rinsed by isopropyl alcohol and dried with N_2. Just before the metalization, 1 min of plasma cleaning was used. The chip metallization after lithography process consisted of 20 nm layer of evaporated chrome as an adhesion layer with 370 nm gold on a top, and the evaporation was done by high vacuum laboratory system PLS 570 (Pfeiffer Vacuum, Germany). The lift-off process was done in a piranha solution with 4:1 (H_2SO_4:H_2O_2) concentration for 50 min and then rinsed with a sufficient amount of Q-water, acetone, isopropyl alcohol, and dried with N_2. To sustain the high voltage and cover the thickness of cells, the electrodes of 370 nm height should be extended up to several micrometers. To fulfill this need, electrochemical growth of gold (electroplating) was used. Briefly, prior electroplating, the chip was cleaned to increase its surface hydrophilicity by ozone cleaner for 10 min and by plasma cleaner for 4 min. The chip was immersed in the gold solution and heated up to 29 °C. The electroplating parameters were: 3.2 V and 12 mA for a duration of 7 h and then 3.2 V and 24 mA for a duration of 4 h (SPA gold electroplating kit, UK). The surface of the electrodes (Figure S1, Supporting Information) as well as the dimensions (Figure S2, Supporting Information) were checked at the end of the fabrication.

Cells and Fluorescence Microscopy: Rat basophilic cell line RBL-2H3 (American Tissue Culture collection, Cat. No. CRL-2256) stably expressing EB3-mNeonGreen (Allele Biotechnology) for visualization of microtubule plus ends (manuscript in preparation) were cultured in DMEM medium, supplemented with 100 U mL^{-1} penicillin, 100 μg mL^{-1} streptomycin, and 10% fetal calf serum. The cells were grown at 37 °C in 5% CO_2 in air and passaged every 2–3 days. For time-lapse imaging, cells were grown to confluence on high-performance cover glasses (18 × 18 mm^2, thickness no. 1 1/2, ZEISS). Cells were imaged on DeltaVision OMX microscope equipped with the Blaze SIM module with oil 60×/NA 1.42 PlanApo N objective using either widefield (The InsightSSI illumination) or SIM mode (488 nm laser). Time-lapse images were acquired every 1 s for 1 min total. Images were deconvoluted with Huygens Professional version 19.04 (Scientific Volume Imaging, The Netherlands, http://svi.nl). Prior to imaging, cells with 20% of density attached on cover glasses as described before were carefully washed with low conductivity buffer (LCB1: 10^{-2} m HEPES, 7×10^{-4} m MgCl$_2$, 3×10^{-4} m CaCl$_2$, 0.25 m sucrose),[54] and the excess of buffer was drained with tissue. After quick preparations, cells on a cover glass were placed on 10 μL drop of LCB1 buffer on the chip. Once the cover glass was placed on the chip, the chip was dried with the tissue to remove excess buffer so that most of the buffer is in the gap. Then, the chip assembly with cells was ready for subsequent experiments.

Supporting Information

Supporting Information is available from the Wiley Online Library or from the author.

Conflict of Interest

The authors declare no conflict of interest.

Author Contributions

D.H., D.E.C., and O.K. contributed equally to this work. Contribution roles according to CRediT: https://www.casrai.org/credit.html. D.H.: Conceptualization (lead—design of whole experimental nsPEF setup and its electrical characterization, simulations), data curation (equal), formal analysis (equal—nsPEF technology), investigation (lead), methodology (design of whole experimental nsPEF setup), visualization (lead), validation, writing—original draft (supporting), writing—review and editing supporting. O.K.: Conceptualization (lead—chip fabrication), methodology (lead—chip fabrication), investigation (supporting), writing—original draft (supporting). D.E.C.: Conceptualization (supporting—chip fabrication), formal analysis (equal—nsPEF technology), data curation (equal), methodology (lead—biological application), investigation (lead—biological application), validation, writing—original draft (supporting), writing—review and editing. A.K.: Investigation (supporting—biological application), visualization (supporting—biological application). F.V.: Investigation (supporting—biological application). L.K.: Funding acquisition, project administration, resources (supporting), writing—review and editing (supporting). P.D.: Funding acquisition, methodology (supporting), project administration, resources (supporting), writing—original draft (supporting), writing—review and editing (supporting). M.C.: Conceptualization, data curation (equal), formal analysis (supporting), funding acquisition, investigation (supporting), project administration, resources (lead), supervision, validation, writing—original draft (lead), writing—review and editing (lead). Marek Chvostek: Methodology (supporting—holder design and fabrication).

[1] M. Golzio, M.-P. Rols, in *Handbook of Electroporation* (Ed: D. Miklavčič), Springer International Publishing, Cham, Switzerland **2017**, pp. 323–336.

[2] G. Serša, M. Bosnjak, M. čemažar, R. Heller, in *Handbook of Electroporation* (Ed: D. Miklavčič), Springer International Publishing, Cham, Switzerland **2017**, pp. 1511–1525.

[3] V. Todorovic, M. Cemazar, in *Handbook of Electroporation* (Ed: D. Miklavčič), Springer International Publishing, Cham, Switzerland **2016**, pp. 1717–1731.

[4] J. Gehl, G. Serša, in *Handbook of Electroporation* (Ed: D. Miklavčič), Springer International Publishing, Cham, Switzerland **2017**, pp. 1771–1786.

[5] A. A. Bulysheva, R. Heller, in *Handbook of Electroporation* (Ed: D. Miklavčič), Springer International Publishing, Cham, Switzerland **2017**, pp. 1665–1677.

[6] S. A. Shirley, in *Handbook of Electroporation* (Ed: D. Miklavčič), Springer International Publishing, Cham, Switzerland **2017**, pp. 1755–1768.

[7] L. Liu, M. P. Morrow, M. Bagarazzi, in *Handbook of Electroporation* (Ed: D. Miklavčič), Springer International Publishing, Cham, Switzerland **2017**, pp. 1933–1952.

[8] C. Rosazza, S. Haberl Meglic, A. Zumbusch, M.-P. Rols, D. Miklavcic, *Curr. Gene Ther.* **2016**, *16*, 98.

[9] S. Bhonsle, R. E. Neal, R. V. Davalos, in *Handbook of Electroporation* (Ed: D. Miklavčič), Springer International Publishing, Cham, Switzerland **2016**, pp. 1527–1542.

[10] A. Patras, P. Choudhary, A. Rawson, in *Handbook of Electroporation* (Ed: D. Miklavčič), Springer International Publishing, Cham, Switzerland **2017**, pp. 2517–2537.

**ADVANCED
SCIENCE NEWS**
www.advancedsciencenews.com

**ADVANCED
MATERIALS
TECHNOLOGIES**
www.advmattechnol.de

[11] J. R. Sarkis, N. Boussetta, E. Vorobiev, in *Handbook of Electroporation* (Ed: D. Miklavčič), Springer International Publishing, Cham, Switzerland **2017**, pp. 2699–2712.

[12] E. Vorobiev, N. Lebovka, in *Handbook of Electroporation* (Ed: D. Miklavčič), Springer International Publishing, Cham, Switzerland **2017**, pp. 2899–2922.

[13] W. Sitzmann, E. Vorobiev, N. Lebovka, in *Handbook of Electroporation* (Ed: D. Miklavčič), Springer International Publishing, Cham, Switzerland **2017**, pp. 2335–2354.

[14] F. Schottroff, A. Krottenthaler, H. Jäger, in *Handbook of Electroporation* (Ed: D. Miklavčič), Springer International Publishing, Cham, Switzerland **2017**, pp. 2539–2557.

[15] W. Zhao, R. Yang, in *Handbook of Electroporation* (Ed: D. Miklavčič), Springer International Publishing, Cham, Switzerland **2017**, pp. 2239–2251.

[16] E. S. Silva, S. Roohinejad, M. Koubaa, F. J. Barba, A. R. Jambrak, T. Vukušić, M. D. Santos, R. P. Queirós, J. A. Saraiva, in *Handbook of Electroporation* (Ed: D. Miklavčič), Springer International Publishing, Cham, Switzerland **2017**, pp. 2115–2133.

[17] T. Kotnik, W. Frey, M. Sack, S. Haberl Meglič, M. Peterka, D. Miklavčič, *Trends Biotechnol.* **2015**, *33*, 480.

[18] S. J. Beebe, in *Handbook of Electroporation* (Ed: D. Miklavčič), Springer International Publishing, Cham, Switzerland **2017**, pp. 1543–1562.

[19] L. Chopinet, M.-P. Rols, *Bioelectrochemistry* **2015**, *103*, 2.

[20] A. Silve, R. Vezinet, L. M. Mir, *IEEE Trans. Instrum. Meas.* **2012**, *61*, 1945.

[21] T. Batista Napotnik, M. Reberšek, P. T. Vernier, B. Mali, D. Miklavčič, *Bioelectrochemistry* **2016**, *110*, 1.

[22] S. Kohler, P. Jarrige, N. Ticaud, R. P. O'Connor, L. Duvillaret, G. Gaborit, D. Arnaud-Cormos, P. Leveque, *IEEE Microwave Wireless Compon. Lett.* **2012**, *22*, 153.

[23] P. Marracino, D. Havelka, J. Průša, M. Liberti, J. Tuszynski, A. T. Ayoub, F. Apollonio, M. Cifra, *Sci. Rep.* **2019**, *9*, 10477.

[24] J. F. Kolb, in *Advanced Electroporation Techniques in Biology and Medicine* (Ed: D. Miklavčič), Springer International Publishing, Cham, Switzerland **2010**, pp. 341–352.

[25] T. Kotnik, P. Kramar, G. Pucihar, D. Miklavcic, M. Tarek, *IEEE Electr. Insul. Mag.* **2012**, *28*, 14.

[26] S. Haberl, D. Miklavcic, G. Sersa, W. Frey, B. Rubinsky, *IEEE Electr. Insul. Mag.* **2013**, *29*, 29.

[27] E. B. Sözer, P. T. Vernier, in *Handbook of Electroporation* (Ed: D. Miklavčič), Springer International Publishing, Cham, Switzerland **2017**, 18, https://doi.org/10.1007/978-3-319-26779-1_115-2.

[28] S. J. Beebe, *Bioelectrochemistry* **2015**, *103*, 52.

[29] D. R. Hekstra, K. I. White, M. A. Socolich, R. W. Henning, V. Šrajer, R. Ranganathan, *Nature* **2016**, *540*, 400.

[30] P. Marracino, F. Apollonio, M. Liberti, G. d'Inzeo, A. Amadei, *J. Phys. Chem. B* **2013**, *117*, 2273.

[31] N. J. English, D. A. Mooney, *J. Chem. Phys.* **2007**, *126*, 091105.

[32] N. J. English, C. J. Waldron, *Phys. Chem. Chem. Phys.* **2015**, *17*, 12407.

[33] E. Nogales, G. Alushin, in *Comprehensive Biophysics* (Ed: E. H. Egelman), Elsevier, Amsterdam **2012**, pp. 72–92.

[34] P. Dráber, E. Dráberová, in *Cytoskeleton and Human Disease* (Ed: M. Kavallaris), Humana Press, Totowa, NJ **2012**, pp. 29–53.

[35] L. Carr, S. M. Bardet, R. C. Burke, D. Arnaud-Cormos, P. Leveque, R. P. O'Connor, *Sci. Rep.* **2017**, *7*, 41267.

[36] C. Dalmay, J. Villemejane, V. Joubert, A. Silve, D. Arnaud-Cormos, O. Français, L. M. Mir, P. Leveque, B. Le Pioufle, *Biosens. Bioelectron.* **2011**, *26*, 4649.

[37] C. Dalmay, M. A. De Menorval, O. Français, L. M. Mir, B. Le Pioufle, *Lab Chip* **2012**, *12*, 4709.

[38] C. Dalmay, J. Villemejane, V. Joubert, O. Français, L. M. Mir, B. Le Pioufle, *Sens. Actuators, B* **2011**, *160*, 1573.

[39] M. Casciola, M. Liberti, A. Denzi, A. Paffi, C. Merla, F. Apollonio, *Integration* **2017**, *58*, 446.

[40] U. Birk, J. v. Hase, C. Cremer, *Sci. Rep.* **2017**, *7*, 3685.

[41] C. Merla, M. Liberti, P. Marracino, A. Muscat, A. Azan, F. Apollonio, L. M. Mir, *Sci. Rep.* **2018**, *8*, 5044.

[42] D. Havelka, O. Krivosudsky, J. Prusa, M. Cifra, *Sens. Actuators, B* **2018**, *273C*, 62.

[43] M. F. Carlier, T. L. Hill, Y. Chen, *Proc. Natl. Acad. Sci. USA* **1984**, *81*, 771.

[44] T. Mitchison, M. Kirschner, *Nature* **1984**, *312*, 237.

[45] C. Duellberg, N. I. Cade, D. Holmes, T. Surrey, *eLife* **2016**, *5*, e13470.

[46] A. Matov, K. Applegate, P. Kumar, C. Thoma, W. Krek, G. Danuser, T. Wittmann, *Nat. Methods* **2010**, *7*, 761.

[47] P. E. Ghaly, C. D. Churchill, R. M. Abou El-Magd, Z. Hájková, P. Dráber, F. West, J. A. Tuszynski, *Can. J. Chem.* **2017**, *95*, 649.

[48] M. Jurášek, M. Černohorská, J. Řehulka, V. Spiwok, T. Sulimenko, E. Dráberová, M. Darmostuk, S. Gurská, I. Frydrych, R. Buriánová, T. Ruml, M. Hajdúch, P. Bartůněk, P. Dráber, P. Džubák, P. B. Drašar, D. Sedlák, *J. Steroid Biochem. Mol. Biol.* **2018**, *183*, 68.

[49] M. Černohorská, V. Sulimenko, Z. Hájková, T. Sulimenko, V. Sládková, S. Vinopal, E. Dráberová, P. Dráber, *Biochim. Biophys. Acta, Mol. Cell Res.* **2016**, *1863*, 1282.

[50] C. D. Katsetos, E. Dráberová, A. Legido, C. Dumontet, P. Dráber, *J. Cell. Physiol.* **2009**, *221*, 505.

[51] Y. Niu, T. Liu, G. M. K. Tse, B. Sun, R. Niu, H.-m. Li, H. Wang, Y. Yang, X. Ye, Y. Wang, Q. Yu, F. Zhang, *Cancer Sci.* **2009**, *100*, 580.

[52] V. Caracciolo, L. D'agostino, E. Dráberová, V. Sládková, C. Crozier-Fitzgerald, D. P. Agamanolis, J.-P. de Chadarévian, A. Legido, A. Giordano, P. Dráber, C. D. Katsetos, *J. Cell. Physiol.* **2010**, *223*, 519.

[53] B. L. Ibey, C. C. Roth, A. G. Pakhomov, J. A. Bernhard, G. J. Wilmink, O. N. Pakhomova, *PLoS One* **2011**, *6*, e15642.

[54] D. E. Chafai, I. Nemogová, P. Dráber, M. Cifra, *Int. J. Bioelectromagn.* **2018**, *20*, 36.

[55] L. Carr, *Ph.D. Thesis*, Université de Limoges **2016**.

[56] D. E. Chafai, V. Sulimenko, D. Havelka, L. Kubínová, P. Dráber, M. Cifra, *Adv. Mater.* **2019**, *31*, 1903636.

[57] A. Denzi, F. Camera, C. Merla, B. Benassi, C. Consales, A. Paffi, F. Apollonio, M. Liberti, *J. Membr. Biol.* **2016**, *249*, 691.

[58] A. De Angelis, A. Denzi, C. Merla, F. Andre, T. Garcia-Sanchez, L. M. Mir, F. Apollonio, M. Liberti, in *Abstract Collection of the Joint Annual Meeting of the Bioelectromagnetics Society and the European BioElectromagnetics Association 2019* **2019**, pp. 223–227.

ADVANCED MATERIALS TECHNOLOGIES

Supporting Information

Nanosecond Pulsed Electric Field Lab-on-Chip Integrated in Super-Resolution Microscope for Cytoskeleton Imaging

Daniel Havelka, Djamel Eddine Chafai, Ondrej Krivosudský, Anastasiya Klebanovych, František Vostárek, Lucie Kubínová, Pavel Dráber, and Michal Cifra*

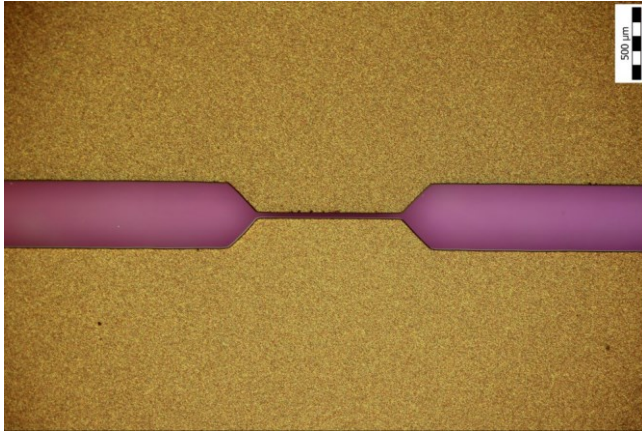# Supplementary data: Figures S1 and S2

Figure S1: Optical reflection microscopy (BX51 with Nomarski Differential Interference Contrast, Olympus, Japan) image, detail of the 1 mm long and 33.8 µm wide gap between the electrodes.
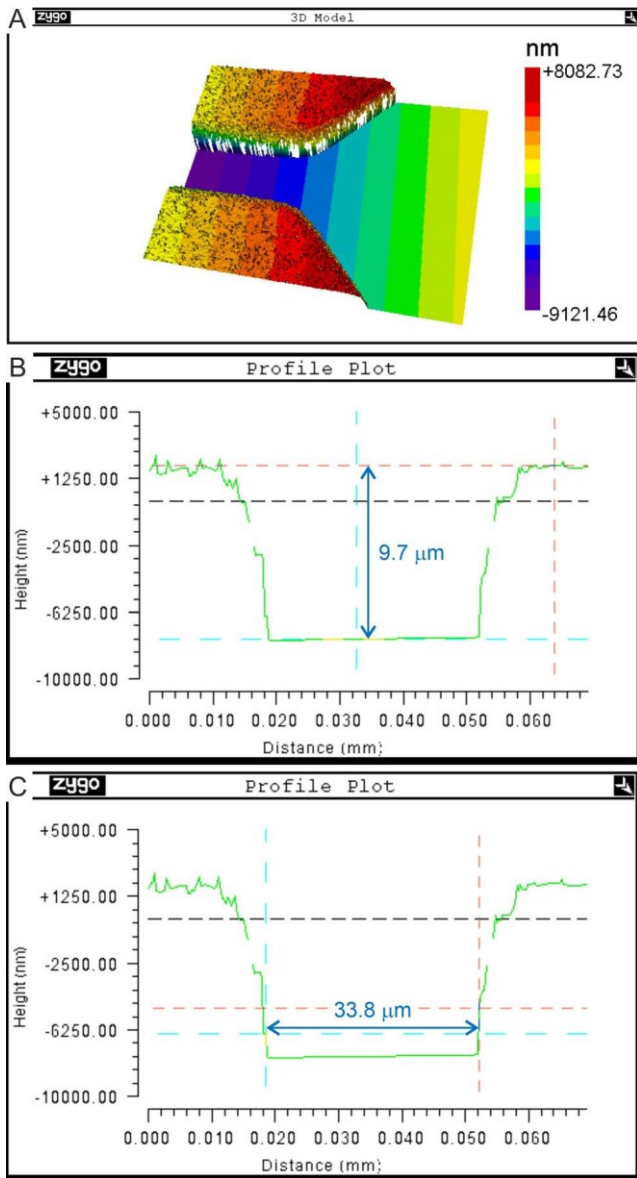
Figure S2: Measurement of the electrode gap height and width by ZYGO NewView 7300 Optical Surface Profiler. A) 3D view on taper into 33.8 μm wide gap. B) The height of the gap forming microfluidic channel. C) The width of the gap forming microfluidic channel.
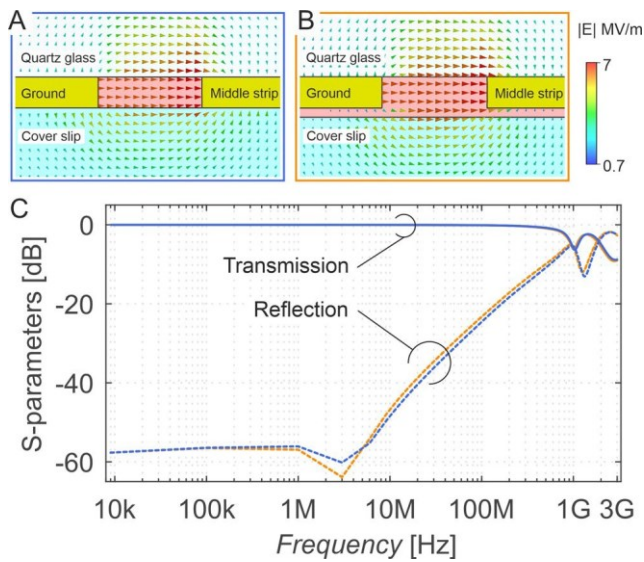
Figure S3: Computer simulation-time snap (Figure 2C) of the electric field at the cross-section of the 33.8 µm wide gap with LCB1 buffer between the quartz glass substrate and the coverslip excited by pulse from the Figure 2C. A) Without the interstitial layer of LCB1 buffer. B) With the interstitial layer of LCB1 buffer. (The same as in the Figure 1D). C) The simulated S-parameters with and without the interstitial layer of LCB1 buffer. Used reference planes are visible in the Figure 1A.